Measurement of Heavy Quark Forward-Backward Asymmetries and the B Mixing Parameter Using Z Decays Recorded with the OPAL Detector at LEP

Dissertation
zur Erlangung des Doktorgrades
des Fachbereichs Physik
der Universität Hamburg

vorgelegt von
Thomas Krämer
aus Bamberg

Hamburg
2004

Gutachter der Dissertation:	Prof. Dr. R.-D. Heuer Prof. Dr. F.-W. Büßer
Gutachter der Disputation:	Prof. Dr. R.-D. Heuer Prof. Dr. B. Naroska
Datum der Disputation:	27. September 2004
Dekan des Fachbereichs Physik:	Prof. Dr. G. Huber
Vorsitzender des Promotionsausschusses:	Dr. H. D. Rüter

Zusammenfassung

Diese Arbeit beschreibt die Messung der b- und c-Quark Vorwärts-Rückwärts-Asymmetrie mit dem OPAL-Detektor. Hierzu werden die hadronischen Zerfälle der am LEP-Beschleuniger in Elektron-Positron-Kollisionen produzierten Z-Bosonen untersucht. Nach einem Überblick über die verschiedenen Methoden, die diesbezüglich bei OPAL zum Einsatz kommen, wird eine Messung detailliert dargestellt. Diese verwendet die semileptonischen Zerfälle von b- und c-Quarks, um $\mathrm{b\overline{b}}$- und $\mathrm{c\overline{c}}$-Ereignisse zu trennen. Zur Separation der Ereignisse voneinander und vom Untergrund dienen künstliche neuronale Netze, die zur Identifikation von $\mathrm{b} \to \ell^-$, bzw. $\mathrm{c} \to \ell^+$ Zerfällen trainiert sind. Ein „Maximum-Likelihood-Fit“ dient zur simultanen Ermittlung der b- und c-Quark Vorwärts-Rückwärts-Asymmetrien $A_{\mathrm{FB}}^{\mathrm{b}}$ und $A_{\mathrm{FB}}^{\mathrm{c}}$ bei drei unterschiedlichen Schwerpunktsenergien $\sqrt{s}$, sowie dem B-Mischungsparameter $\overline{\chi}$ aus Ereignissen mit mindestens einem identifizierten Elektron oder Myon im Endzustand. Unter Verwendung aller mit dem OPAL-Detektor in der Nähe der Z-Resonanz von 1990 bis 2000 aufgezeichneten Daten werden folgende Asymmetrien gemessen:

$$
\begin{aligned}
A_{\mathrm{FB}}^{\mathrm{b}} &= (\ 4{,}7\ \pm 1{,}8\ \pm 0{,}1\ )\,\%, & A_{\mathrm{FB}}^{\mathrm{c}} &= (-6{,}8\ \pm 2{,}5\ \pm 0{,}9\ )\,\% & \text{bei } \langle\sqrt{s}\rangle &= 89{,}51 \text{ GeV},\\
A_{\mathrm{FB}}^{\mathrm{b}} &= (\ 9{,}72 \pm 0{,}42 \pm 0{,}15)\,\%, & A_{\mathrm{FB}}^{\mathrm{c}} &= (\ \ 5{,}68 \pm 0{,}54 \pm 0{,}39)\,\% & \text{bei } \langle\sqrt{s}\rangle &= 91{,}25 \text{ GeV},\\
A_{\mathrm{FB}}^{\mathrm{b}} &= (10{,}3\ \pm 1{,}5\ \pm 0{,}2\ )\,\%, & A_{\mathrm{FB}}^{\mathrm{c}} &= (\ 14{,}6\ \pm 2{,}0\ \pm 0{,}8\ )\,\% & \text{bei } \langle\sqrt{s}\rangle &= 92{,}95 \text{ GeV}.
\end{aligned}
$$

Für den B-Mischungsparameter erhält man:

$$\overline{\chi} = (13,12 \pm 0,49 \pm 0,42)\,\%.$$

Die statistische Unsicherheit der Messwerte wird jeweils durch den zweiten, die systematische durch den dritten Wert angegeben. Diese Ergebnisse werden mit den Resultaten der anderen OPAL-Messungen der b- und c-Quark Vorwärts-Rückwärts-Asymmetrien kombiniert, um daraus die OPAL-Asymmetrien am Maximum der Z-Resonanz zu ermitteln.

Die kombinierten Resultate aller elektroschwachen Observablen von LEP und SLD bilden die Grundlage zur Diskussion des aktuellen Standes hinsichtlich der Asymmetrieparameter $\mathcal{A}_{\mathrm{b}}$ und $\mathcal{A}_{\mathrm{c}}$, der Vektor- und Achsialvektorkopplungskonstanten v und a für b- und c-Quarks, sowie des leptonischen elektroschwachen Mischungswinkels $\sin^2\theta_{\mathrm{eff}}^{\ell}$. Abschließend wird der aus den b- und c-Quark Vorwärts-Rückwärts-Asymmetrien extrahierte Wert von $\sin^2\theta_{\mathrm{eff}}^{\ell}$ zur Abschätzung der Masse des im Standard-Modell postulierten Higgs-Bosons verwendet.

Abstract

This thesis deals with the measurement of the b and c quark forward-backward asymmetries of hadronic Z decays recorded with the OPAL experiment at the electron positron collider LEP. After an overview over the different kinds of heavy flavour forward-backward asymmetry measurements made within the OPAL collaboration, one of the methods is described in full detail. This method is based on the semileptonic b and c quark decays in order to identify primary $\mathrm{b\overline{b}}$ and $\mathrm{c\overline{c}}$ events. Two neural networks are used to separate the $\mathrm{b\overline{b}}$ and $\mathrm{c\overline{c}}$ events from each other and from the background. The first neural network is trained to identify $\mathrm{b} \rightarrow \ell^-$, the second to identify $\mathrm{c} \rightarrow \ell^+$ decays. A maximum likelihood fit is used to extract the b and c quark forward-backward asymmetries $A_{\mathrm{FB}}^{\mathrm{b}}$ and $A_{\mathrm{FB}}^{\mathrm{c}}$ at three centre-of-mass energies $\sqrt{s}$ and the average B mixing parameter $\overline{\chi}$ from a sample with at least one identified electron or muon in the final state. Using all data collected by OPAL near the Z resonance between 1990 and 2000, the asymmetries are measured to be:

$$
\begin{aligned}
A_{\mathrm{FB}}^{\mathrm{b}} &= (\ 4.7 \pm 1.8 \pm 0.1\ )\,\%, & A_{\mathrm{FB}}^{\mathrm{c}} &= (-6.8 \pm 2.5 \pm 0.9\ )\,\%, & \text{at } \langle\sqrt{s}\rangle &= 89.51 \text{ GeV},\\
A_{\mathrm{FB}}^{\mathrm{b}} &= (\ 9.72 \pm 0.42 \pm 0.15)\,\%, & A_{\mathrm{FB}}^{\mathrm{c}} &= (\ 5.68 \pm 0.54 \pm 0.39)\,\%, & \text{at } \langle\sqrt{s}\rangle &= 91.25 \text{ GeV},\\
A_{\mathrm{FB}}^{\mathrm{b}} &= (10.3 \pm 1.5 \pm 0.2\ )\,\%, & A_{\mathrm{FB}}^{\mathrm{c}} &= (\ 14.6 \pm 2.0 \pm 0.8\ )\,\%, & \text{at } \langle\sqrt{s}\rangle &= 92.95 \text{ GeV}.
\end{aligned}
$$

For the average B mixing parameter, a value of

$$\overline{\chi} = (13.12 \pm 0.49 \pm 0.42)\,\%$$

is obtained. The second value gives the statistical, the third the systematic error on the measurements. These results are combined with other OPAL measurements of the b and c quark forward-backward asymmetries, in order to derive values for the OPAL pole asymmetries.

The results of a global fit to all electroweak observables from LEP and SLD are taken to discuss the current situation concerning the asymmetry parameters $\mathcal{A}_{\mathrm{b}}$ and $\mathcal{A}_{\mathrm{c}}$, the vector and axial-vector coupling constants v and a for b and c quarks, and the effective electroweak mixing angle $\sin^2\theta_{\mathrm{eff}}^{\ell}$ for leptons. Finally, a prediction for the value of the Standard Model Higgs boson mass is given using $\sin^2\theta_{\mathrm{eff}}^{\ell}$ extracted from the b and c quark forward-backward asymmetries.

Contents

List of Figures

List of Tables

Chapter 1

Introduction

The development of science and technology during the 20th century led to a rapid acceleration of accumulating knowledge in a structured way. Concerning the subject of elementary particle physics, a systematic study of the fundamental processes and structures observable is believed to deliver a fundamental theory describing nature and thus allowing the prediction of all phenomena one could possibly think of. Often the development of physical theories means finding a common formalism for seemingly different effects. It is hoped that this unification process finally results in a single theory describing all known particles and interactions at all energy and distance scales. Today it seems as if modern physics already has made some important steps towards finding a unified theory.

A great success of theoretical and experimental particle physics of the last decades is the unification of electromagnetic and weak interactions, which is comparable to the development of Maxwell's equations in the 19th century providing a common theoretical description of electric and magnetic phenomena. As Maxwell's theory predicted electromagnetic waves which were subsequently experimentally confirmed, the unified description of electromagnetic and weak interactions postulated the existence of heavy gauge bosons (W, Z).

With the observation of neutral-current interactions in neutrino-nucleon scattering in 1973 [1] and the discovery of the W and Z bosons in proton-antiproton ($\mathrm{p\bar{p}}$) collisions ten years later [2, 3], the Standard Model of electroweak interactions is well supported experimentally. The further investigation of the electroweak interaction required a very clean environment. Such experimental conditions can be reached in the head-on collision of electrons and positrons (they are currently believed to be elementary particles). At this point experiments involving $\mathrm{e^+e^-}$ colliders contribute significantly to the understanding of the neutral-current sector of the Standard Model. The Z/γ interference, first observed in the scattering of polarised electrons from deuterium [4], can be confirmed by forward-backward asymmetry measurements of $\mathrm{e^+e^- \to f\bar{f}}$ reactions at PETRA and PEP [5].

After the commissioning of the LEP [6] and SLC [7] e^+e^- accelerators, experimental results on the neutral-current sector of the Standard Model are dominated by the experiments performed at these facilities. Both machines were designed during the 1980s to produce copious numbers of Z bosons, allowing detailed studies of the properties of the Z. While SLC only produced e^+e^- collisions at the Z pole, the LEP physics program was split in two phases. During the first phase – usually referred to as LEP1 (1989-1995) – the accelerator was operated at the Z resonance. The measurements of the total $e^+e^- \rightarrow f\bar{f}$ cross-section – one of the fundamental Standard Model parameters – at different energies at and around the Z peak allows a precise determination of the Z mass and width. The total and partial decay widths of the Z result in the unambiguous determination of the number of light neutrino families. The observed lepton forward-backward asymmetries and the tau polarisation measurements allow the experimental determination of the coupling constants between the Z and charged leptons. A comparison of the couplings among the three lepton generations leads to one of the cornerstones of the Standard Model: the concept of lepton universality. During the subsequent LEP2 phase (1995-2000) the LEP centre-of-mass energy was increased beyond the Z mass up to a maximum of 209 GeV, opening the possibility to investigate W pairs or to search for the Higgs boson [8] or other new particles.

All experimental results must be compared to theoretical predictions. Within the Standard Model theoretical predictions can only be made by perturbative calculations. The precision reached at LEP and SLC requires the calculation of higher order terms of the perturbation theory (radiative corrections) in order to give an adequate theoretical description of the measured quantities. Since the mass of the top quark and the Higgs boson enter those higher order terms, results from LEP and SLC allow the prediction of these masses. An impressive demonstration of the power of this method has been the prediction of the top mass value from precision measurements at LEP and SLC, before the direct discovery of the top quark in $p\bar{p}$ collisions at the TEVATRON in 1995 [9–12]. The same method is currently used to predict the mass of the one important missing particle in the Standard Model, the Higgs boson. With the precise knowledge of the parameters of the Standard Model from LEP, SLD, and the TEVATRON, and in particular with the measured value of the top quark mass, the dependence of the radiative corrections on the value of the mass of the hypothetical Higgs boson can be studied and compared to data. Currently all data point towards a comparatively light Higgs Boson, with masses below 200 GeV – beyond the reach of LEP or SLC, but well within the discovery range of the next generation of colliders like LHC or the Linear Collider.

Compared to the situation before LEP, SLC, and the TEVATRON data became available, the precision with which the parameters of the electroweak interaction are known has improved by – in some cases – three orders of magnitude. By measuring more observables than the number of parameters of the theory, its predictions and hence its consistency can be verified within the same experiments. In the same way as the experiments increased the knowledge of the theory parameters, the electroweak theory became more and more predictive and the tests of its consistency very stringent. Up to now none of the tests shows a significant discrepancy, so that the Standard Model stands on more solid ground than ever.

Nevertheless, after data taking at LEP, some effects of the order of three standard deviations still remained. One of these occurs by comparing different measurements which determine the effective electroweak mixing angle. Measurements using only leptons deliver significantly smaller results than results based on hadronic Z decays. The difference is mainly driven by the two most precise determinations: the measurement of the b quark forward-backward asymmetry $A_{\mathrm{FB}}^{\mathrm{b}}$ at LEP and the left-right polarisation asymmetry A_{LR} at SLD. The electroweak mixing angle mainly puts the weak and electromagnetic coupling strength into relation and consequently plays a central role in the concept of unifying the two interactions. In addition, radiative corrections render the effective mixing angle sensitive to the mass of the Higgs boson. For both reasons it is therefore important to understand the cause of the discrepancy between the mixing angle results, and to decide if it originates from a statistical fluctuation or gives a hint at a new physical phenomenon.

This thesis presents a measurement of the b and c quark forward-backward asymmetry, using semileptonic b and c decays reconstructed from hadronic Z boson decays recorded with the OPAL detector at LEP during its time of operation from 1990 to 2000. The results [13, 14] are a significant part of the OPAL contribution to the LEP combined b and c forward-backward asymmetries, and therefore also to the LEP and SLD result for the effective electroweak mixing angle.

This thesis is organised as follows: After a brief introduction to the Standard Model of electroweak interactions emphasising the features relevant for the neutral-current reaction $\mathrm{e^+e^-} \rightarrow \mathrm{Z} \rightarrow \mathrm{f\bar{f}}$, which are important for the b and c quark forward-backward asymmetry measurement (Chapter 2), a short description of the LEP accelerator and the OPAL detector is given together with the description of the available data and Monte Carlo events used (Chapter 3). The three different methods to determine the forward-backward asymmetry employed by OPAL are then outlined (Chapter 4), before the simultaneous measurement of the b and c quark forward-backward asymmetry using semileptonic quark decays is described in full detail (Chapter 5). Using all OPAL b and c quark forward-backward asymmetry measurements, the final OPAL values for these observables are determined (Chapter 6). For a broader discussion of the current situation the combination of all observables from the heavy flavour sector are used to extract the effective vector and axial-vector coupling constants of b and c quarks, as well as the effective electroweak mixing angle for leptons and for heavy quarks

(Chapter 6). The results of the thesis are summarised in Chapter 7.

Chapter 2

The Theoretical Foundation

In this chapter the main features of the Standard Model are outlined. The discussion focuses on the properties most relevant for Z physics at LEP. Particular emphasise is given to the theoretical aspects concerning the forward-backward asymmetry analysis presented later in this text. For a complete overview of the Standard Model, well established text books are available.

2.1 The Standard Model of Electroweak Interactions

The purpose of particle physics is to investigate the properties of the fundamental particles of which matter consists and the forces between them. The groups of elementary particles in nature – according to current knowledge – are the fermions which are the constituents of matter and the bosons which mediate the fundamental forces between the fermions. The four fundamental forces known in nature are the gravity, the weak, the electromagnetic, and the strong force. Gravity does not play any role in particle physics because of its small strength. The remaining three interactions are described in the framework of a relativistic quantum field theory which interprets interactions as exchanges of force carrier particles. This has led to the Standard Model of particle physics, a gauge theory based on the mathematical framework of local $\mathrm{SU}(3) \otimes \mathrm{SU}(2) \otimes \mathrm{U}(1)$ invariance. This symmetry is spontaneously broken, involving three distinct types of fields respectively particles: the gauge fields, the fermion matter fields and the Higgs field. The twelve different gauge fields correspond to the eight spin-1 bosons mediating the strong interaction, the gluons, and the four vector bosons of the electroweak theory ($\mathrm{W}^{\pm}$, Z, γ). The Higgs field is responsible for the elementary particle masses and will be introduced in the context of the electroweak theory. Its associated particle, the Higgs boson, has not yet been discovered [15].

			Q	T	T_3	Y
$\begin{pmatrix}\nu_\mathrm{e}\\ \mathrm{e}\end{pmatrix}_\mathrm{L}$	$\begin{pmatrix}\nu_\mu\\ \mu\end{pmatrix}_\mathrm{L}$	$\begin{pmatrix}\nu_\tau\\ \tau\end{pmatrix}_\mathrm{L}$	0 -1	$1/2$ $1/2$	$1/2$ $-1/2$	-1 -1
$\begin{pmatrix}\mathrm{u}\\ \mathrm{d}'\end{pmatrix}_\mathrm{L}$	$\begin{pmatrix}\mathrm{c}\\ \mathrm{s}'\end{pmatrix}_\mathrm{L}$	$\begin{pmatrix}\mathrm{t}\\ \mathrm{b}'\end{pmatrix}_\mathrm{L}$	$2/3$ $-1/3$	$1/2$ $1/2$	$1/2$ $-1/2$	$1/3$ $1/3$
$\mathrm{e_R}$	μ_R	τ_R	-1	0	0	-2
$\mathrm{u_R}$	$\mathrm{c_R}$	$\mathrm{t_R}$	$2/3$	0	0	$4/3$
$\mathrm{d'_R}$	$\mathrm{s'_R}$	$\mathrm{b'_R}$	$-1/3$	0	0	$-2/3$

Table 2.1: The three families of fermions and their quantum numbers (hypercharge Y, weak isospin T, and electric charge $Q = T_3 + \frac{Y}{2}$). Quantum numbers of antiparticles have reversed signs. The primed quarks d′, s′, b′ denote states which are mixed with respect to the strong interaction eigenstates d, s, b.

2.1.1 The Fermions

The fermions f (leptons and quarks) are considered to be point-like objects which is experimentally verified down to distances of $\mathcal{O}(10^{-16}$ cm). Quarks contrary to leptons do participate in strong interactions described by the theory of Quantum Chromodynamics (QCD). The fermion fields are two-component spinor fields as summarised in Table 2.1. There are three known generations of fermions with identical properties. Fermions of different generations are only distinguishable by their masses m_f and not by their electroweak or strong interactions. Measuring and comparing the couplings of fermions thus is an important test of the theory. For each fermion there is an antiparticle $\bar{\mathrm{f}}$ with the same mass but opposite additive quantum numbers (i.e. electric charge, or lepton number). Each quark species exists in three different colours, the analogue of the electric charge in strong interactions.

The Standard Model of electroweak interactions is based on the invariance of the Lagrangian under local gauge transformations. Electroweak interactions among the fundamental fermions are described by gauge invariant transformations of the weak isospin $\mathrm{SU(2)_L}$ and the weak hypercharge U(1). The fundamental fermions carry the quantum numbers of the weak isospin T, with its third component T_3, and the weak hypercharge Y (see Table 2.1.). The left-handed components of the fermions form isospin doublets and the right-handed components isospin singlets.

2.1.2 The Bosons

Between 1960 and 1970 S. L. Glashow, A. Salam, and S. Weinberg developed the electroweak theory [16–18], a unified theory of electromagnetism and weak force based on the group $\mathrm{SU}(2)_\mathrm{L} \otimes \mathrm{U}(1)$, which was extended to the hadronic sector via a mechanism introduced by S. L. Glashow, J. Iliopoulos, and L. Maiani [19], leading to the concept of N. Cabibbo, M. Kobayashi, and K. Maskawa for quark flavour mixing [20, 21]. The crucial new phenomenological input to the electroweak theory motivated by experiments [22] is that the weak interaction does not respect reflection symmetry, or parity[1]. The gauge fields of $\mathrm{SU}(2)_\mathrm{L}$ are the triplet $\overrightarrow{W_\mu} = \left(W_\mu^{(1)}, W_\mu^{(2)}, W_\mu^{(3)}\right)$, which exclusively couple to the left-handed fermion fields via a common coupling constant $\hat{g}$. Such a coupling has the spin structure of vector minus axial-vector, $V-A$. In the Dirac algebra it is represented by a factor $1-\gamma_5$, where γ_5 applied to a Dirac spinor, ψ, forms the axial-vector part of the coupling. Hereby the left-handed components (L) of the fermion fields form doublets, while the right-handed ones (R) are singlets under $\mathrm{SU}(2)_\mathrm{L}$ (indices in Table 2.1). A singlet B_μ together with the coupling constant g is assigned to the group U(1), acting on the fields of both helicity states (L and R),

$$\psi_\mathrm{L} = \frac{1-\gamma_5}{2}\psi \quad \text{and} \quad \psi_\mathrm{R} = \frac{1+\gamma_5}{2}\psi \,. \tag{2.1}$$

To comply with the massive gauge bosons observed in experiments, the $\mathrm{W}^\pm$ and Z bosons, the existence of a weakly interacting scalar field seems necessary: the Higgs field [8]. It is a complex doublet written as

$$\Phi = \frac{1}{\sqrt{2}}\begin{pmatrix}\phi_1 + \mathrm{i}\phi_2 \\ \phi_3 + \mathrm{i}\phi_4\end{pmatrix} \qquad \text{with} \qquad \Phi_0 = \frac{1}{\sqrt{2}}\begin{pmatrix}0 \\ v\end{pmatrix} \quad \text{and} \quad v^2 > 0 \tag{2.2}$$

with a non-vanishing vacuum expectation value Φ_0. The coupling to the Higgs field introduces spontaneous symmetry breaking of the massless gauge fields with respect to isospin rotation. This symmetry breaking leads to non-diagonal mass terms

$$\frac{1}{2}\left(\frac{\hat{g}}{2}v\right)^2\left((W_\mu^{(1)})^2 + (W_\mu^{(2)})^2\right) + \frac{v^2}{4}(W_\mu^{(3)}, B_\mu)\begin{pmatrix}\hat{g}^2 & g\hat{g} \\ g\hat{g} & g^2\end{pmatrix}\begin{pmatrix}W_\mu^{(3)} \\ B_\mu\end{pmatrix} \tag{2.3}$$

for the gauge fields in the Lagrangian energy density. The transformation from the gauge fields to the physical fields is realised via the linear transformation

$$\begin{aligned} W_\mu^\pm &= \frac{1}{\sqrt{2}}\left(W_\mu^{(1)} \mp \mathrm{i}W_\mu^{(2)}\right) \\ \begin{pmatrix}Z_\mu \\ A_\mu\end{pmatrix} &= \begin{pmatrix}\cos\theta_\mathrm{W} & -\sin\theta_\mathrm{W} \\ \sin\theta_\mathrm{W} & \cos\theta_\mathrm{W}\end{pmatrix}\begin{pmatrix}W_\mu^{(3)} \\ B_\mu\end{pmatrix} \end{aligned} \tag{2.4}$$

[1]Parity violation means that the interaction is different for the left-handed (L) and for the right-handed (R) components of the fermion fields.

This transformation introduces the weak mixing angle θ_w:

$$\cos\theta_\mathrm{W} = \frac{\hat{g}}{\sqrt{g^2+\hat{g}^2}} \quad \text{and} \quad \sin\theta_\mathrm{W} = \frac{g}{\sqrt{g^2+\hat{g}^2}} \tag{2.5}$$

In these fields the mass term (Eq. 2.3) is diagonal, giving

$$m_\mathrm{A} = 0 \quad , \quad m_\mathrm{W} = \frac{\hat{g}\cdot v}{2} \quad , \quad m_\mathrm{Z} = \frac{v}{2}\sqrt{g^2+\hat{g}^2} = \frac{m_\mathrm{W}}{\cos\theta_\mathrm{W}} \tag{2.6}$$

The derivative in the full electroweak Lagrangian related to the spin-1 boson A, the charge operator, leaves the vacuum expectation value Φ_0 of the Higgs field in (Eq. 2.2) invariant. Gauge fields coupled to unbroken symmetries do not acquire mass, and A can be identified with the massless photon γ. It couples to the charged fermions via the electric charge e (or the electromagnetic coupling constant $\alpha = e^2/4\pi$), expressed here using the gauge couplings

$$e = \frac{g\cdot\hat{g}}{\sqrt{g^2+\hat{g}^2}} = \hat{g}\cdot\sin\theta_\mathrm{W} = g\cdot\cos\theta_\mathrm{W} \tag{2.7}$$

The charged weak current is mediated by $\mathrm{W}^\pm$ bosons. As a linear combination of the $W_\mu^{(1,2)}$ gauge bosons of $\mathrm{SU(2)_L}$, (Eq. 2.4), the $\mathrm{W}^\pm$ bosons couple only to left-handed particles (right-handed antiparticles). The Z boson turns out to be the carrier of the neutral weak current. Its coupling to fermions do not show a pure $(V-A)$ structure any more due to the mixed state of $W_\mu^{(3)}$ and B_μ. The Z coupling is therefore modified to

$$(v_\mathrm{f} - a_\mathrm{f}\cdot\gamma_5) \tag{2.8}$$

The vector and axial-vector coupling coefficients v_f and a_f depend on the fermion charges, Q_f, the three-components of the weak isospin, T_3^f, and the electroweak mixing angle, θ_w:

$$v_\mathrm{f} = T_3^\mathrm{f} - 2Q_\mathrm{f}\sin^2\theta_\mathrm{W} \qquad \text{and} \qquad a_\mathrm{f} = T_3^\mathrm{f} \tag{2.9}$$

This interference between vector and axial-vector coupling of fermions to the Z boson is the origin of the forward-backward asymmetry occurring in the $\mathrm{e^+e^-} \to \mathrm{Z} \to \mathrm{q\overline{q}}$ process at centre-of-mass energies around the mass of the Z boson. In the Standard Model the coupling constants a_f and v_f are universal for all generations. In particular, the equality of these coupling constants for the three charged leptons, referred to as lepton universality, has been verified with high accuracy at LEP. From (Eq. 2.9) the relative couplings of the Z to left- and right-handed fermions, c_L^f and c_R^f, are obtained:

$$\begin{aligned} c_\mathrm{L}^\mathrm{f} &= v_\mathrm{f} + a_\mathrm{f} = 2\left(T_3^\mathrm{f} - Q_\mathrm{f}\sin^2\theta_\mathrm{W}\right) \\ c_\mathrm{R}^\mathrm{f} &= v_\mathrm{f} - a_\mathrm{f} = -2Q_\mathrm{f}\sin^2\theta_\mathrm{W} \end{aligned} \tag{2.10}$$

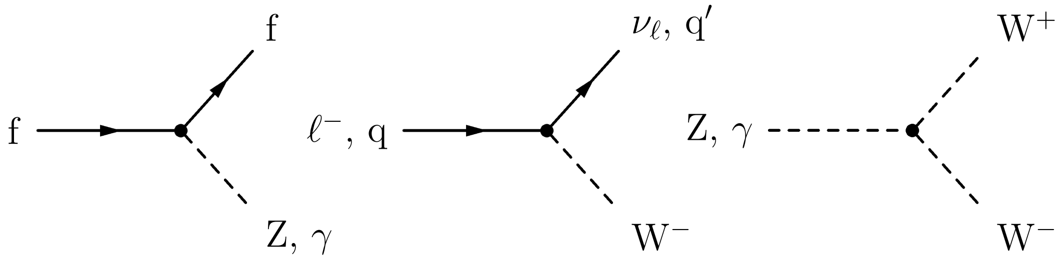

Figure 2.1: The fundamental Feynman graphs of the electroweak theory. From left to right is shown the neutral current, the charged current and the boson self-coupling.

Calculations in the Standard Model are expressed as a perturbative expansion in terms of the coupling constant, where the terms are represented by Feynman diagrams containing increasing numbers of fundamental vertices. The different types of fundamental electroweak vertices are shown in Figure 2.1. The neutral current manifests itself as radiation of a photon or Z by a fermion as well as in the crossed processes, fermion pair production and annihilation. The mid diagram shows the charged current via radiation of a $\mathrm{W}^\pm$ boson, hereby changing the flavour, i.e. a charged lepton ℓ^- into its neutrino ν_ℓ and a quark q into its isospin partner quark q'. Also, the coupling between gauge bosons is possible: the decay of a neutral boson into charged $\mathrm{W}^\pm$ bosons as observed at centre-of-mass energies above 161 GeV.

The fermions spontaneously acquire mass as well; this time via a generic "Yukawa" interaction, $g_\mathrm{f}\bar{\psi}\psi\mathbf{\Phi}$. This type of interaction is not a gauge interaction, and the fermion masses are not predicted by the electroweak theory. Instead, they are determined not only by the scale of the electroweak symmetry breaking, v, but also by their Yukawa coupling to the Higgs field. This coupling, $g_\mathrm{f} = m_\mathrm{f}\sqrt{2}/v$, is arbitrary in the Standard Model. Here it can be seen from the coupling that the Higgs couples most strongly to the heaviest particles.

Only the weak interaction is able to change a member of an isospin doublet to the corresponding partner within one family. As a consequence, the lighter quark in each family is stable — like the neutrino in the case of the lepton doublets. However, stable particles with s or b quark content are not found in nature; instead, the decay of s quarks into u quarks is observed. The reason for that is the electroweak eigenstates d$'$, s$'$ and b$'$ not coinciding with the mass eigenstates, but forming a linear combination,

$$\begin{pmatrix} \mathrm{d}' \\ \mathrm{s}' \\ \mathrm{b}' \end{pmatrix} = \mathrm{U} \begin{pmatrix} \mathrm{d} \\ \mathrm{s} \\ \mathrm{b} \end{pmatrix} \tag{2.11}$$

The transformation matrix U is called Cabibbo-Kobayashi-Maskawa (CKM) matrix. It is not diagonal, and hence leads to transitions between quark generations in the charged current interaction. However, U is unitary, so that the neutral current part becomes diagonal in the mass basis, i.e. flavour-changing neutral currents do not exist. Since the CKM matrix describes a rotation around an axis in three dimensions, it has four free parameters: three "rotational angles" and one CP-violating phase.

The minimal Standard Model, as outlined above, contains only one complex scalar doublet. However, symmetry breaking can also be achieved by the introduction of more complicated structures. One defines the ρ_0 parameter by the ratio of neutral to charged current coupling strength or equivalently as the deviation from the vector boson mass relation (Eq. 2.12):

$$\rho_0 = \frac{m_{\mathrm{W}}^2}{m_{\mathrm{Z}}^2 \cos^2\theta_{\mathrm{W}}} \tag{2.12}$$

The ρ_0 parameter is unity in the Standard Model with one Higgs doublet, and the introduction of further isospin doublets does not modify the ρ_0 parameter. Deviations from $\rho_0 = 1$ then can originate only from radiative corrections (see Section 2.4).

2.2 Quantum Chromodynamics (QCD)

At about the same time in the 1960ies, M. Gell-Mann, Y. Ne'eman, and G. Zweig derived the quark hypothesis from the ordinance of the more and more copiously discovered hadrons [23–25]. This hypothesis implies that all strongly interacting particles consist of elementary particles called quarks. According to the knowledge of those days the Δ^{++} resonance (uuu) or the ρ particle (ddd) had identical quantum numbers, violating the Pauli principle. In order to conserve the Pauli principle, the quarks have to carry a new degree of freedom, colour[2].

In Quantum Chromodynamics, $\mathrm{SU}(3)_{\mathrm{C}}$ is therefore selected as a gauge group, implying that quarks carry colour charge, which the eight gauge bosons of $\mathrm{SU}(3)_{\mathrm{C}}$, the gluons, couple to. The $\mathrm{SU}(3)_{\mathrm{C}}$ group is believed to be an exact gauge symmetry so that the gluons are massless. Its non-abelian structure makes the gluons themselves carriers of colour and allows self-coupling between differently colour-charged gluons, analogous to the $\mathrm{ZW}^+\mathrm{W}^-$ and $\gamma\mathrm{W}^+\mathrm{W}^-$ vertices in the electroweak interaction. The fundamental processes of QCD are the gluon radiation or quark pair production, and the self-coupling of three and four gluons.

[2] The colour charge exists in three states, termed red, green and blue. A $\mathrm{SU}(3)_{\mathrm{C}}$ triplet consists of a red, green and blue quark of identical flavour; hence the strong interaction does not change flavour.

The choice of $SU(3)_C$ is confirmed experimentally by many processes that directly measure the number of different existing colour charge states, N_c^f. An example is the measurement of the ratio $R = \sigma(e^+e^- \to q\overline{q})/\sigma(e^+e^- \to \mu^+\mu^-)$ of the hadronic cross-section to the muon cross-section in e^+e^- annihilation which is directly proportional to N_c^f. The data clearly indicate $N_c^f = 3$ [26].

Experiments only observe colour-neutral bound states, the hadrons. They are divided into two groups: The Baryons consist of three quarks, one in each colour state. In analogy to chromatics this forms a colour-neutral state. The mesons consist of a quark-antiquark pair, so that colour and anti-colour add to a neutral state. Baryons have half-numbered spins while mesons have integral spin. There are two very striking properties of the dynamical behaviour of the strong interaction causing quarks not to appear as single (colour charged) states: confinement and asymptotic freedom.

- Confinement is a mechanism which encloses bound state partons in the space of the size of about a nucleus. Terms rapidly rising with distance in the potential between quarks make it energetically impossible to separate them. If quark pairs are created in high energy collision experiments and move apart in their centre-of-mass rest frame, the energy stored in the colour field is sufficient to create additional quark-antiquark pairs in a process called fragmentation, thus neutralising colour. Confinement also explains the short-range nature of nuclear forces, while exchange of massless gluons otherwise is long-range.

- The asymptotic freedom allows the quasi-free movement at small distances equivalent to high energies.

This behaviour is expressed in the theory by a scale dependent coupling constant α_s, which rises rapidly with decreasing energy.

The energy dependence is derived from renormalisation (see also Section 2.4), a technique to cancel divergences in the Feynman amplitudes of higher order perturbation theory by including them into the coupling "constant". This *running* of the coupling constant has to solve the renormalisation group equation (RGE), which itself is a consequence of requiring the renormalisation process to be independent of the renormalisation scale μ. In next-to-leading order the RGE reads

$$\mu^2 \frac{\mathrm{d}\,\alpha_s(\mu^2)}{\mathrm{d}\mu^2} = -b_0\alpha_s^2 - b_1\alpha_s^3 + \mathcal{O}(\alpha_s^4) \tag{2.13}$$

with $\quad b_0 = \dfrac{33 - 2n_f}{12\pi}\,, \qquad b_1 = \dfrac{153 - 19n_f}{24\pi^2}\,, \qquad n_f = \text{no. of flavours}\,.$

Its most general solution is

$$\alpha_s = \frac{1}{b_0 \log \frac{\mu^2}{\Lambda^2}} - \frac{b_1 \log\left(\log \frac{\mu^2}{\Lambda^2}\right)}{\left(b_0 \log \frac{\mu^2}{\Lambda^2}\right)^2} + \mathcal{O}\left(\frac{\log^2\left(\log \frac{\mu^2}{\Lambda^2}\right)}{\log^2 \frac{\mu^2}{\Lambda^2}}\right) \tag{2.14}$$

Although the forward-backward asymmetry is the result of a purely electroweak process, a precise model for the running of α_s is needed in the correction for QCD effects in the measured asymmetry and in the simulation of hadronic final states.

2.3 The Standard Model Parameters

The Standard Model of electroweak and strong interaction features altogether 18 free parameters. They are not predicted by the model but must be determined by experiment and used as inputs to the model. A commonly used set of these input parameter is the on-shell renormalisation scheme [27]:

α, m_Z, m_W, m_H
6 quark and 3 lepton masses
α_s, 4 CKM matrix parameters

The number of parameters probably needs to be complemented by the neutrino masses and a corresponding mixing matrix [28]. But neutrino masses are too small to be detected directly and may have a different origin than the masses of the quarks and charged leptons, so this has not yet been fully implemented in the Standard Model.

Given the QED coupling constant $\alpha = e^2/4\,\pi$ and the two vector boson masses m_W and m_Z, all observables in $e^+e^- \to f\bar{f}$ reactions can be calculated in lowest order. In fact, only these three parameters enter in the Standard Model formulae given in the previous section. In particular, the weak mixing angle is defined by the ratio of the W and Z mass.

To incorporate mass effects and higher order diagrams in the calculations the masses of all fermions are required. Corrections to the massive gauge boson propagators, as well as Higgs production cross-section, depend on the mass m_H of the Higgs boson. In hadronic final states the strong coupling constant α_s enters through QCD radiative corrections. The Cabbibo-Kobayashi-Maskawa (CKM) matrix relates the electroweak and mass eigenstates of quarks.

These parameters are all measured by now, except the mass of the still undiscovered Higgs boson. In Standard Model calculations of electroweak observables assumptions about m_H based on experimental and theoretical limits have to be made. The mass of the top quark plays an important role in precise Standard Model calculations. The QED coupling constant α is measured at low momentum transfer (Thomson scattering limit) for instance with the Quantum Hall effect or in $g-2$ experiments with very high precision. Going to higher energies α is not a constant any more but growth with increasing energy (see Section 2.4). Also the mass of the Z is now precisely determined by the experiments at LEP and does not introduce any sizeable uncertainty in Standard Model calculations. However, the W mass is only known to a relative precision of $\Delta m_{\mathrm{W}}/m_{\mathrm{W}} = 2 \cdot 10^{-3}$. This is not adequate for the measurements performed at LEP which are of similar or sometimes even better accuracy. This parameter is therefore replaced by the Fermi coupling constant G_{F} determined from the muon lifetime τ_μ [29] (see Section 2.4).

The Standard Model has been firmly established by the enormous success in predicting new particles (c, b, t, $\mathrm{W}^\pm$ and Z) and by its ability to accurately describe the bulk of the present data.

Problems and Questions

The existence of the Higgs boson and the parameters in the neutrino sector are the main open questions raised by the Standard Model, which have to be answered in the future. In addition there are aesthetic reasons why the gauge theory based on $\mathrm{SU}(3)_{\mathrm{C}} \otimes \mathrm{SU}(2)_{\mathrm{L}} \otimes \mathrm{U}(1)$ is not considered as the final theory:

- The total number of fermion families in the theory is neither predicted nor restricted.
- The sum of the electric charges in each family vanishes, which is not explained but turned out to be necessary for the construction of a renormalisable theory.
- The fermion masses are arbitrary parameters in the Standard Model. A fundamental theory is expected to explain their very wide spectrum.
- $\mathrm{SU}(3)_{\mathrm{C}} \otimes \mathrm{SU}(2)_{\mathrm{L}} \otimes \mathrm{U}(1)$ is not a unified theory. For each group factor there is a different coupling constant. In addition, there is no reason why the electric charge is quantised, as in Abelian QED.

Theories beyond the Standard Model try to unify the three forces by regarding $\mathrm{SU}(3)_{\mathrm{C}} \otimes \mathrm{SU}(2)_{\mathrm{L}} \otimes \mathrm{U}(1)$ as the remnants of a larger, but simple group G, which is spontaneously broken at very high energies. All possible candidates for such a grand unified theory (GUT) suffer from the hierarchy problem, the need of having a very fine-tuned cancellation of the quadratic divergences in the mass correction terms of the scalar particles. This problem is technically solved by supersymmetric GUTs (SUSY). They are theoretically very interesting extensions of the Standard Model. Supersymmetry is a symmetry between fermions and bosons. This symmetry is realised by adding "super-partners" to all Standard Model particles, leading to a 1:1 correspondence of fermions and bosons. Of course, if Supersymmetry is realised in nature, it must be broken, because otherwise the super-partners would have the same mass as their Standard Model partners. Models that assume a specific SUSY breaking process[3] are able to express all the low-energy parameters in terms of a few free parameters at the GUT scale. The specific models are much more predictive than the unconstrained SUSY, which makes no specific assumptions but uses a parameterisation of all SUSY-breaking terms instead. Further theories, which go beyond SUSY, replace the model of point-like particles by a theory of vibrating superstrings. Currently Supersymmetry or superstrings cannot be verified or excluded by experiments.

2.4 Radiative Corrections

The Feynman rules are used to calculate exchange amplitude matrix elements to predict processes and observables in the framework of the Standard Model. The matrix elements or probabilities of all graphs with identical initial and final state have to be added, thus leading to a perturbation expansion in orders of the coupling constant. Already the lowest order, the Born level, gives a meaningful prediction. The measurements at LEP and SLC are sensitive to one-loop effects and even higher orders. In addition the high quality of the fits to all data confirms the presence of these radiative corrections. Therefore theory predictions have to account for virtual loops and higher-order corrections. Within one theoretical model, i.e. concerning the relation between the free parameters, the choice of the renormalisation scheme is relevant.

For the electroweak corrections the "on shell" scheme is chosen. One of its advantages is the possibility of treating weak and photonic corrections separately in first order perturbation theory. The different radiative corrections are summarised in the following; a more detailed description can be found in [30].

Weak Radiative Corrections

The Fermi coupling constant G_{F} can be determined from the muon lifetime τ_μ ($\mu \rightarrow \mathrm{e}\bar{\nu}_{\mathrm{e}}$):

[3] The most prominent of these specific models or scenarios are minimal Supergravity (mSUGra), minimal Gauge Mediated SUSY Breaking (mGMSB), and minimal Anomaly Mediated SUSY Breaking (mAMSB).

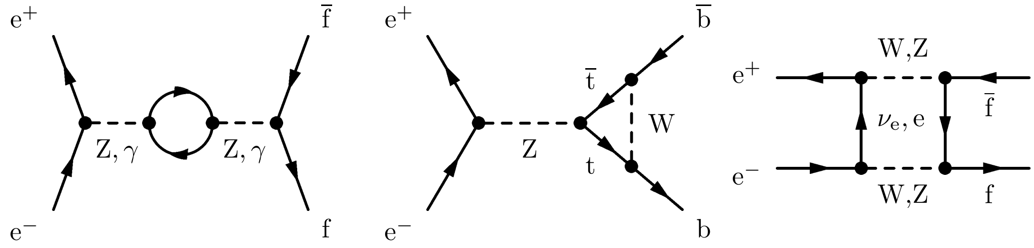

Figure 2.2: The principal Feynman diagrams of the weak radiative corrections: correction to the Z/γ propagator, vertex correction, and box diagram (from left to right).

$$
\begin{aligned}
\frac{1}{\tau_\mu} &= \frac{G_F^2}{192\,\pi^3}\, m_\mu^5 \left(1 - 8\,\frac{m_e^2}{m_\mu^2}\right)\left(1 + \frac{3}{5}\,\frac{m_e^2}{m_W^2} + \delta_{QED}\right) \\
\delta_{QED} &= \frac{\alpha}{2\,\pi}\left(\frac{25}{4} - \pi^2\right)
\end{aligned}
\tag{2.15}
$$

The experimental result $\tau_\mu = 2.197\,03 \pm 0.000\,04$ μs yields $G_F = 1.166\,39(1) \cdot 10^{-5}$ GeV^{-2} [26]. Mass effects and photonic corrections, δ_{QED}, to the lowest order diagram of the muon decay are taken into account in the definition of G_F. Other higher order corrections are contained in the definition of the physical mass m_W, but are not accounted for in Eq. 2.15 where G_F is defined. The relation between m_W and G_F thus contains a term Δr describing the electroweak radiative corrections:

$$
\frac{G_F}{\sqrt{2}} = \frac{\pi\,\alpha}{2}\,\frac{1}{m_W^2 \sin^2\theta_W}\,\frac{1}{1 - \Delta r} \tag{2.16}
$$

It can be split into QED corrections due to the running of the QED coupling constant $\Delta\alpha$ and pure weak corrections $\Delta r_w = \cot^2\theta_w \cdot \Delta\rho$:

$$
\Delta r = \Delta\alpha - \cot^2\theta_w \cdot \Delta\rho + \Delta r_{rem} \tag{2.17}
$$

The second-order weak corrections (one-loop diagrams) can be divided into three groups: corrections to the Z/γ propagator, vertex corrections, and box diagrams. For each of them an example is given in Figure 2.2. In the first two graphs virtual particles contribute (t quark, Higgs boson), although they cannot be produced kinematically at LEP energies as real particles.

The close coupling between t and b quark within the electroweak isospin doublet enables a $t\bar{t}$ pair to be produced and later converted to a $b\bar{b}$ final state by W exchange. Weak isospin symmetry breaking by fermion doublets with large mass splitting modifies the ρ-parameter [31–33] which is unity in lowest order (see Eq. 2.12 and text in Section 2.1.2). The leading contribution is quadratic in m_{t}:

$$\begin{aligned}\bar{\rho} &= 1 + \Delta\rho \\ \Delta\rho &= \frac{3\,G_{\mathrm{F}}\,m_{\mathrm{W}}^2}{8\sqrt{2}\,\pi^2}\frac{m_{\mathrm{t}}^2}{m_{\mathrm{W}}^2} - \frac{3\,G_{\mathrm{F}}\,m_{\mathrm{W}}^2}{8\sqrt{2}\,\pi^2}\frac{\sin^2\theta_{\mathrm{W}}}{\cos^2\theta_{\mathrm{W}}}\left(\ln\frac{m_{\mathrm{H}}^2}{m_{\mathrm{W}}^2} - \frac{5}{6}\right) + \cdots \end{aligned} \tag{2.18}$$

The effect of the top quark mass is large and the precision measurements at LEP of the Z widths and the asymmetries have been used to constrain m_{t} in the Standard Model, before the t quark was discovered at the TEVATRON in 1995 [9–12]. Now it is the experimental error of its direct measurement that influences the interpretation of heavy quark results.

For the Higgs boson mass, however, the corrections proportional to m_{H}^2 are cancelled out, leaving only logarithmic terms. Also the two-loop level radiative corrections are relatively insensitive to m_{H}, so that it is difficult to extract the Higgs boson mass from fits to the electroweak precision data.

Box diagrams refer to the exchange of two massive bosons and become resonant only at LEP 2 energies near the WW and ZZ thresholds, at 161 GeV and above. Their effect turns out to be negligibly small at the Z resonance, but is nevertheless included in the flavour-dependent form factors ρ_{f} (Eq. 2.22) [30, 34].

Since the weak corrections do not depend on the experimental set-up, they can be absorbed into the energy dependence of the electromagnetic coupling, the definition of an effective electroweak mixing angle, and the re-definition of the couplings to the Z boson [35].

$$\alpha \;\rightarrow\; \alpha(m_{\mathrm{Z}}^2) = \frac{\alpha}{1-\Delta\alpha} \approx 1.064\cdot\alpha \tag{2.19}$$

$$\sin^2\theta_{\mathrm{W}} \;\rightarrow\; \sin^2\theta_{\mathrm{eff}}^{\mathrm{f}} = \left(1 + \frac{\cos^2\theta_{\mathrm{W}}}{\sin^2\theta_{\mathrm{W}}}\Delta\bar{\rho}_{\mathrm{f}} + \cdots\right)\sin^2\theta_{\mathrm{W}} \tag{2.20}$$

$$a_{\mathrm{f}} \;\rightarrow\; \bar{a}_{\mathrm{f}} = \sqrt{\bar{\rho}_{\mathrm{f}}}\cdot a_{\mathrm{f}} \tag{2.21}$$

$$v_{\mathrm{f}} \;\rightarrow\; \bar{v}_{\mathrm{f}} = \sqrt{\bar{\rho}_{\mathrm{f}}}\cdot\left(T_3^{\mathrm{f}} - 2Q_{\mathrm{f}}\sin^2\theta_{\mathrm{eff}}^{\mathrm{f}}\right) \tag{2.22}$$

This definition is termed the improved Born level, indicating that the structure of the tree level equations does not need to be modified. In the following it will be used as lowest order in the theory predictions.

In principle, the effective couplings are different for the fermions, because of the flavour dependent corrections to the $\mathrm{Zf\bar{f}}$ vertex resulting in slightly different $\bar{\rho}_{\mathrm{f}}$ values. However, with the exception of the $\mathrm{Zb\bar{b}}$ vertex the differences are small compared to the current experimental error on these quantities.

In this section the weak radiative corrections originating from Standard Model effects are outlined. The interpretation of observables like $\sin^2\theta^{\ell}_{\text{eff}}$ in terms of m_{t} or m_{H} thus implies the validity of the Standard Model and that there are no other causes changing the effective couplings of the fermions to the Z. Possible effects could originate from additional particles predicted by Supersymmetry, which would modify the ρ-parameter obtained from measurements at the Z resonance [36].

The interpretation of direct experimental observables (total cross-sections, asymmetries) in terms of physical parameters is done in steps of increasing level of assumptions about the underlying theory. The extraction of Z parameters (mass and width) can be done in a way which relies only on the validity of QED and without assuming that weak radiative corrections originate from known Standard Model processes and particles only. Also, the effective couplings $\bar{v}_{\text{f}}$ and $\bar{a}_{\text{f}}$, and thus $\sin^2\theta^{\text{f}}_{\text{eff}}$, can be obtained from the measured asymmetries, corrected only for QED effects. This is often called "model independent" just because it allows the comparison of these derived quantities with the Standard Model without restricting them to their Standard Model expectations.

Using these results to constrain parameters like m_{H} depends on the validity of the Standard Model and ignores possible contributions to the observed cross-sections and asymmetries from physics not described by the Standard Model.

QED Radiative Corrections

The QED radiative corrections comprise all Feynman diagrams with an emission of a real photon and with an internal photon loop. The QED corrections are calculated with very high precision and do not add to the sensitivity of the Standard Model parameters. However, in e^+e^- annihilation the corrections due to photon emission in the initial e^+e^- state (Initial State Radiation: ISR) are particularly large:

- At energies far above the Z peak, the emission of a photon reduces the centre-of-mass energy available to the e^+e^- system so that the annihilation reaction takes place at the Z peak, which is favoured due to its much higher cross-section. The total cross-section is thereby increased, and observables (such as the forward-backward asymmetries) receive contributions from the effective lower energies $\sqrt{s'} < \sqrt{s}$.
- At energies which are just a few GeV above the Z peak, it is sufficient to include the ISR correction in the theory prediction.
- At the Z peak the ISR correction still represents the main part of the QED correction, leading to a reduction of both cross-section and asymmetry of

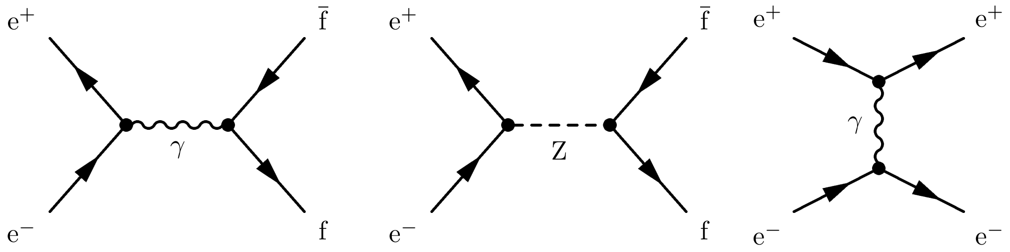

Figure 2.3: The Feynman diagrams for e^+e^- annihilation into fermions at energies close to the Z resonance. Directly at $\sqrt{s} = m_Z$, the Z exchange (middle) is by far the dominant channel. The reaction $e^+e^- \to e^+e^-$ receives a contribution from the t channel exchange (right diagram).

the order of 10 %. The correction to the forward-backward asymmetry due to final state radiation amounts to 0.17 %, and the interference between both is negligibly small.

The QED corrections are calculated within the ZFITTER programme package [34]; their effect on the b and c asymmetries are discussed in more detail in Section 2.6.

QCD Radiative Corrections

Radiating gluons in the quark final state differs from photon final state radiation only by the strong coupling constant and its characteristics. However, as colour-charged particles the radiated gluons are subject to confinement and contribute to the hadron formation. The treatment of gluon radiation is therefore a part of the phenomenological models for the transition from quarks to hadrons (see Section 2.7.2), and is not combined with the other radiative corrections to the analytic theory prediction. The effects of gluon radiation on the asymmetry depend on the experimental set-up. Their correction is described later in Section 5.8.

2.5 Fermion Pair Production in e^+e^- Collision

The production of a fermion-antifermion pair in electron-positron annihilation is described in lowest order by the exchange of a photon and a Z boson as shown in Figure 2.3. In particular, heavy quark final states can only be created by the s-channel exchange of a neutral gauge boson. The two s-channel diagrams on the left side lead to three terms in the cross-section corresponding to the exchange of a photon, a Z boson and the interference of both with their individual contributions depending on $s = E_{\mathrm{CMS}}^2$. The electroweak theory predicts the cross-section as a function of the scattering angle θ (angle between the incoming electron e^- and the outgoing fermion f) in the reaction $e^+e^- \to f\bar{f}$ at the improved Born level (allowing for mass effects) to

$$\begin{aligned}\frac{\mathrm{d}\,\sigma_\mathrm{f}}{\mathrm{d}\,\cos\theta} &= \frac{2\pi\alpha^2}{4s} N_c^\mathrm{f} \sqrt{1-4\mu_\mathrm{f}}\,\cdot \\ &\cdot \left[G_1(s)(1+\cos^2\theta) + 4\mu_\mathrm{f} G_2(s)\sin^2\theta + \sqrt{1-4\mu_\mathrm{f}}\,G_3(s)\cdot 2\cos\theta\right]\end{aligned} \tag{2.23}$$

$$\begin{aligned}G_1(s) &= Q_\mathrm{f}^2 - 2v_\mathrm{e}v_\mathrm{f}Q_\mathrm{f}\mathrm{Re}\chi(s) + (v_\mathrm{e}^2+a_\mathrm{e}^2)(v_\mathrm{f}^2+a_\mathrm{f}^2-4\mu_\mathrm{f}a_\mathrm{f}^2)\,|\chi(s)|^2 \\ G_2(s) &= Q_\mathrm{f}^2 - 2v_\mathrm{e}v_\mathrm{f}Q_\mathrm{f}\mathrm{Re}\chi(s) + (v_\mathrm{e}^2+a_\mathrm{e}^2)v_\mathrm{f}^2\,|\chi(s)|^2\ , \\ G_3(s) &= \underbrace{\quad}_{\gamma\text{-exch.}} - \underbrace{2a_\mathrm{e}a_\mathrm{f}Q_\mathrm{f}\mathrm{Re}\chi(s)}_{\gamma\text{–Z-interference}} + \underbrace{4v_\mathrm{e}a_\mathrm{e}v_\mathrm{f}a_\mathrm{f}|\chi(s)|^2}_{\text{pure Z-exchange}}\end{aligned} \tag{2.24}$$

with $\mu_\mathrm{f} = m_\mathrm{f}^2/s$ (m_f = fermion mass). The number of colour degrees of freedom N_c^f is 1 for leptons and 3 for quarks.

The vector and axial-vector couplings defined in Eq. 2.9 and Eq. 2.22 as well as the Z propagator

$$\chi(s) = \underbrace{\frac{1}{4\,\sin^2\theta_\mathrm{W}\,\cos^2\theta_\mathrm{W}}}_{\lambda} \cdot \underbrace{\frac{s}{s - m_\mathrm{Z}^2 + \mathrm{i}\,m_\mathrm{Z}\,\Gamma_\mathrm{Z}}}_{\chi_0} \tag{2.25}$$

with the total decay width

$$\Gamma_\mathrm{Z} = \sum_\mathrm{f} N_c^\mathrm{f}\,\frac{\alpha\lambda}{3}\,m_\mathrm{Z}\,\sqrt{1-4\mu_\mathrm{f}}\,\left(v_\mathrm{f}^2(1+2\mu_\mathrm{f}) + a_\mathrm{f}^2(1-4\mu_\mathrm{f})\right) \tag{2.26}$$

is used.

Eq. 2.23 is valid only for unpolarised initial states and for the sum of all polarisation states of the final states. Furthermore, it is restricted to the case that the outgoing fermion is not an electron, as for electrons the t channel exchange (Bhabha scattering) has to be added (Figure 2.3 on the right). For the analysis of Z decays to heavy quarks it forms a background contribution, that can be fully suppressed by selection cuts, and is therefore neglected in the following.

The total cross-section $e^+e^- \to f\bar{f}$ is found to be:

$$\sigma_\mathrm{f}(s) = \int_{-1}^{1} \frac{\mathrm{d}\,\sigma_\mathrm{f}}{\mathrm{d}\,\cos\theta}\,\mathrm{d}\,\cos\theta = \frac{\pi\alpha^2}{4s}N_c^\mathrm{f}\,\sqrt{1-4\mu_\mathrm{f}}\,\left(\frac{8}{3}G_1 + 2\pi\mu_\mathrm{f}G_2\right) \tag{2.27}$$

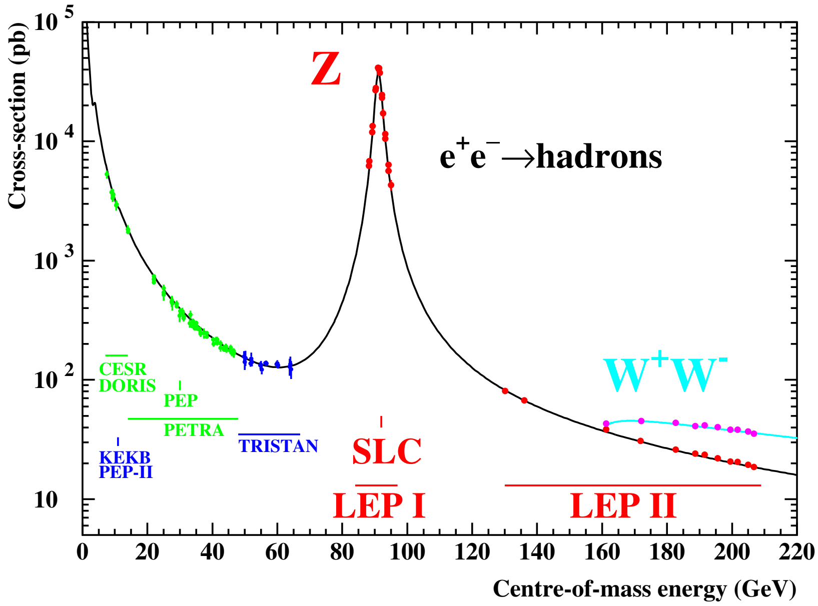

Figure 2.4: The hadronic cross-section as a function of centre-of-mass energy. The solid line is the prediction of the Standard Model, and the points are the experimental measurements. Also indicated are the energy ranges of various e^+e^- accelerators. The cross-sections have been corrected for the effects of photon radiation.

At $\sqrt{s} = m_Z$ the Z propagator (Eq. 2.25) becomes resonant so that the photon exchange and its interference with the Z exchange can be neglected.

Figure 2.4 shows the total cross-section for $e^+e^- \to$ hadron as a function of the centre-of-mass energy $\sqrt{s}$. One notices the enormous increase of the cross-section at the Z pole as compared to the $1/s$ dependence of the pure photon exchange in QED. Indicated are the approximate energy ranges of e^+e^- accelerators. The effect of the Z on the total cross-section is small for the previous generation of e^+e^- accelerators PEP, PETRA, and TRISTAN. For the experiments performed at LEP and SLC at the Z resonance, the cross-section $e^+e^- \to$ hadron is about thousand times larger than the cross-section from photon exchange.

2.6 The Forward-Backward Asymmetry

The terms proportional to $\cos\theta$ in the differential cross-section (Eq. 2.23) lead to a difference in the number of fermions produced in the forward and backward

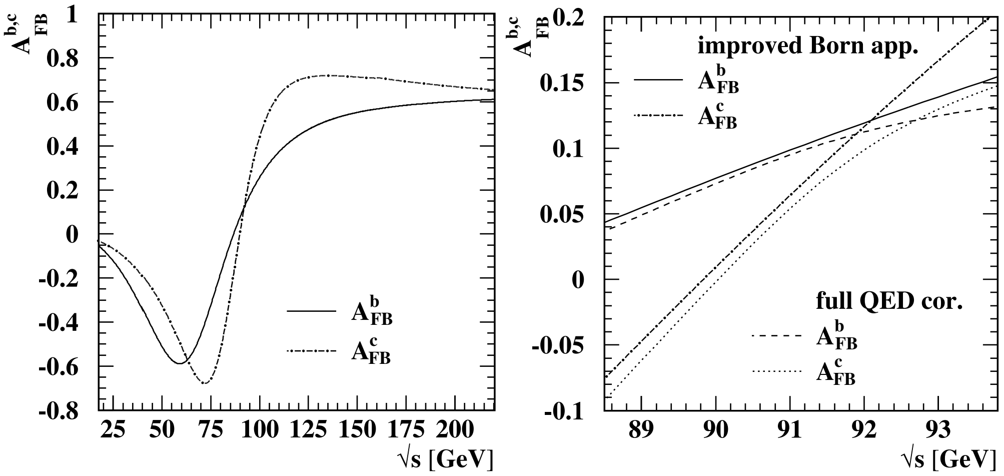

Figure 2.5: The forward-backward asymmetry as a function of the centre-of-mass energy. The left plot displays the improved Born calculation for b and c quarks. In the zoomed region around the Z resonance (right plot), a comparison between the improved Born and full QED corrected b and c quark asymmetries is given. In both cases ZFITTER [34] was used.

hemispheres. This is parameterised by the forward-backward asymmetry

$$A_{\rm FB} \equiv \frac{\sigma_{\rm F} - \sigma_{\rm B}}{\sigma_{\rm F} + \sigma_{\rm B}} \tag{2.28}$$

where $\sigma_{\rm F}$ ($\sigma_{\rm B}$) denotes the contribution to the total cross-section from a fermion moving to the forward (backward) hemisphere with respect to the electron beam axis.

$$\sigma_{\rm F} = \int_0^1 \frac{{\rm d}\,\sigma}{{\rm d}\cos\theta}\,{\rm d}\cos\theta\ , \qquad \sigma_{\rm B} = \int_{-1}^0 \frac{{\rm d}\,\sigma}{{\rm d}\ \cos\theta}\,{\rm d}\ \cos\theta \tag{2.29}$$

The advantage of the asymmetry observable, compared to the cross-section, is its independence of the total event rate[4], while it provides the same sensitivity to the predictions of the electroweak theory.

Inserting Eq. 2.23 into Eq. 2.28 leads to the dependence of the forward-backward asymmetry on the centre-of-mass energy and fermion type,

$$A^{\rm f}_{\rm FB}(s) = \frac{3}{4}\cdot\frac{G^{\rm f}_3(s)\sqrt{1-4\mu_{\rm f}}}{G^{\rm f}_1(s) + 2\mu_{\rm f} G^{\rm f}_2(s)} \tag{2.30}$$

Figure 2.5 shows $A^{\rm f}_{\rm FB}(s)$ for a wide range of the centre-of-mass energy at the improved Born level. In addition a comparison with the full QED and electroweak

[4]The total event rate is only known with limited precision and introduces an additional systematic error in the total cross-section measurements.

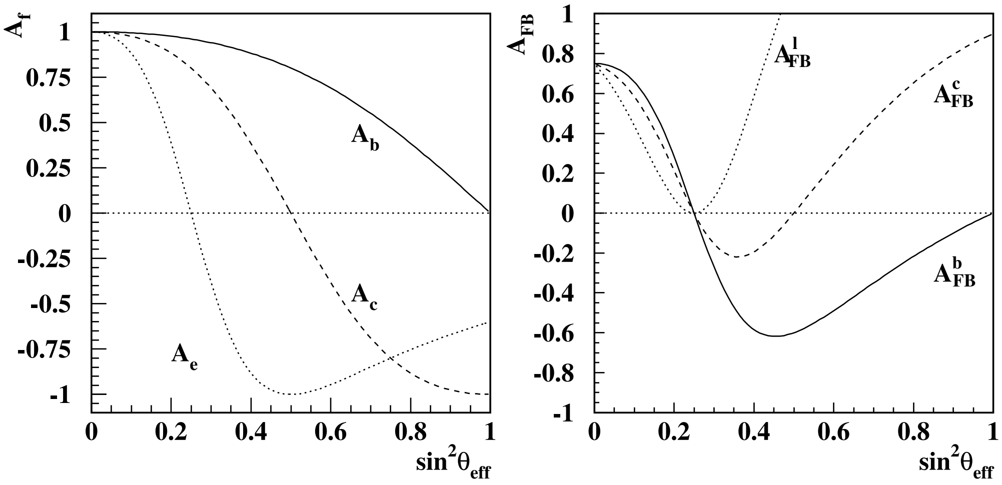

Figure 2.6: In the Standard Model the variation of $\mathcal{A}_\mathrm{f}$ with $\sin^2\theta^\mathrm{f}_\mathrm{eff}$ is controlled by the charge and weak isospin assignment of the fermion species involved. The measured values of $\sin^2\theta^\mathrm{f}_\mathrm{eff}$ are close to 0.23. In this region, $\mathcal{A}_\ell$ (for leptons) depends strongly on $\sin^2\theta^\mathrm{f}_\mathrm{eff}$, while $\mathcal{A}_\mathrm{c}$ and $\mathcal{A}_\mathrm{b}$ (for b and c quarks) depend much more weakly on $\sin^2\theta^\mathrm{f}_\mathrm{eff}$. This behaviour also influences the forward-backward asymmetries displayed on the right side.

corrections for the energy range close to $\sqrt{s} = m_\mathrm{Z}$ – which is relevant for this analysis – is given. The programme ZFITTER [34] was used to compute both diagrams in Figure 2.5.

The term from the Z/γ-interference is strongly forward-backward asymmetric at energies above and below the Z resonance. This leads to the large values of up to 0.6 for A_FB in Figure 2.5. The interference of photon and Z has been observed at experiments performed at PEP, PETRA and TRISTAN through the forward-backward asymmetry [34]. The interference term vanishes at $\sqrt{s} = m_\mathrm{Z}$ together with the pure (symmetric) photon exchange. As a consequence, A_FB at $\sqrt{s} = m_\mathrm{Z}$ observes the parity-violating properties in the coupling of the Z to fermions directly.

The pole asymmetry $A^{0,\mathrm{f}}_\mathrm{FB}$, ($A^\mathrm{f}_\mathrm{FB}$ at $\sqrt{s} = m_\mathrm{Z}$ in improved Born calculation) can be expressed (neglecting the fermion masses and the contributions from the photon exchange) as the product of the fermion asymmetry parameters $\mathcal{A}_\mathrm{f}$. These parameters describe the coupling to the initial ($\mathcal{A}_\mathrm{e}$) and final ($\mathcal{A}_\mathrm{f}$) state fermions:

$$A^{0,\mathrm{f}}_\mathrm{FB} = \frac{3}{4}\mathcal{A}_\mathrm{e}\mathcal{A}_\mathrm{f} = \frac{3}{4}\,\frac{2v_\mathrm{e}/a_\mathrm{e}}{1+(v_\mathrm{e}/a_\mathrm{e})^2}\,\frac{2v_\mathrm{f}/a_\mathrm{f}}{1+(v_\mathrm{f}/a_\mathrm{f})^2}\,. \tag{2.31}$$

- The asymmetry parameters depend solely on the ratio of the vector and axial-vector couplings. This ratio yields the effective electroweak mixing angle,

$$\frac{v_\mathrm{f}}{a_\mathrm{f}} = \left(1 - 4|Q_\mathrm{f}|\sin^2\theta^\mathrm{f}_\mathrm{eff}\right) . \tag{2.32}$$

- Using the Standard Model expectation for the electroweak mixing angle, the behaviour of $\mathcal{A}_\mathrm{f}$ as a function of $\sin^2\theta^\mathrm{f}_\mathrm{eff}$ depends only on the fermion charge.
  - For charged leptons ℓ the parameter $\mathcal{A}_\ell$ varies rapidly with $\sin^2\theta^\mathrm{f}_\mathrm{eff}$.
  - For quarks this dependence is much weaker: While $\mathcal{A}_\mathrm{d,s,b}$ in the case of down type quarks is almost constant and almost 1 in the interesting region of $\sin^2\theta^\mathrm{f}_\mathrm{eff}$ close to 0.23, $\mathcal{A}_\mathrm{u,c,t}$ for up type quarks still shows a slight dependence on $\sin^2\theta^\mathrm{q}_\mathrm{eff}$.

  Following these considerations, the heavy quark forward-backward asymmetries are expected to be much more sensitive to $\mathcal{A}_\mathrm{e}$, originating from the coupling of the electrons and positrons of the accelerator beams to the Z than to $\mathcal{A}_\mathrm{q}$ coming from the coupling to the final state b and c quarks. This mainly determines the leptonic effective electroweak mixing angle $\sin^2\theta^\ell_\mathrm{eff}$. The behaviour of $\mathcal{A}_\mathrm{f}$ and A^f_FB on $\sin^2\theta^\mathrm{f}_\mathrm{eff}$ is illustrated in Figure 2.6.

  The light quark forward-backward asymmetries would have the same sensitivity as the b and c quark forward-backward asymmetries, but the separation from primary u, d or s quark events from each other is not sufficient at the LEP experiments to use them for competitive measurement.
- As a consequence, the results from the forward-backward asymmetry of b and c quarks can be combined with lepton final state measurements to determine $\sin^2\theta^\ell_\mathrm{eff}$ with high precision, and to put constraints on the Higgs boson mass, which enters the effective mixing angle via higher order electroweak corrections.

Even though the Higgs boson mass dependence is only logarithmic, $\sin^2\theta^\ell_\mathrm{eff}$ is still the most sensitive quantity to m_H in the Standard Model. This provides an additional strong motivation for the LEP experiments to measure the b and c quark asymmetries with optimal precision.

2.7 From Quarks to Stable Particles

Quarks are always confined to colourless objects (Section 2.2), the hadrons. Thus, the primary quarks cannot be observed directly. As a consequence, the final state consists of colour-neutral particles, which are grouped to jets pointing along the flight direction of the primary quark. To test the theoretical predictions it is necessary to simulate the behaviour of the final states with event (Monte Carlo) generators. For this purpose, the process $e^+e^- \rightarrow$ hadrons is divided into four phases for centre-of-mass energies close to m_Z:

1. The annihilation of the e^+e^- pair and the subsequent creation of the initial quark antiquark pair is a pure electroweak process. It can be calculated according to Sections 2.1.2, 2.4 and 2.5.

2. The emission of gluons with high energy, which lead to the creation of further $q\overline{q}$ pairs (parton cascade). This QCD processes can be calculated perturbatively. The calculations in perturbative QCD are limited by a minimal momentum transfer of $\sim 1\,\mathrm{GeV}/c$ due to the running of α_s.

3. Beyond this threshold, the transition from the quasi-free partons to bound-state hadrons, the fragmentation process, has to be predicted by phenomenological models.

4. In the last phase, the decays of τ leptons and unstable hadrons determine the experimentally observable final state. Hereby it has to be taken into account that long-lived unstable hadrons potentially decay during the detection process, that is in or in-between sub-detectors.

Both parton cascade and fragmentation are explained in detail in the following two sections. Details on the decays and transformations of hadrons with b and c quark content are given in Section 2.8.

2.7.1 The Parton Cascade

After the initial quark production and the subsequent splitting into more quarks and gluons with high momentum transfer, the hard gluon radiation is the regime of perturbative QCD. It means that the running coupling constant α_s is sufficiently smaller than 1, so that the perturbative expansion converges.

One way to obtain the probability for the resulting final state is its direct computation by means of QCD matrix elements. This can be performed up to the second order in α_s, resulting in a qqqq or qqgg final state and leaving a possible further splitting into more partons to the fragmentation model.

The other way consists of an iterative procedure like the QCD cascade model. It produces a quark-gluon shower by calculating the process of gluon emission or gluon splitting into partons in leading logarithmic approximation in an iterative way, which uses the split virtuality (i.e. squared momentum) as input to the next iteration. A cut-off parameter is used to keep off the non-perturbative region and to stop the iteration, preventing infrared divergences at low momenta. This model is implemented in the JETSET 7.4 simulation programme [37] used throughout this analysis.

2.7.2 String Fragmentation

At a momentum transfer of below $\sim 1\,\mathrm{GeV}/c$, the strong coupling constant α_s exceeds unity, and perturbative treatment is not justified anymore. The transition from partons to hadrons happens at this energy scale. Since detailed descriptions of the hadronisation process that are based on first principles of QCD are not yet available, phenomenological models are used.

A simple approach to describe the creation of jets of hadrons from a primary or secondary parton, created in the fragmentation process, is the independent fragmentation picture [38, 39]. Even though this model is not used any more in modern Monte Carlo generators, it is well suited for a demonstration of the basic ideas about the hadronisation process. An independent hadronisation process is performed for each parton in this model. In an iterative procedure, a $\mathrm{q}\overline{\mathrm{q}}$ quark pair is created in each step. One of the two new (anti)quarks is combined with the isolated parton to form a meson. The other (anti)quark remains as isolated parton for the next step. During each step of the hadronisation, a fraction z of the light cone momentum of the isolated parton is assigned to the resulting hadron:

$$z = \frac{\left(E + p_\parallel\right)_\mathrm{hadron}}{\left(E + p_\parallel\right)_\mathrm{quark}} \tag{2.33}$$

The remaining momentum fraction $(1-z)$ is left for further iterations. The actual fraction z assigned to the hadron is described by a probability distribution $f(z)$, which is assumed to be the same in each step. The probability to find a hadron with momentum fraction between z and $z+\mathrm{d}z$ is $F(z)\mathrm{d}z$. The contribution from primary hadrons is $f(z)\mathrm{d}z$. A second contribution comes from the possibility that a hadron of momentum fraction z can occur as a secondary hadron, created in the splitting of another hadron with larger momentum fraction $1-\eta$, $\eta > z$. A primary hadron of momentum fraction between $1-\eta$ and $1-\eta+\mathrm{d}\eta$ occurs with probability $f(1-\eta)\mathrm{d}\eta$, and the probability for a hadron of momentum fraction z to appear in the remainder jet of it (which has a momentum fraction of η) is $F(z/\eta)\mathrm{d}z/\eta$. The total probability to find a hadron with momentum fraction z is then [39]:

$$F(z)\mathrm{d}z = f(z)\mathrm{d}z + \int_z^1 f(1-\eta)F(z/\eta)\mathrm{d}z\mathrm{d}\eta/\eta \tag{2.34}$$

$$\Longleftrightarrow \quad F(z) = f(z) + \int_z^1 f(1-\eta)F(z/\eta)\mathrm{d}\eta/\eta \tag{2.35}$$

The most prominent assumption in this equation is scale invariance. $F(z)$ describes the energy distribution of any hadron created during the hadronisation process, and $f(z)$ describes the energy distribution of hadrons containing the initial parton. Both functions are called fragmentation function.

A large class of models describes hadronisation involving colour flux tubes, or strings, each spanned between two quarks created during the perturbative event phase. Usually the motion of a string is described by classical, relativistic dynamics. As the quarks move apart from each other and the string is stretched, the energy stored in the string increases linearly with growing distance d of quark and antiquark at the end of the string: $E \propto \kappa d$. The string tension (energy density,), κ of about 1 GeV/fm is constant along the string, if the transverse extension of the string (~ 1 fm) is assumed to be constant over its full length and much smaller than the longitudinal extension. Because the string is assumed to be uniform along its length, the probability for a $\mathrm{q\overline{q}}$ pair creation to occur on the string per unit length and per unit time is a constant.

The creation of $\mathrm{q\overline{q}}$ pairs along the string in the Lund model takes into account the quark masses. This has important consequences: $\mathrm{q\overline{q}}$ pairs are expected to be created locally, i.e. at one space point. However, in order to transfer a virtual $\mathrm{q\overline{q}}$ pair into mass-shell particles, energy has to be taken from the string. For quarks of mass m_{q}, and a transverse momentum p_{t} with respect to the string, the minimum required energy is $E_{\mathrm{min}} = 2\sqrt{m_{\mathrm{q}}^2 + p_{\mathrm{t}}^2} = 2m_{\mathrm{T}}$. Here $m_{\mathrm{T}} = \sqrt{m_{\mathrm{q}}^2 + p_{\mathrm{t}}^2}$ is called transverse mass. It is assumed that both members of the $\mathrm{q\overline{q}}$ pair have a transverse momentum p_{t} of same size, but opposite direction. Otherwise the string would acquire a transverse excitation, which is assumed not to happen. The required energy can only be obtained by a spatial separation of quark and antiquark along the string of $\Delta x_{\mathrm{min}} = E_{\mathrm{min}}/\kappa = 2m_{\mathrm{T}}/\kappa$. The string fission is thus suppressed by the probability for a tunnelling process of a locally created $\mathrm{q\overline{q}}$ pair to spatially separated on-shell quarks. The suppression factor was found to have two terms [40]. The first term provides an automatic suppression of heavy quark production during string hadronisation. The ratio of flavour production rates is estimated to be $P_{\mathrm{u}} : P_{\mathrm{d}} : P_{\mathrm{s}} : P_{\mathrm{c}} = 1 : 1 : 0.3 : 10^{-11}$ using kinematical quark masses. The second term in the tunnelling probability corresponds to a suppression of large transverse momenta. The transverse momentum distribution is predicted to be independent of the quark flavour. A further prediction is that baryon production (requiring two quarks and two antiquarks) is less likely than meson production, in accordance with observations. If a virtual $\mathrm{q\overline{q}}$ pair fluctuates out of the vacuum somewhere along the string, and if this $\mathrm{q\overline{q}}$ pair has the same colour as the endpoint quarks of the string, the colour field is locally compensated and the string breaks into two pieces. This procedure happens repeatedly until the remaining energy of the individual string segments is not sufficient to transform another virtual $\mathrm{q\overline{q}}$ pair into a real one.

In the following, parametrisations for $f(z)$ for the Lund string hadronisation scheme will be presented. Both independent and string hadronisation are performed iteratively, with the basic assumption of a scale invariant fragmentation function. The integral evolution Eq. 2.35 is therefore equally valid in the Lund string hadronisation picture. For light hadrons in a jet the fragmentation function $f(z) = (1-z)/z$ delivers an adequate description of longitudinal momentum spectra in energy regimes where only u, d or s quarks are produced. The energy distribution of hadrons containing a heavy (b or c) quark cannot be explained with the above parametrisation [41]. Dedicated heavy quark fragmentation functions are therefore necessary.

The most well known fragmentation parametrisation for heavy quarks is the one suggested 1983 by Peterson et al. [42]. It is based on the assumption that the amplitude $T \propto 1/\Delta E$ of the transition of a heavy quark Q into a heavy hadron $\mathrm{H} = (\mathrm{Q}\overline{\mathrm{q}})$ plus a light quark q is mainly determined by the energy difference

$$\Delta E \approx \frac{m_{\mathrm{Q}}^2}{2P}\left(\frac{1}{z} + \frac{m_{\mathrm{q}}^2/m_{\mathrm{Q}}^2}{1-z} - 1\right) \propto 1 - \frac{1}{z} - \frac{\varepsilon_{\mathrm{Q}}}{1-z} \tag{2.36}$$

between initial and final state. The actual fragmentation function is a probability distribution of hadrons carrying the momentum fraction z, and as such it is proportional to T^2. Together with a phase space factor of $1/z$ one obtains

$$f_{\mathrm{Q}}(z) = N\frac{1}{z}\left(1 - \frac{1}{z} - \frac{\varepsilon_{\mathrm{Q}}}{1-z}\right)^{-2} \tag{2.37}$$

with a normalisation factor N.

Collins and Spiller noted that the Peterson parametrisation shows a behaviour $\propto (1-z)^2$ for $z \rightarrow 1$ [43]. This is in contradiction to the $(1-z)$ behaviour expected for mesons from dimensional counting arguments by Brodsky et al. [44]. For the same reason they stated that the Peterson parametrisation cannot fulfill the reciprocity relation [45–47] which connects exclusive heavy meson H structure functions F_H^{Q} to exclusive fragmentation functions $D_{\mathrm{Q}}^H(z)$ at high z. Collins and Spiller have suggested a fragmentation parametrisation which takes care of reciprocity and dimensional counting:

$$f_{\mathrm{Q}}(z) = N\left(\frac{1-z}{z} + \frac{(2-z)\varepsilon_{\mathrm{Q}}}{1-z}\right)(1+z^2)\left(1 - \frac{1}{z} - \frac{\varepsilon_{\mathrm{Q}}}{1-z}\right)^{-2} . \tag{2.38}$$

ε_{Q} is defined as in Eq. 2.36. As indicated by the common terms in Eq. 2.37 and Eq. 2.38, the latter is a modification of the former.

A similar approach like the one by Collins and Spiller has been followed by Kartvelishvili et al. already in 1978 [48]:

$$F_H^{\mathrm{Q}}(z) = N z^{\alpha_{\mathrm{Q}}}(1-z) \tag{2.39}$$

particle	**fraction** [%]	**mass** [MeV/c^2]	**lifetime** [ps]
B^+	38.8 ± 1.3	5279.0 ± 0.5	1.65 ± 0.02
B_d^0	38.9 ± 1.3	5279.4 ± 0.5	1.55 ± 0.04
B_s^0	10.6 ± 1.3	5369.6 ± 2.4	1.46 ± 0.05
b baryons	11.8 ± 2.0	—	1.21 ± 0.05
Λ_b	—	5624. ± 9.	1.23 ± 0.08
D^+	23.6 ± 1.6	1869.3 ± 0.5	1.051 ± 0.013
D^0	54.3	1864.5 ± 0.5	0.412 ± 0.003
D_s^+	12.6 ± 2.6	1968.5 ± 0.6	0.490 ± 0.009
c baryons	9.5 ± 2.3	—	—
Λ_c^+	—	2284.9 ± 0.6	0.200 ± 0.006

Table 2.2: Properties such as production fraction, mass and lifetime of the most important b and c hadrons in their ground state, from [50]. The baryon production fractions in $b\overline{b}$ and $c\overline{c}$ events are given for the admixture of all ground state band c baryons. The c hadron fractions are normalised to 100 %, hence no measurement error is quoted for the D^0 fraction [51].

According to the string fragmentation model, hadrons are created iteratively at each end of the string. The z distribution determines the actual positions of breaks on the string. Andersson et al. have imposed the requirement that hadronisation from either (q or $\bar{q}$) end of the string should lead to the same distribution of string breaks. They have shown [49] that this symmetry condition[5], is sufficient to constrain the functional form of the fragmentation function to:

$$f_Q(z) = N\frac{1}{z}(1-z)^a \exp\left(-\frac{b\,m_T^2}{z}\right) \tag{2.40}$$

2.8 Properties of Hadrons with b and c Quarks

At LEP energies only quarks with five different flavours (u, d, s, c, b) are produced. Together with light quarks from the fragmentation, b and c quarks form different types of B mesons (mesons with a b quark as heaviest quark), D mesons (mesons with a c quark as heaviest quark) and baryons. Usually heavy quarks are produced in the primary Z decay. Besides that there is a small contribution from hard gluons from the parton shower, splitting into $b\overline{b}$ or $c\overline{c}$ pairs, producing

[5] along with additional assumptions like no transverse string excitations and a constant string tension

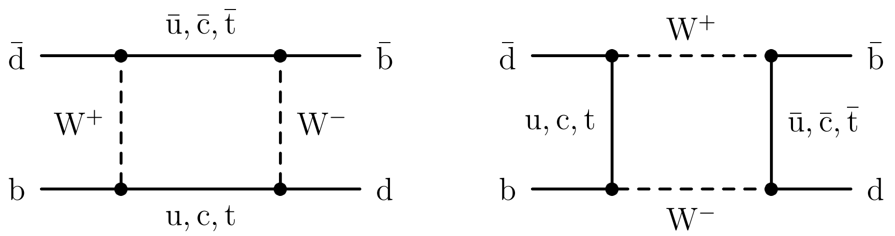

Figure 2.7: Feynman diagrams showing the $\mathrm{B_d^0} - \mathrm{\bar{B}_d^0}$ oscillation.

heavy hadrons also in light quark events. Measurements at LEP and SLC show that the rate of heavy quarks created by gluon splitting is rather small [52].

As decay products of b hadrons, c hadrons also appear in $\mathrm{b\overline{b}}$ events. By taking into account such cascade decays and little corrections due to gluon splitting, primary $\mathrm{b\overline{b}}$ and $\mathrm{c\overline{c}}$ events can be accessed directly via the study of b and c hadrons produced at LEP. The most important b and c hadrons produced at LEP and some of their properties are listed in table 2.2. Some properties of the heavy hadrons like their mass and lifetime are used to reconstruct them. The inclusive reconstruction can only be used to identify primary $\mathrm{b\overline{b}}$ events with high efficiency but with limited purity. The exclusive technique fully reconstructs the decay of a b or c hadron, including its charge, by identifying all stable particles from the considered decay. This method yields a highly enriched set of $\mathrm{b\overline{b}}$ or $\mathrm{c\overline{c}}$ events with limited efficiency. Especially the identification of leptons from semileptonic b or c decays is an excellent method to get a very pure sample of $\mathrm{b\overline{b}}$ and also of $\mathrm{c\overline{c}}$ events with a strong correlation between the primary quark charge and the lepton charge. It is the leading method to measure the c quark forward-backward asymmetry and a good alternative to the inclusive method to measure the b quark forward-backward asymmetry.

Oscillations of Neutral B Mesons

The charge of a b quark can be identified by exploiting the correlation to the track charges in inclusively reconstructed b hadron decays or even better by reconstructing the charge of the lepton of a semileptonic b decay. In the case of neutral $\mathrm{B_d^0}$and $\mathrm{B_s^0}$ mesons, oscillations between particle and antiparticle dilute the charge correlation already before the decay. The leading order diagrams for the $\mathrm{B_d^0} - \mathrm{\bar{B}_d^0}$ oscillation are shown in Figure 2.7.

Starting with a $\mathrm{B_q^0}$ state at time $t = 0$, the probability to observe a $\mathrm{\bar{B}_q^0}$ decaying at the proper time t can be expressed by

$$\mathcal{P}^{\mathrm{mixed}}_{\mathrm{B_q^0}}(t) = \frac{1}{2\tau_{\mathrm{B}}} \cdot \exp\left(-\frac{t}{\tau_{\mathrm{B}}}\right) \cdot \Big[1 - \cos(\Delta m_{\mathrm{q}} \cdot t)\Big] \tag{2.41}$$

while a B_q^0 is still observed with the probability

$$\begin{aligned}\mathcal{P}_{B_q^0}^{\text{not mixed}}(t) &= \frac{1}{2\tau_B}\exp\left(-\frac{t}{\tau_B}\right)\cdot\left[1+\cos(\Delta m_q\cdot t)\right] \\ &= \frac{1}{\tau_B}\exp\left(-\frac{t}{\tau_B}\right)\cdot\left[1-\sin^2\left(\frac{\Delta m_q\cdot t}{2}\right)\right]\end{aligned} \tag{2.42}$$

Here τ_B denotes the lifetime of the B_q^0 and $\Delta m_q = m_{B_q^0} - m_{\bar{B}_q^0}$ the mass difference between the mass eigenstates of the oscillating mesons. Effects from CP violation as well as a possible difference between the B_q^0 lifetimes of the heavy and light mass eigenstates are neglected. The time-integrated mixing probability, χ_q, then becomes

$$\chi_q = \int_0^\infty \mathcal{P}_{B_q^0}^{\text{mixed}}(t)\,\mathrm{d}t = \frac{x_q^2}{2(1+x_q^2)}\ , \quad x_q = \Delta m_q \tau_B \tag{2.43}$$

The mass difference Δm_d in the B_d^0 system is small, allowing both, a time-dependent measurement aimed at a direct determination of Δm_d (Eq. 2.41) and a time-integrated measurement of χ_d (Eq. 2.43). The current world average for the total mixing probability is $\chi_d = 0.181 \pm 0.004$ [26]. Using the measured B_d^0 lifetime (see Table 2.2), the Particle Data Group [26] quotes a result for the mass difference of $\Delta m_d = 0.502 \pm 0.007\ \text{ps}^{-1}$.

Due to the apparently larger mass difference Δm_s in the B_s^0-system, only a time-dependent measurement is possible which leads to a lower limit on the mass difference of $\Delta m_s > 14.1\ \text{ps}^{-1}$ [26]. The total mixing probability χ_s is compatible with 0.5, implying that no information on the primary quark charge can be deduced from the B_s^0 decay products [26].

The total average mixing parameter $\overline{\chi}$ is the probability that a b quark decays as its antiparticle due to mixing. It is defined by

$$\overline{\chi} = f_{B_d^0}\cdot\chi_d + f_{B_s^0}\cdot\chi_s\ . \tag{2.44}$$

The fractions $f_{B_d^0}$ and $f_{B_s^0}$ can be taken from table 2.2. The current world average for the total B mixing parameter is [26]:

$$\overline{\chi} = 0.1184 \pm 0.0045\ . \tag{2.45}$$

This value does not include the result from the measurement presented later in this work.

Chapter 3

The OPAL Detector at LEP

3.1 The Large Electron Positron Collider (LEP)

LEP [6] was an electron-positron collider ring at CERN[1] with a circumference of approximately 27 km, making it the largest particle accelerator in the world. It was situated in a tunnel approximately 100 m below the Swiss and French surface near Geneva. The collider layout included eight straight sections, with collisions between electron and positron bunches allowed to take place in four of them. The four interaction regions were each instrumented with a multipurpose detector: ALEPH [53, 54], DELPHI [55, 56], L3 [57–59], and OPAL [60–64], as indicated in Figure 3.1.

LEP was commissioned in 1989 and has been very successfully operated until it was shut down and dismantled at the end of 2000. In the time period from 1989 to 1995, it was operating at a beam energy of about 45.6 GeV or half of the Z mass. This operation energy was chosen to take advantage of the Z resonance in the e^+e^- collision cross section, which enhances the total cross section by several orders of magnitude with respect to the non-resonant photon exchange cross section which is dominant at lower energies (see Section 2.5). In summer 1989 the first Z bosons were produced at LEP and observed by the four experiments. Over the following years the operation of the machine and its performance were steadily improved. At the end of LEP data taking around the Z resonance in autumn 1995 the peak luminosity had reached $2 \cdot 10^{31}$ cm^{-2}s^{-1}, well above its design value of $1.6 \cdot 10^{31}$ cm^{-2}s^{-1}. At this luminosity, approximately 1 000 Z bosons were recorded every hour by each of the four experiments, making LEP a true Z factory.

[1] "European Laboratory for Particle Physics" — the abbreviation has been kept from the first name of the laboratory: "**C**onseil **E**uropéen pour la **R**echerche **N**ucléaire".

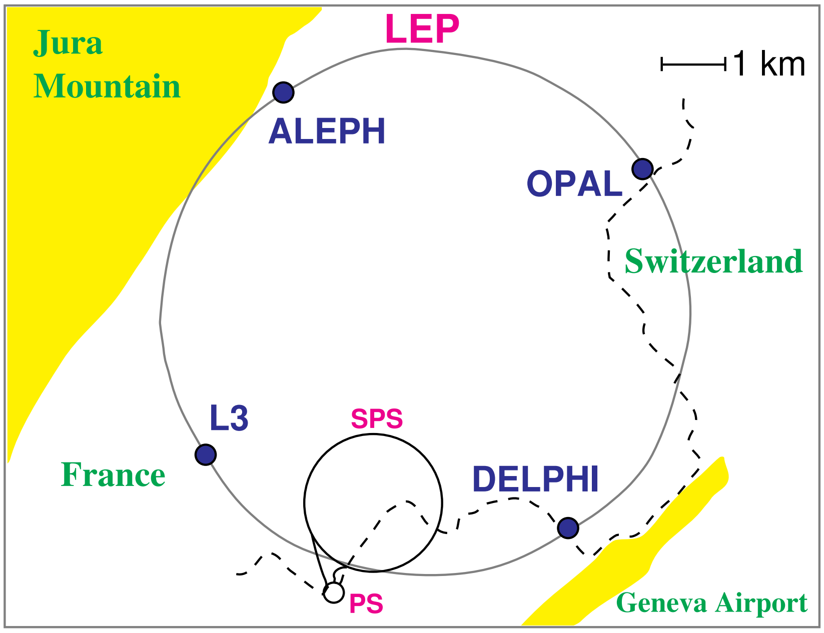

Figure 3.1: The LEP storage ring, showing the locations of the four experiments, and the existing accelerators (PS, SPS) used as pre-accelerators for the electron and positron bunches.

The data collected in 1989 constitute only a very small subset of the total statistics and are of lower quality, and therefore these are not used in the final analyses. In the years 1990 and 1991 “energy scans” were performed at seven different centre-of-mass energies around the peak of the Z resonance, placed about one GeV apart. In 1992 and 1994 there were “high-statistics runs” only at the peak energy. In 1993 and 1995 data taking took place at three centre-of-mass energies, about 1.8 GeV below and above the peak and at the peak. The accumulated event statistics amount to about 17 million Z decays recorded by the four experiments.

Starting in 1996, the LEP energy was gradually increased up to a maximum of 209 GeV achieved in 2000. Main physics goals pursued in this LEP2 programme were a detailed investigation of $W^{\pm}$ properties and the search for new phenomena beyond those previously accessible to accelerator-based particle physics.

Originally four bunches of electrons and four bunches of positrons circulated in the ring, leading to a collision rate of 45 kHz. The luminosity was increased in 1992 by using eight equally spaced bunches (“Pretzel scheme”), or alternatively four trains of bunches with a spacing of order a hundred metres between bunches in a train.

Electrons and positrons were accelerated to about 20 GeV in the already existing linear accelerator LIL and the PS and SPS ring accelerators, then injected and accumulated in bunches in the LEP ring. When the desired bunch currents of more than 3 mA were achieved, the beams were accelerated and only then brought into collision at the interaction regions at the nominal centre-of-mass energy for that “fill”. A fill would continue for up to about 10 hours before the remaining beams were dumped and the machine refilled. The main bending field was provided by 3 280 concrete-reinforced dipole magnets in the eight 2 840 m long arcs. At 45 GeV beam energy the required field is 0.048 T. Hundreds of quadrupole and sextupole magnets were used for focusing and correcting the beams in the arcs and in the straight sections. On both sides of each experiment the beam is focused with superconducting quadrupole magnets, increasing the luminosity. For LEP1 running, the typical energy loss per turn of 125 MeV was compensated by a radio-frequency accelerating system comprised of copper cavities, with a total power of 16 MW, installed in just two of the straight sections, to either side of L3 and OPAL.

Much effort was dedicated to the determination of the energy of the colliding beams. Several techniques have been employed to measure it, the most precise being the one using resonant spin depolarisation [65,66]. This technique was successfully established in late 1991 during the scan of the Z resonance. A precision of about 2 MeV in the centre-of-mass energy was achieved, corresponding to a relative uncertainty of about $20 \cdot 10^{-6}$ on the absolute energy scale. This level of accuracy is vital for the precision of the measurements of the mass and width of the Z and for the correction which has to be made to come from the measured forward-backward asymmetry to the forward-backward asymmetry at the Z pole.

Numerous potential causes of shifts in the centre-of-mass energy were investigated and some unexpected sources identified. These included the effects of earth tides generated by the moon and sun and local geological deformations following heavy rainfall or changes in the level of Lake Geneva. While the beam orbit length was constrained by the RF accelerating system, the focusing quadrupoles were fixed to the earth and moved with respect to the beam, changing the effective total bending magnetic field and the beam energy by 10 MeV over several hours. Leakage currents from electric trains operating in the vicinity provoked a gradual change in the bending field of the main dipoles, directly affecting the beam energy. The collision energy at each interaction point also depended for example on the exact configuration of the RF accelerating system. All these effects are large compared to the less than 2 MeV systematic uncertainty on the centre-of-mass energy eventually achieved through careful monitoring of the running conditions and modelling of the beam energy.

3.2 The OPAL Detector

The OPAL ("**O**mni **P**urpose **A**pparatus for **L**EP") detector was one of the four large experiments at LEP. It is described in full detail elsewhere [60–64]. In this chapter the design requirements, the detector components, and their performance are summarised in the light of the measurements that are presented in this thesis.

The conceptual idea for this detector was to build a functionary detector at relatively low cost with a well-known and tested detector technology. This should ensure a reliable running of the OPAL detector from the beginning of the LEP physics program.

The OPAL detector has been designed as a general purpose experiment to study all physics processes in e^+e^- collisions at centre-of-mass energies around the Z resonance and beyond. This leads to the following main requirements:

- precision measurement of charged particle tracks: determination of their momentum and charge and identification of the particle species,
- reconstruction of both the primary event vertex and possible secondary vertices from the tracks,
- measurement of energy and direction of neutral particles, both photons and hadrons,
- coverage of as much of the solid angle as possible to identify events with missing energy due to non-interacting particles and
- precision luminosity measurement via low-angle Bhabha scattering.

The general layout of the OPAL detector is described in the following and is also shown in Figure 3.2. Charged particle track reconstruction is achieved by the central tracking system, consisting of a set of three different drift chambers complemented by a silicon micro-vertex detector around the beam pipe. The central tracking system is located inside a solenoid which provides a uniform axial magnetic field. The beam axis coincides with the z axis of the detector coordinate system[2]. The tracking system provides precise momentum measurements of charged particles and a determination of the charge sign via the curvature of

[2] Two coordinate systems are used at OPAL: (a) A right-handed Cartesian coordinate system, with the x axis pointing in the plane of the LEP collider towards the centre of the ring. The flight direction of the beam electrons is used as z axis. (b) A polar coordinate system with the same z axis as (a). The azimuthal angle ϕ is counted from the x axis, the polar angle θ describes the angular distance to the z axis. The radial distance from the electron beam is denoted r.

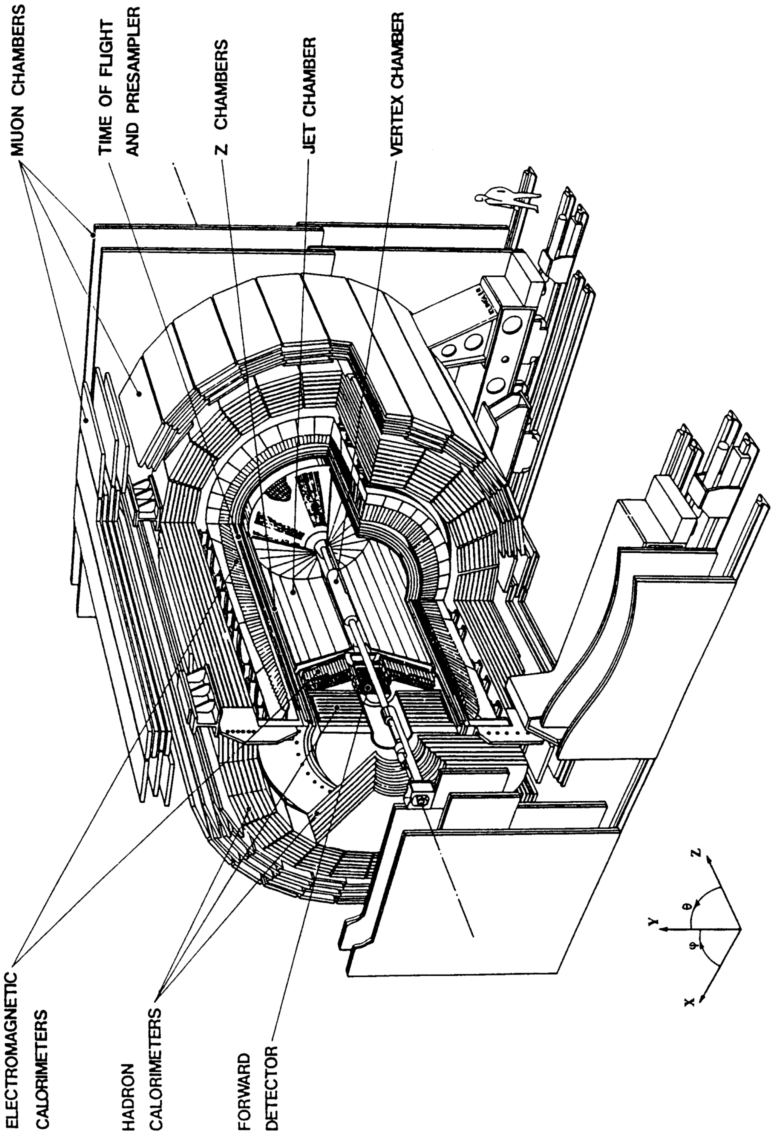

Figure 3.2: The OPAL detector.

the track, an identification of the particle species by a measurement of the specific energy loss $\mathrm{d}E/\mathrm{d}x$, and the possibility to reconstruct primary and secondary decay vertices.

Outside the magnet coil follows the electromagnetic calorimeter system, consisting of segmented lead glass, which measures the direction and energy of electromagnetic showers initiated by photons or electrons.

The iron return yoke and pole pieces of the magnet are instrumented with streamer tubes and thin multiwire chambers to act as a hadronic calorimeter. It is surrounded by four layers of muon chambers. The endcaps are equipped with similar detector layers. Additional detectors are installed close to the beam pipe in the very forward regions of the detector for a measurement of the luminosity via Bhabha scattering.

3.2.1 Central Tracking System

The central part of the OPAL detector is equipped for the reconstruction of charged particle tracks. It consists of a silicon micro-vertex detector and three drift chambers, embedded in a homogeneous magnetic field of 0.435 T parallel to the beam pipe, provided by an aluminium solenoid.

The silicon micro-vertex detector was first operational in 1991 [61], in order to improve the track resolution in the immediate neighbourhood of the interaction point and thus to reconstruct secondary vertices of heavy flavour hadrons or other long-living particles. Lifetime measurements of around 10^{-13} s are achievable. This sub-detector was mounted directly outside of a beryllium beam pipe. It consisted of two concentric layers of single sided silicon strip detectors located at a distance of 6.1 cm and 7.5 cm from the centre of the LEP beam pipe. The length of the detector was 18.3 cm, covering an angular range of $|\cos\theta| < 0.83$ with the inner, and $|\cos\theta| < 0.77$ with the outer layer. The intrinsic spatial resolution in r-ϕ was about 10 μm. In 1993 it was upgraded to measure tracks in both r-ϕ and r-z planes [62]. Since then, a z resolution of 15 μm had been achieved for particles that pass the silicon strips perpendicularly. In 1996 a further upgrade extended the angular coverage of the detector for at least one silicon measurement from $|\cos\theta| < 0.83$ to $|\cos\theta| < 0.93$ ($|\cos\theta| < 0.89$ for two hits) [63]. After the upgrades, the inner and outer layers consist of 12 and 15 ladders, respectively, where each ladder is equipped with two silicon strip detectors for r-ϕ and r-z coordinate readout, glued back-to-back. A measure of the precision is the impact parameter resolution as determined from lepton pairs produced in Z decays. A resolution of $\sigma(d_0) = 18$ μm in the x-y plane and of $\sigma(z_0) = 24$ μm in z direction is obtained.

The central drift chamber system consists of vertex drift detectors and the jet chamber [67]. It is complemented by so-called "z-chambers" to improve the resolution in the z direction. The vertex drift chambers are directly connected to the silicon detector. The central drift chambers are embedded in a pressure vessel, keeping the chamber gas[3] at 4 bar. A high pressure allows a more precise measurement of the specific energy loss, $\mathrm{d}E/\mathrm{d}x$, of a particle within the jet chamber, at the cost of enlarging the error on momentum measurement especially for low momenta particles due to multiple scattering. The choice of a suitable pressure was a compromise between both effects.

The vertex chamber consists of two parts segmented azimuthally into 36 sectors. The inner part covers the region between 8.8 cm and 15.5 cm radially from the interaction point. The radius of the outer chamber part is 23.5 cm. The vertex chamber covers the polar angle range of $|\cos\theta| < 0.98$. The wires of the inner part are parallel to the beam axis, whereas the so-called "stereo-wires" of the outer chamber part are tilted by 4° with respect to the beam axis, to allow for a more precise determination of the z coordinate. The hit resolution in the r-ϕ plane is ~ 55 μm. The z resolution of the inner part (4 cm) can be improved by the additional use of the stereo-wires to ~ 700 μm.

The jet chamber – the largest component of the tracking system – surrounds the vertex chamber and has an outer radius of 1.85 m and a length of 4 m. It consists of 24 azimuthal sectors, which are each equipped with 159 anode wires along the beam direction. The sector boundaries consist of cathode planes of 475 wires each with 3.36 mm interspacing. The maximum drift length is 3 cm to the innermost and 25 cm to the outermost signal wire. Tracks within a polar angle range of $|\cos\theta| < 0.73$ (barrel region) pass all 159 wires; for a particle to pass at least eight wires, the requirement is $|\cos\theta| < 0.98$. The coordinates of the tracks of charged particles in the r-ϕ plane are determined by the position of the wires and a measurement of the drift time, achieving a spatial resolution of 135 μm. The z coordinate is obtained with a resolution of 6 cm from the difference of integrated charges as measured at the two ends of each wire.

The sum of the integrated charges is used to measure the specific energy loss per path length $\mathrm{d}E/\mathrm{d}x$ of the charged particle. The mean specific energy loss $\mathrm{d}E/\mathrm{d}x$ of a charged particle due to ionisation, as given by the Bethe-Bloch formula, is a function of the particle velocity. Thus, the measurement of the specific energy loss in the gas of the chamber, when combined with the momentum measurement, allows a determination of the mass of the charged particle and therefore an identification of the particle type. A relative error of 3.3 % on the energy loss is achieved for tracks where $\mathrm{d}E/\mathrm{d}x$ samplings from all wires in the jet chamber can be used. Given the track momentum, the predictions for different particle hypotheses are compared with the measured value $\mathrm{d}E/\mathrm{d}x$(meas.) and the

[3]The drift gas was a mixture of 88.2 % argon, 9.8 % methane, and 2.0 % isobutane.

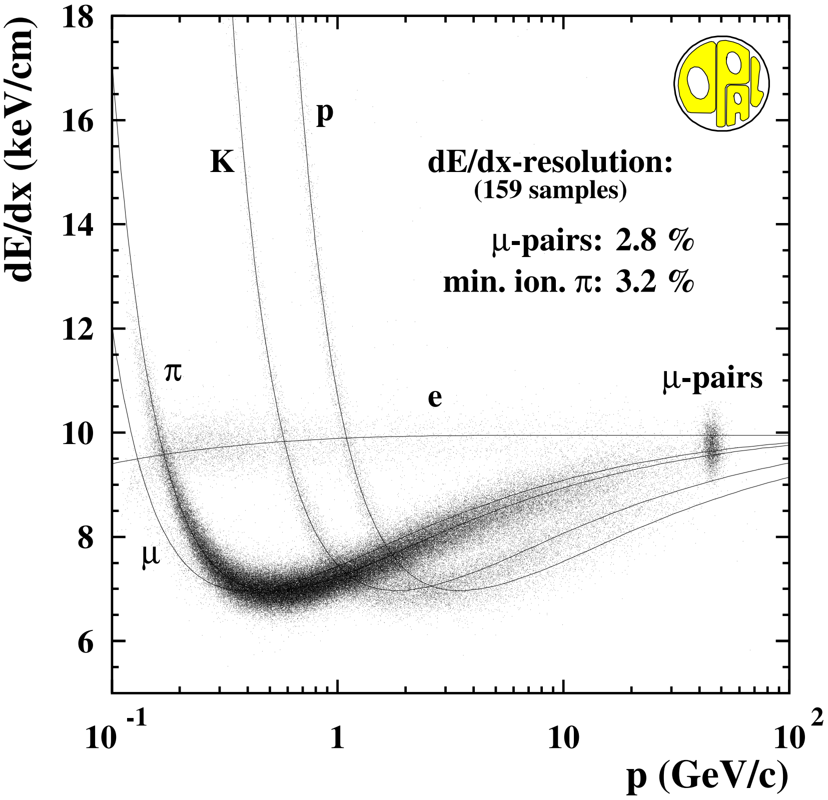

Figure 3.3: The specific energy loss $\mathrm{d}E/\mathrm{d}x$ in the jet chamber as a function of the momentum for different particles.

measurement uncertainty $\sigma(\mathrm{d}E/\mathrm{d}x)$. Either the normalised deviation from the expected value,

$$\frac{\mathrm{d}E/\mathrm{d}x(\mathrm{meas.}) - \mathrm{d}E/\mathrm{d}x(\mathrm{exp.})}{\sigma(\mathrm{d}E/\mathrm{d}x)} \tag{3.1}$$

is taken to select a given charged particle type, or this quantity is transformed into a χ^2 probability. The $\mathrm{d}E/\mathrm{d}x$ weight W is then defined as the χ^2 probability, signed according to the sign of the normalised deviation. In Figure 3.3 the $\mathrm{d}E/\mathrm{d}x$ for a sample of tracks is shown as a function of the momentum. The separating power for electrons is clearly visible. This is important for efficient electron identification as used for the analysis presented in Chapter 5. More precise information on the performance of the jet chamber can be found in [68].

For charged particles, the momentum component p_t perpendicular to the beam axis is measured from the curvature of the track in the magnetic field. The track fit within the central jet chamber includes information from all parts of the central tracking system. The average momentum resolution obtained at OPAL, using the information of the central vertex, jet and z-chamber described above, is found to be

$$\frac{\sigma_{p_\mathrm{t}}}{p_\mathrm{t}} = \sqrt{0.02^2 + \left(1.3 \cdot 10^{-3} (\mathrm{GeV}/c)^{-1}\right)^2 \cdot p_\mathrm{t}^2}\ . \tag{3.2}$$

The constant term is due to multiple scattering in the chamber medium. The second term describes the limitation of the resolution by geometrical issues and the magnetic field. Including the additional tracking information from the silicon micro-vertex detector, the coefficient of the second term improves to $1.25 \cdot 10^{-3} (\mathrm{GeV}/c)^{-1}$.

The z-chamber is needed for a second precise measurement of the z coordinate in addition to that in the micro-vertex detector, in order to obtain an accurate measurement of the momentum component along the beam. The z-chamber surrounds the full 4 m length of the jet chamber. It consists of 24 flat drift chambers of 50 cm width and 0.59 cm thickness, each of which is divided in z into 8 cells of 50 cm length with wires perpendicular to the beam direction. The z coordinate is determined with an accuracy between 100 μm and 300 μm, while the ϕ measurement relies on the charge division method (as used for the z coordinate in the jet chamber) and reaches a resolution of 1.5 cm. For tracks outside the geometrical acceptance of the z-chamber of $|\cos\theta| < 0.73$, the second precise measurement of the z coordinate along a track is obtained from the radius of the outermost measurement wire in the jet chamber. The total track momentum is obtained from the transverse momentum and the polar angle of the track.

3.2.2 Calorimeter System and Muon Chambers

The central tracking chambers and the magnet coil are surrounded by the electromagnetic calorimeter system, which is used to determine the energy and position of electromagnetic showers initiated by photons and electrons. It consists of a time-of-flight counter, a so-called presampler, and a lead-glass calorimeter. The magnet return yoke outside the electromagnetic calorimeter is equipped as a hadronic sampling calorimeter for the measurement of the energy and position of hadronic showers. On the outside, the detector is surrounded with chambers for muon identification.

Already at LEP1 there was a time-of-flight counter surrounding the barrel part of the detector. At the beginning of the LEP2 programme the second part of the time-of-flight counter was installed in the endcap regions. The barrel system consists of 160 scintillator counters, each 6.84 m long, 9.1 cm wide, and 4.5 cm thick. It is read out with photomultipliers and covers an acceptance region of $|\cos\theta| < 0.82$. In the endcaps, 120 scintillating tiles with fibre readout are installed in front of the electromagnetic calorimeter blocks. The time-of-flight counters are used for triggering purposes and to reject events from cosmic rays.

The material in the central detector and the magnet coil corresponds to roughly two electromagnetic radiation lengths, and thus, most electromagnetic showers are initiated before the electromagnetic calorimeter. Unless tracks from a converted photon can be reconstructed, this effect degrades the energy and angular resolution of the electromagnetic calorimeter. This loss is partly recuperated with the presampler, which is installed on the inside of the calorimeter to measure the multiplicity of electromagnetic showers. In the barrel region, it consists of 16 streamer chambers of 6.6 m length, 94 cm width, and 3 cm thickness. The endcap part is made of 32 drift chambers. The lateral spread of electromagnetic showers in the presampler varies between 2 mm and 6 mm. An angular resolution of ~ 2 mrad is achieved.

The electromagnetic calorimeter is also divided into a barrel, covering the region $|\cos\theta| < 0.82$, and two endcap parts for polar angles within $0.82 < |\cos\theta| < 0.98$. The barrel part consists of 9 440 lead glass blocks with a cross-section of 10×10 cm^2, corresponding to roughly 40×40 mrad^2, and a length of 37 cm, equivalent to 24.6 electromagnetic radiation lengths. The blocks are arranged in a pointing geometry; they are oriented towards a point on the z axis close to the interaction region. This arrangement helps in the reconstruction of electromagnetic showers, while preventing particles from escaping through the small gaps between the calorimeter blocks. In the endcaps, 1 132 lead glass blocks with a cross-section of 9.2×9.2 cm^2 and roughly 22 radiation lengths thickness are aligned parallel to the beam. The energy resolution is

$$\frac{\sigma_E}{E} = \sqrt{(0.015 \pm 0.003)^2 + \frac{(0.16 \pm 0.003)^2}{E\,(\,\mathrm{GeV})}} \tag{3.3}$$

in the barrel and

$$\frac{\sigma_E}{E} = \sqrt{(0.018 \pm 0.003)^2 + \frac{(0.218 \pm 0.025)^2}{E\,(\,\mathrm{GeV})}} \tag{3.4}$$

in the endcap regions, respectively [69]. For isolated electromagnetic showers, an intrinsic spatial resolution of around 11 mm is achieved, when using an energy-weighted mean from several adjacent lead glass blocks ("cluster").

With help of the hadronic calorimeter, the energy of particles passing the electromagnetic calorimeter can be measured. The iron return yoke of the magnetic coil serves as the absorbing material of the calorimeter. It is segmented into 10 layers of 10 cm thick iron. The space in-between is filled in a sandwich technique with thin streamer chambers. The iron yoke covers a polar angle of 97 % with a hadronic radiation length of more than four. The energy resolution is limited by the material of the electromagnetic calorimeter, which corresponds to two hadronic radiation length. Thus the showers are formed before the hadronic calorimeter is reached. By combining the signals of the electromagnetic and hadronic calorimeter, an energy resolution of $\sigma_{\mathrm{E}}/\mathrm{E} = 120\%/\sqrt{E/GeV}$ for hadrons can be achieved.

The hadronic calorimeter is surrounded by the muon chambers. Of the full solid angle, 93 % are covered with at least one detector layer, while the coverage for most of the detector is three or more layers of muon chambers. The detector can be divided into a barrel, which consists of four layers of drift chambers, and two endcaps, where four layers of streamer chambers are used. Over most of the full solid angle, a pion traverses more than seven absorption lengths to reach the outside of the hadronic calorimeter, corresponding to a probability not to interact of less than 0.001. The identification of muons is based on the extrapolation of charged particle tracks from the central detector through the calorimeter and the identification of a matching track segment in the muon chambers. The required positional and angular accuracy is determined by multiple scattering in the material in front of the muon chambers to about 2 mm and 3 mrad, respectively. Isolated muons with momentum greater than 3 GeV/c are identified within the 93 % of the solid angle with an efficiency of close to 100 %, while the misidentification probability for isolated pions of 5 GeV/c is less than 1 %.

3.2.3 Forward Detectors

In the forward region a system of drift chambers, calorimeters, and scintillating tiles is installed to measure small angle Bhabha events ($\mathrm{e}^+\mathrm{e}^- \rightarrow \mathrm{e}^+\mathrm{e}^-$). The cross-section of this process is dominated by the t-channel γ-exchange, a pure QED process, which is calculated theoretically with a very high precision. Therefore this process is ideal to determine the luminosity very accurately by a measurement of the number of selected Bhabha events and the efficiency. The forward detectors are mounted at a minimal distance of 2.4 m away from the interaction point. The system consists of drift chambers in the front plane, the gamma catcher, a ring of lead-scintillator sandwich modules, and the far forward luminosity monitor, a lead-scintillator calorimeter positioned 7.9 m from the interaction point. The system is complemented 1993 by a silicon-tungsten calorimeter, improving the precision for the luminosity measurement from 1 % to 0.1 %.

3.3 OPAL Dataset and Simulated Events

The yearly winter shutdown periods at LEP were used for machine and detector maintenance and upgrades. As a consequence, the detector setup, calibration, and data quality vary among the datasets of different years. Especially the identification quality of events with a primary $\mathrm{b\overline{b}}$ or $\mathrm{c\overline{c}}$ quark pair relies on the reconstruction precision of secondary vertices. The vertex reconstruction performance for the data that were taken without silicon micro-vertex detector is much poorer than that for the rest of the sample. Therefore the data recorded in 1990-1991 (before the installation of the micro-vertex detector), a period in 1992 and two periods in 1994 (no silicon information due to technical problems) have to be treated differently in the forward-backward asymmetry measurement presented later in this text. A total of ~ 4.1 million “gold plated” multi hadron events (GPMH) [70] with silicon micro-vertex detector and ~ 750 thousand events without silicon detector are available for physics analyses from the LEP1 phase, recorded from 1989-1995. During the LEP2 programme, a further ~ 490 thousand events were recorded at the Z pole for detector calibration purposes. So the full 1990-2000 OPAL data set could be used for the determination of the b and c forward-backward asymmetries. An overview of the OPAL datasets taken at or close to the Z resonance is given in Table 3.1.

The measurement process of the detector can be simulated using Monte Carlo methods. The GEANT package [71] is such a tool to simulate the interactions of particles traversing the detector. The simulation package GOPAL [72] is a GEANT application to obtain detector level information for the final state particles from events simulated with Monte Carlo event generators. To do so, the GOPAL program contains a precise geometrical description of the detector, an inventory of the materials used, and simulations for the response of the subdetectors.

The GOPAL program produces raw event data files which have the same format as the event data files obtained from the online detector readout. This allows the use of the same reconstruction and analysis code for simulated data and data recorded with the detector.

Distributions for quantities calculated from event information can therefore be compared directly for data and Monte Carlo simulation. An estimate for reconstruction efficiencies and purities as well as efficiencies for cuts can be obtained.

Dedicated JETSET 7.4 [37, 73] Monte Carlo samples are available with detailed simulation of the detector setup of all years, and for all energies of data-taking. A global fit to OPAL data has been performed to optimise the JETSET 7.4 [37, 73] parameters [74]. The OPAL tune of the JETSET 7.4 Monte Carlo generator uses the Lund string hadronisation scheme [49] per default with a Bowler parametrisation for u, d, s quarks ($a = 0.11; b = 0.52$), and a Peterson parametrisation [42] for charm ($\varepsilon_\mathrm{c} = 0.031$) and bottom ($\varepsilon_\mathrm{b} = 0.0038$) quarks. A total of 10.29 million five-flavour hadronic events is available, plus 6.02 million $\mathrm{b\overline{b}}$ and 2.43 million $\mathrm{c\overline{c}}$ events. A detailed list of all subsamples is shown in Table 3.1.

The full JETSET 7.4 $\mathrm{q\overline{q}}$ sample with 1994 detector simulation, 1 million events of the JETSET 7.4 $\mathrm{b\overline{b}}$ 1994 sample, and 1 million events of the JETSET 7.4 $\mathrm{c\overline{c}}$ 1994

Year	**Energy [GeV]**	**OPAL data**	**Monte Carlo (JETSET) $q\overline{q}$**	**$b\overline{b}$**	**$c\overline{c}$**
1989		not used for physics			
1990	peak-2	0.016 M	—	—	—
	peak	0.114 M	0.300 M	0.075 M	0.075 M
	peak+2	0.022 M	—	—	—
1991	peak-2	0.026 M	0.100 M	0.025 M	0.025 M
	peak	0.304 M	0.467 M	0.125 M	0.125 M
	peak+2	0.022 M	0.100 M	0.025 M	0.025 M
1992	peak	0.856 M	1.500 M	0.400 M	0.400 M
1993	peak-2	0.118 M	0.200 M	0.050 M	0.050 M
	peak	0.553 M	1.000 M	0.275 M	0.275 M
	peak+2	0.160 M	0.264 M	0.075 M	0.075 M
1994	peak	1.886 M	4.000 M	3.740 M	1.000 M
1995	peak-2	0.111 M	0.200 M	0.050 M	0.050 M
	peak	0.558 M	1.000 M	0.250 M	0.250 M
	peak+2	0.162 M	0.300 M	0.075 M	0.075 M
1996	peak	0.037 M	0.060 M	—	—
1997	peak	0.070 M	0.100 M	—	—
1998	peak	0.109 M	0.200 M	0.250 M	—
1999	peak	0.136 M	0.250 M	0.250 M	—
2000	peak	0.142 M	0.250 M	0.250 M	—

Table 3.1: Summary of OPAL data recorded close to the Z pole and approximately 2 GeV above and below it, separately for the different years of data taking. The numbers given for the data are for gold plated multi hadron (GPMH) events. In addition the numbers of general purpose Monte Carlo events are listed. The sample sizes are given in units of a million events. $q\overline{q}$ denotes five-flavour hadronic Monte Carlo event samples. $b\overline{b}$ and $c\overline{c}$ samples are dedicated heavy flavour Monte Carlo sets. All OPAL data and Monte Carlo samples listed in this table are used for the measurement of the b and c quark forward-backward asymmetry measurement presented in Chapter 5 of this text.

sample were created with JETSET 7.404, whereas all other samples were generated with JETSET 7.408. It was found that the older JETSET variant contains a coding bug which distorts the b hadron energy spectrum slightly. The average energy is shifted by 1.0 %. The energy spectrum of primary charmed hadrons is not affected. The whole $c\overline{c}$ sample is therefore used in the measurement. The $b\overline{b}$ events of these samples, with correction weights enabled, are only used for cross-checks and do not enter the final results.

The 1994 JETSET 7.4 $\mathrm{q\overline{q}}$ sample differs from the remaining Monte Carlo (including the JETSET 7.404 $\mathrm{b\overline{b}}$ and $\mathrm{c\overline{c}}$ samples) in another respect. The Peterson fragmentation function is used with different parameters for b ($\varepsilon_\mathrm{b} = 0.0057$) and c ($\varepsilon_\mathrm{c} = 0.046$) quark hadronisation. These values are comparatively far from current estimates of these parameters [75].

Chapter 4

Forward-Backward Asymmetry Measurements at OPAL

As an introduction, this chapter qualitatively describes and compares the different methods employed by the OPAL collaboration to measure the bottom and charm forward-backward asymmetries $A_{\mathrm{FB}}^{\mathrm{b}}$ and $A_{\mathrm{FB}}^{\mathrm{c}}$. There are three different analysis types to measure $A_{\mathrm{FB}}^{\mathrm{b}}$ [13,76,77] and two types to measure $A_{\mathrm{FB}}^{\mathrm{c}}$ [13,77] (equivalent methods are used by the other three LEP experiments).

The following tasks have to be performed in these analyses:

- selection of hadronic Z events,
- identification of the primary quark flavour,
- determination of the $\mathrm{q\overline{q}}$ flight direction, in particular of $|\cos\theta|$, where θ is the polar angle between the incoming electron beam and the outgoing fermion momenta,
- determination of the sign of $\cos\theta$ by distinguishing between primary quarks and antiquarks.

The knowledge of the primary quark flavour and $\cos\theta$ is essential for measurements of the forward-backward asymmetries. The measurement of $\cos\theta$ is split into the determination of the absolute value and its sign: At leading order $\mathrm{b\overline{b}}$ and $\mathrm{c\overline{c}}$ events result in two back-to-back jets, each containing the decay products of one of the b or c quarks. This assumption also holds for events with primary light quarks (u, d, s). A schematic illustration of a typical Z decay into two jets is given in Figure 4.1 for a light quark event (a) and a $\mathrm{b\overline{b}}$ event (b). In both cases the Z decays into a $\mathrm{q\overline{q}}$ pair at the primary vertex. Hadrons are formed

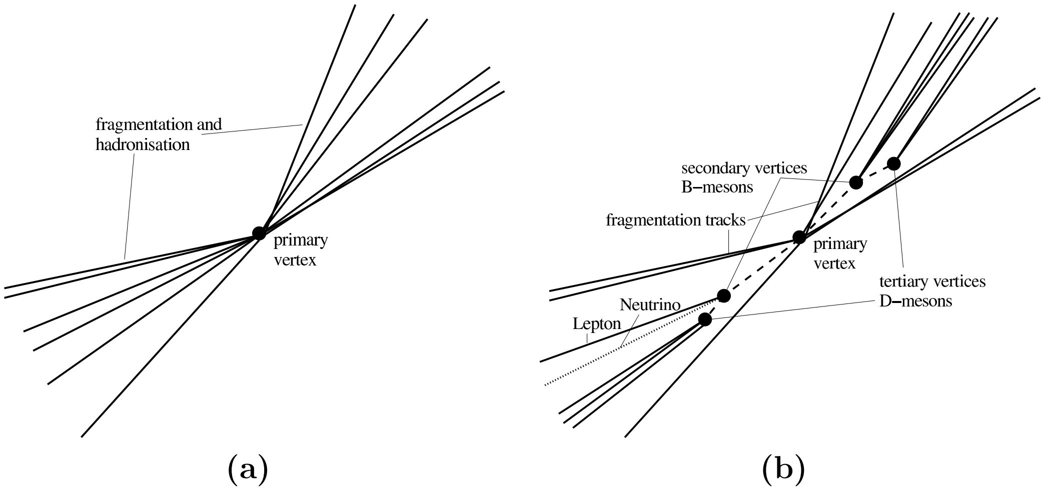

Figure 4.1: Schematic view of the typical topology of a light quark event (a) in comparison with a $b\overline{b}$ event (b). Tracks from the fragmentation and a possible strong decay of excited B states originate from the primary vertex, while the particle trajectories from the heavy hadron decay point to the secondary vertex. In addition, there is a cascade decay via a B and D meson shown on the right side of (b). The left side of (b) is a semileptonic b decay ($b \to \ell^-$).

by the fragmentation and hadronisation process. This happens very close to the interaction point. Excited hadron states decay rapidly via the strong interaction to the corresponding ground state, so that their decay point cannot be disentangled from the production vertex. For that reason a large majority of the hadron tracks start closely to the primary event vertex. However the ground states of the heavy hadrons decay weakly, allowing a relatively long lifetime. The most common b and c hadron ground states and their lifetimes are listed in Table 2.2. In combination with their large mass and hence large momentum, the long lifetime corresponds to a decay length of several millimetres. This leads to a decay vertex (secondary vertex) which is displaced from the production vertex (primary vertex). The production and decay of secondary c hadrons produced in b hadron decays is likewise controlled by the weak interaction, so that a cascade of secondary and tertiary vertices can appear. The average distance between production and decay of B mesons is 3 mm, of D^0 1.5 mm and of D^+ 4 mm. These distances are large enough to be resolved by the micro-vertex detectors operated at LEP. Apart from the heavy hadrons, only the Λ_b and the K^0_s have a similar average decay length, so that an observed secondary vertex and in particular the use of the reconstructed flight length provides a good method of identifying b and c quark events with only low contamination from u, d and s quark events. Another distinctive feature of b and c hadrons is their high mass (see Table 2.2) and consequently the high decay multiplicity. The relative mass difference between b and c hadrons of about a factor three is sufficiently large to be used also to separate b hadrons from primary c hadrons.

Unfortunately, the primary parton flight direction is not directly accessible in hadronic events, therefore a good approximation for it is necessary. In the exclusive measurements (Section 4.2 and Section 4.3 [13, 77]) the direction of the leptons or the reconstructed D mesons respectively give a rough estimate of the primary quark direction, however, leptons as well as D mesons from b or c decays have a non negligible transverse momentum p_{t} with respect to the closest jet axis, leading to a mismatch between the lepton or D meson flight direction and the direction of the $\mathrm{q\overline{q}}$ axis of the event. Another method – especially for the inclusive analysis (Section 4.1 [76]) – is to take the jet axis of a b or c jet. In addition these approaches all have the problem, that there can be more than one observed $\cos\theta$ value for the primary quark per event, which requires a procedure to decide which angle to choose as the primary quark flight direction. A remedy to overcome both problems at once is offered by the determination of the event thrust axis [78]. This method is also more robust with respect to effects from high energetic neutrinos from semileptonic decays.

The thrust value is defined as the maximum sum of the longitudinal momenta $\vec{p}_i \cdot \vec{n}$, normalised to the sum of the absolute momenta [78]:

$$\mathrm{T} = \max_{\vec{n}} \left(\frac{\sum_i |\vec{p}_i \cdot \vec{n}|}{\sum_i |\vec{p}_i|} \right) \quad , \quad \mathrm{T} \in [1/2, 1] \in \mathbb{R} \tag{4.1}$$

The direction $\vec{n}$ of the thrust axis $\vec{\mathrm{T}} = \mathrm{T}\vec{n}$ is the axis of projection, for which the sum of the longitudinal momenta of all charged and neutral particles reaches its maximal value [78]. In the limit of vanishing transverse momenta, the thrust value is 1, hence characterising pure back-to-back topologies. In contrast, a thrust value of 1/2 is obtained in the limit of isotropic events, rendering the thrust axis direction arbitrary [78].

The thrust axis is calculated using tracks and electromagnetic calorimeter clusters not associated to any track. The energies measured in the electromagnetic calorimeter are converted to momenta by assuming that the absorbed particles are pions [79]. The polar angle θ_{T} of the thrust axis with respect to the electron beam direction is determined modulo π. This technique has been used in many previous publications (see [13, 76, 77, 80–84] for the OPAL results) and will not be discussed further here.

Each event is divided into two hemispheres by a plane perpendicular to the event thrust axis, containing the interaction point. The hemisphere containing the pos-

method	flavour identification		$\mathrm{sign}(\cos\theta)$		statistics	application
	$\mathrm{b\overline{b}}$	$\mathrm{c\overline{c}}$	$\mathrm{b\overline{b}}$	$\mathrm{c\overline{c}}$		
secondary vertex tag / hemisphere charge	++		∘	∘	++	R_b, A^b_FB
semileptonic decays	+	+	++	++	+	A^b_FB, A^c_FB
$\mathrm{D}^{(*)}$ meson decays (exclusive)	∘	+	++	++	−	(Z resonance)
charged pions from D^{*+} decays	−	∘	++	++	∘	(A^b_FB,) A^c_FB

Table 4.1: An overview of the different methods used in heavy flavour measurements. While an inclusive secondary vertex tag provides the best method to identify bottom events, the selection of semileptonic or $\mathrm{D}^{(*)}$ decays is superior for charm tagging and forward-backward asymmetry measurements. The potential of the different methods concerning flavour identification and Quark anti-quark separation is indicated: ++ = very good, + = good, ∘ = fair and − = bad. The different methods are introduced in the three sections of this chapter.

itive z axis is labelled "forward", and the other hemisphere "backward". Typically, each of the two hemispheres contain one b or c jet. The decision into which event thrust hemisphere the primary quark of the $\mathrm{q\overline{q}}$ pair is emitted is more difficult. For that reason different techniques are applied to tag heavy flavour events together with the charge sign of the primary quark. In Table 4.1 an overview of different heavy flavour tagging techniques, which are the basis for the forward-backward asymmetry analyses, is given, together with an indication of their potential to tag heavy flavour events and to determine the sign of $\cos\theta$. Their application to the measurements of the heavy flavour forward-backward asymmetries is introduced in the following three sections by describing the OPAL analyses. The analysis in this work is mainly based on the principles described in Section 4.3. For further details on the other two analyses see [76,77].

4.1 Inclusive Tag

Two methods are used to tag $\mathrm{b\overline{b}}$ events, based on displaced secondary vertices and high momentum leptons. Due to the long lifetime and high boost of b hadrons produced in $\mathrm{e^+e^-} \to \mathrm{b\overline{b}}$ events, their decays lead to secondary vertices that are displaced from the primary interaction point by decay lengths of the order of millimetres. With the silicon micro-vertex detector installed at OPAL, these secondary vertices can be reconstructed and used as an indication of a b hadron decay. Since the secondary vertex tag makes use of a common property of all weakly decaying b hadrons, it yields a comparatively large event sample. It follows that the secondary vertex tag is the principal method for a measurement of R_{b} (R_{b} is the measured fraction of the $\mathrm{b\overline{b}}$ events with respect to all hadronic Z decays).

- In the inclusive analysis each event is divided into two hemispheres which are considered independently.
- In order to reduce inter-hemisphere tagging correlations the primary vertex position is first reconstructed separately in each hemisphere, using tracks from that hemisphere combined with a common beamspot constraint.
- Jet-finding is done with a cone algorithm [85] using charged tracks and electromagnetic calorimeter clusters not associated to any track. Since this algorithm assumes that a jet has the shape of a cone and therefore is started with a certain value for the opening angle of the cone, it is possible to find more than one jet per hemisphere.
- An attempt is then made to reconstruct a secondary vertex in each jet of the event, using a subset of well-measured tracks [70, 86].
- If a secondary vertex is found with a significant separation from the hemisphere primary vertex, a neural network with five inputs (derived from decay length, vertex multiplicity and invariant mass information) is used [86] to further separate b decays from c and light quark background. The neural network delivers a value in the interval $[0, 1] \in \mathbb{R}$. This output value indicates the quality of the distinction of b decays of c and light quark background. A short introduction to artificial neural networks is given in the appendix Chapter A.
- For each jet in the hemisphere under study the neural network output is calculated. The highest output value defines the vertex tag variable B for the hemisphere [86]. Three classes of hemisphere tags are defined [86]:
  - a "tight" vertex tag T,
  - a "medium" tag M and
  - a "soft" tag S.

  The hemisphere b tagging efficiencies of the T,M and S tags are quoted to be 18 %, 6 % [86] and 5 %, and the fractions of tagged hemispheres originating from non-$\mathrm{b\overline{b}}$ events are about 3 %, 15 % and 25 % [86].

Electrons and muons with momentum $p > 2$ GeV/c and transverse momentum $p_{\mathrm{t}} > 1$ GeV/c are also used to tag $\mathrm{b\overline{b}}$ events. The purity of the tagged lepton hemispheres is further enhanced in semileptonic b decays by using information from the lepton p and p_{t} and its degree of isolation from the rest of the jet by another neural network algorithm [87]. Hemispheres are defined to be tagged with the lepton tag L if any lepton in the hemisphere fulfills a certain cut on the lepton b tagging neural network output corresponding to a b tagging efficiency of 8 % at a non-$\mathrm{b\overline{b}}$ impurity of 20 % [86]. These cuts are agreed in the OPAL collaboration. In this case a vertex T, M or S tag in this hemisphere is ignored and the hemisphere considered only as an L tag.

Events containing at least one hemisphere with a T, M, S or L b tag are accepted and used for the asymmetry analysis. Each combination of tags in the two hemispheres (T-nothing, L-nothing, T-T, T-S etc.) define a separate tagging class, resulting in 14 different classes. In the data, 520 133 b tagged events are assigned to one of the 14 classes [86]. with a $\mathrm{b\overline{b}}$ event tagging efficiency of about 54 % as determined with Monte Carlo simulation [86]. For most of the events a T, L, S or M tag hemisphere is found together with an untagged hemisphere. These events comprise 33 %, 22 %, 14 % and 13 % of the tagged data sample [86].

In the subsequent step the b quark from the $\mathrm{b\overline{b}}$ system has to be identified thus defining the sign of $\cos\theta$. For this purpose an inclusive hemisphere charge technique is applied so that the total tagged sample can be used. The production flavour (b or $\mathrm{\bar{b}}$) of the b quark is determined independently in the two hemispheres of each selected event. It exploits the fact that statistically some information about the primary quark charge is conserved in the observed hadrons after the hadronisation process. Charged particles with high momenta are more likely to have the same charge sign as the primary quark than particles at low momenta [81].

Up to four pieces of information are used per hemisphere: the momentum-weighted average track charge with two different weighting factors (evaluated for the highest energy jet in each hemisphere), the charge of a secondary vertex reconstructed in the hemisphere, and the charge of any kaon in the hemisphere. The jet charges can be calculated for every hemisphere, whilst the vertex and kaon charges are only available for a subset of hemispheres. All available information is combined using a neural network algorithm to produce a single production flavour tag variable Q for each hemisphere [1].

[1]Note that although semileptonic b decays are used to tag $\mathrm{b\overline{b}}$ events, the charge of the lepton in L tagged hemispheres is not used in the production flavour tag Q, in order to reduce the correlation with the b quark asymmetry analysis based on semileptonic decays, introduced later in this chapter.

The jet charge $Q^{\kappa}_{\mathrm{jet}}$ is calculated for the highest energy jet in each hemisphere as [81]:

$$Q^{\kappa}_{\mathrm{jet}} = \frac{\sum_i (p^{\mathrm{l}}_i)^{\kappa} q_i}{\sum_i (p^{\mathrm{l}}_i)^{\kappa}}\,, \tag{4.2}$$

where p^{l}_i is the longitudinal momentum component with respect to the jet axis and q_i the charge (±1) of track i, and the sum is taken over all tracks in the jet [39]. Two jet charges $Q^{\kappa=0.5}_{\mathrm{jet}}$ and $Q^{\kappa=1.0}_{\mathrm{jet}}$ are calculated for each jet. The value $\kappa = 0.5$ optimises the separation between hemispheres containing b and $\bar{\mathrm{b}}$ quarks for a single jet charge [88], and including the second jet charge with $\kappa = 1.0$ provides a small amount of additional separation power, although the two jet charges are strongly correlated.

For hemispheres containing a reconstructed secondary vertex, the charge of this vertex Q_{vtx} is calculated as:

$$Q_{\mathrm{vtx}} = \sum_i w_i q_i\,, \tag{4.3}$$

and the uncertainty $\sigma_{Q_{\mathrm{vtx}}}$ as:

$$\sigma_{Q_{\mathrm{vtx}}} = \sum_i w_i(1-w_i) q_i\,, \tag{4.4}$$

where w_i is the weight for track i to have come from the secondary, rather than the primary, vertex [89], and the sum was again taken over all tracks in the jet. The weights w_i are obtained from a neural network algorithm using as input the track momentum, transverse momentum with respect to the jet axis, and impact parameters with respect to the reconstructed primary and secondary vertices, as in [88]. A well-reconstructed (small $\sigma_{Q_{\mathrm{vtx}}}$) vertex charge close to $+1$ (-1) indicates a B^+ (B^-) hadron, tagging the hemisphere as containing a $\bar{\mathrm{b}}$ (b) quark, whilst a vertex charge close to zero indicates a neutral b hadron, (e.g. B^0 or $\overline{\mathrm{B}^0}$), giving no information on the b quark production flavour. A vertex charge with large $\sigma_{Q_{\mathrm{vtx}}}$ cannot distinguish between charged and neutral b hadrons, and also provides no information on the b quark production flavour.

Charged kaons produced from the b hadron decay can also be used to tag the b production flavour, via the underlying quark decay cascade $\mathrm{b} \to \mathrm{c} \to \mathrm{s}$. Candidate kaon tracks are selected in the highest energy jet in each hemisphere, using $\mathrm{d}E/\mathrm{d}x$ information. If more than one track in the jet is selected, the one with the highest weight w_i to come from the secondary vertex is retained. If no secondary vertex is reconstructed in the jet, the weights are calculated using only the track momentum, transverse momentum and impact parameters with respect to the primary vertex.

The hemispheres are then categorised into one of four classes:

1. neither vertex nor kaon charge,
2. vertex charge only,
3. kaon charge only,
4. both vertex and kaon charges.

The available tagging variables ($Q_{\rm jet}^{\kappa=0.5}$ and $Q_{\rm jet}^{\kappa=1.0}$, $Q_{\rm vtx}$ and $\sigma_{Q_{\rm vtx}}$, w_i of kaon track, signed by its charge) are combined using a neural network separately for each of the four classes. The continuous tagging variable Q is derived from the output x of the neural network, and is defined such that

$$Q = \frac{N_{\bar{\rm b}}(x) - N_{\rm b}(x)}{N_{\bar{\rm b}}(x) + N_{\rm b}(x)}\,, \tag{4.5}$$

where $N_{\rm b}(x)$ and $N_{\bar{\rm b}}(x)$ are the number densities of b and $\bar{\rm b}$ hemispheres with a particular value of x taken from simulated events. Hemispheres with $Q = +1$ (-1) are tagged with complete confidence as being produced from $\bar{\rm b}$ (b) quarks, and hemispheres with $Q = 0$ are equally likely to be from either a b or a $\bar{\rm b}$ quark. The modulus $|Q|$ satisfies $|Q| = 1 - 2\xi$ where ξ is the probability to tag the production flavour incorrectly. The effects of $\rm B_d^0$ and $\rm B_s^0$ mixing (see Section 2.8) contribute to ξ, since the decay flavour of a mixed b hadron is opposite to its production flavour.

The four classes comprise about 25 %, 36 %, 15 %, and 24 % of the data sample, and have effective mistag fractions of 33.1 %, 31.2 %, 32.5 %, and 29.1 % [86].

The asymmetry is determined by a counting method: For a sample consisting of a mixture of quark species and a varying tagging efficiency as a function of the thrust direction $|\cos\theta_{\rm T}|$ for each flavour, the mean difference of the production flavour tag values in the two hemispheres $\langle Q_{\rm F} - Q_{\rm B}\rangle$ is given by

$$\langle Q_{\rm F} - Q_{\rm B}\rangle = \sum_{\text{flavours q}} s_{\rm q} P_{\rm q} C_{\rm q} \delta_{\rm q} A_{\rm FB}^{\rm q}. \tag{4.6}$$

In this equation, $Q_{\rm F}$ and $Q_{\rm B}$ are the production flavour tags in the forward and backward hemispheres as measured in the data, $s_{\rm q}$ is $+1$ (-1) for down-like (up-like) quarks, $P_{\rm q}$ is the fraction of events of flavour q in the data sample, derived mainly from the data, and $\delta_{\rm q}$ is the charge separation for flavour q which is determined from Monte Carlo simulation for $\rm u\bar{u}$, $\rm d\bar{d}$, $\rm s\bar{s}$, and $\rm c\bar{c}$ events and directly from the data for $\rm b\bar{b}$ events, once the flavour fractions $P_{\rm q}$ are known. The factors $C_{\rm q}$, which are taken from simulation, account for variations of the asymmetry and the tagging efficiency with $\cos\theta_{\rm T}$ and are given by

$$C_{\rm q} = \frac{8}{3}\frac{\int \overline{\eta}_{\rm q}(y) y \,{\rm d}y}{\int \overline{\eta}_{\rm q}(y)(1+y^2)\,{\rm d}y} = \frac{8}{3}\frac{\sum_{\rm events} y}{\sum_{\rm events}(1+y^2)}\,, \tag{4.7}$$

with $y = |\cos\theta_{\mathrm{T}}|$; $\overline{\eta}_{\mathrm{q}}$ is the efficiency to tag an event of flavour q in a given small interval of y. The sums run over all tagged Monte Carlo events of flavour q. The asymmetry $A_{\mathrm{FB}}^{\mathrm{b}}$ is derived by solving Eq. 4.6, using the Standard Model expectations for the charm and light quark asymmetries, together with fractions R_{q} of hadronic Z decays to each quark flavour as calculated by ZFITTER 6.36 [34]. The asymmetry fit procedure is applied separately to the events collected in each of the five $|\cos\theta_{\mathrm{T}}|$ bins and 14 tag classes, resulting in 70 different values for $A_{\mathrm{FB}}^{\mathrm{b}}$ for each energy bin and data taking period. All the $A_{\mathrm{FB}}^{\mathrm{b}}$ measurements for each energy point are then combined, weighted according to their statistical errors.

The measured asymmetry values, after correcting to the quark level, are:

$$\begin{aligned}
A_{\mathrm{FB}}^{\mathrm{b}} &= (\ \ 5.82\pm1.53\pm0.12)\ \%\ \text{at}\ \langle\sqrt{s}\rangle = 89.50\,\mathrm{GeV},\\
A_{\mathrm{FB}}^{\mathrm{b}} &= (\ \ 9.77\pm0.36\pm0.18)\ \%\ \text{at}\ \langle\sqrt{s}\rangle = 91.26\,\mathrm{GeV},\\
A_{\mathrm{FB}}^{\mathrm{b}} &= (12.21\pm1.23\pm0.25)\ \%\ \text{at}\ \langle\sqrt{s}\rangle = 92.91\,\mathrm{GeV},
\end{aligned}$$

where the first error is statistical and the second systematic in each case. The largest single contribution to the overall systematic uncertainty arises from the correlation between the production flavour tag determinations in the hemispheres of the primary b and $\bar{\mathrm{b}}$ quarks (charge correlation). It is of the order of 0.09 % for the peak data.

For the identification of charm events, the secondary vertex tag is less suitable for two main reasons:

1. The lifetimes of weakly decaying charm hadrons are smaller than those of weakly decaying bottom hadrons, typically by a factor of 3 for mesons. Because of the smaller mass, the fragmentation of charm quarks is softer than that of bottom quarks. Together with the smaller lifetimes, this leads to typically much shorter decay lengths for secondary vertices in primary charm events.

2. At large decay lengths the contribution from bottom events becomes dominant, which means that a pure charm sample is difficult to obtain.

4.2 D Mesons

Since charmed hadrons are only rarely produced (Section 2.7.2) during light quark fragmentation, their presence tags c quarks coming either from the primary Z decay or from decay products of a b quark. For this analysis type the D^{*+} meson and its decay products D^0 and D^+ are used.[2]

[2] Throughout this text charge conjugate modes are always implicitly included.

The flavour of D mesons also measures the flavour of the original quark. In $c\bar{c}$ events the primary quark is directly contained in the D meson, while in $b\bar{b}$ events the c quark is coming from the decay chain $b \to c$. The decay $b \to \bar{c}$ (via $b \to cW^-, W^- \to \bar{c}s$) is suppressed, so that the quark flavour tag using D mesons is unique, contrary to the lepton tag, where the $b \to \ell^-$ and $b \to c \to \ell^+$ decays have to be disentangled. Another advantage of D mesons is that one separates directly the quark from the antiquark and not positively from negatively charged quarks as in the forward-backward asymmetry measurement using semileptonic decays, so that the sensitivity of the measurements to the sample composition is largely reduced. Since the absolute efficiency cancels in the asymmetries many different states can be used.

For this analysis D^{*+} mesons are reconstructed in five different decay channels:

$$
\begin{array}{lll}
D^{*+} \to D^0\pi^+ & & \\
\quad \hookrightarrow K^-\pi^+ & \text{“3 prong”} & , \\
\quad \hookrightarrow K^-\pi^+\pi^0 & \text{“satellite”} & , \\
\quad \hookrightarrow K^-\pi^+\pi^-\pi^+ & \text{“5 prong”} & , \\
\quad \hookrightarrow K^-e^+\nu_e & \text{“electron”} & , \\
\quad \hookrightarrow K^-\mu^+\nu_\mu & \text{“muon”} & .
\end{array}
$$

A number of tracks appropriate for the selected channel are combined to form a D^0 candidate and their invariant mass is calculated. Only candidates with the correct charge combinations are retained. Candidates are selected if the reconstructed mass lies within the expected range for that channel. After adding a further track as a possible pion from the D^{*+} decay, the combined mass is calculated and the candidate is selected if the mass difference $\Delta M = M_{D^{*+}} - M_{D^0}$ is within certain limits. ΔM is the effective mass difference, calculated from the visible tracks of the candidate. The ΔM spectra for the five reconstructed D^{*+} channels are presented in Figure 4.2 [77].

The D^0 and D^+ mesons are identified in the decay modes:

$$
\begin{array}{l}
D^0 \to K^-\pi^+ \quad , \\
D^+ \to K^-\pi^+\pi^+ \quad .
\end{array}
$$

The invariant mass is calculated from the appropriate number of tracks. A D^+ candidate is rejected if its reconstructed mass is compatible with the mass of a D^{*+} candidate, coming from the same three tracks. The long lifetime of the weakly decaying D mesons is used to enrich the signal purity by cutting on the distance between the primary vertex and the secondary vertex from the tracks forming the D candidate.

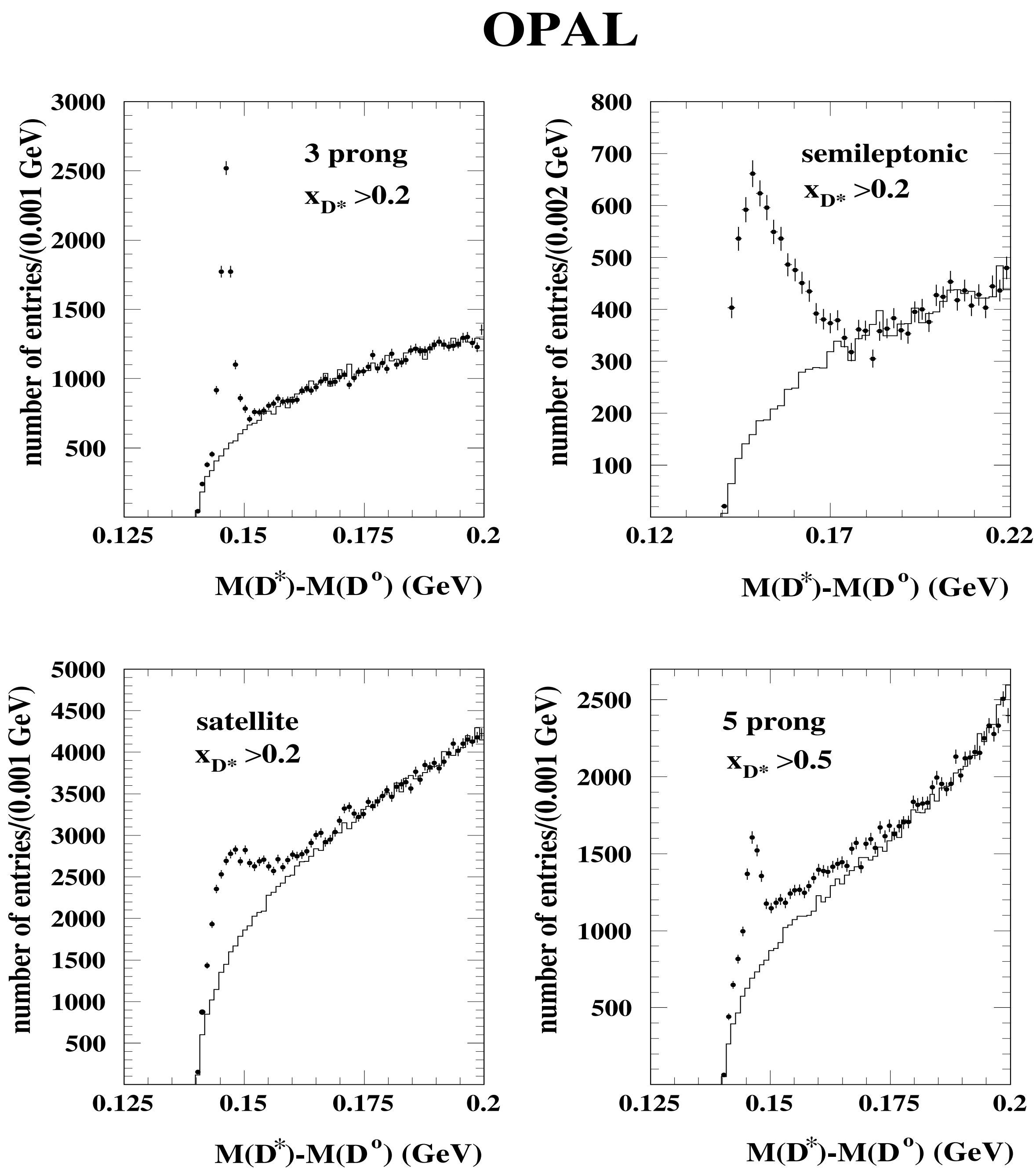

Figure 4.2: Distributions of the difference $M_{D^{*+}} - M_{D^0}$ reconstructed in the four different D^{*+} channels. The semileptonic decays have been combined into one plot. Superimposed are the background estimator distributions, normalised to the upper sidebands in ΔM. The scaled energy x_D is the energy of the D Meson with respect to the beam energy.

Only one measurement per event is needed to orientate the thrust axis such that it points towards the flight direction of the primary quark. If more than one D meson candidate is found per event, a hierarchy is used to select the best one: low background is preferred and low multiplicity final states are favoured. The hierarchy used, from best to worst, is: 3 prong, semileptonic, satellite, 5 prong, D^0, D^+. The number of candidates is reduced by 34.6 % by the multiple candidate rejection [77]. After all cuts a total of 73 870 D candidates is found [77].

For the purpose of the asymmetry analysis, a signal event is defined as any event that contains enough information to reconstruct correctly the charge and flavour of the primary quark. For the D^{*+} decays two classes of events contribute to the signal sample: events where a D meson is completely reconstructed in one of the channels described, and events where a D^{*+} decay is partially found, but where the slow pion is correctly tagged [77]. The fraction of events which is considered as signal for this analysis is determined with a background estimator, which uses a hemisphere mixing technique first described in [84]. This method ensures that no correctly identified slow pions enter the background sample. No requirements are put on the charge of the D^0 candidate tracks, except that the sum of the charges of all tracks including the slow pion candidate should be ± 1. The background is determined by normalising the estimator distribution for ΔM to the sideband of the signal distribution and subtracting the normalised background from the signal. The level of background in the D^0 and D^+ channels is determined from a fit to the observed mass spectra with an empirically determined functional form for the background.

A problem in all channels is the presence of background where the correlation between the primary quark charge and the charge q tagged by the D candidate is preserved, but no true slow pion is present. These events will not be considered as signal, but they are assumed to be asymmetric in $q\cos\theta$, thereby introducing an asymmetry into the background. Such correlations are expected since the sample of candidate tracks is enriched in true kaons. Many kaons are originating from the primary quark in the event, thereby preserving the charge correlation. Similar effects are expected for leptons. These events are present at levels of a few percent in all modes considered. Altogether $24\,195 \pm 150$ D^{*+} mesons and $8\,439 \pm 132$ D^0 and D^+ mesons are reconstructed after background subtraction, over backgrounds of $24\,664 \pm 150$ events and $16\,558 \pm 132$ events, respectively [77].

In this analysis the D^{*+}, D^0 and D^+ mesons are used as tags for primary charm and bottom decays of the Z. Both processes are expected to contribute roughly equally to the tagged sample, in addition to sizeable contributions from combinatorial background [77]. Lifetime information and jet shape variables are used to separate the different sources of D mesons. The remaining signal is composed essentially only of $c\overline{c}$ and $b\overline{b}$ events. Since $b\overline{b}$ events are significantly different in lifetime and jet shape properties from other events, the fraction of $b\overline{b}$ events in the sample can be determined, and therefore the $c\overline{c}$ content inferred. Finally for each event a probability is calculated from lifetime information, whether this event is a $b\overline{b}$ or a $c\overline{c}$ event. The probabilities are obtained for two jets in the event: the jet containing the reconstructed D meson (the D jet) and the jet with the highest energy not containing the D meson candidate (the secondary jet). They are calculated, as functions of the D meson scaled energy, and the decay length significance δ of the secondary vertex in each jet. These probabilities are used in the asymmetry fit to separate primary charm and bottom events.

The bottom asymmetry, the charm asymmetry, and the background asymmetries are determined in a simultaneous, unbinned likelihood fit to the $y = q\cos\theta_{\mathrm{T}}$ distribution, where q is the sign of the charge of the D meson (sign of the charge of the charm quark) and θ_{T} is the angle of the thrust axis with respect to the electron beam. The orientation of the thrust axis is chosen such that the scalar product of the thrust axis with the D direction is positive. The likelihood function has the form [77]:

$$\log\mathcal{L} = \sum_i \log(1 + y_i^2 + \frac{8}{3}A_{\mathrm{FB}}^{\mathrm{obs}} y_i) \; - \sum_i \log N_{\mathrm{norm}}^i . \tag{4.8}$$

The sum runs over all candidates i considered. The normalisation does not depend on the asymmetry itself, and therefore is dropped from the further discussion. The likelihood for one event i is:

$$\mathcal{L}_i \;\; = \;\; 1 + y_i^2 + \frac{8}{3}\left[w_{\mathrm{b}}^i\,(1 - 2\,C_{\mathrm{D}}^i(\delta))\,A_{\mathrm{FB}}^{\mathrm{b}} + w_{\mathrm{c}}^i\,A_{\mathrm{FB}}^{\mathrm{c}} + w_{\mathrm{bgd}}^i\,A_{\mathrm{FB}}^{\mathrm{bgd}}\right] y_i \tag{4.9}$$

Here $w_{\mathrm{bgd,b,c}}$ are the probabilities that a D meson originates from the source indicated and $A_{\mathrm{FB}}^{\mathrm{bgd}}$ allows for a possible asymmetry in the background. Mixing and non-prompt production of D mesons can change the charge correlation between the primary quark and the detected D meson in the bottom sample. These effects are collectively described by the charge correlation factor $C_{\mathrm{D}}^i(\delta)$. This factor also accounts for the jet charge identification probability which is determined to be $0.642 \pm 0.003 \pm 0.013$ for $b\overline{b}$ events and $0.699 \pm 0.010 \pm 0.012$ for $c\overline{c}$ events [77].

The measured b and c forward-backward asymmetry values, after correcting to the quark level, are quoted to be:

$$\begin{aligned}
A_{\mathrm{FB}}^{\mathrm{b}} &= (\;8.7 \pm 10.8 \pm 2.9)\,\%, & A_{\mathrm{FB}}^{\mathrm{c}} &= (\;\;3.9 \pm 5.1 \pm 0.9)\,\% & \text{at } \langle\sqrt{s}\rangle &= 89.45 \text{ GeV},\\
A_{\mathrm{FB}}^{\mathrm{b}} &= (\;9.5 \pm \;\;2.7 \pm 2.2)\,\%, & A_{\mathrm{FB}}^{\mathrm{c}} &= (\;\;6.3 \pm 1.2 \pm 0.6)\,\% & \text{at } \langle\sqrt{s}\rangle &= 91.21 \text{ GeV},\\
A_{\mathrm{FB}}^{\mathrm{b}} &= (\text{-}2.1 \pm \;\;9.0 \pm 2.6)\,\%, & A_{\mathrm{FB}}^{\mathrm{c}} &= (15.8 \pm 4.1 \pm 1.1)\,\% & \text{at } \langle\sqrt{s}\rangle &= 92.91 \text{ GeV},
\end{aligned}$$

with a statistical correlation coefficient between the b and c asymmetry of -0.28 on-peak (-0.27 for both, the low and high energy off-peak points). The first error is statistical and the second systematic in each case.

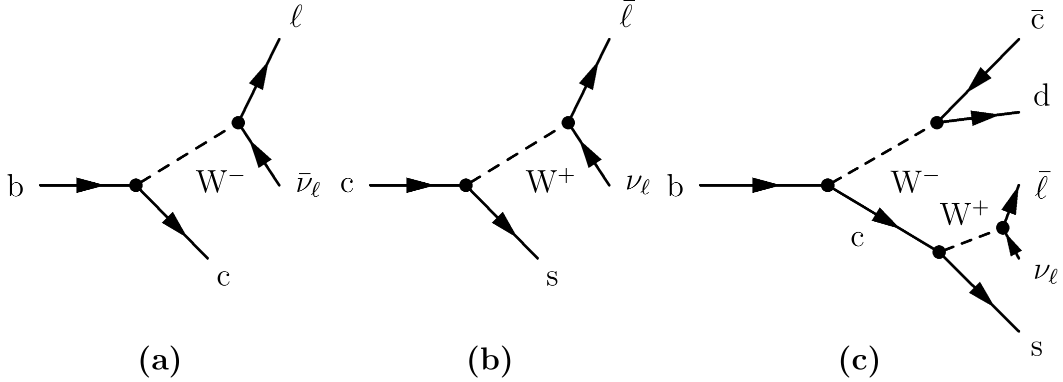

Figure 4.3: Feynman diagrams of the semileptonic b and c decays relevant for the forward-backward asymmetry measurements with semileptonic decays. (a) shows a $b \to \ell^-$ decay, (b) a $c \to \ell^+$ decay and (c) a $b \to c \to \ell^+$ decay. In case ℓ is a τ lepton it will decay to an electron or muon forming a $b \to \tau^- \to \ell^-$ decay. The decay $b \to \overline{c} \to \ell^-$ can be understood using (c). The $\bar{c}$ quark can decay to a s quark via a W boson. The W then decays into a lepton.

4.3 Semileptonic Decays

This method uses leptons produced in semileptonic decays of b and c hadrons, usually referred to as "prompt leptons" to measure the b and c quark forward-backward asymmetries. Prompt leptons are employed to tag simultaneously the flavour and the charge of the primary quark. As will be shown in this work this method provides smaller statistical uncertainties than the method using D mesons (Section 4.2) [77]. However, it leads to somewhat larger statistical errors than the inclusive method (Section 4.1) [76] which is based on most recent developments within the OPAL collaboration.

After the fragmentation, a b or c hadron can decay semileptonically into hadrons consisting of lighter quarks via the emission of a $W^\pm$ boson. The $W^\pm$ boson itself can then decay into a lepton and an antineutrino. According to recent measurements b quarks decay in (10.65 ± 0.23) % via $b \to \ell^-$ decays, in (8.08 ± 0.18) % via $b \to c \to \ell^+$ decays, in (1.62 ± 0.44) % via $b \to \overline{c} \to \ell^-$ decays, and in (0.42 ± 0.05) % via $b \to \tau^- \to \ell^-$ decays to leptons [26, 52]. The c quarks decay in (9.77 ± 0.32) % via $c \to \ell^+$ decays [26, 52].

Figure 4.3 summarises the most important Feynman graphs of semileptonic b and c decays relevant for this measurement. These semileptonic decay channels can be used to identify the flavour of the primary quark. The charge of the lepton is correlated with the sign of the charge of the quark from which decay it was produced. Together with the knowledge of the primary quark flavour of the event and the semileptonic decay channel which produced the lepton, the charge of the lepton is used to distinguish between primary quarks and antiquarks.

The analysis uses only events where at least one lepton candidate can be identified. Particles with momentum greater than 2 GeV/c are considered as lepton candidates. Electron candidate tracks are required to have at least 20 good measurements of $\mathrm{d}E/\mathrm{d}x$ from jet chamber hits. Electrons are then identified using a neural network algorithm (see Section 5.4.1). The identification relies on ionisation energy loss ($\mathrm{d}E/\mathrm{d}x$) measured in the tracking chamber, together with spatial and energy-momentum (E/p) matching between tracking and calorimetry. Electrons originating from photon conversions are rejected using another neural network algorithm. Muons are identified by requiring a spatial match between a track reconstructed in the central tracking detectors and a track segment reconstructed in the external muon chambers. In this analysis, only leptons from the decay of a b or c hadron in a $\mathrm{b\overline{b}}$ or $\mathrm{c\overline{c}}$ event are considered as signal. Any other genuine electron or muon and any hadron misidentified as a lepton is considered as background.

The primary vertex position and the thrust axis is first reconstructed for all events, passing the multihadronic event selection (see Section 5.2). Each event is divided into two hemispheres by a plane perpendicular to the event thrust axis and containing the interaction point. An attempt is made to reconstruct a secondary vertex in each jet, using a subset of well-measured tracks.

The relationship between the lepton charge and the charge of the decaying primary quark or antiquark is vital for the asymmetry measurement. According to the sign correlation between primary quark and lepton candidates, the lepton candidates can be categorised into four groups:

1. Leptons coming directly from the weak decay of b hadrons are denoted $\mathrm{b} \to \ell^-$. A negatively charged lepton comes from the decay of a hadron containing a b quark, and a positive lepton from a $\bar{\mathrm{b}}$ [2] (see Figure 4.3 (a)). Electrons and muons from leptonic τ decays where the τ lepton comes from a direct b decay ($\mathrm{b} \to \tau^- \to \ell^-$), and cascade decays ($\mathrm{b} \to \overline{\mathrm{c}} \to \ell^-$) where a b hadron decays to a c hadron, which then decays semileptonically, have the same sign correlation as the $\mathrm{b} \to \ell^-$ decays. The $\mathrm{b} \to \overline{\mathrm{c}} \to \ell^-$ decays are also explained in Figure 4.3.

2. Cascade decays, $\mathrm{b} \to \mathrm{c} \to \ell^+$ and $\mathrm{b} \to \mathrm{c} \to \tau^+ \to \ell^+$, have the opposite sign correlation as group 1, see Figure 4.3 (c).

3. Leptons from the decay of c hadrons produced in $\mathrm{c\overline{c}}$ events, $\mathrm{c} \to \ell^+$, and $\mathrm{c} \to \tau^- \to \ell^-$ decays have the opposite sign correlation to direct $\mathrm{b} \to \ell^-$

decays (Figure 4.3 (b)). A primary c quark produces a positive lepton.

4. All other decays in leptons and hadrons identified as leptons are classified as background.

A neutral B meson may have mixed before decay (Section 2.8), so that a primary b quark decays as a $\bar{\mathrm{b}}$, or vice versa. This is quantified by the average B mixing parameter, $\overline{\chi}$ (Eq. 2.44), which is the probability that a produced b hadron decays as its antiparticle. Leptons from these mixed mesons are classified according to the decaying b quark and contribute to the asymmetry with the wrong sign for their category, causing a reduction in the observed $\mathrm{b\overline{b}}$ asymmetry:

$$A_{\mathrm{FB}}^{\mathrm{b,obs}} = (1 - 2\overline{\chi})\, A_{\mathrm{FB}}^{\mathrm{b}} \tag{4.10}$$

For the measurement of the b and c quark forward-backward asymmetries it is especially important to separate direct b and c decays from each other and from all other contributions. In order to optimise the separation, a multi-variable analysis is performed, where two different neural networks are used to distinguish the source of the lepton candidate. This method was first introduced in [83]. One of the networks, NETb, is to separate direct $\mathrm{b} \to \ell^-$ decays from the remaining contributions. The separation power is mainly determined from the momentum p of the lepton and the transverse momentum p_t with respect to the closest jet axis [90]. Another neural net, NETc, helps to distinguish between $\mathrm{c} \to \ell^+$ decays and the other classes. Here the main information comes from lifetime information. Furthermore for both neural nets as much of the available information as possible is used, including jet and vertex properties which have already proven to be efficient in heavy flavour tagging techniques [83].

With the knowledge of the primary quark flavour, the charge of the lepton, the decay channel of the b or c decay, and the hemisphere in which the lepton has been emitted, the thrust axis can be orientated, such that it points into the flight direction of the primary quark.

An optimal separation is reached by using the net outputs NETb and NETc simultaneously for each lepton candidate to produce two-dimensional distributions for different $\cos\theta_\mathrm{T}$ bins. Monte Carlo events are used to calculate event probabilities for the different NETb and NETc bins. These probabilities are used in the forward-backward asymmetry fit (see Section 5.5) to separate the different contributions ($\mathrm{b} \to \ell^-$, $\mathrm{c} \to \ell^+$, $\mathrm{b} \to \mathrm{c} \to \ell^+$, ...).

The forward-backward asymmetries $A_{\mathrm{FB}}^{\mathrm{b}}$ and $A_{\mathrm{FB}}^{\mathrm{c}}$ are extracted from single lepton events using a binned maximum likelihood fit on a three dimensional space. For this purpose binned distributions in $|\cos\theta_\mathrm{T}|$ and the optimised flavour discriminating variables NETb and NETc are employed.

The average B mixing parameter $\overline{\chi}$ is obtained simultaneously with the asymmetries by counting the number of like-sign leptons in events with at least two "opposite leptons" (i.e. leptons associated to jets that do not belong to the same thrust hemisphere) with NETb > 0.6. For events containing more than two candidate leptons that satisfy these criteria, the two leptons with the highest NETb values are used.

Chapter 5

Measurement of the b and c Quark Forward-Backward Asymmetry using Leptons

In this chapter a measurement of the heavy quark forward-backward asymmetries $A_{\rm FB}^{\rm b}$, and $A_{\rm FB}^{\rm c}$ is described. Here leptons produced in semileptonic decays of b and c hadrons, usually referred to as "prompt leptons", are used to identify heavy flavour events. In addition, the lepton charge is used to distinguish between decaying quarks and antiquarks. The contributions of $\rm b\overline{b}$ and $\rm c\overline{c}$ events to the lepton samples are separated from each other and from background by using several kinematic variables describing the lepton and its associated jet, combined using neural network flavour separation algorithms. The B mixing parameter $\overline{\chi}$ is measured from the fraction of like-sign lepton pairs in events with an identified lepton in each of the two thrust hemispheres. The forward-backward asymmetries $A_{\rm FB}^{\rm b}$ and $A_{\rm FB}^{\rm c}$ and the mixing parameter $\overline{\chi}$ are measured in a simultaneous fit to events with one or two identified leptons in the final state.

5.1 Outline of the Measurement

Several steps have to be performed to extract the quark level forward-backward asymmetries $A_{\rm FB}^{\rm b}$ and $A_{\rm FB}^{\rm c}$ from the data. While the physics background of the forward-backward asymmetry measurement using semileptonic b and c decays has already been described in Section 4.3, this section gives an outline of this analysis, which will be described in detail in this chapter.

- *Event Selection:*
  The data is searched for $\rm Z \rightarrow$ hadrons decays, suppressing events with only

a $\ell\bar{\ell}$ pair in the final state, two-photon events as well as events from cosmic rays.

- *Reconstruction of Event Properties:*
  The primary event vertex is reconstructed using all charged particles visible in the OPAL detector. To get an estimate for the $\mathrm{q\overline{q}}$ flight direction, the event thrust axis [78] is reconstructed. A plane perpendicular to the thrust axis and containing the interaction point divides the event into two hemispheres.

- *Reconstruction of Secondary Vertices and Jets:*
  Tracks from charged particles are used to reconstruct secondary vertices which are displaced from the primary event vertex. Track information from the tracking system, together with clusters found in the electromagnetic calorimeter not associated to tracks in the tracking system, is used to form jets with a cone jet finding algorithm [85].

- *Lepton Identification:*
  Only events with at least one electron or muon candidate in the final state are considered by the analysis. The largest contribution to the background fractions are electrons from $\gamma \to \mathrm{e^+e^-}$ reactions. They have to be suppressed by a second algorithm.

- *Determination of the Event Flavour:*
  Two neural networks are used to distinguish between $\mathrm{b\overline{b}}$, $\mathrm{c\overline{c}}$, and light quark events. The first network, NETb, is trained to identify $\mathrm{b} \to \ell^-$ decays as signal and anything else as background. The second network, NETc, considers $\mathrm{c} \to \ell^+$ decays as signal and all other decays as background.

- *Ranking of Lepton Candidates:*
  In a significant number of events there are more than one lepton candidates. In those cases the candidates are ranked according to their b purity using the neural network output value of NETb.

- *Maximum Likelihood Fit to two Event Classes:*
  Events with one lepton candidate are used to extract simultaneously the b and c quark forward-backward asymmetries. The events with two lepton candidates in opposite thrust hemispheres are used to determine the B mixing parameter $\overline{\chi}$ in the same fit. The idea of a simultaneous determination of $A_{\mathrm{FB}}^{\mathrm{b}}$ and $A_{\mathrm{FB}}^{\mathrm{c}}$ is first realised at OPAL in 1992 [90]. Some years later also the B mixing parameter is extracted together wit $A_{\mathrm{FB}}^{\mathrm{b}}$ in one fit [83].

In order to interpret the measurements of the asymmetries in terms of the Standard Model, the elementary electroweak process has to be separated from the effects of the strong interaction in the final state. Analytical calculations for the

QCD effects of the asymmetries are available in first and second order [35, 91–95], but they cannot be applied directly to the measurements, because the amount of QCD corrections actually seen in the analysis depends significantly on the details of the analysis [96, 97]. The QCD corrections applied to the measured asymmetries also take the experimental bias – estimated using the Monte Carlo simulation – into account.

In the next chapter the forward-backward asymmetries from different measurements are combined to average OPAL and LEP values. This procedure is done such, that the statistical and systematic correlations of the individual measurements are taken into account [98]. From the combined results of the heavy flavour asymmetries together with the other heavy flavour parameters, the electroweak coupling constants are extracted and the weak mixing angle is derived. Further interpretations are discussed there using these quantities.

5.2 Data Sample and Event Simulation

The analysis is based on the entire Z data set recorded with the OPAL detector from 1990 to 2000 at centre-of-mass energies between 89 GeV and 93 GeV. The additional Z events recorded from 1996 to 2000 are originally taken for detector calibration purposes during the higher energy LEP2 running period. The current knowledge about these runs is good enough to include them in today's LEP1 physics analyses. Information provided by the tracking system (including silicon micro-vertex detector and muon chambers) and the calorimetry in the barrel and endcap region of the detector are used. For events entering the analysis nominal working conditions during data taking are required for at least these subdetector systems.

Some flavour separation aspects of this analysis exploit the long lifetimes of b and c hadrons and therefore rely in particular on the silicon micro-vertex detector. This detector was first operational in 1991, providing measurements in the r-ϕ plane [61]. In 1993 it was upgraded to measure tracks in both r-ϕ and r-z planes [62], and in 1996 the $\cos\theta$ coverage for at least one silicon measurement was extended from $|\cos\theta| < 0.83$ to $|\cos\theta| < 0.93$ [63]. The resolution of the vertex drift chamber is sufficient to ensure some flavour separation even in data taken without silicon micro-vertex detector information, therefore also the data taken without the silicon micro-vertex detector is used. The changing detector performance with time is taken into account in the analysis.

Apart from hadronic Z boson decays other events are recorded by the OPAL detector which have to be excluded from the analysis. Such background events can be e^+e^- reactions with non-hadronic final states, like leptonic Z decays or two-photon events, which form the signal for other measurements. Also reactions totally unrelated to e^+e^- collisions may happen, such as interactions of beam electrons with the remaining gas, or with the beam pipe wall or particles from the cosmic radiation crossing the detector [70]. Hadronic Z decays are well distinguishable from the other kinds of events by their high number of charged particles, which can be traced back to the central interaction region.

Events with hadronic Z decays are selected using a well established method, first introduced in 1991 [70] and just slightly changed since then [86]. The criteria used to select hadronic Z decays in this analysis are based on energy clusters in the electromagnetic calorimeter and the charged track multiplicity. Clusters in the barrel region are required to have an energy E_{clus} of at least 100 MeV, and clusters in the end cap detectors are required to contain at least two adjacent lead glass blocks and have a total energy of at least 200 MeV [70]. Tracks are required to have at least 20 measured space points and a distance of closest approach to the interaction point of less than 2 cm in the direction perpendicular to the beam axis and less than 40 cm along the beam axis [70, 86]. Tracks are also required to have a minimum momentum component transverse to the beam direction of 50 MeV.

The following four requirements defined a candidate for a multihadronic Z event:

- at least 7 clusters in the electromagnetic calorimeter
- at least 7 charged tracks in the central tracking detector
- a total energy deposited in the lead glass of at least 10 % of the centre-of-mass energy:
$$R_{vis} \equiv \Sigma E_{clus}/\sqrt{s} > 0.1,$$
where the sum runs over all clusters found in the lead glass calorimeter
- an energy imbalance along the beam direction which satisfies
$$R_{bal} \equiv \mid \Sigma(E_{clus} \cdot \cos\theta) \mid / \Sigma E_{clus} < 0.65$$
where θ is the polar angle of the cluster.

The cut on the number of clusters and the number of tracks efficiently eliminated Z decays into charged lepton pairs and events from cosmic radiation. Two-photon events as well as beam-gas or beam-wall interactions carry an energy usually far below the e^+e^- centre-of-mass energy. Hence such events can be suppressed by making a cut on R_{vis}. The vertex requirements on tracks serve to eliminate events caused by cosmic rays. The cut in R_{bal} rejected beam-wall, beam-gas, and beam-halo events, as well as cosmic rays in the end caps, because these background events that do not originate from e^+e^- collisions are often unbalanced.

The thrust value and the direction of the thrust axis [78] of each hadronic Z event are calculated using charged tracks together with clusters found in the electromagnetic calorimeter with no associated tracks. Two additional cuts are applied to each event: the thrust value T [78] must be at least 0.6, and the polar angle of the thrust axis θ_{T} [78] must satisfy $\cos\theta_{\mathrm{T}} < 0.95$.

Over 4 million hadronic Z events are selected. The exact numbers are listed in Table 5.1. As indicated in the table, some events are recorded at centre-of-mass energies above and below the Z peak. The bulk of these off-peak data is recorded in 1993 and 1995 at centre-of-mass energies approximately 1.8 GeV away from the peak. The other off-peak centre-of-mass energy samples from 1990 and 1991 are combined with these main samples, yielding measurements of the forward-backward asymmetries at three separate energy points. These are called "peak-2" "peak", and "peak+2" during the rest of this text.

Mean Energy of Z events		Selected Z decays	Single lepton events		Dilepton events
			Electrons	Muons	
peak–2	$\langle\sqrt{s}\rangle = 89.51$ GeV	194 211	11 567	19 809	321
peak	$\langle\sqrt{s}\rangle = 91.25$ GeV	4 079 047	239 505	410 877	6 014
peak+2	$\langle\sqrt{s}\rangle = 92.95$ GeV	278 257	16 977	30 066	394

Table 5.1: The number of hadronic events selected below, on and above the Z peak. The average centre-of-mass energies of the selected Z events, the number of Z events, and the number of events with identified leptons are shown. Note that dilepton events are only selected in a region of high b purity.

The remaining backgrounds due to $\tau\tau$, Bhabha, and two-photon events as well as contributions from beam-gas or beam-wall interactions can be neglected after the subsequent selection of Z decays to b or c quarks with a semileptonic $\mathrm{b} \to \ell^-$ or $\mathrm{c} \to \ell^+$ decay.

Monte Carlo simulated events are generated using JETSET 7.4 [37, 73] with parameters tuned by OPAL [74] (see Section 3.3). The fragmentation function of Petersson *et al.* [42] is used to describe the fragmentation of b and c quarks. The semileptonic decay model of Altarelli *et al.* [99] with parameters fixed by CLEO [100], DELCO [101] and MARKIII data [102] is used to predict the lepton momentum in the rest frame of b and c hadrons. The generated events are passed through a program that simulates the response of the OPAL detector [72] and through the same reconstruction algorithms as the data.

5.3 Vertex and Jet Reconstruction

The primary vertex for each event is reconstructed using a three dimensional version of the algorithm described in [103]. The position and uncertainty of the e^+e^- collision region (beam spot) is used as a constraint. The beam spot position is measured using charged tracks from many consecutive events, thus following any significant shifts in beam position during a LEP fill [104, 105]. All good tracks ($>$ 20 hits in jet chamber, transverse momentum with respect to beam axis $>$ 0.15 GeV/c, and distance of closest approach to beam spot in r-ϕ plane $<$ 5 cm.) in one event are fitted to a common vertex in three dimensions. Tracks with a large χ^2 contribution to the primary vertex fit are removed one by one until each remaining track contributes less than 4 to the χ^2 [86]. In about 0.7 % of the events, no tracks remain after this procedure. In these cases the beam spot position is used. Monte Carlo simulated events with the 1994 silicon detector setup are employed to determine the primary vertex resolution. It is found to be 50 μm in x, 15 μm in y (where it is dominated by the beam spot constraint) and 80 μm in z.

Jets are reconstructed using a cone jet-finding algorithm [85] by combining all charged tracks and unassociated electromagnetic calorimeter energy clusters. The procedure requires a cone half-angle of 0.65 rad and a minimum jet energy of 5.0 GeV. This algorithm is preferred over the JADE algorithm [106, 107] for this measurement, because it leads to a higher probability of correct assignment of tracks to secondary b vertices within a jet [83,86]. It is shown in [75] that the cone jet-finder provides the best b hadron energy and direction resolution compared to other jet-finders.

Leptons are searched for in each jet using the algorithms described in Section 5.4.1. Only events where at least one lepton or two “opposite-jet” leptons are identified are used. For dilepton events, the two jets containing the leptons are defined to be “opposite”, if their axes do not belong to the same thrust hemisphere. Table 5.1 summarises also the total number of events containing at least one candidate electron or muon.

A three dimensional version of the algorithm described in [103] is used to reconstruct a secondary vertex in each jet. All tracks in the jet with momentum $p >$ 0.5 GeV/c, a distance of closest approach to the primary vertex in the r-ϕ plane (“impact parameter”) $d <$ 0.3 cm, and an impact parameter error $\sigma_d <$ 0.1 cm, are fitted to a common vertex in three dimensions. Tracks with a large χ^2 contribution to the fit are removed one by one until each track contributes less than 4 to the overall χ^2. At least three tracks are required to remain in the fit for the secondary vertex finding to be considered successful.

The vertex decay length L is calculated as the length of the vector from the primary to the secondary vertex. The vector is constrained to lie along the direction of the jet axis. L is given a positive sign, if the secondary vertex is displaced from the primary in the direction of the jet momentum, and a negative sign otherwise. Vertices with $L > 0$ are used to tag b hadron decays.

5.4 Neural Network based Quark Flavour Separation using Leptons

Dedicated neural network algorithms are used for the electron identification and the quark flavour separation. A short introduction is given in the appendix Chapter A. All neural networks used for this analysis are trained using the JETNET 3.5 [108] program library.

A neural network is a powerful tool for classification problems, if the specific class properties can be evaluated in a set of distributions of some variables. For each event the network calculates an output value[1], which is a limited real function of the input variables and contains information about the classification of the event. The way the neural network works is to cut certain subspaces of the space, spanned by the input variables, which are populated predominantly by a certain event class. Therefore a neural network does basically nothing but performing a very complicated set of cuts on the input variables with one important difference. While a purely cut based method performs its separation along sharp cut planes, a neural network has continuous decision boundaries. This allows the selection of events, where not all variables indicate that the chosen event belongs to one of the defined classes. This makes it possible to classify events, where one of the input quantities is slightly displaced. Therefore neural nets are particularly useful, if the differences among the input variable distributions for the classes are small and correlated among each other, because they can perform nonlinear cuts in the multidimensional space, spanned by the input variables, and automatically take care of the correlations.

An analysis using neural networks can be divided into two phases. First the network has to be built. For this, two event samples with events of known classification have to be available. They are called the training and test sample. During an iterative process called training which is done using the training sample the parameters of the neural network (weights and thresholds) are defined so that the optimal cuts in the space of the variables can be performed. The test sample is then used to investigate the response of the network to events from the different classes. In the second phase the network can be applied to an unknown event sample. Since its response to the event classes is known, the output of the network

[1]Both the output value of a neural network as well as the network itself will be denoted NET in this text. Indices will classify the different networks with respect to their application.

can be interpreted to find the contributions of the different classes in the unknown sample.

Neural networks are used in three different ways in the forward-backward asymmetry analysis:

1. *To support a yes/no decision:*
   To identify electrons coming from direct quark decays, cuts are applied to the outputs of two different neural networks. The first network is trained to decide whether the found particle is an electron or not. The second network rejects electrons, originating from photon conversions. An electron is considered to be identified, if both cuts are passed.

2. *To deliver more information to another neural network:*
   To improve the quality of the quark flavour separation, the outputs of the neural networks used for the electron identification are fed as an input into the two neural networks, trained to identify $\mathrm{b} \to \mathrm{e}^-$ and $\mathrm{c} \to \mathrm{e}^+$ decays.

3. *To separate multiple event classes and produce event weights:*
   In order to use the whole sample of lepton candidates two types of neural networks are constructed: the first is trained to separate $\mathrm{b} \to \ell^-$ decays from all others, the second to separate $\mathrm{c} \to \ell^+$ decays from all other decays. The outputs of both networks are used to fill a binned two dimensional distribution of the lepton candidates. Altogether there are four different classes of lepton candidates ($\mathrm{b} \to \ell^-$, $\mathrm{b} \to \mathrm{c} \to \ell^+$, $\mathrm{c} \to \ell^+$ and background), as introduced in Section 4.3. In different regions of the two dimensional histogram the contribution of the different channels vary. Since the ratio between the four event classes is known, the same neural networks can be used to produce weights representing probabilities for the different event classes for each of the bins separately. These weights are calculated from simulated events with known classification. The weights are used in the maximum likelihood fit to calculate the appropriate asymmetry of each bin.

While the neural networks used for the electron identification are part of the standard OPAL code [109] and therefore have been tested earlier within the framework of other analyses, the algorithms used for the quark flavour separation are trained for this analysis.

5.4.1 Lepton Identification

Leptons are searched for in hadronic Z events using well established methods [86,109,110]. While the electron selection is based on artificial neural network algorithms, the muons are identified by applying cuts.

Electron Selection

The electron identification [109] is based on a set of six (eight in the endcap region) physical quantities measured for each track in the central tracking chambers and the lead-glass electromagnetic calorimeter. In the jet chamber the specific energy loss per path length $\mathrm{d}E/\mathrm{d}x$ of the charged particle is measured [67, 68]. Together with the expected specific energy loss for an electron $(\mathrm{d}E/\mathrm{d}x)_{\mathrm{exp}}$ the dimensionless normalised quantity $(\mathrm{dE}/\mathrm{d}x)_{\mathrm{norm}}$ is calculated[2].

For charged particles, the momentum component perpendicular to the beam axis is measured from the curvature of the track in the jet chamber caused by the axial magnetic field. Using the polar angle θ of the track, the total momentum p can be calculated. The electromagnetic calorimeter is constructed such that electrons can be completely absorbed. Hence, the ratio of E/p is expected to be close to 1. Furthermore, electrons deposit their energy in a narrow shower around the extrapolated particle trajectory. Therefore the energy E_{cone}, which is deposited in the electromagnetic calorimeter blocks whose centres are contained within a cone of half-angle 30 mrad and are associated to the same electromagnetic calorimeter cluster as the candidate track under consideration, is used [109].

The electron selection is realised with six quantities for tracks within the barrel region (1-6) and eight (1-8) for those in the endcaps:

1. total momentum p of the track,
2. the $|\cos\theta|$ of the track,
3. $(\mathrm{dE}/\mathrm{d}x)_{\mathrm{norm}}$, this is equivalent to the $\mathrm{d}E/\mathrm{d}x$ weight,
4. $\sigma_{\mathrm{dE}/\mathrm{d}x}$, the estimated error on $\mathrm{d}E/\mathrm{d}x$,
5. $\mathrm{E}_{\mathrm{cone}}/p$,
6. $\mathrm{N}_{\mathrm{block}}^{\mathrm{cone}}$, the number of ECAL blocks used in the E_{cone} determination,
7. $\Delta\phi$, the absolute ϕ difference between the track and ECAL cluster (endcaps only),
8. $\Delta\theta$, the θ difference between the track and ECAL cluster (endcaps only).

The high level of complementarity and redundancy between these variables, provided by several independent subdetectors, ensures a good efficiency and rejection

[2]Often the quantity $(\mathrm{dE}/\mathrm{d}x)_{\mathrm{norm}}$ is also referred to as $\mathrm{d}E/\mathrm{d}x$ weight as introduced in Section 3.2.1.

over the whole detector [109]. These quantities are used as input to a neural network NETel (feed-forward, one hidden layer) [108, 109], which provides the final classification, in order to make optimal use of all the available information. Separate networks for the barrel and endcap are implemented as this results in a better overall performance.

The chosen set of inputs is selected from a much larger set of potentially discriminating or meaningful variables [109]. While most of those retained have intrinsic separating power between hadrons and electrons (such as $(\mathrm{dE}/\mathrm{d}x)_{\mathrm{norm}}$, E/p, ...), some variables which are not discriminating by themselves (e.g., the momentum p and the polar angle $\cos\theta$ of the track) are nevertheless useful, since they contain important information about existing correlations between all inputs.

The network used is trained on simulated data. Tracks produced by electrons are given as signal, anything else (predominantly hadrons) as background. All training patterns are chosen to have a momentum of $p > 2$ GeV/c [109].

After the electron selection, electrons from photon conversions are the dominant background to prompt electrons. They are tagged and rejected using an algorithm that tries to associate any given candidate electron track with all possible partner tracks in the event. The current version of this algorithm, which is used for this analysis is also described in [109]. The conversion finder considers the following information: the probability for the two tracks to originate from a common vertex, the compatibility between the position of the reconstructed vertex with the first measured point of each track, and the probability for the partner to be an electron. In addition it is required that the invariant mass is close to 0 for true photons and the impact parameter peaked at 0 for photons which are produced mainly in decays of π^0 from the fragmentation.

The decision whether a pair of tracks forming a vertex are compatible with a photon conversion relies on the measurement of nine quantities:

1. the distance in r-ϕ between the two tracks at their point of tangency,
2. the radius of the first measured hit of both tracks: r_1 and $r_{1\mathrm{P}}$ (the P denotes the partner) and
3. the radius of the reconstructed vertex r_V (A radius is measured with respect to the beam pipe.),
4. the invariant mass of the pair assuming both tracks to be electrons and
5. the impact parameter of the parent photon with respect to the primary vertex of the event,
6. the two track momenta times the sign of their charge,

7. the output NETel of the partner track.

These variables are combined using a three layer feed-forward neural network.

In addition to the hadronic event selection, the following requirements to the tracks have to be satisfied in order to select electron candidates:

- track momentum $p > 2$ GeV/c,
- $|\cos\theta| < 0.96$,
- $-2 < (\mathrm{dE/d}x)_{\mathrm{norm}} < 4$, this rejects most hadrons whilst retaining practically all electrons,
- number of good dE/dx measurements in the jet chamber > 20. This rejects the tracks with poor dE/dx modelling in the jet chamber,
- NETel > 0.9 and
- NETcv < 0.65.

Muon Selection

The main principle of the method is first mentioned in [111] and published in [110]. The further development especially concerning systematic uncertainties is documented in [112, 113]. The muon identification uses information from the central tracking system and the muon chambers. Muons are identified by requiring a spatial match between a track reconstructed in the central tracking detectors and a track segment reconstructed in the external muon chambers [110, 111]. A χ^2 fit is applied to quantify the matching quality of the tracks, given by the value χ_{pos}. The candidate track in the tracking system must be the best match to the track segment found in the muon chamber. If dE/dx is measured well, a soft dE/dx cut is used to reduce the amount of kaons, which decay into a muon and a neutrino, before they interact in the calorimeters [112, 113].

In addition to the hadronic event selection, the following cuts are applied to the tracks in order to select a muon candidate:

- total momentum $p > 2$ GeV/c,
- $\chi_{\mathrm{pos}} < 3.0$,
- $-0.05 < (\mathrm{dE/d}x)_{\mathrm{norm}} < 0.00$ in case there are more than 20 good dE/dx measurements.

The main advantage of this muon identification algorithm is that it is very well understood and has reasonable systematic errors on both efficiency and fake rate [112,113]. On the other hand, the purity is limited for muons within hadronic jets. For that reason a neural network has been developed by Frank Fiedler [114]. Unfortunately, the increase of systematic uncertainties on $A^{\mathrm{b}}_{\mathrm{FB}}$ and $A^{\mathrm{c}}_{\mathrm{FB}}$, induced by the use of this neural network, is larger than the reduction of the statistical error due to a higher muon purity. Therefore the cut based algorithm is used.

Performance Summary

In this analysis, only leptons from semileptonic b or c hadron decays in primary $\mathrm{b\overline{b}}$ or $\mathrm{c\overline{c}}$ events are considered as signal. Any other genuine electron or muon and any hadron misidentified as a lepton, is considered as background. The determination of the efficiency is based only on the sensitive region of the detector. Particles with momentum $p < 2$ GeV/c are not used. With these definitions the efficiency of the selection for genuine electrons, not considering electrons from photon conversions, is 66 %. The purity is 73 %, where electrons from photon conversions are included in the background. Muons are selected with an efficiency of 74 % and a purity of 53 %. About 11 % of the electron background is from genuine electrons in light quark events, 49 % from misidentified hadrons in any primary quark flavour event, and 40 % from photon conversions. This is in good agreement with the results published in [109]. About 68 % of the muon background originates from pions and 28 % from kaons. The remaining 4 % are from other sources. Similar contributions to the muon background fraction are found in [113].

5.4.2 Quark Flavour Separation

At this point the total observed quark forward-backward asymmetry [115] can be written as the sum of all involved quark asymmetries:

$$A^{\mathrm{obs}}_{\mathrm{FB}} = f_1(1-2\overline{\chi})A^{\mathrm{b}}_{\mathrm{FB}} - f_2(1-2\overline{\eta\chi})A^{\mathrm{b}}_{\mathrm{FB}} - f_3A^{\mathrm{c}}_{\mathrm{FB}} + f_4A^{\mathrm{background}}_{\mathrm{FB}} \tag{5.1}$$

Assuming that the semileptonic branching ratios are known from the combination [52] of other measurements [116–122] and implemented in the Monte Carlo simulation with full detector simulation and event reconstruction, the fractions f_i can be taken from the Monte Carlo simulation after applying the event selection and lepton identification mentioned above. To measure the heavy flavour forward-backward asymmetries $A^{\mathrm{b}}_{\mathrm{FB}}$ and $A^{\mathrm{c}}_{\mathrm{FB}}$, quark flavour separation has to be done. A simple approach is to look for quantities associated with an identified lepton candidate which has an acceptable intrinsic separation. In previous analyses [90, 123] this is done with two variables which describe best the kinematical properties of the candidate lepton: the total (longitudinal) momentum p and the transverse momentum p_{t} of the candidate lepton with respect to the closest jet axis. However, this simple method in the $p \times p_{\mathrm{t}}$ plane gives poor results concerning the flavour separation. In 1995 already, the use of two new separation variables was motivated by this fact, combining several sources of jet and vertex information, and kinematical properties of the candidate lepton with the help of artificial neural network algorithms [82, 83]. The first algorithm, NETb, was trained to identify $\mathrm{b} \to \ell^-$ decays, the second, NETc to select $\mathrm{c} \to \ell^+$ decays. Due to a limited performance of those algorithms using OPAL data after the final recalibration (especially concerning the $\mathrm{c} \to \ell^+$ separation) it is decided to train new neural networks for this analysis to take full advantage of the improved detector calibrations. Again the approach is to construct two different network types for $\mathrm{b} \to \ell^-$ and $\mathrm{c} \to \ell^+$ decays. In order to reach optimal separation power, the different network types are trained separately for electrons and muons.

In the next section the sources of information, which are used as input quantities for the neural networks are introduced. In the subsequent sections the architecture, the training and testing of the networks is described in more detail.

Variables for Quark Flavour Separation

The goal is a measurement of the b and c quark forward-backward asymmetries and the average B mixing parameter in a simultaneous fit. This implies that the quark flavour separation must not introduce any bias to the identified $\mathrm{b\overline{b}}$ and $\mathrm{c\overline{c}}$ events concerning these quantities. On the other hand the magnitude of the statistical error (dominant uncertainty) is directly correlated to the efficiency and purity of the quark flavour separation. At this point there is the choice to trade the reduction of the statistical error, caused by an improvement of the performance of the quark flavour separation, against the increase of the systematical uncertainty due to corrections which are necessary to get rid of biases of the measured quantities. To obtain the smallest possible total uncertainty on the measurements, it is decided to build a quark flavour separation which is free of any biases. For that reason the used input variables for the neural networks are chosen to neither bias the heavy flavour forward-backward asymmetries nor the B mixing parameter $\overline{\chi}$.

The four groups of lepton candidates introduced in Section 4.3, which are to be separated, contain direct b and c decays $\mathrm{b} \to \ell^-$ and $\mathrm{c} \to \ell^+$ and cascade decays $\mathrm{b} \to \mathrm{c} \to \ell^+$, $\mathrm{b} \to \overline{\mathrm{c}} \to \ell^-$, and $\mathrm{b} \to \tau^- \to \ell^-$. There is no practicable method to distinguish between $\mathrm{b} \to \mathrm{c} \to \ell^+$, $\bar{\mathrm{b}} \to \bar{\mathrm{c}} \to \ell^-$ and $\mathrm{b} \to \overline{\mathrm{c}} \to \ell^-$ $\bar{\mathrm{b}} \to \mathrm{c} \to \ell^+$ decays with a neural network because both decay channels have the same topology. However it is sufficient for the separation of the decays categorised in groups 1-4 to have two types of neural networks, denoted NETb and NETc. The first network, NETb, is trained to distinguish between b $\to \ell^-$ events and all other categories. The second network, NETc, is trained to distinguish c $\to \ell^+$ events from the other categories, including b $\to \ell^-$. For the measurement of the b and c quark asymmetries it is important to separate direct b and c decays (types 1 and 2) from each other and from all other contributions. Cascade decays dilute both, the asymmetries and mixing, and are thus considered being part of the background fraction for flavour separation.

The flavour information is expected to be contained in variables connected either directly to the lepton candidate track or to the jet or vertex properties of the jet from which the lepton candidate originates [83, 123].

The variable NETb is constructed from a set of five discriminating variables which are explained later in detail:

- p, the total (longitudinal) momentum of the lepton candidate,
- p_t, the transverse momentum of the lepton candidate with respect to the nearest jet axis. Here the jet axis is calculated excluding the momentum of the lepton candidate.
- $E_{\mathrm{sub-jet}}$, the energy of the lepton sub-jet,
- $E_{\mathrm{jet}}^{\mathrm{vis}}$, the total visible energy of the lepton jet,
- $(\sum p_\mathrm{t})_{\mathrm{jet}}$, the scalar sum of the transverse momenta with respect to the jet axis of all particles within the jet

$$(\sum p_\mathrm{t})_{\mathrm{jet}} = \sum_{\mathrm{jet}} |p_\mathrm{t}|. \tag{5.2}$$

In direct b decays the lepton momentum reflects the hard fragmentation of the primary meson and is thus particularly efficient for separating b $\to \ell^-$ and c $\to \ell^+$ from the others. The large mass of the b quark also induces high lepton energies in the rest frame of the decaying b hadrons, which translates, unaffected by the boost along the quark (jet) direction, into hard p_t spectra, characteristical of direct and cascade b decays (b $\to \ell^-$ and b $\to$ c $\to \ell^+$, b $\to \overline{\mathrm{c}} \to \ell^-$).

One expects leptons from primary b decays to be more isolated than leptons from semileptonic charm decays due to the larger b hadron masses and higher energy neutrinos. To quantify this isolation the jet containing the lepton candidate is split into two sub-jets using an iterative procedure. At the beginning one sub-jet (called lepton sub-jet) contains only the lepton candidate track. The other sub-jet (remaining sub-jet) is the remainder of the original jet with the lepton track removed. Particles are then reassigned iteratively until each particle is closer in angular distance to the sub-jet to which it is assigned than to the other sub-jet. The energy of the lepton sub-jet, with the energy of the lepton candidate subtracted, is taken as a measure of the isolation of the lepton candidate. The energy $E_{\mathrm{sub-jet}}$ of the lepton sub-jet, unlike p_{t}, does not depend on the lepton momentum. The concept of a lepton sub-jet as it is used here is first introduced in [87].

Due to the emission of an energetic neutrino, b jets, where the b hadron has decayed semileptonically, tend to have lower visible energy than b jets from cascade decays. The total visible energy $E_{\mathrm{jet}}^{\mathrm{vis}}$ of the jet is calculated using all tracks and unassociated calorimeter clusters comprising the jet.

The decay products of b hadrons have on average a high transverse momentum with respect to the flight direction of the original b hadron because of their large mass. Since the jet-axis can be considered as a good approximation of the flight direction of the b hadron [79], the variable $(\sum p_{\mathrm{t}})_{\mathrm{jet}}$ characterises both the width and multiplicity within the jet, which differ significantly for b quarks compared to lighter quarks [79].

The variable NETc is constructed by combining the five discriminating quantities used for NETb with three additional measured quantities:

- $(L/\sigma_L)_1$, the decay length significance of the jet containing the lepton (jet 1), as well as
- $(L/\sigma_L)_2$, the decay length significance of the most energetic jet in the event not containing the lepton candidate (jet 2),
- d/σ_d, the impact parameter significance of the lepton candidate with respect to the primary vertex.

The long lifetime and high boost of bottom hadrons produced in $\mathrm{e^+e^-} \rightarrow \mathrm{b\overline{b}}$ events is leading to secondary vertices that are displaced from the primary interaction point (Figure 4.1) by decay lengths L of the order of millimetres. The lifetimes of weakly decaying charm hadrons are smaller than those of weakly decaying bottom hadrons, typically by a factor of 3 for mesons. Due to the fact that the distributions of the decay lengths for b and c events overlap especially in the region of large L, a pure sample of $\mathrm{c} \rightarrow \ell^+$ decays is difficult to obtain. However, the decay lengths L is useful to separate $\mathrm{c} \rightarrow \ell^+$ from $\mathrm{b} \rightarrow \ell^-$ and $\mathrm{b} \rightarrow \mathrm{c} \rightarrow \ell^+$ and also from light meson decays which have very different lifetimes. The decay length significance is defined as the distance L of the secondary vertex from the primary vertex, divided by the estimated error σ_L on L, which comes from the uncertainties in the primary and secondary vertex positions.

For each track, the impact parameter significance is the ratio of the distance d between the primary vertex and the track at the point of closest approach, to the error σ_d on this distance. The impact parameter allows the distinction between secondary tracks and tracks from fragmentation [83]. Both the decay length and the impact parameter are defined in the r-ϕ plane only.

In addition to the five and eight inputs used for the neural networks NETb and NETc respectively, it is found that the output variables NETel and NETcv of the neural networks for electron identification and conversion electron rejection improve the separation power of NETb and NETc. Although these variables are already used to remove the main part of the hadronic and photon conversion contribution, they also help in the flavour separation networks to further reduce these two types of background. Since NETb and NETc are trained separately for electrons and muons these two additional variables are included only in NETb $\rightarrow$ e and NETc $\rightarrow$ e as input quantities.

The distributions of the input quantities to the four neural networks used for quark flavour separation NETb $\rightarrow \mu$, NETb $\rightarrow$ e, NETc $\rightarrow \mu$ and NETc $\rightarrow$ e are shown in Figures 5.1-5.4. In general the intrinsic separation of the inputs of the b $\rightarrow \ell^-$ separation networks (NETb) is much better than that of the c $\rightarrow \ell^+$ networks (NETc). Therefore it is evident that the separation of b $\rightarrow \ell^-$ decays from the others is significantly better than that of c $\rightarrow \ell^+$ decays. Table 5.2 gives an quantitative overview of the separation power of the inputs for the four nets using the figure of merit (Eq. A.12) [124] which is introduced in the appendix about neural networks.

Architecture of the Neural Networks

Before the neural networks can be trained and applied to data the proper architecture (number of layers and number of nodes per layer) has to be found. The complexity of the algorithm has to be adjusted to the complexity of the separation problem and to the number of available training patterns [125]. Once this is done, the separation quality is only limited by the finite precision of the measurement process of the OPAL detector and the nature of the semileptonic b and c decays. There is no general rule which predicts the optimal architecture of a neural network. The structure depends on the details of the classification problem to be solved and it has to be found in a series of trials.

The four neural networks NETb $\rightarrow$ e, NETb $\rightarrow \mu$, NETc $\rightarrow$ e, and NETc $\rightarrow \mu$, employed for the quark flavour separation in this analysis, are all of type feed-forward [108, 125] with $n_{\mathrm{lay}} = 3$ layers: an input layer, a hidden layer and an output layer. The output layer always has $n_{\mathrm{out}} = 1$ output node and there are always $n_{\mathrm{hid}} = 15$ nodes in the hidden layer. The number of input nodes n_{in} is different for any of the nets as already mentioned in the last section (NETb $\rightarrow \mu$: $n_{\mathrm{in}} = 5$, NETb $\rightarrow$ e: $n_{\mathrm{in}} = 7$, NETc $\rightarrow \mu$: $n_{\mathrm{in}} = 8$ and NETc $\rightarrow$ e: $n_{\mathrm{in}} = 10$). The

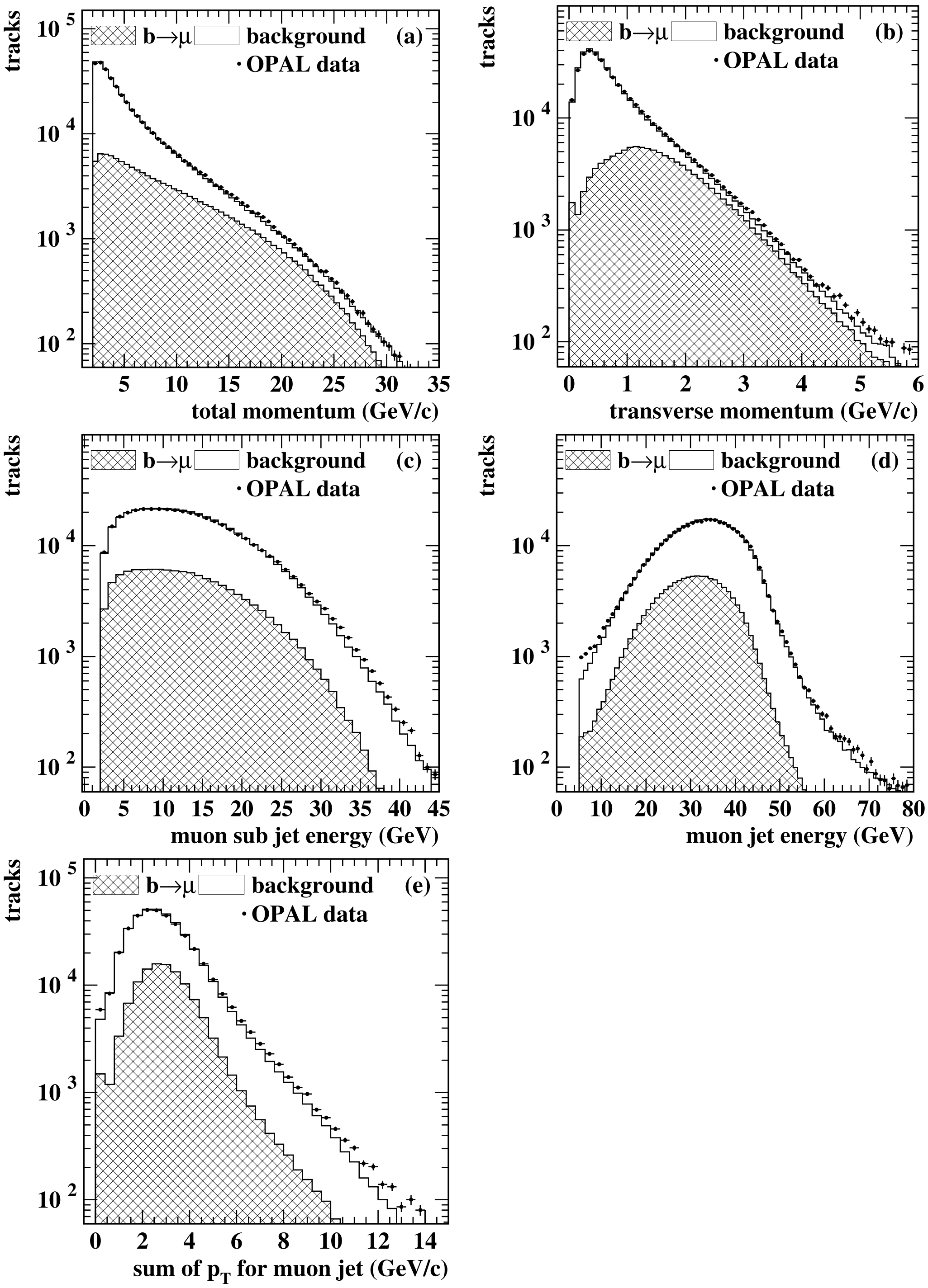

Figure 5.1: Distributions of the five input quantities to NETb $\rightarrow \mu$ used for the separation of b $\rightarrow \mu^-$ decays from the background. The histograms show the distributions for the signal and background fraction taken from Monte Carlo simulation. On the vertical axis the number of muon candidates is given. The dots represent the distribution of the data. Due to the large sample, the errors are very small and partially hidden beneath the dots. The precise definition of the different variables is given in the text. The separation power of the momentum and the transverse momentum plotted in (a) and (b) is very good. The data is reproduced well by the Monte Carlo simulation.

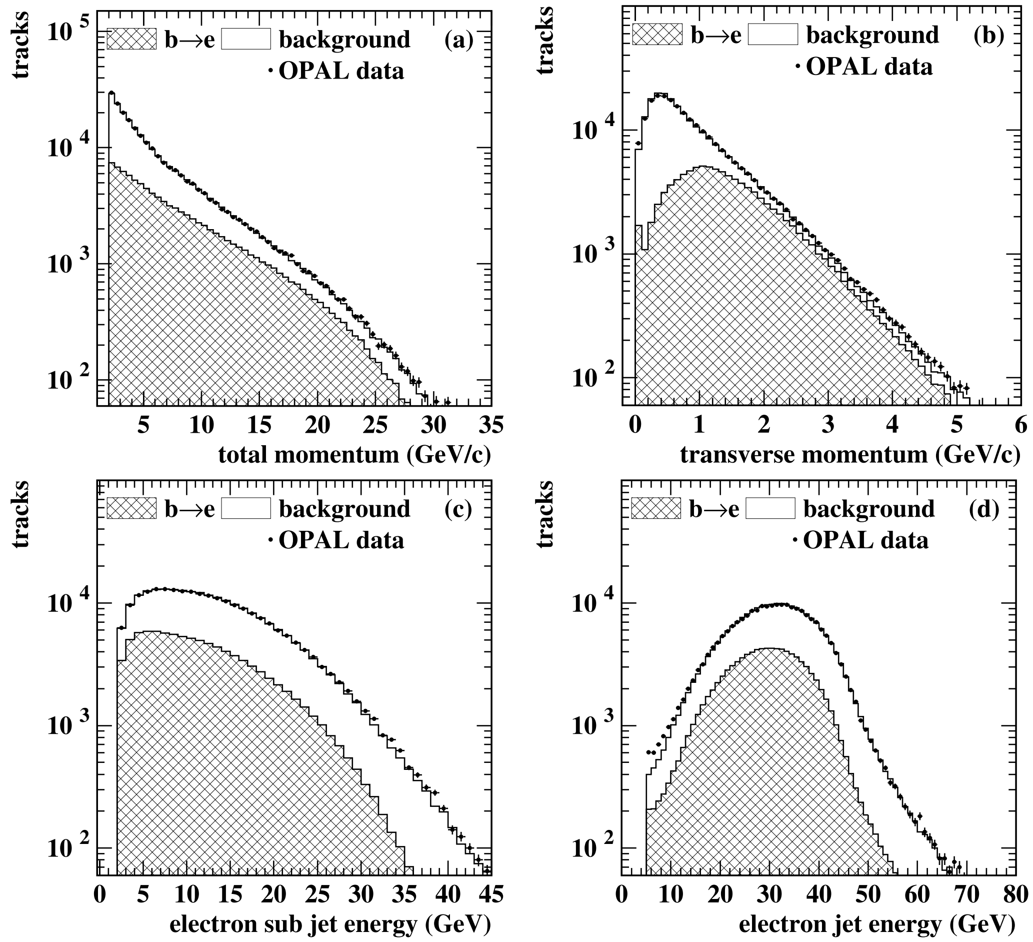

tracks
b→e
background
OPAL data
(a)
(b)
(c)
(d)
total momentum (GeV/c)
transverse momentum (GeV/c)
electron sub jet energy (GeV)
electron jet energy (GeV)

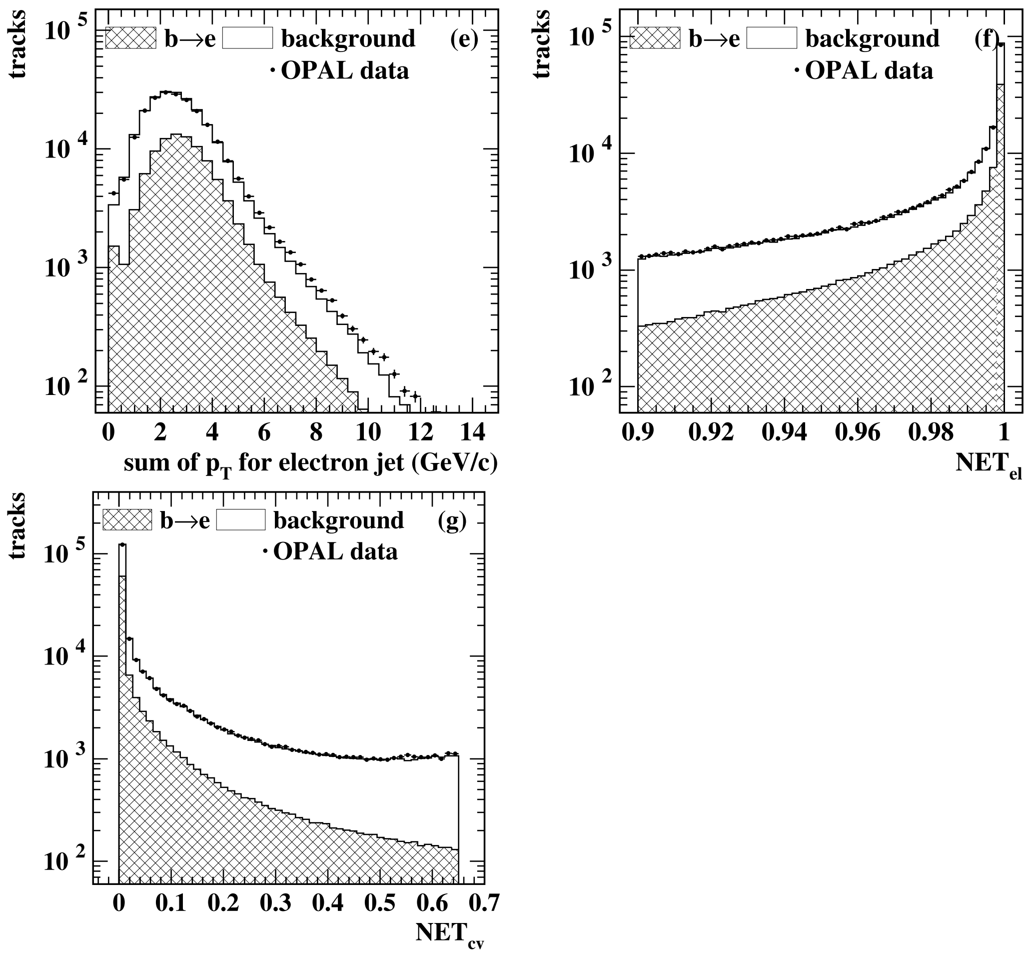

Figure 5.2: Distributions of the seven input quantities to NETb → e used for the separation of b → e$^-$ decays from the background. The histograms show the distributions for the signal and background fraction taken from Monte Carlo simulation. On the vertical axis the number of electron candidates is given. The dots represent the distribution of the data. Due to the large sample, the errors are very small. The precise definition of the different variables is given in the text. The separation power of the momentum and the transverse momentum plotted in (a) and (b) is very good. The separation of the other quantities (plot (c)-(g)) is hardly visible with the eye. The data is reproduced well by the Monte Carlo simulation.

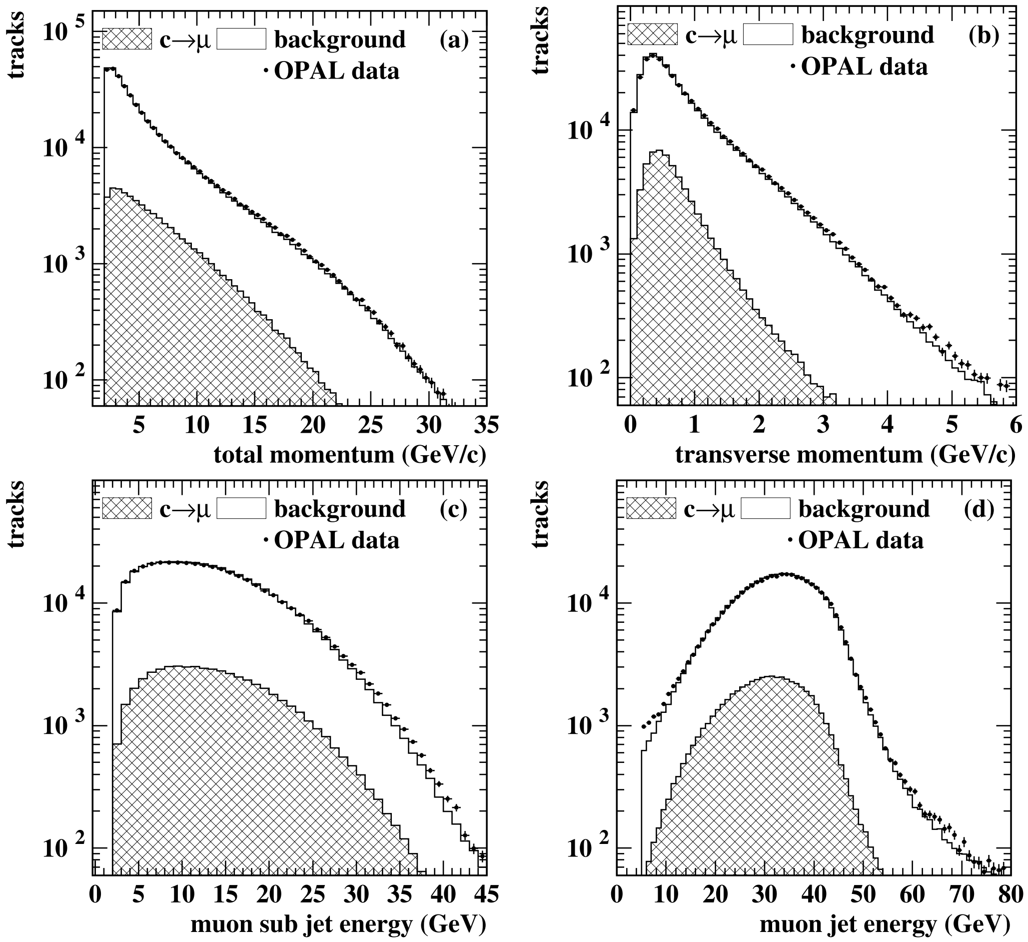
tracks
c→μ
background
(a)
· OPAL data
total momentum (GeV/c)
(b)
transverse momentum (GeV/c)
(c)
muon sub jet energy (GeV)
(d)
muon jet energy (GeV)

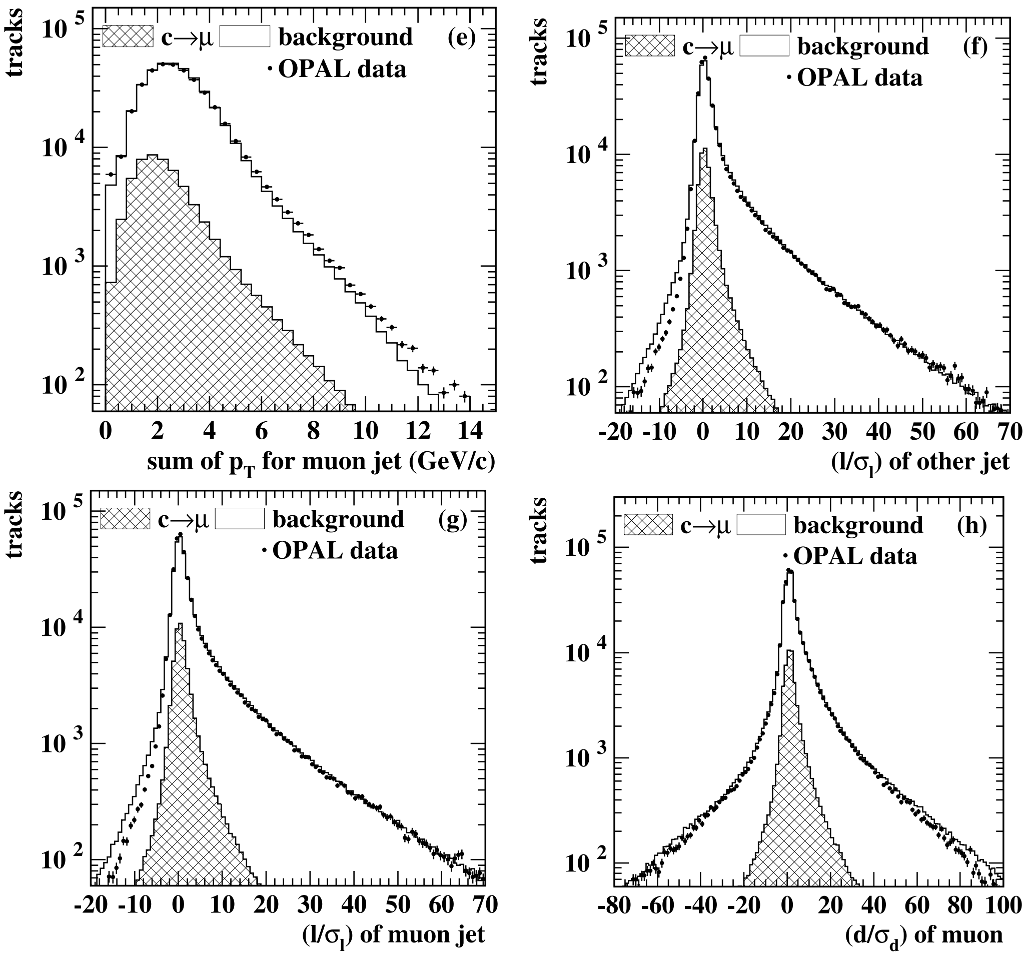

Figure 5.3: Distributions of the eight input quantities to NETc $\rightarrow \mu$ used for the separation of c $\rightarrow \mu^+$ decays from the background. The histograms show the distributions for the signal and background fraction taken from Monte Carlo simulation. On the vertical axis the number of muon candidates is given. The dots represent the distribution of the data. Due to the large sample, the errors are very small. The precise definition of the different variables is given in the text. The intrinsic separation power of all variables is quite low. The separation of the transverse momentum p_{t} in (b), $(\sum p_{\mathrm{t}})_{\mathrm{jet}}$ in (e), and $(L/\sigma_L)_{1,2}$ in (f) and (g) is slightly better than that of the others. The data is reproduced well by the Monte Carlo simulation.

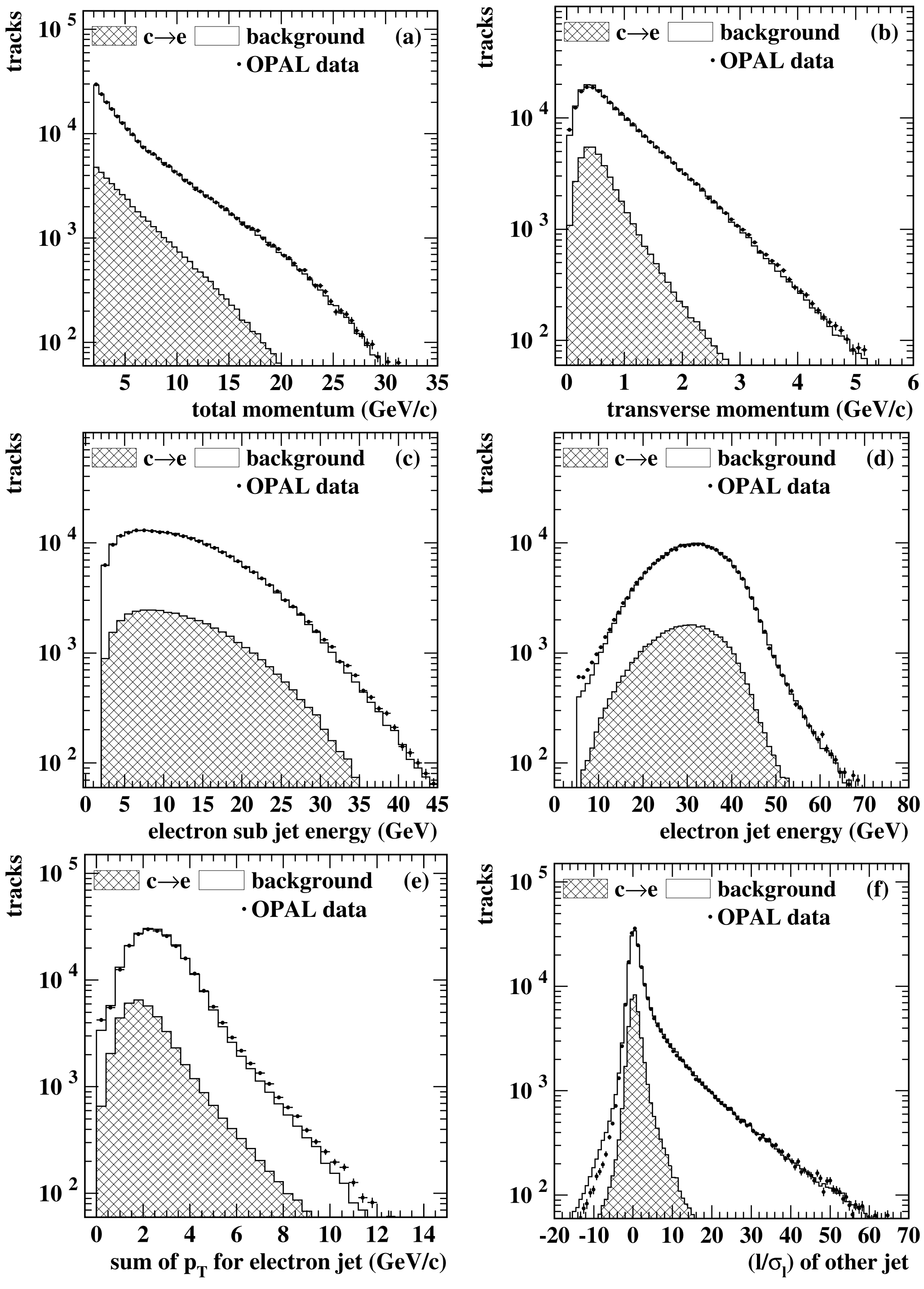
tracks
c→e
background
OPAL data
(a)
total momentum (GeV/c)
(b)
transverse momentum (GeV/c)
(c)
electron sub jet energy (GeV)
(d)
electron jet energy (GeV)
(e)
sum of p_T for electron jet (GeV/c)
(f)
(l/σ_l) of other jet

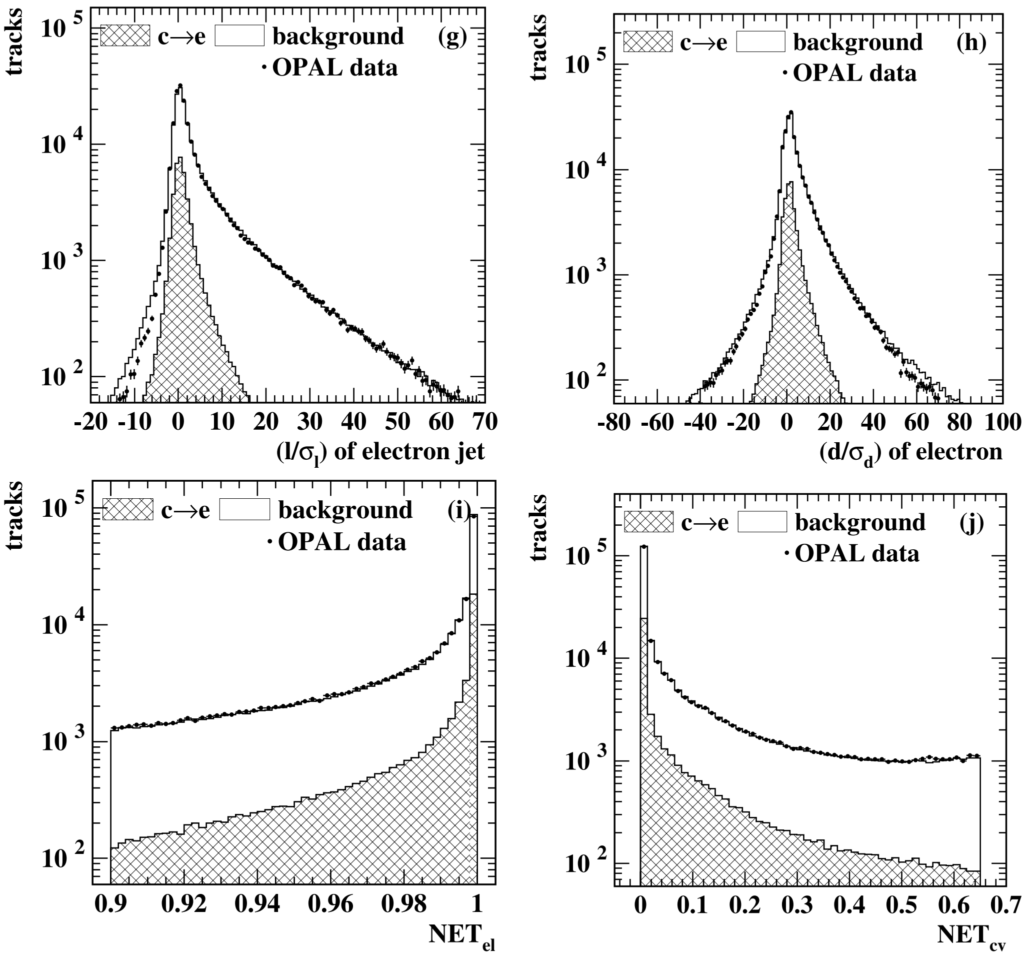

Figure 5.4: Distributions of the ten input quantities to NETc $\rightarrow$ e used for the separation of c $\rightarrow$ e$^+$ decays from the background. The histograms show the distributions for the signal and background fraction taken from Monte Carlo simulation. On the vertical axis the number of electron candidates is given. The dots show the distribution of the data. Due to the large sample, the errors are very small. The precise definition of the different variables is given in the text. The intrinsic separation power of all variables is quite low. The separation of the transverse momentum p_{t} in (b), $(\sum p_{\mathrm{t}})_{\mathrm{jet}}$ in (e), $(L/\sigma_L)_{1,2}$ in (f) and (g), and d/σ_d in (h) is slightly better than that of the others. The data is reproduced well by the Monte Carlo simulation.

Type of input quantity	**Separation power of input quantity**			
	electrons		**muons**	
	NETb	NETc	NETb	NETc
total momentum p	0.082±0.002	0.005±0.005	0.110±0.002	0.012±0.005
transverse momentum p_{t}	0.363±0.002	0.036±0.005	0.350±0.002	0.022±0.005
lepton sub-jet energy $E_{\mathrm{sub-jet}}$	0.014±0.002	0.001±0.005	0.010±0.002	0.003±0.005
lepton jet visible energy $E^{\mathrm{vis}}_{\mathrm{jet}}$	0.021±0.002	0.004±0.005	0.020±0.002	0.005±0.005
scalar sum of transverse momenta $(\sum p_{\mathrm{t}})_{\mathrm{jet}}$	0.026±0.002	0.033±0.005	0.029±0.002	0.040±0.004
$(L/\sigma_L)_1$ of lepton jet	—	0.052±0.005	—	0.025±0.004
$(L/\sigma_L)_2$ of other jet	—	0.045±0.005	—	0.039±0.004
impact parameter significance d/σ_d	—	0.030±0.005	—	0.004±0.005
NETel	0.007±0.002	0.007±0.005	—	—
NETcv	0.051±0.002	0.008±0.005	—	—

Table 5.2: The intrinsic separation of the input quantities used in the four neural networks for the quark flavour separation. The separation power is quantified using the figure of merit. The quoted errors are due to the finite amount of events in the distributions. For the inputs of NETb only true $\mathrm{b} \to \ell^-$ decays are counted as signal and all others as background. Concerning NETc, the $\mathrm{c} \to \ell^+$ decays are considered as signal and anything else as background. The values for the figure of merit given in the table correspond to the distributions of the input quantities shown in Figure 5.1-5.4.

activation function [125] of the hidden nodes and the output node is a sigmoid function (Eq. A.4). There are 16 thresholds [125] in each net: one for each hidden and output node, but there are no thresholds to the input nodes. A summary of the configuration of all four networks can be found in Table 5.3.

The input variables x_i are rescaled to fit into the intervall $[-1, 1] \in \mathbb{R}$ to reduce the time consumption during the training phase:

$$x_i^{\mathrm{net}} = \tanh(ax_i - b) \tag{5.3}$$

The parameters a and b to shrink (stretch) and shift the distributions are adjusted individually for each input x_i. The hyperbolic tangent is there to shrink long tails with very little information. Quantities which are already bounded and do not have tails like NETel or NETcv are rescaled without the hyperbolic tangent.

Training of the Neural Networks

A total of two millions of simulated events which take up to five quark flavours into account are used to generate the training and test samples for the training procedure. The event selection, the reconstruction of vertices, jets and the thrust axis and the lepton identification are done with the same tools and cuts as in the analyses (see Sections 5.2, 5.3 and 5.4.1). This procedure gives 135 945 (33 % $\mathrm{b} \to \mathrm{e}^-$ and 18 % $\mathrm{c} \to \mathrm{e}^+$) electron and 145 448 (31 % $\mathrm{b} \to \mu^-$ and 16 % $\mathrm{c} \to \mu^+$) muon candidates. These samples are divided into two statistically independent sets of patterns: 75 % of the patterns are used during the learning phase to adjust the internal parameters of the neural network (training sample), and the remaining are used for testing the performance during the training with independent patterns. A lepton candidate is only used for the training, if all quantities serving as inputs to the network currently trained are reconstructed correctly. In particular the vertex decay length of the involved jets has to be determined.

For the final training the composition (signal and background) of the used training sample is identical to the composition expected in real data. In a series of trials this is found to give the best results. The networks are trained to return the value "1" for the signal fraction ($\mathrm{b} \to \ell^-$ or $\mathrm{c} \to \ell^+$ for NETb and NETc respectively) and "0" for the background (all other events).

Weights and thresholds are recalculated after presenting ten additional patterns to the training algorithm. A training epoch is defined by n_{upt} updates of the weights. During the training, all events of the training sample are presented several times to the training algorithm. After a training cycle, all patterns of the training sample are evaluated. The performance of the network on the training sample is monitored continuously during the training. At the end of each cycle in

Parameter	**Description**	**Value**			
		b$\to$ e	b$\to$ μ	c$\to$ e	b$\to$ μ
n_{lay}	number of layers in the net	3			
n_{in}	number of inputs	7	5	10	8
n_{hid}	number of nodes in the hidden layer	15			
n_{out}	number of outputs	1			
n_{weights}	number of weights and thresholds in the net	136	106	181	151
$g(x)$	activation function	$1/(1+\exp(-2x/T))$			
n_{pat}	number of training patterns per update	10			
n_{upd}	number of updates which define one epoch	600		1500	3300
n_{trep}	total number of training epochs	6797	8824	3789	2173
n_{cycle}	total number of training cycles	400		600	
η	initial step size	0.5			
η_{red}	reduction factor per epoch	0.001		0.002	0.004
α	momentum parameter	0.9		0.5	
β	overall inverse network temperature $\beta = 1/T$	1.0			
n_{train}	number of patterns in training sample	101958	132364	91746	119561
n_{test}	number of patterns in test sample	33987	44122	30583	39854
$\mathrm{FOM}_{\mathrm{train}}$	net performance (training sample)	0.464	0.479	0.237	0.196
$\sigma(\mathrm{FOM}_{\mathrm{train}})$	error on performance	0.002	0.002	0.004	0.004
$\mathrm{FOM}_{\mathrm{test}}$	net performance (test sample)	0.464	0.479	0.235	0.196
$\sigma(\mathrm{FOM}_{\mathrm{test}})$	error on performance	0.003	0.003	0.007	0.007

Table 5.3: Summary of the parameters describing the architecture and the training conditions of the four neural networks used for quark flavour separation. All parameters are described in the text. In addition some information about performance of the algorithms is given.

addition the performance is calculated using the test sample. The initial learning parameter $\eta = 0.5$ is chosen rather large for all networks. After each epoch η is iteratively reduced by a factor $1 - \eta_{\mathrm{red}}$ down to $\eta \approx 10^{-4}$. The momentum parameter α is set to an individual value for each of the four neural networks. The optimal α is found after several trials. For the network temperature $T = 1$ is used. A variation of the temperature shows little change of the performance of the networks. A constant reduction of T and α after each training epoch as done with the learning parameter, does not lead to a higher separation power of the trained networks. Therefore those parameters are kept fix during the training.

After n_{cycle} ($n_{\mathrm{cycle}} = 400$ for NETb $\rightarrow$ e and NETb $\rightarrow \mu$, $n_{\mathrm{cycle}} = 600$ for NETc $\rightarrow$ e and NETc $\rightarrow \mu$) there is no observable improvement of the performance of the networks after another n_{cycle} cycles. Also a change of one or several of the training parameters shows no further improvement. Since the performance stays constant the training is finished at this point. The plots in Figure 5.5 show the performance of the four neural networks on the test and training samples as a function of the training cycles for the first n_{cycle} cycles, expressed using the figure of merit (Eq. A.12). During the first cycles the learning of the networks is very fast. The largest step is visible after the first cycle. The performance on the training and the test sample is very similar, if one considers the statistical error due to the finite size of the samples. Together with the monotonic behaviour of the performance curve on the test sample this shows that the networks are not overtrained and the training samples are large enough for the given complexities of the nets. A summary of the parameters used for the training can be found in Table 5.3. This table also contains the values for the figure of merit for the four networks for the training and test sample. Those values are an indication for the separation power of the algorithms.

Since all the events used in the training sample are taken from simulated data for the 1994 detector configuration, tests are made to show that the performance of the produced networks is independent of the detector simulation of the different years. Different networks NET_i are trained using Monte Carlo events produced for the 1992, 1993, 1994 and 1995 detector configuration. Then output distributions with statistically independent samples of simulated data with identical detector simulation are produced with different networks NET_k and NET_l. The statistical compatibility of those distributions is the same as that of two output distributions produced with one neural network using two statistical independent test samples from one year.

The used input quantities to NETb and NETc are not all possible sources of information available for the separation of the $\mathrm{b} \rightarrow \ell^-$ and $\mathrm{c} \rightarrow \ell^+$ decays from each other and from the background. Concerning NETb there are two additional types of variables which could improve the separation:

- The vertex decay lengths $(L/\sigma_L)_{1,2}$, which are already used in NETc would also help NETb to separate the $\mathrm{b} \to \ell^-$ decays from the $\mathrm{c} \to \ell^+$ decays.

- The comparison of the charge of the lepton candidate Q_ℓ with the jet charge Q_{jet} of either the lepton jet or the most energetic jet not containing the lepton candidate (other jet). This can be done with the variable

$$Q_{\ell,\mathrm{jet}} = Q_\ell \cdot Q_{\mathrm{jet}} \tag{5.4}$$

$Q_{\ell,\mathrm{jet}}^{\mathrm{lepton\ jet}}$ is positive for $\mathrm{b} \to \ell^-$ and $\mathrm{c} \to \ell^+$ decays and negative for $\mathrm{b} \to \mathrm{c} \to \ell^+$ decays, assuming that Q_{jet} is the jet charge of the lepton jet. Here $Q_{\ell,\mathrm{jet}}$ is very helpful to reject the cascade decays from direct $\mathrm{b} \to \ell^-$ and $\mathrm{c} \to \ell^+$ decays.

Distributions of these additional variables are given in Figure 5.6. The intrinsic separation can be seen from these distributions. NETb $\to$ e and NETb $\to \mu$ are retrained with either $(L/\sigma_L)_{1,2}$ or $Q_{\ell,\mathrm{jet}}^{\mathrm{lepton\ jet}}$ and $Q_{\ell,\mathrm{jet}}^{\mathrm{other\ jet}}$ as additional input quantities. In both cases the figure of merit indicated a significant improvement of the separation quality (see Table 5.4). Adding $Q_{\ell,\mathrm{jet}}$ as an input to NETc $\to$ e and NETc $\to \mu$ changes the separation quality just very little. The price one has to pay for this improvement is a strong dependence of the B mixing parameter $\overline{\chi}$ on the output value of NETb which can be seen in Figure 5.7. Unfortunately the increase of the systematic uncertainty due to the correction which is necessary to account for this bias is not compensated by the small reduction of the statistical error caused by the better performance of NETb. For that reason these variables are not included in NETb. The small bias introduced by $(L/\sigma_L)_{1,2}$, which is used as an input to NETc is discussed in Section 5.9.

The additional use of $Q_{\ell,\mathrm{jet}}$ in the $\mathrm{c} \to \ell^+$ neural networks does not improve the performance, so they are not used there either.

The NETb and NETc output distributions produced with OPAL data are shown in Figure 5.8, together with the predictions from Monte Carlo. The hatched histograms show the distribution of the different decay channels 1-4 introduced earlier. At high NETb values, the separation of group 1 ($\mathrm{b} \to \ell^-$, $\mathrm{b} \to \overline{\mathrm{c}} \to \ell^-$, $\mathrm{b} \to \tau^- \to \ell^-$) events from all other lepton sources is clearly visible in figures (a) and (b). For example, requiring NETb > 0.7 gives a sample 89 % pure in group 1 decays, with 3 % $\mathrm{b} \to \mathrm{c} \to \ell^+$ and 4 % $\mathrm{c} \to \ell^+$, whilst retaining 45 % of all $\mathrm{b} \to \ell^-$, $\mathrm{b} \to \overline{\mathrm{c}} \to \ell^-$, and $\mathrm{b} \to \tau^- \to \ell^-$ decays with an identified lepton (averaged over electrons and muons). The separation of leptons from $\mathrm{c} \to \ell^+$ decays from other leptons is more difficult as can be seen in the output distributions of NETc in figures (c) and (d). Requiring NETc > 0.7 gives a sample 59 % pure in $\mathrm{c} \to \ell^+$ decays, with 12 % $\mathrm{b} \to \ell^-$, $\mathrm{b} \to \tau^- \to \ell^-$, and $\mathrm{b} \to \overline{\mathrm{c}} \to \ell^-$ and 6 % $\mathrm{b} \to \mathrm{c} \to \ell^+$, whilst retaining 19 % of all $\mathrm{c} \to \ell^+$ decays with an identified lepton. For both NETb and NETc, the Monte Carlo gives a reasonable description of the data, and the effects of the small discrepancies visible are discussed in Section 5.9.4.

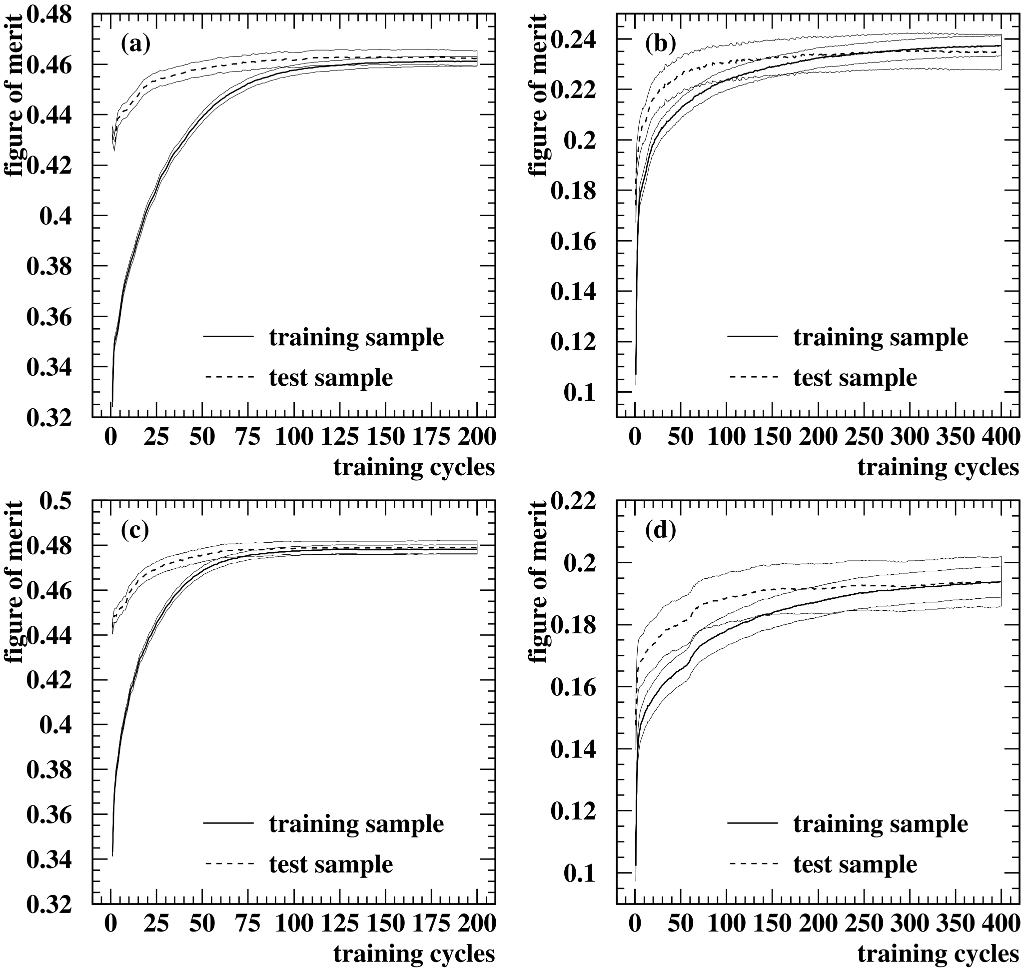

Figure 5.5: The four plots show the figure of merit of the test and training samples as a function of the training cycles. For all four networks the figure of merit shows a monotonic behaviour over the training cycles for both, the training and test sample. The performance of the $b \to \ell^-$ networks is always better than that of the $c \to \ell^+$ ones. At the beginning the performance improves rapidly. Towards the end, the performance on the test and training sample is almost the same. The thin lines give the statistical error on the figure of merit caused by the finite number of training and test events.

The output distributions (Figure 5.8) and the corresponding values for the figure of merit (Table 5.3) reflect the better intrinsic separation of the input parameters used for NETb compared with those for NETc (Table 5.2 as well as Figures 5.1-5.4). The strong overlap of the inputs to NETc makes it very difficult to separate

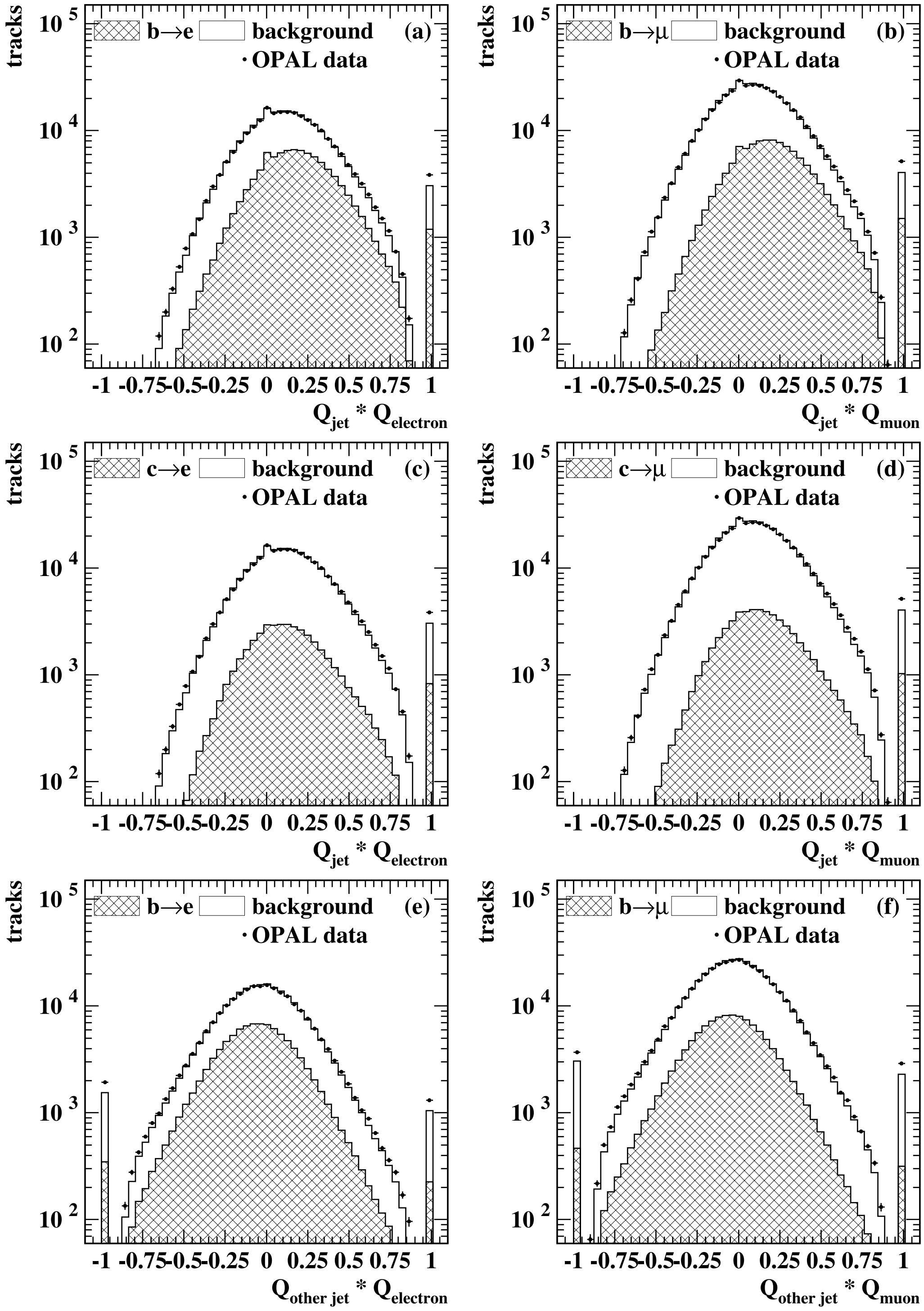

tracks
b→e
background
OPAL data
(a)
$Q_{jet} * Q_{electron}$
b→μ
(b)
$Q_{jet} * Q_{muon}$
c→e
(c)
c→μ
(d)
(e)
$Q_{other\ jet} * Q_{electron}$
(f)
$Q_{other\ jet} * Q_{muon}$

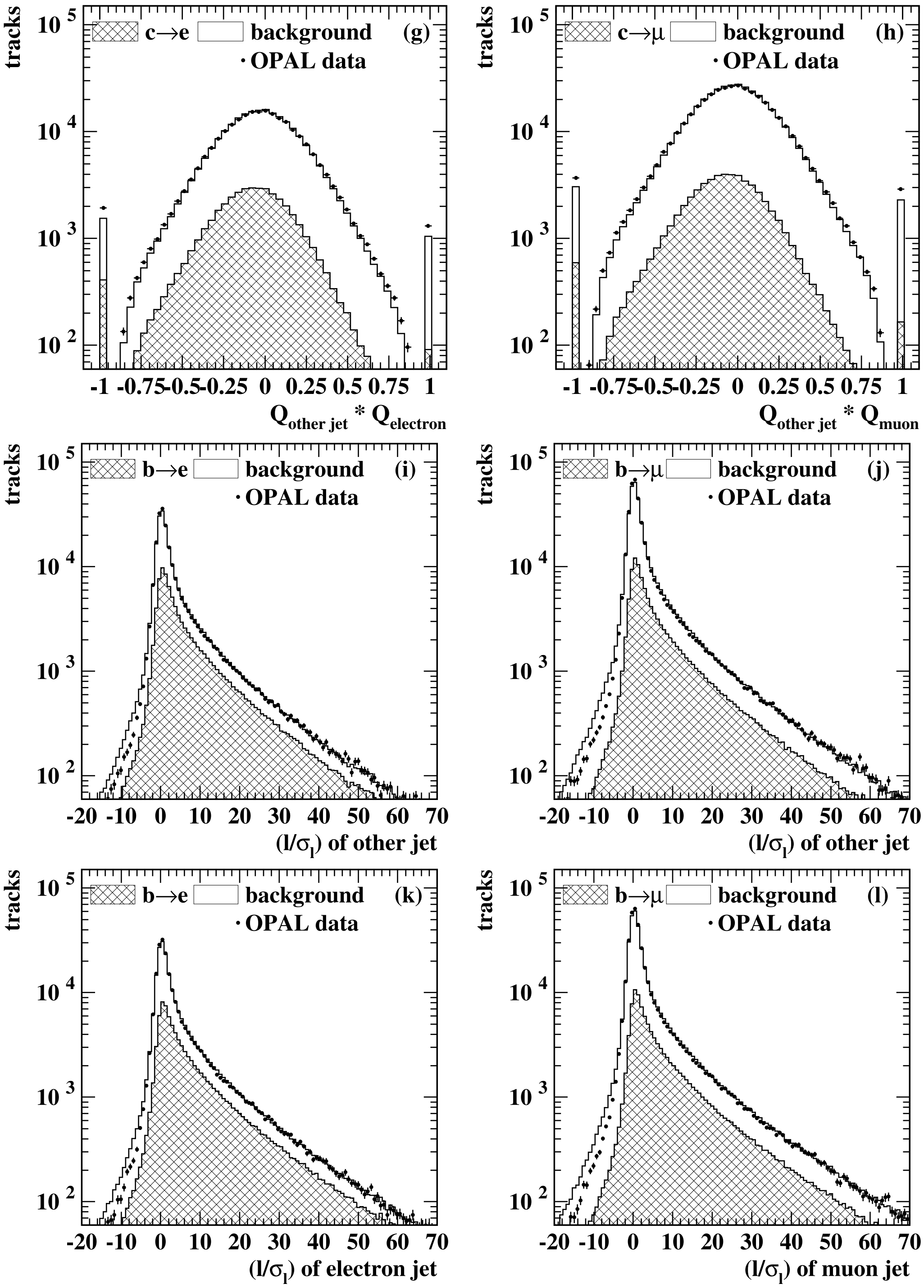

Figure 5.6: Distributions of additional input variables for quark flavour separation. The histograms give the signal and background distributions taken from Monte Carlo simulation. On the vertical axis the number of electron or muon candidates is given. The small dots represent the distribution of the same variable in the data. Plot (a)-(d) shows $Q_{\ell,\mathrm{jet}}^{\mathrm{lepton\ jet}}$, plot (e)-(h) show $Q_{\ell,\mathrm{jet}}^{\mathrm{other\ jet}}$, and plot (i)-(l) show $(L/\sigma_L)_{1,2}$. The distributions all have intrinsic separation.

network type	figure of merit	
	NETb $\rightarrow$ e	NETb $\rightarrow \mu$
used in analysis	0.464 ± 0.002	0.479 ± 0.002
with $Q_{\ell,\mathrm{jet}}$	0.475 ± 0.002	0.492 ± 0.002
with $(L/\sigma_L)_{1,2}$	0.500 ± 0.002	0.510 ± 0.002
with $Q_{\ell,\mathrm{jet}}$ and $(L/\sigma_L)_{1,2}$	0.502 ± 0.002	0.511 ± 0.002

Table 5.4: Comparison of the performance of NETb $\rightarrow$ e and NETb $\rightarrow \mu$ for four different sets of input quantities. The performance is expressed with the figure of merit. In the first line the performance of the networks used in the analysis is shown. Values for the performance after adding $Q_{\ell,\mathrm{jet}}^{\mathrm{lepton\ jet}}$ and $Q_{\ell,\mathrm{jet}}^{\mathrm{other\ jet}}$, $(L/\sigma_L)_{1,2}$ or both to the list of inputs are given in the subsequent lines. The improvement with all four additional inputs is small compared to the net using only $Q_{\ell,\mathrm{jet}}$ or $(L/\sigma_L)_{1,2}$.

the signal from the background. This cannot be compensated by the larger number of inputs to NETc. Also the correlations between the different input parameters to NETc do not provide more information than those between the inputs to NETb.

The values of NETb and NETc are evaluated for all lepton candidates. When more than one lepton is identified in an event, the candidates are ranked according to the value of NETb. If the best two lepton candidates in an event satisfy NETb > 0.6, and if the axis of the two jets containing the leptons do not belong to the same thrust hemisphere, then both candidates are retained, and this is classified as a dilepton event. Otherwise only the best lepton candidate is considered, and the event is classified as a single lepton event. The numbers of single and dilepton events selected are given in Table 5.1.

5.5 Fit Method

To measure the forward-backward asymmetry, A_{FB}, the definition given in Eq. 2.28 has to be modified in order to take detector efficiency effects into account. Usually the acceptance is a function of the polar angle $|\theta|$. Assuming the detection efficiency is known for all $|\theta|$, the total cross-section in forward and backward direction can be calculated.

A solution to this problem is offered by measuring the forward-backward asymmetry using two small bins at the polar angles $\pm\theta$ in forward and backward direction. The width of the bins must be chosen such that the efficiency can be

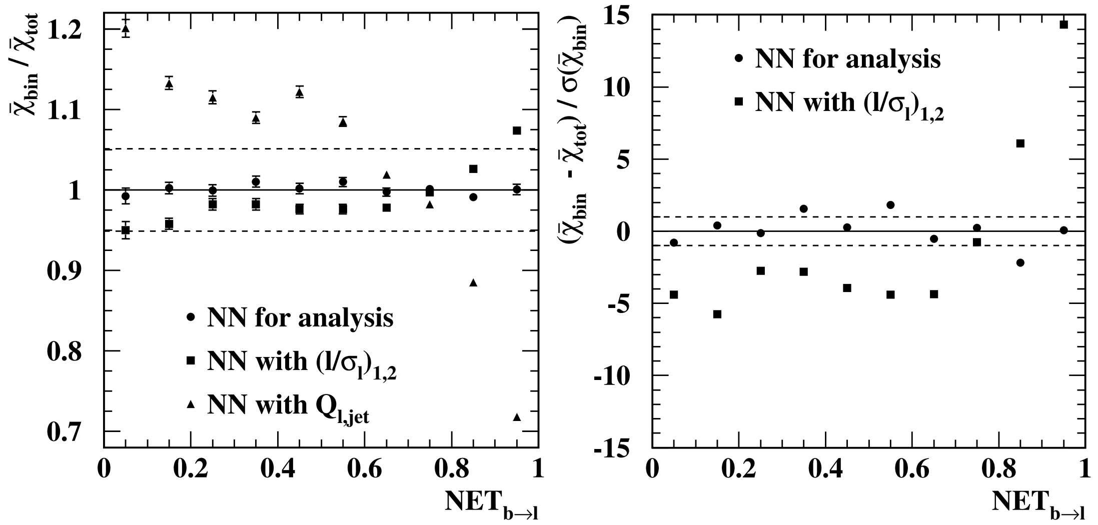

Figure 5.7: The B mixing parameter $\overline{\chi}$ as a function of the output of NETb. The used neural networks are trained with different sets of input quantities. On the left hand plot the fraction $\bar{\chi}_{\rm bin}/\bar{\chi}_{\rm tot}$ of the B mixing parameter $\bar{\chi}_{\rm bin}$, determined in bins of NETb and the total mixing parameter $\bar{\chi}_{\rm tot}$ of the sample, is plotted as a function of NETb. The dashed lines indicate the uncertainty of the OPAL $\overline{\chi}$ measurement. It can be seen that $Q_{\ell,\rm jet}$ as additional input induces a strong bias. The influence of the other additional inputs is better visible looking at the pull: $(\bar{\chi}_{\rm bin} - \bar{\chi}_{\rm tot})/\sigma(\bar{\chi}_{\rm bin+tot})$ plotted on the right diagram. Again the dashed lines indicate the error of the OPAL measurement. The neural network used in the analyses has no bias at all because the values show a random distribution. $(L/\sigma_L)_{1,2}$ as an additional input introduces a bias but in the opposite direction compared to $Q_{\ell,\rm jet}$.

assumed to be constant within the bin. To obtain the relationship between the total forward-backward asymmetry and the forward-backward asymmetry measured in a specific bin pair, the differential cross-section of the $\rm e^+e^- \to q\overline{q}$ process (Eq. 2.23) at the Z pole is used:

$$\frac{\mathrm{d}\,\sigma_{\rm q}}{\mathrm{d}\,\cos\theta} \propto 1+\cos^2\theta + \frac{8}{3}A_{\rm FB}\;\cos\theta = \mathrm{d}\sigma(\theta)\;. \tag{5.5}$$

Together with the definition of the forward-backward asymmetry (Eq. 2.28) the forward-backward asymmetry at a certain polar angle $|\theta|$ is a function of $|\theta|$:

$$\mathrm{d}A_{\rm FB}(|\theta|) = \frac{\mathrm{d}\sigma(|\theta|)-\mathrm{d}\sigma(-|\theta|)}{\mathrm{d}\sigma(\theta)+\mathrm{d}\sigma(-\theta)} = \frac{8}{3}A_{\rm FB}\frac{|\cos\theta|}{1+\cos^2\theta} \tag{5.6}$$

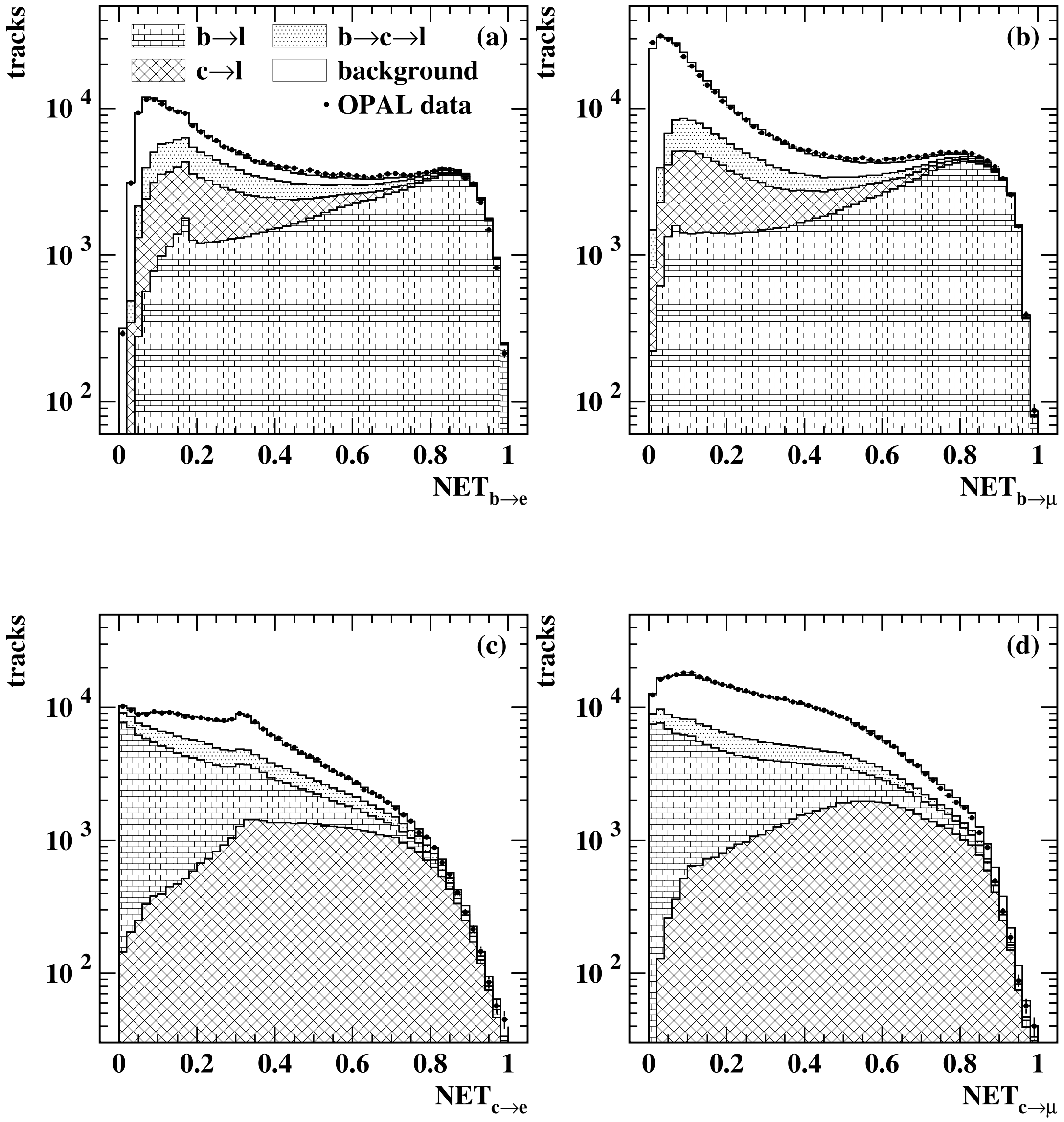

Figure 5.8: Outputs of the neural networks designed to select (a) b → e, (b) b → μ, (c) c → e and (d) c → μ decays. The data are shown by the points with error bars, and the expected contributions from different lepton sources by the hatched histograms. On the vertical axis the number of electron or muon candidates is given.

This relation is also valid if the width $\Delta\theta$ of the bin is chosen such that the vari-

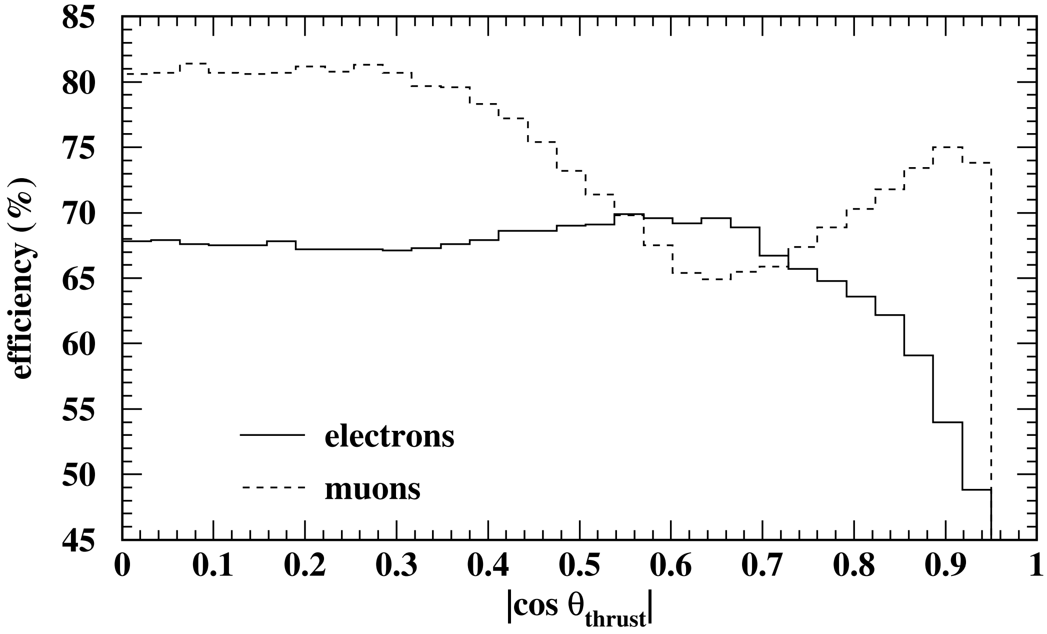

Figure 5.9: Efficiency to detect a b or c event using prompt leptons as a function of $|\cos\theta_{\mathrm{T}}|$.

ation of $A_{\mathrm{FB}}(\theta) = A_{\mathrm{FB}}(|\theta|)$ over θ within the bin is negligible. For the forward-backward asymmetry measurement a binning in θ, symmetric to a plane perpendicular to the beam pipe and containing the interaction point, is introduced. Binning the events in θ allows the inclusion of the full statistics of the selected events in the analysis. The measurement now is done by counting events:

$$\Delta A_{\mathrm{FB}i} = \frac{n_{\mathrm{F},i} - n_{\mathrm{B},i}}{n_{\mathrm{F},i} + n_{\mathrm{B},i}} = A_{\mathrm{FB}} \cdot \frac{8}{3} \frac{|\cos\theta_i|}{1 + \cos^2\theta_i} \tag{5.7}$$

Here the events $n_{\mathrm{F},i}$ and $n_{\mathrm{B},i}$ detected in bin i in forward and backward direction are used. The value of $\cos\theta_i$ is taken at the mean of bin i. The polar angle θ of the event is given by the direction of the thrust axis [78], $\cos\theta_{\mathrm{T}}$.

The efficiency to detect a b or c event with at least one prompt electron or muon as a function of $|\cos\theta_{\mathrm{T}}|$ is shown in Figure 5.9. The binning of the efficiency curve in $|\cos\theta_{\mathrm{T}}|$ is three times narrower than the binning used to calculate the differential forward-backward asymmetry in the analysis. It can be seen that the variation of the efficiency over three bins in the plot is rather small, so that the differential asymmetry can be used for the measurement. A cross check with different sizes of the bins to show that this assumption is justified can be found in Section 5.10.

In the central part of the detector the detection efficiency using electrons is nearly

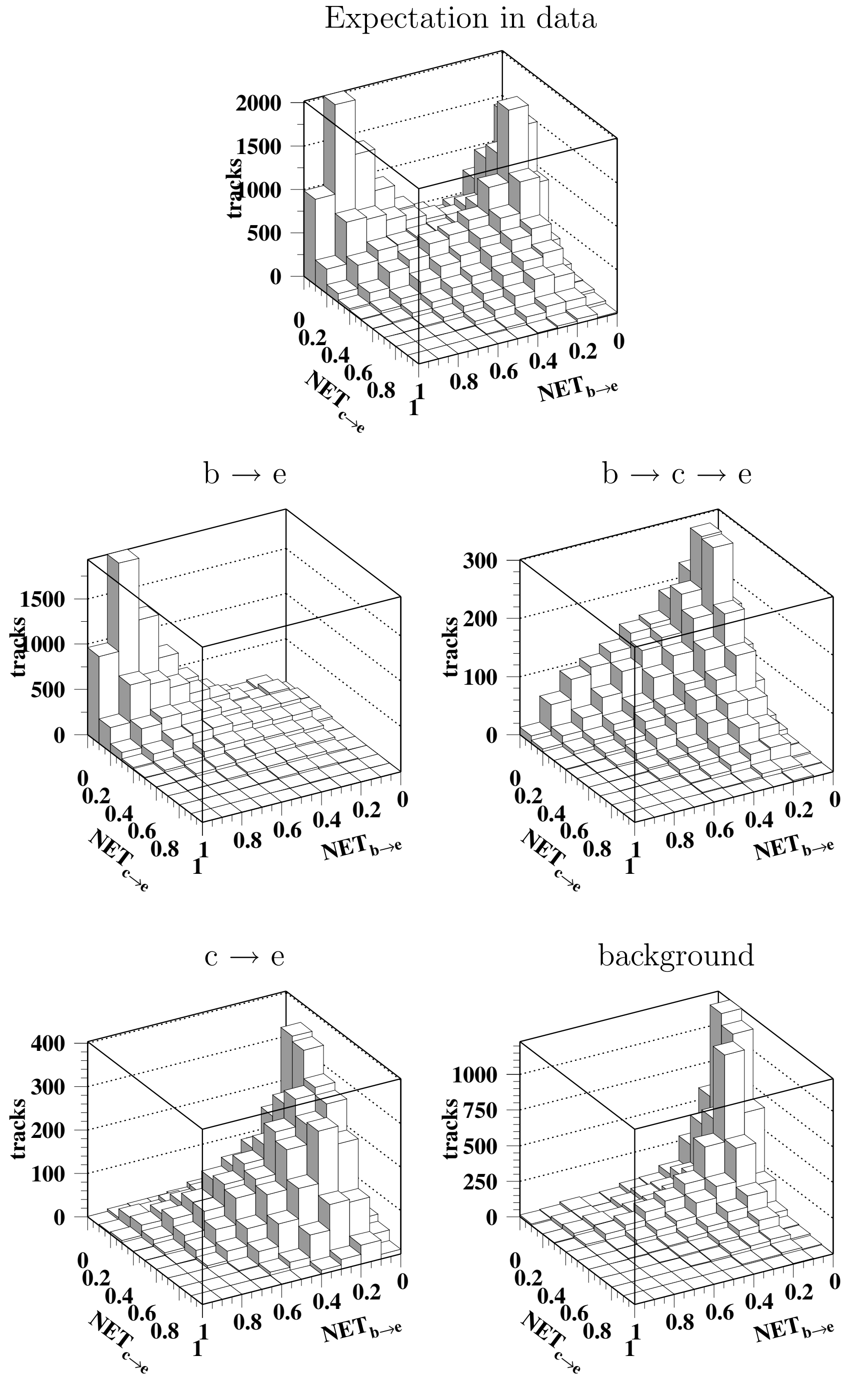

Figure 5.10: NETb × NETc distributions of a large y bin in the barrel part of the detector for electron candidates only. The histogram at the top shows the distribution expected in data, which is a superposition of the four histograms for the different decay channels. The different shapes ensure a good separation of the four groups of events. Especially the $b \rightarrow e^-$ decays are accumulated in one corner of the appropriate distribution. Also the $c \rightarrow e^+$ decays can be separated quite well from the background.

constant, but in the endcaps the efficiency drops. A particle track in the endcap region crosses fewer wires in the jet chamber than in the barrel region [60]. Therefore the probability to produce a given number of hits is smaller in the endcaps, leading to a reduced efficiency. In addition the energy measurement in the electromagnetic calorimeter is worse in the endcaps compared to the barrel due to more material in front of the calorimeter and noise effects (non-pointing geometry of the lead glass blocks and photo diodes instead of photo multipliers due to high magnetic field [60]).

The detection efficiency using muons drops in the overlap region of the central part of the detector and the endcaps. In this region there is more material in front of the external muon chambers originating from the edge of the pressure tank [60]. In addition there is a big iron support in the overlap region between the hadron calorimeter and the muon chambers of about 80 cm. Due to such a big amount of material the probability that a muon initialises a shower is rather high, leading to a change of the flight direction of the muons. This dilutes the quality of matching of a track in the central tracking system and the external muon chambers, which is used to identify muons.

The thrust axis of each event is used to estimate the flight direction of the primary quark, and the charge Q_ℓ of the identified leptons is used to distinguish between the quark and antiquark direction. For single lepton events, the observable $y = -Q_\ell \cos\theta_{\mathrm{T}}$ classifies events as forward, with $y > 0$, or backward, with $y < 0$.

To measure the b and c forward-backward asymmetries the total observable asymmetry (Eq. 5.1) needs to be known for at least two samples with different quark flavour composition. This can be realised with the help of the quark flavour separation neural networks described above by placing cuts in order to get a b and a c enriched sample. Even though the cut points can be optimised to get samples with large statistics, some information will be lost. To keep as much as possible of the available information for the determination of the asymmetries a method is developed which uses all events with at least one lepton for the measurement [82, 83].

Since all b and c events carry information about $A_{\mathrm{FB}}^{\mathrm{b}}$ and $A_{\mathrm{FB}}^{\mathrm{c}}$ it is useful to use all of them. This is done by producing two dimensional NETb $\times$ NETc distributions with 10×10 bins. All single lepton events are grouped into 20 bins [3], with respect to their y value. The events in each y bin are sorted in the NETb $\times$ NETc distribution according to their NETb and NETc values. Now there are 100 (=10×10) y distributions. With the help of the differential forward-backward asymmetry the total asymmetry for each of this y distributions can be calculated for the data events. The composition of each NETb, NETc and y bin can be taken from Monte Carlo simulation by sorting the four different groups of

[3] 10 bins in forward ($y > 0$) and 10 in backwards ($y < 0$) direction.

b and c decays:

1. $\mathrm{b} \to \ell^-$, $\mathrm{b} \to \tau^- \to \ell^-$ and $\mathrm{b} \to \overline{\mathrm{c}} \to \ell^-$,
2. $\mathrm{b} \to \mathrm{c} \to \ell^+$,
3. $\mathrm{c} \to \ell^+$ and
4. background

separately into NETb, NETc and y bins. These NETb $\times$ NETc distributions can be used to calculate the relative composition of each NETb-NETc-y bin of the data histograms.

Figure 5.10 shows an example of a NETb $\times$ NETc distribution as it will look like using data events. This distribution can be constructed as a superposition of the four NETb $\times$ NETc distributions for the different decay channels taken from simulated data. The distributions for the four decay channels each have a very characteristic shape ensuring a good separation amongst each other. Already the distribution of the superposition – taken from data – shows b and c enriched regions. With two of these data NETb $\times$ NETc distributions for two equivalent y bins, one in forward and one in backward direction, the differential forward backward asymmetry can be measured separately for any of the NETb, NETc bins.

The B mixing parameter $\overline{\chi}$ can be measured by counting the number of dilepton events with both leptons having the same charge and comparing them to the number of dilepton events where both leptons have opposite charge. Dilepton events are events where both leptons belong to different thrust hemispheres and where both leptons survive a cut of NETb > 0.6. This cut is chosen in order to minimise the total error (statistical plus systematic) on the mixing measurement. Of events with more than two lepton candidates satisfying this cut, the two with the highest value of NETb are taken. Each of the two leptons of the dilepton event (ij) can be of type 1 to 4. Events of type $i = 1$ and $j = 1$ (11) are the signal, while (12) and (14) are the main background contributions which reduce the sensitivity of the measurement.

Both, the measurement of the differential forward-backward asymmetries (the quark in an event is either moving in forward or backward direction) and the measurement of the B mixing parameter (a B meson may or may not have mixed), involve binomial probability distributions. For both, the measurement of the B mixing parameter $\overline{\chi}$ and the b and c forward-backward asymmetries, it is possible to give the probability density as a function of the fit parameters and the measured numbers of forward and backward events as a function of $|\cos\theta_{\mathrm{T}}|$. Therefore the maximum likelihood method is best suitable to estimate the values for $A^{\mathrm{b}}_{\mathrm{FB}}$, $A^{\mathrm{c}}_{\mathrm{FB}}$ and $\overline{\chi}$. As a first step the likelihood function $\mathcal{L}$ has to be constructed. To extract the values for the measured quantities the maximum of the likelihood function has to be found. This is usually done with a multi-parameter fit. Due to technical reasons it is preferred to search for the global minimum of $-\log \mathcal{L}$ rather than for the maximum of $\mathcal{L}$ [126].

As an alternative to a maximum likelihood fit one could think of doing a χ^2 fit[4] to the differential cross-section in the different NETb-NETc bins. Unfortunately this will not work properly because there are regions of the NETb $\times$ NETc plane where the bins of the y distributions have very few entries, so that the bin errors are not Gaussian as assumed by a χ^2 fit. This introduces a bias in the results and in the statistical errors. Throwing away all y distributions containing bins with too few entries would cut out information and thus raise the statistical error.

To account for the correlation between the B mixing parameter $\overline{\chi}$ and the b quark forward backward asymmetry, $A^{\mathrm{b}}_{\mathrm{FB}}$, originating from the type of measurement and the correlation between the b and c asymmetries due to the limited purity of the quark flavour separation, all three parameters are determined with a simultaneous fit to the data. The values of the asymmetries and $\overline{\chi}$ are extracted from the observed numbers of single lepton events as a function of $\cos\theta_{\mathrm{T}}$, NETb and NETc, and the numbers of dilepton events as a function of $\cos\theta_{\mathrm{T}}$.

The total likelihood to be maximised is the product:

$$\mathcal{L} = \mathcal{L}_{\text{single e}} \cdot \mathcal{L}_{\text{single }\mu} \cdot \mathcal{L}_{\text{double}} \ . \tag{5.8}$$

The single and double lepton likelihood terms are discussed in more detail below.

5.5.1 Single Lepton Likelihood Function

The forward-backward asymmetry is examined in bins of NETb, NETc and $|y|$. The fit considers four classes of leptons according to the lepton charge and primary quark flavour as mentioned above. Direct $\mathrm{b} \to \ell^-$ decays and the other decays in class (1) contribute to the observed asymmetry with the opposite sign to classes (2) and (3). The asymmetry of events coming from b decays is scaled by a factor $(1-2\overline{\chi})$ for category (1) decays and $(1-2\overline{\eta}\,\overline{\chi})$ for category (2), to account for the effects of neutral B meson mixing. The additional correction factor $\overline{\eta}$ takes into account that the two samples include different fractions of different species of b hadrons: B^0, B^+, $\mathrm{B}^0_{\mathrm{s}}$, b baryons etc., mainly due to the different semileptonic branching ratios of D^0 and D^+ mesons [26]. The value of $\overline{\eta}$ is set to 1.083, evaluated from the Monte Carlo simulation. No equivalent correction

[4]The maximum likelihood fit method and the χ^2 fit method are equivalent if the probability density function is a Gaussian.

factor is used for the small fraction of $b \to \bar{c} \to \ell^-$ events included in category (1).

The fractions of each single lepton category in the full data sample are given in Table 5.5. Note that these are fitted fractions. The fit adjusts the overall rate of background in the sample.

		electrons	muons
(1)	$b \to \ell^-$	35.6 %	24.6 %
	$b \to \bar{c} \to \ell^-$	2.8 %	2.3 %
	$b \to \tau^- \to \ell^-$	1.1 %	0.7 %
(2)	$b \to c \to \ell^+$	12.6 %	9.7 %
(3)	$c \to \ell^+$	19.3 %	14.9 %
(4)	background	28.6 %	47.8 %

Table 5.5: The composition of the single lepton samples. The first three lines are combined into category (1) in the fit. The fractions given correspond to the fractions f_i' after the fit.

The likelihood for single lepton events is an improved version of that used earlier [82, 83, 123]. It has two terms:

$$\mathcal{L}_{\text{single }\ell} = \prod_{\text{NETb,NETc}} \prod_{|y|} \overbrace{\frac{(n_\mathrm{F}+n_\mathrm{B})!}{n_\mathrm{F}!\, n_\mathrm{B}!}}^{\text{normalisation}} \overbrace{\left(\frac{1+A_\mathrm{FB}}{2}\right)^{n_\mathrm{F}}}^{\text{forward}} \overbrace{\left(\frac{1-A_\mathrm{FB}}{2}\right)^{n_\mathrm{B}}}^{\text{backward}} \cdot \prod_{\text{NETb,NETc}} \underbrace{\frac{1}{\sqrt{2\pi}\sigma_m} \exp\left(-\frac{(n_\mathrm{T}-m)^2}{2\sigma_m^2}\right)}_{\text{background fraction}} . \tag{5.9}$$

The first term is a product over all NETb, NETc and $|y|$ bins. For each bin there is a forward and a backward contribution. The number of forward n_F and backward n_B events observed in each bin of the data follow a binomial probability distribution.

The fit uses ten equidistant bins in each of NETb, NETc and $|y|$. The second term constrains the total number of events n_T in a given NETb, NETc bin (no binning in $|y|$) to the expected number m and allows the overall normalisations of the electron and muon background contributions to be determined from the data, reducing the overall uncertainty. The determination of the background contribution in the fit was first introduced in [82]. The shapes of the distributions of the background events as a function of $|\cos\theta_\mathrm{T}|$, however, are taken from Monte Carlo simulation. In Figure 5.11 the distribution of the background events as a

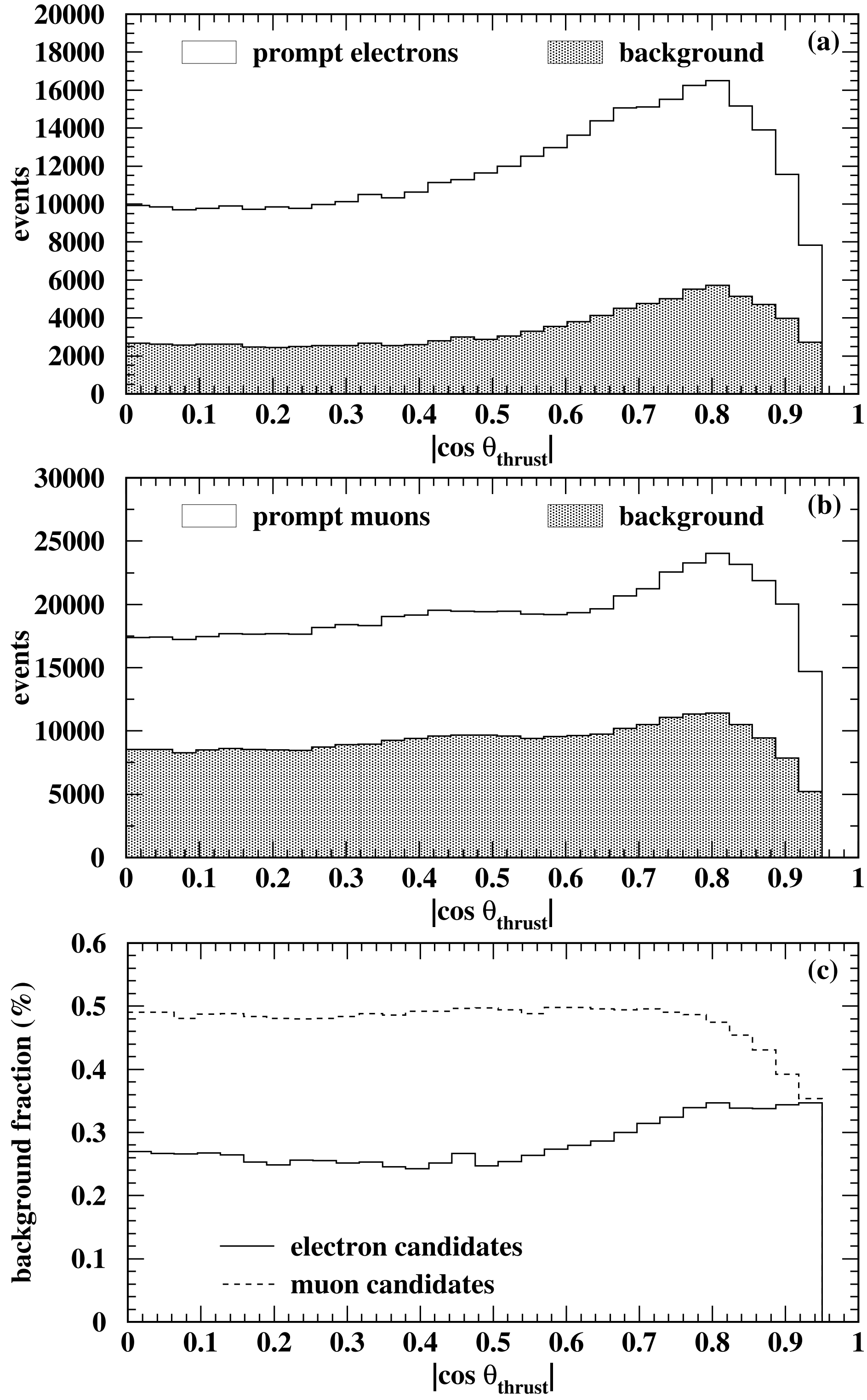

Figure 5.11: Number of events tagged using an electron (a) or muon (b) candidate as a function of $|\cos\theta_{\mathrm{T}}|$. The hatched part of the bins shows the contribution from background events. The normalisation of the background fraction is a fit result while the shape of the distributions is taken from Monte Carlo simulation. The background fraction of each bin is shown in plot (c).

function of $|\cos\theta_{\rm T}|$ is shown. While the events tagged with an electron candidate have the highest purity in the central part of the detector and a steady increase of the background fraction towards the endcap regions, the events which are tagged using a muon candidate have more or less the same background contribution over the whole $|\cos\theta_{\rm T}|$ range. Just in the far forward region the background contribution decreases slightly.

In the following the different contributions to $\mathcal{L}_{\text{single }\ell}$ Eq. 5.9 are explained. The definition of the forward-backward asymmetry (Eq. 2.28) can be written with the probabilities of $p_{\rm F}$ and $p_{\rm B}$ of an event to be forward or backward.

$$A_{\rm FB} \equiv \frac{\sigma_{\rm F}}{\sigma_{\rm F}+\sigma_{\rm B}} - \frac{\sigma_{\rm B}}{\sigma_{\rm F}+\sigma_{\rm B}} = p_{\rm F} - p_{\rm B} = 2p_{\rm F} - 1 \tag{5.10}$$

Due to the binomial character of the problem, $p_{\rm F}$ and $p_{\rm B}$ sum up to 1. Therefore the probability of an event in a specific NETb, NETc and $|y|$ bin to be forward is $p_{\rm F} = (1 + A_{\rm FB})/2$, where $A_{\rm FB} = A_{\rm FB}(\text{NETb}, \text{NETc}, |y|)$ is the total expected forward-backward asymmetry for the considered bin:

$$A_{\rm FB}(\text{NETb}, \text{NETc}, |y|) = \sum_{i=1}^{4} f'_i \rho_i(\text{NETb}, \text{NETc}, |y|) A^i_{\rm FB}\, \frac{8}{3}\frac{|y|}{1+y^2}\,. \tag{5.11}$$

In this expression, f'_i denotes the fraction of leptons in class i, while ρ_i is the normalised distribution of leptons from class i in bins of NETb, NETc and $|y|$, taken from Monte Carlo simulation. The source fractions f'_i are derived from the Monte Carlo fractions f_i. However, the fraction of background f'_4 is a free parameter in the fit, and the fractions of prompt sources with $i = 1, 2, 3$ are given by

$$f'_i = (1 - f'_4)\frac{f_i}{f_1 + f_2 + f_3}\,. \tag{5.12}$$

In this way, the relative rates of the prompt leptons are fixed by the prediction of the Monte Carlo simulation, and the fractions satisfy $\sum_i f'_i = 1$. The nominal asymmetries $A^i_{\rm FB}$ of Eq. 5.11 for each class are:

$$\begin{array}{lcll} A^1_{\rm FB} & = & & (1-2\overline{\chi})A^{\rm b}_{\rm FB} \\ A^2_{\rm FB} & = & - & (1-2\overline{\eta}\,\overline{\chi})A^{\rm b}_{\rm FB} \\ A^3_{\rm FB} & = & - & A^{\rm c}_{\rm FB} \\ A^4_{\rm FB} & = & & A^{\rm Background}_{\rm FB} \end{array} \tag{5.13}$$

The background asymmetry $A^{\rm Background}_{\rm FB}$ also depends on the primary quark asymmetries. It is expressed as a sum over quark flavours:

$$A^{\rm Background}_{\rm FB} = \sum_{\rm q} f^{\rm q\overline{q}}_{\rm back} c^{\rm q\overline{q}}_{\rm dilute} A^{\rm q\overline{q}}_{\rm FB}\,. \tag{5.14}$$

This introduces a very weak additional dependence on the fitted values of the b and c forward-backward asymmetries. The central values of the light quark

$\langle\sqrt{s}\rangle$ [GeV]	A_{FB} (%) (ZFITTER prediction) 89.51	91.25	92.95
$\mathrm{s\bar{s}}$	5.95± 5.0	9.64±1.3	11.89± 5.0
$\mathrm{u\bar{u}}$	-3.08±20.0	6.32±7.3	12.07±20.0
$\mathrm{d\bar{d}}$	5.96±10.0	9.64±3.7	11.89±10.0

Table 5.6: The values of the forward-backward asymmetries for light flavours taken from ZFITTER [34] and the variations used for calculating the background asymmetry [127, 128].

	electrons		muons	
	$f^{\mathrm{q\bar{q}}}_{\mathrm{back}}$	$c^{\mathrm{q\bar{q}}}_{\mathrm{dilute}}$	$f^{\mathrm{q\bar{q}}}_{\mathrm{back}}$	$c^{\mathrm{q\bar{q}}}_{\mathrm{dilute}}$
$\mathrm{b\bar{b}}$	0.139	0.028	0.192	0.093
$\mathrm{c\bar{c}}$	0.146	-0.104	0.178	-0.043
$\mathrm{s\bar{s}}$	0.214	0.025	0.243	0.103
$\mathrm{u\bar{u}}$	0.220	-0.114	0.169	-0.123
$\mathrm{d\bar{d}}$	0.218	0.107	0.218	0.083

Table 5.7: The fractions of background coming from each primary quark flavour for electrons and muons and the dilution factors by which the primary quark forward-backward asymmetries are scaled to evaluate the background asymmetry.

forward-backward asymmetries are taken from the predictions of ZFITTER 6.36 [34] and are listed in Table 5.6. The quoted uncertainties in these asymmetries are taken from measurements of the strange quark asymmetry by DELPHI [127] and of the light quark asymmetries by OPAL [128]. These measurements are consistent with the ZFITTER expectations, with relatively large statistical errors. The fractions $f^{\mathrm{q\bar{q}}}_{\mathrm{back}}$ of each quark flavour contributing to the background are taken from the Monte Carlo prediction, as are the dilution factors $c^{\mathrm{q\bar{q}}}_{\mathrm{dilute}}$ which take into account the fraction of the primary quark forward-backward asymmetry that is seen in background events of this flavour. The fractions and dilutions are listed in Table 5.7. Some contributions to the background, for example for photon conversions, have zero forward-backward asymmetry. Others, in particular kaons in $\mathrm{s\bar{s}}$ events, inherit a significant fraction of the primary quark forward-backward asymmetry. The background asymmetry actually varies as a function of NETb and NETc, but this effect is neglected in the fit, and the small resulting bias is treated as part of the overall bias correction described in Section 5.9.3. The uncertainty from this procedure is discussed in Section 5.9.3.

In the second term of the single lepton likelihood the number of events m expected

	ee	$\mu\mu$	eμ
(1)(1)	86.9 %	86.3 %	86.4 %
(1)(2)	10.3 %	8.5 %	9.6 %
(2)(2)	0.3 %	0.2 %	0.3 %
(3)(3)	0.4 %	0.4 %	0.5 %
(1)(4)	1.8 %	4.0 %	2.8 %
others	0.3 %	0.6 %	0.4 %
total number	1 308	2 067	3 354

Table 5.8: Fractions of events in the most important categories in the double lepton sample, together with the total number of ee, $\mu\mu$ and eμ events.

in a NETb and NETc bin is calculated as:

$$m(\mathrm{NETb}, \mathrm{NETc}) = N^{\ell}_{\mathrm{Data}} \sum_{i=1}^{4} f'_i \overline{\rho_i}(\mathrm{NETb}, \mathrm{NETc})\,, \tag{5.15}$$

where N^{ℓ}_{Data} denotes the total number of single lepton events in the data ($\ell = e,\ \mu$), and $\overline{\rho_i}$ is the normalised distribution in bins of NETb and NETc for leptons in class i. The observed number of events n_{T} in a bin is assumed to be Gaussian distributed with mean m and standard deviation σ_m computed as

$$\sigma_m^2 = m + (\delta_m^{\mathrm{MC}})^2\,, \tag{5.16}$$

where δ_m^{MC} is the uncertainty on the expected number m of events in this bin due to limited Monte Carlo statistics.

5.5.2 Double Lepton Likelihood Function

The double lepton likelihood is designed in order to be sensitive to both, the B mixing parameter $\overline{\chi}$ and the forward-backward asymmetries $A^{\mathrm{b}}_{\mathrm{FB}}$ and $A^{\mathrm{c}}_{\mathrm{FB}}$. It is a product in bins of $|y|$ of multinomial probabilities for the event to be forward, p_{F}, backward, p_{B}, or same-sign, p_{S}. An event is called:

- *forward* if the two leptons have opposite charge and fulfil $y_1 = y_2 > 0$,
- *backward* if the two leptons have opposite charge and fulfil $y_1 = y_2 < 0$ and
- *same-sign* if the two leptons have the same charge. This means $y_1 = -y_2$ (these events contain no information about the forward-backward asymmetry).

Both leptons of a identified dilepton event have NETb > 0.6 in order to suppress cascade decays and background from light flavour events. No further subdivision in NETb or NETc is made. The composition of the double lepton sample is given in Table 5.8. A two lepton event can be written as ij, where the two indices i, j refer to one of the categories 1-4 introduced for a lepton candidate. Only certain combinations of the four categories to a double lepton event ij are possible. Any flavour event can give a background lepton, but lepton classes 1 and 2 can only come from $\mathrm{b\overline{b}}$ events, and class 3 only from $\mathrm{c\overline{c}}$ events. The eight possible dilepton classes are therefore: $ij = 11, 12, 22, 33, 14, 24, 34, 44$.

In the fit electron-electron (ee), electron-muon (eμ), and muon-muon ($\mu\mu$) events are considered together:

$$\mathcal{L}_{\mathrm{double}} = \prod_{|y|} \frac{(n_{\mathrm{F}} + n_{\mathrm{B}} + n_{\mathrm{S}})!}{n_{\mathrm{F}}!\ n_{\mathrm{B}}!\ n_{\mathrm{S}}!}\ (p_{\mathrm{F}})^{n_{\mathrm{F}}}\ \ (p_{\mathrm{B}})^{n_{\mathrm{B}}}\ \ (p_{\mathrm{S}})^{n_{\mathrm{S}}}\ . \tag{5.17}$$

In this case, n_{F}, n_{B}, and n_{S} are the number of forward, backward and same-sign events observed in the data in a certain $|y|$ bin. A dilepton event with opposite charged leptons is called forward or backward according to the direction of the negative lepton. The probability of such an event being forward or backward usually depends on the forward-backward asymmetry of the dilepton category ij. The fraction of same-sign dilepton events depends only on the mixing parameter $\overline{\chi}$. The overall probabilities for an event to be forward, backward or same-sign is given by the sum over all possible classes ij:

$$p_X = \sum_{ij} f_{ij}(|y|) p_X^{ij}(|y|)\ . \tag{5.18}$$

Here the variable X stands for F, B or S. Since the contribution of events with at least one lepton of type 4 to the double lepton sample is small (see Table 5.8), the fractions f_{ij} are taken directly from the Monte Carlo simulation, without being corrected for the rates of background leptons fitted in the single lepton sample. Similarly, the small residual asymmetries of the background leptons are neglected. Writing $Y = 8|y|/3(1 + y^2)$, the probabilities p_{F}, p_{B}, and p_{S} for an event to be forward, backward or same-sign for each dilepton category, can be derived[5]:

Source 11: double $\mathrm{b} \to \ell^-$**:** This produces a same-sign event if one of the leptons has mixed and an opposite sign event if non or both leptons have mixed. In case both leptons have mixed the observed asymmetry has opposite sign (wrong tag):

$$\begin{aligned} p_{\mathrm{F,B}}^{11} &= \tfrac{1}{2}(1 - 2\overline{\chi} + 2\overline{\chi}^2 \pm (1 - 2\overline{\chi}) A_{\mathrm{FB}}^{\mathrm{b}} Y)\ , \\ p_{\mathrm{S}}^{11} &= 2\overline{\chi}(1 - \overline{\chi})\ . \end{aligned} \tag{5.19}$$

[5]The upper signs are taken for p_{F} and the lower signs for p_{B}.

Source 12: $\mathrm{b} \to \ell^- + \mathrm{b} \to \mathrm{c} \to \ell^+$**:** This category is independent of the forward-backward asymmetry and only depends on the mixing parameter. This is because in the absence of mixing these events would all be same sign, losing the information about the forward-backward asymmetry. If they are of opposite sign without knowing which lepton comes from the mixed meson, the forward-backward asymmetry information cannot be recovered:

$$\begin{aligned} p^{12}_{\mathrm{F,B}} &= \tfrac{1}{2}\overline{\eta}\,\overline{\chi}(1-\overline{\chi}) + \tfrac{1}{2}\overline{\chi}(1-\overline{\eta}\,\overline{\chi}) \;, \\ p^{12}_{\mathrm{S}} &= (1-\overline{\chi})(1-\overline{\eta}\,\overline{\chi}) + \overline{\eta}\,\overline{\chi}^2 \;. \end{aligned} \tag{5.20}$$

Source 22: double $\mathrm{b} \to \mathrm{c} \to \ell^+$**:** This is like source 11 but the signs of the forward-backward asymmetry is vice versa because of the opposite sign correlation between the primary quark and the final state lepton of the $\mathrm{b} \to \mathrm{c} \to \ell^+$ decay compared to the $\mathrm{b} \to \ell^-$ decay:

$$\begin{aligned} p^{22}_{\mathrm{F,B}} &= \tfrac{1}{2}(1 - 2\overline{\eta}\,\overline{\chi} + 2(\overline{\eta}\,\overline{\chi})^2 \mp (1-2\overline{\eta}\,\overline{\chi})A^{\mathrm{b}}_{\mathrm{FB}}Y) \;, \\ p^{22}_{\mathrm{S}} &= 2\overline{\eta}\,\overline{\chi}(1-\overline{\eta}\,\overline{\chi}) \;. \end{aligned} \tag{5.21}$$

Source 33: double $\mathrm{c} \to \ell^+$**:** Since there is no mixing for $\mathrm{c} \to \ell^+$ decays this source gives always two leptons with opposite charge. A $\mathrm{c} \to \ell^+$ produces a ℓ^+, not a ℓ^-, therefore the forward-backward asymmetry has opposite sign to class 11:

$$\begin{aligned} p^{33}_{\mathrm{F,B}} &= \tfrac{1}{2}(1 \mp A^{\mathrm{c}}_{\mathrm{FB}}Y) \;, \\ p^{33}_{\mathrm{S}} &= 0 \;. \end{aligned} \tag{5.22}$$

Source 14: $\mathrm{b} \to \ell^-$ **+ background:** The sign correlation of the background lepton candidate to the primary quark is random. In 50 % of the cases it has the same sign as the $\mathrm{b} \to \ell^-$ lepton sign, destroying the information about the asymmetry. In the other 50 % of the cases it will have opposite sign and the asymmetry can be measured. In the second case there still can occur mixing in the $\mathrm{b} \to \ell^-$ decay:

$$\begin{aligned} p^{14}_{\mathrm{F,B}} &= \tfrac{1}{4}(1-\overline{\chi})(1 \pm A^{\mathrm{b}}_{\mathrm{FB}}Y) + \tfrac{1}{4}\overline{\chi}(1 \mp A^{\mathrm{b}}_{\mathrm{FB}}Y) \;, \\ p^{14}_{\mathrm{S}} &= \tfrac{1}{2} \;. \end{aligned} \tag{5.23}$$

Source 24: $\mathrm{b} \to \mathrm{c} \to \ell^+$ **+ background:** In this case the situation is the same as with source 14 but with the sign of the forward-backward asymmetry reversed, since the information comes through the cascade decay:

$$\begin{aligned} p^{24}_{\mathrm{F,B}} &= \tfrac{1}{4}(1-\overline{\eta}\,\overline{\chi})(1 \mp A^{\mathrm{b}}_{\mathrm{FB}}Y) + \tfrac{1}{4}\overline{\eta}\,\overline{\chi}(1 \pm A^{\mathrm{b}}_{\mathrm{FB}}Y) \;, \\ p^{24}_{\mathrm{S}} &= \tfrac{1}{2} \;. \end{aligned} \tag{5.24}$$

Source 34: $c \to \ell^+$ **+ background:** Again in 50 % of the cases the signs of the leptons are the same. In the remaining 50 % the sign of the $c \to \ell^+$ decay can be used to determine the direction of the primary quark. This is like source 14 but there is no mixing involved. The sign of the forward-backward asymmetry is reversed (opposite charge correlation between quark and lepton for $c \to \ell^+$ decays than for $b \to \ell^-$ decays):

$$\begin{aligned} p^{34}_{\mathrm{F,B}} &= \tfrac{1}{4}(1 \mp A^{\mathrm{c}}_{\mathrm{FB}} Y) \;, \\ p^{34}_{\mathrm{S}} &= \tfrac{1}{2} \;. \end{aligned} \tag{5.25}$$

Source 44: double background: All the signs have random distribution. In this case 50 % of the events have two leptons with the same sign. The other events have opposite sign. In this case half of the events are forward and the other half are backward:

$$\begin{aligned} p^{44}_{\mathrm{F,B}} &= \tfrac{1}{4} \;, \\ p^{44}_{\mathrm{S}} &= \tfrac{1}{2} \;. \end{aligned} \tag{5.26}$$

5.6 Testing the Maximum Likelihood Fit

The likelihood function $\mathcal{L}$ combines four different types of quantities with the appropriate probability densities:

1. the observables $A^{\mathrm{b}}_{\mathrm{FB}}$, $A^{\mathrm{c}}_{\mathrm{FB}}$ and $\overline{\chi}$ (fit parameters),
2. the fractions f_i, f_{ij}, and the normalised NETb $\times$ NETc distributions, taken from the Monte Carlo simulation,
3. a model for the differential cross-section which allows the combination of the bin asymmetries to the total forward-backward asymmetry,
4. the number n_{F} and n_{B} of forward and backward events as a function of NETb, NETc and $|y|$ and the number of same and opposite sign two lepton events, both measured in the data.

The estimates for the observables are functions of the model parameters (2) and the quantities measured in the data (4). The variation of the results due to uncertainties of the model parameters is discussed in the systematic error section. Limited numbers of events in the data sample also introduce a statistical error on the measurement. Since the likelihood function does not need to be symmetric about the maximum with respect to a specific observable (fit parameter) the statistical uncertainties might result to be asymmetric. This asymmetry can cause a bias in the estimate of the observables, because the estimate is more likely to tend into the direction where the likelihood function has smaller slope (larger statistical error). Logical errors in the construction of the likelihood function or mistakes introduced by the technical realization of the fit can also be sources of biased results.

In order to maximise the likelihood function $\mathcal{L}$, a software program is developed to find the global minimum of $-\log \mathcal{L}$. The minimum is searched for by a multi-parameter fit using the `MINUIT` [126] package. To allow for a separate test of the fit the whole analysis is divided into two independent modules:

- The first module produces the normalised NETb $\times$ NETc distributions separately for the different b and c decays and for the background fraction for the y bins using a full detector Monte Carlo. In addition the fractions f_i and f_{ij} are calculated.

  This module also extracts the total bin forward-backward asymmetries for the NETb, NETc and $|y|$ bins from the data. For test purposes these bin asymmetries can also be extracted from Monte Carlo simulation.

- The fit is encoded in a second module, taking the normalised NETb $\times$ NETc distributions and the fractions f_i and f_{ij} from the Monte Carlo simulation and the bin forward-backward asymmetries from the data as inputs.

To search for biases of the fit parameters, a large number of fits (Monte Carlo experiments) is performed on simulated data where the forward-backward asymmetries and the B mixing parameter is known. In order to obtain the correct biases the fits on the simulated data must be made with the same number of events than used for the measurement. About 10^4 Monte Carlo experiments are needed to reach a precision of 2.5 % of the statistical uncertainty of the fit to the data. To investigate the independence of the fit on the specific values of the fit parameters, different combinations of $A_{\mathrm{FB}}^{\mathrm{b}}$, $A_{\mathrm{FB}}^{\mathrm{c}}$ and $\overline{\chi}$ are used. If ten values for each of the three fit parameters are taken, $10^3 \cdot 10^4$ experiments have to be performed. Each experiment has to be done with $4 \cdot 10^6$ multihadronic events, leading to a total need of $4 \cdot 10^{13}$ Monte Carlo events (including detector simulation). With a modern 3.0 GHz processor it takes about ten seconds to generate a LEP1 five flavour event together with a full detector simulation and event reconstruction to get DST level information. Processing all $4 \cdot 10^{13}$ events in one year a total of 1 270 000 CPUs is required and the output will fill about 400 000 200 Gb hard disks. Fortunately, it is not necessary to produce such a huge number of fully simulated events, because the fit takes its information extracted from the data only from the NETb $\times$ NETc distributions of the forward and backward events for different bins in $|y|$. So, it is sufficient to generate those distributions rather than all events required to produce the distributions. Of course the shape of the distributions has to be known with high precision and varied according to the statistical uncertainty. For this purpose a *toy Monte Carlo generator* is developed.

5.6.1 The Toy Monte Carlo Generator

The behaviour of the fit results together with the statistical uncertainties has to be studied as a function of:

- the number n_{mhd} of multihadronic events,
- the b and c quark forward-backward asymmetries $A_{\mathrm{FB}}^{\mathrm{b}}$ and $A_{\mathrm{FB}}^{\mathrm{c}}$,
- the B mixing parameter $\overline{\chi}$, and
- the background fraction for the electron and muon candidates.

Therefore the toy Monte Carlo generator must allow for producing its output as a function of these parameters. In addition the generator needs the following constants as input:

- the total number of lepton candidates for a given number of multihadronic events,
- the relative contribution of electrons and muons to the one lepton events and the contribution of electron-electron, electron-muon and muon-muon events to the two lepton events,
- the composition of the lepton candidates after the lepton selection given by the four fractions f_i of the different decay channels (separately for electrons and muons),
- the composition of the two lepton sample after the lepton selection and the reduction of non-b background and cascade decays with a cut on the output of NETb (eight fractions f_{ij}), and
- the normalised NETb $\times$ NETc distributions for the different $|y|$ bins separately for electrons and muons.

To ensure that these constants are very close to reality they are taken from multihadronic events from a Monte Carlo with full detector simulation. These events are treated the same way as the data events (reconstruction of detector response, cuts for event selection and lepton identification).

The total number of lepton candidates n_ℓ is not set to a fix value for the different experiments but is assumed to have a statistical error of $\sigma(n_\ell) = \pm\sqrt{(n_\ell)}$. Due to the large number of lepton candidates, this uncertainty can be supposed to be symmetric about n_ℓ and the shape is well approximated by a Gaussian function with width $2\sigma(n_\ell)$. Using a random number the total number of lepton candidates is determined separately for each toy experiment. The probability of a lepton candidate to originate from a two lepton event is $n_{\rm dilep}/n_\ell$ ($n_{\rm dilep}$ is the number of leptons from a dilepton event). The statistical uncertainty of the number of dilepton candidates is correlated to the total number of lepton candidates n_ℓ:

$$\sigma(n_{\rm dilep}) = \pm\sqrt{n_\ell \cdot \frac{n_{\rm dilep}}{n_\ell} \cdot \left(1 - \frac{n_{\rm dilep}}{n_\ell}\right)} \,. \tag{5.27}$$

Due to the rather large number of dilepton candidates this error is assumed to be symmetric and Gaussian-shaped with width $\sigma(n_{\rm dilep})$. The number of dilepton candidates is also determined separately for each toy Monte Carlo experiment using random numbers.

The number of electrons and muons in the one and two lepton samples taken from the full Monte Carlo are used to get the probabilities for an electron or muon event ($p_{\rm e}$ and p_μ) for the one lepton events or the probability for an electron-electron (e,e), electron-muon (e,μ), and muon-muon (μ,μ) event ($p_{\rm e,e}$, $p_{\rm e,\mu}$ and $p_{\mu,\mu}$) of the two lepton events. Looping over all one and two lepton events, random numbers with uniform distribution decide according to these probabilities of which kind (electron or muon event for one lepton events, (e,e), (e,μ) or (μ,μ) for dilepton events) the event should be.

In a subsequent random decision, each lepton candidate is assigned to either a one or a two lepton decay channel. The fractions f_i and f_{ij} taken from the full Monte Carlo are used as probabilities.

After the determination of the lepton flavour and the decay channel, the decision whether the event is a forward or a backward event is done. To enable cutting on $|\cos\theta_{\rm T}|$ or even implementing a detection efficiency for the lepton candidates as a function of $|\cos\theta_{\rm T}|$, the differential cross-section (see Eq. 2.23)

$$\frac{{\rm d}\sigma}{{\rm d}\cos\theta} = 1 + \cos^2\theta + \frac{8}{3} A^i_{\rm FB}\cos\theta \tag{5.28}$$

is used with the appropriate asymmetries $A^i_{\rm FB}$ as listed in Eq. 5.13. The quark level forward-backward asymmetries and the B mixing parameter are given as input parameters to the toy Monte Carlo generator. The four equations for the differential cross-section are normalised and used as probability densities for a random number generation in the interval $[-1, 1]$ [6]. The generated random

[6] The range of generated random numbers used to determine the value of y could be changed to any interval symmetric about 0 and smaller or equal $[-1, 1]$.

number with the appropriate differential cross-section is taken as the value of y for each one lepton event. The events are grouped into ten forward and ten backward bins according to their value for y. The corresponding normalised NETb $\times$ NETc distribution for each $|y|$ bin of the lepton candidates of channel $i = 1, 2, 3, 4$ is used as a two dimensional probability density to generate simultaneously two random numbers to assign a NETb and a NETc value to the event.

Now all necessary quantities for a one lepton event are determined and stored in a three dimensional histogram in NETb, NETc and y which can be used by the fit to determine the total bin forward-backward asymmetry for each NETb, NETc and y bin.

The B mixing parameter $\overline{\chi}$ determines the number of two lepton events where both leptons have the same or opposite charge. The appropriate probabilities for the eight different sources ij can be derived from the probabilities $p^{ij}_{\mathrm{F,B}}$ and p^{ij}_{S} introduced in Section 5.5.2. Only events with opposite charged leptons where mixing has occurred either on both sides or not at all can have a asymmetric y distribution. This is the case for source 11, 22 and 33. Source 12 has only opposite charged leptons if one of the primary b quarks has mixed (see Section 5.5.2). Since it is not measurable which of the quarks has mixed, the y distribution for type 12 dilepton events is symmetric. The y values for the three remaining asymmetric two lepton events is a sum of the asymmetric contribution from the appropriate event with two opposite charged leptons and the symmetric contribution from the events with two leptons with the same charge. The y of the opposite charged two lepton events is generated with the appropriate differential cross-section from the single lepton events with type 1, 2 or 3.

The y distribution for the two lepton events is given by the corresponding distributions for the eight different sources. There are two distributions, one for the two lepton events with two opposite charged leptons. This distribution is used in the fit to measure the b and c forward-backward asymmetries. The symmetric distribution of the events with two equally charged leptons is not needed in the fit.

Even though the toy Monte Carlo generator seems to be rather simple each toy Monte Carlo experiment already relies on a large quantity of random numbers. It is crucial that the random number generator is of high quality so that it is ensured that the results are not influenced by an artifact of the generator. For that reason RANLUX [129,130] is used with the highest luxury level (4). Tests of the RANLUX generator can be found in [131] and in the references given there.

5.6.2 Biases of the Fit

The toy Monte Carlo generator is used to produce 10^4 sets of pseudo data for each combination of the five fit parameters ($A_{\mathrm{FB}}^{\mathrm{b}}$, $A_{\mathrm{FB}}^{\mathrm{c}}$, $\overline{\chi}$ and the electron and muon background fractions). According to these samples it is found, that the generated parameters follow a Gaussian distribution about their mean which is in good agreement with the input values given to the generator. Each set of pseudo data is fed into the fit procedure to determine the asymmetries, the mixing parameter, and the overall background fractions. The fractions f_i, f_{ij} and the NETb $\times$ NETc reference distributions are identical for all fits. After a pseudo experiment, the input value to the toy Monte Carlo generator and the fit result together with its statistical uncertainty of a specific quantity are used to calculate the pull p of the individual result. For the forward-backward asymmetry the pull is

$$\mathrm{p} = \frac{A_{\mathrm{FB}}^{\mathrm{measurement}} - A_{\mathrm{FB}}^{\mathrm{input}}}{\sigma(A_{\mathrm{FB}}^{\mathrm{measurement}})} \,. \tag{5.29}$$

All results of the pseudo experiments with identical parameter combination are used to produce pull distributions. In Figure 5.12 distributions of the fitted values together with their statistical errors are shown for 10^4 pseudo experiments. The chosen input parameters are very close to the results obtained from the OPAL data. The fitted values and their errors form Gaussian-shaped distributions. In addition, the figure shows the pull distribution calculated with these results. Using a maximum likelihood fit, a Gaussian function is fitted to each pull distribution in order to extract the mean $\bar{\mathrm{p}}$ and the width σ_{p} of the distributions. The fitted means and widths are in very good agreement with the means and the spreads of the distributions. The spread of the distribution, showing the statistical uncertainty of the fit is mainly due to the variation of the total number of one and two lepton events during the event generation.

Concerning $A_{\mathrm{FB}}^{\mathrm{b}}$ and $A_{\mathrm{FB}}^{\mathrm{c}}$, the means of the pull distributions $\bar{\mathrm{p}}(A_{\mathrm{FB}}^{\mathrm{b}})$ and $\bar{\mathrm{p}}(A_{\mathrm{FB}}^{\mathrm{c}})$ slightly tend to positive values, indicating fit results which are a little bit too large. For the B mixing parameter $\overline{\chi}$, $\bar{\mathrm{p}}(\overline{\chi})$ is displaced towards negative values, caused by a small negative bias of the fit results. The widths σ_{p} of the pull distributions are in all three cases compatible to unity as expected.

Ten different values for each of the three parameters

$$\begin{array}{lcllll}
A_{\mathrm{FB}}^{\mathrm{b}} & = & 5\,\%, & 6\,\%, & \cdots & 14\,\% \\
A_{\mathrm{FB}}^{\mathrm{c}} & = & 2\,\%, & 3\,\%, & \cdots & 11\,\% \\
\overline{\chi} & = & 8\,\%, & 9\,\%, & \cdots & 17\,\%
\end{array}$$

are used for a systematic search for biases, leading to 10^3 tests. The results of these tests are summarised in Figure 5.13-5.15. The two different kinds of

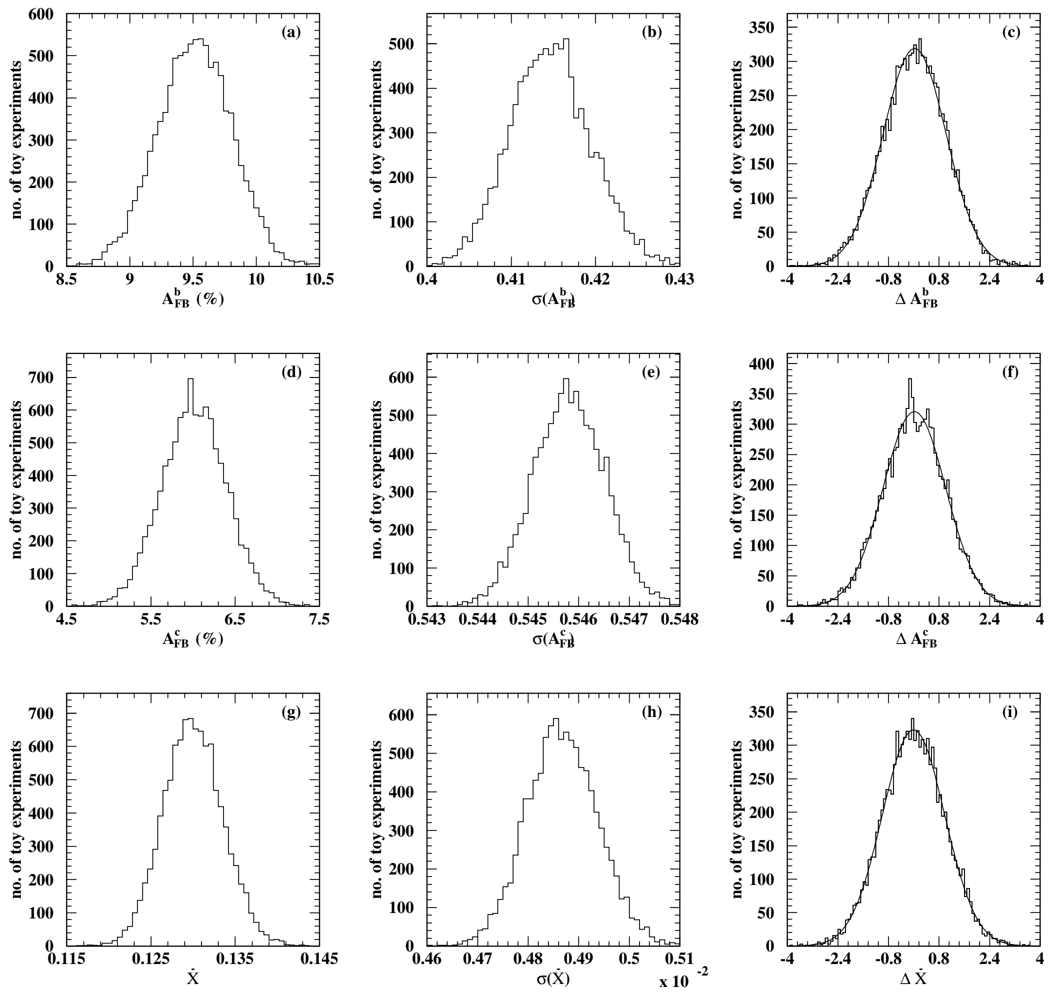

Figure 5.12: Distributions of the fit results for the forward-backward asymmetries $A_{\mathrm{FB}}^{\mathrm{b}}$ (a) and $A_{\mathrm{FB}}^{\mathrm{c}}$ (d), as well as the B mixing parameter $\overline{\chi}$ (g) are shown for 10^4 toy Monte Carlo experiments. As input values to the generator $A_{\mathrm{FB}}^{\mathrm{b}} = 9.5$ %, $A_{\mathrm{FB}}^{\mathrm{c}} = 6.0$ % and $\overline{\chi} = 13.0$ % are used. The values are very close to the results obtained from the OPAL measurement. Plots (b), (e), and (h) show the corresponding distributions of the statistical errors. The three plots on the right side show the pull distributions together with the Gaussian function fitted to them using a likelihood fit.

plots show the behaviour of the fit parameters and the modelling of their statistical uncertainties as a function of $A_{\mathrm{FB}}^{\mathrm{b}}$ (Figure 5.13), $A_{\mathrm{FB}}^{\mathrm{c}}$ (Figure 5.14) and $\overline{\chi}$ (Figure 5.15). Each dot shows either $\bar{\mathrm{p}}$ or σ_{p} produced with 10^4 pseudo experiments with identical input parameters. The given errors originate from the finite number of toy experiments.

There is no visible dependence of the means and widths of the pull distributions on the asymmetries and the mixing parameter. The widths of the pull distributions shown in the three figures are distributed statistically about one as expected. Concerning the means, the situation is not so simple. The fit results for $A_{\mathrm{FB}}^{\mathrm{b}}$ are always too large because the average of all $\bar{\mathrm{p}}(A_{\mathrm{FB}}^{\mathrm{b}})$ is shifted from 0 to $+0.020 \pm 0.002$. For $A_{\mathrm{FB}}^{\mathrm{c}}$ the average of all $\bar{\mathrm{p}}(A_{\mathrm{FB}}^{\mathrm{c}})$ is at $+0.007 \pm 0.002$ and for the mixing parameter $\overline{\chi}$ at -0.004 ± 0.002. The shifts of the three parameters are calculated using the corresponding ten values for $\bar{\mathrm{p}}$, shown in Figure 5.13-5.15. The magnitude of these shifts does not change if all 10^3 pull distributions of the $10 \times 10 \times 10$ variations are taken into account. Even though the estimates for the three fit parameters seem to have a significant bias the size of the bias is very small compared to the statistical and also systematic uncertainty of the measurement using real OPAL data. All biases quoted above are given as fraction of the statistical error of the fit (definition of pull). Furthermore, bias tests have been performed for different values for the background fraction concerning the lepton candidates, showing identical results.

Constant behaviour of the normalised statistical errors of the fit as a function of the asymmetries and the mixing parameter is found. For the b asymmetry the size of the statistical error depends on both, the absolute value of the b forward-backward asymmetry and the value of the B mixing parameter because of the correlation between both quantities originating from the factor $(1 - 2\overline{\chi})$ between the observed asymmetry and the quark level b forward-backward asymmetry. This correlation is of the order of 0.3 and is caused by the method of the measurement. In addition the statistical uncertainties scale correctly with the used number of multihadronic events. The correlations between the b and c forward-backward asymmetries – semileptonic b and c decays cannot be separated totally – is almost independent of the values for $A_{\mathrm{FB}}^{\mathrm{b}}$ and $A_{\mathrm{FB}}^{\mathrm{c}}$.

5.7 Results

The data are divided into three separate energy bins. Their mean energies are shown in Table 5.1. The asymmetries are fitted simultaneously at all energy points, the overall likelihood being the product of the likelihood in Eq. 5.8 for each point. Therefore, the fit has nine free parameters: the forward-backward asymmetries $A_{\mathrm{FB}}^{\mathrm{b}}$ and $A_{\mathrm{FB}}^{\mathrm{c}}$ at three energy points, together with values common

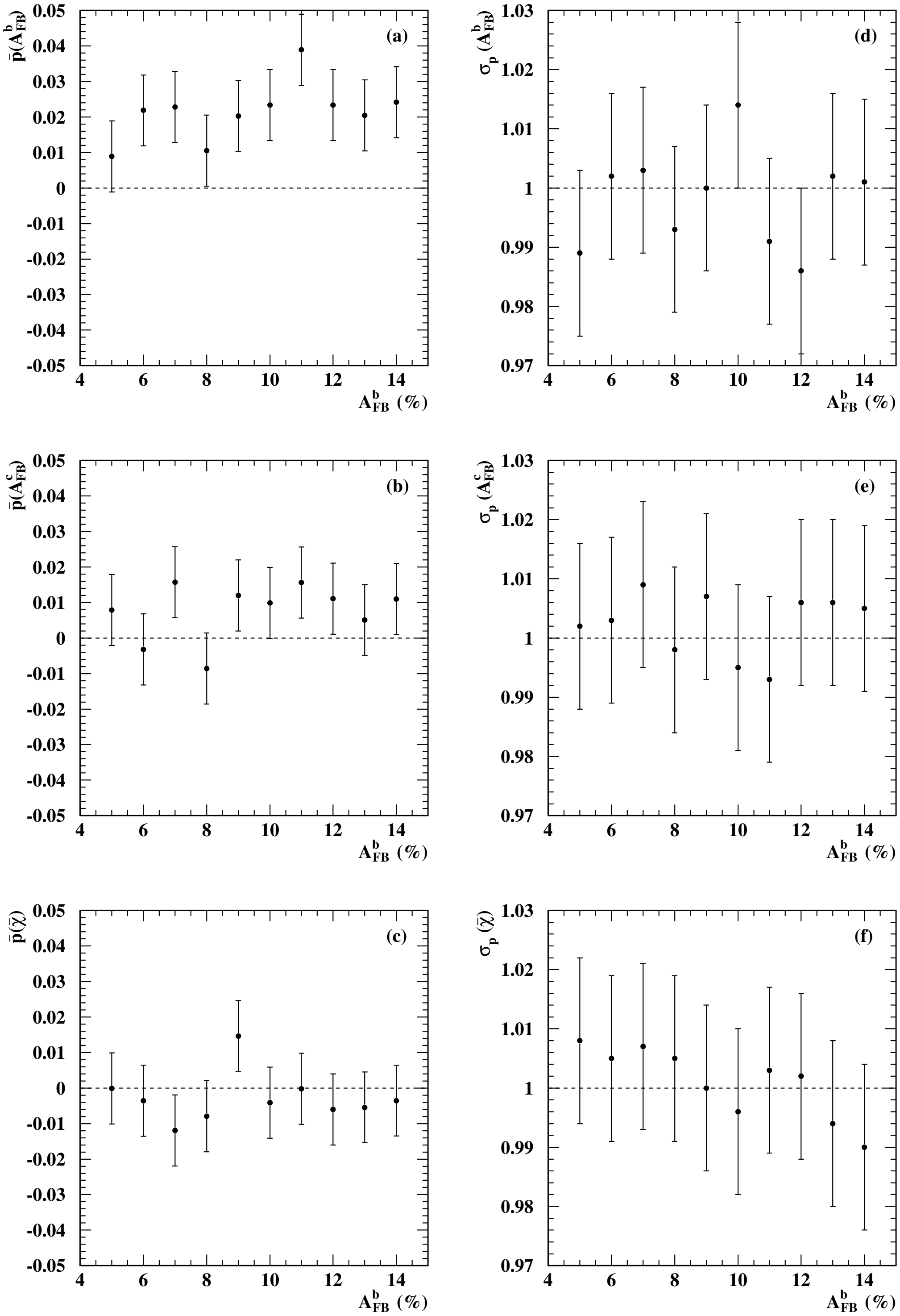

Figure 5.13: Mean $\bar{\mathrm{p}}$ and width σ_{p} of the pull distributions of $A_{\mathrm{FB}}^{\mathrm{b}}$, $A_{\mathrm{FB}}^{\mathrm{c}}$ and $\overline{\chi}$ as a function of $A_{\mathrm{FB}}^{\mathrm{b}}$. The errors given are the statistical precision of the means and widths limited by the number of pseudo experiments.

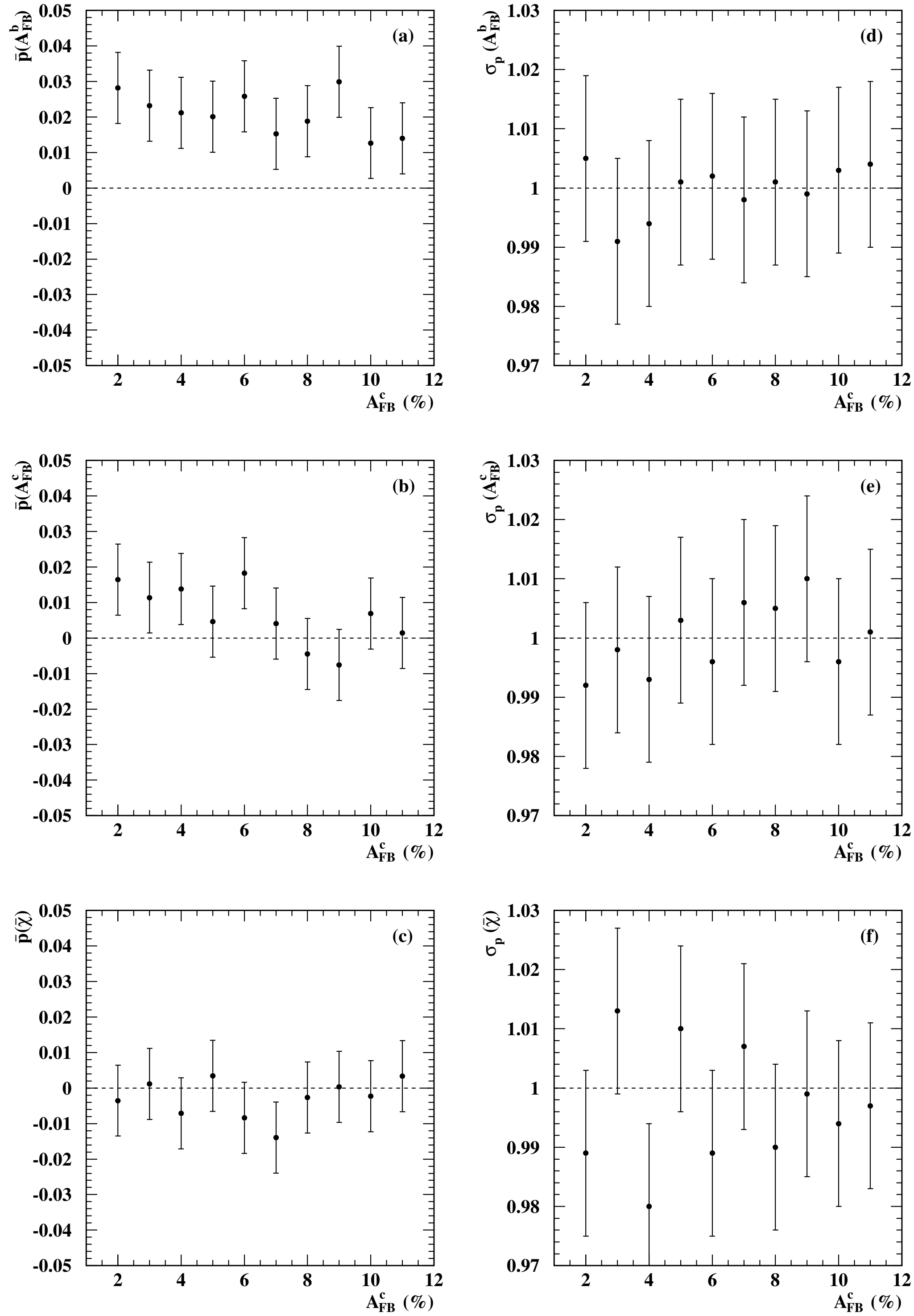

Figure 5.14: Mean $\bar{\mathrm{p}}$ and width σ_{p} of the pull distributions of $A_{\mathrm{FB}}^{\mathrm{b}}$, $A_{\mathrm{FB}}^{\mathrm{c}}$ and $\overline{\chi}$ as a function of $A_{\mathrm{FB}}^{\mathrm{c}}$. The errors given are the statistical precision of the means and widths limited by the number of pseudo experiments.

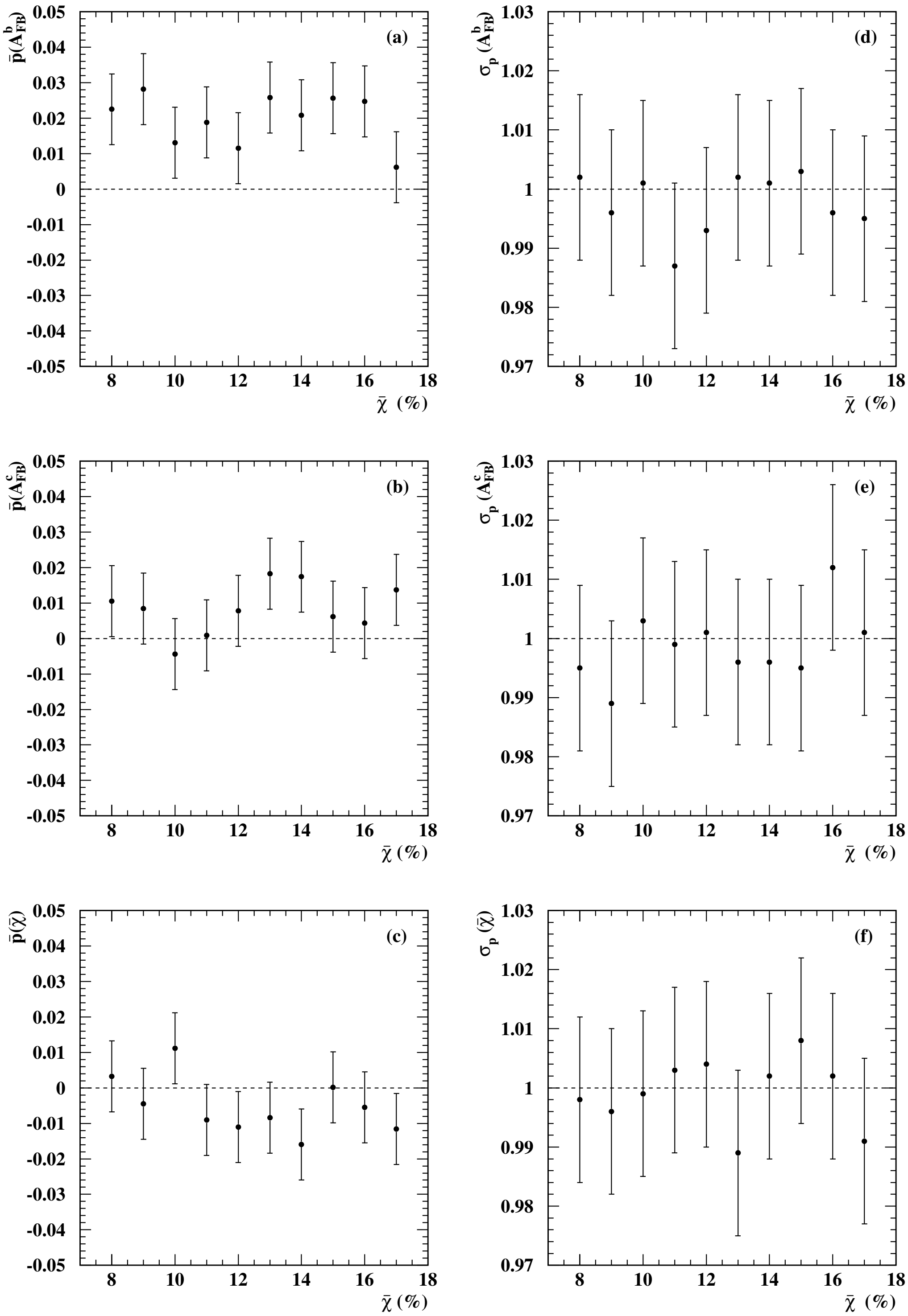

Figure 5.15: Mean $\bar{\mathrm{p}}$ and width σ_{p} of the pull distributions of $A_{\mathrm{FB}}^{\mathrm{b}}$, $A_{\mathrm{FB}}^{\mathrm{c}}$ and $\overline{\chi}$ as a function of $\overline{\chi}$. The errors given are the statistical precision of the means and widths limited by the number of pseudo experiments.

to all three energy points for the B mixing parameter $\overline{\chi}$, and the electron and muon background fractions f_4'. Data from all years are fitted simultaneously with the various fractions and NETb$\times$NETc distributions, determined from an appropriate mix of Monte Carlo events with different simulated detector configurations, taking into account the changes in the performance of the OPAL detector over time. A small bias correction is applied to the fitted asymmetries to correct for the effects of gluon radiation from the primary quark pair and the approximation of the original quark direction by the experimentally measured thrust axis [96]. This correction also accounts for any residual biases in the fit.

After correcting for all biases, the results are:

$$\begin{array}{ll}
A_{\mathrm{FB}}^{\mathrm{b}} = (\ 4.7\ \pm 1.8\ \pm 0.1\ )\,\%, & A_{\mathrm{FB}}^{\mathrm{c}} = (-6.8\ \pm 2.5\ \pm 0.9\ )\,\%, \text{ at } \langle\sqrt{s}\rangle = 89.51 \text{ GeV}, \\
A_{\mathrm{FB}}^{\mathrm{b}} = (\ 9.72 \pm 0.42 \pm 0.15)\,\%, & A_{\mathrm{FB}}^{\mathrm{c}} = (\ \ 5.68 \pm 0.54 \pm 0.39)\,\%, \text{ at } \langle\sqrt{s}\rangle = 91.25 \text{ GeV}, \\
A_{\mathrm{FB}}^{\mathrm{b}} = (10.3\ \pm 1.5\ \pm 0.2\ )\,\%, & A_{\mathrm{FB}}^{\mathrm{c}} = (\ 14.6\ \pm 2.0\ \pm 0.8\ )\,\%, \text{ at } \langle\sqrt{s}\rangle = 92.95 \text{ GeV}.
\end{array}$$

For the average B mixing parameter, a value of:

$$\overline{\chi} = (13.12 \pm 0.49 \pm 0.42)\,\%$$

is obtained. The first error is always the statistical and the second the systematic uncertainty. The evaluation of the systematic errors is described in Section 5.9. The statistical correlations between the results are given in Table 5.9. Compared to the measurement using D mesons [77], the correlations between the b and c forward-backward asymmetries is much smaller here (see end of Section 4.2). The background levels in the electron and muon samples are fitted to be $(89.4 \pm 0.6)\,\%$ and $(94.4 \pm 0.3)\,\%$ of the rates estimated from Monte Carlo simulation, where the quoted errors are statistical only. These values are consistent with the known uncertainties in modelling the lepton background levels [86, 109, 112, 113].

The result of the fit is illustrated in Figure 5.16. For this plot, two regions of the NETb $\times$ NETc plane are selected, one 93 % pure in $\mathrm{b} \to \ell^-$ events and the other 59 % pure in $\mathrm{c} \to \ell^+$ events. The total charge forward-backward asymmetry observed in the data in bins of $|y|$ together with the expected values according to Eq. 5.11 are shown. Using only events from those two regions, the b and c forward-backward asymmetries are found to be:

$$A_{\mathrm{FB}}^{\mathrm{b}} = (9.3 \pm 0.5)\ \%, \tag{5.30}$$
$$A_{\mathrm{FB}}^{\mathrm{c}} = (5.4 \pm 0.8)\ \%. \tag{5.31}$$

The given errors are just the statistical uncertainties. This simple method does not allow the calculation of both asymmetries simultaneously. In order to calculate one of the asymmetries in the appropriate b or c enriched region the other asymmetry is set to its Standard Model expectation at 91.25 GeV ($A_{\mathrm{FB}}^{\mathrm{b}} = 9.6$ %,

peak	$A_{\mathrm{FB}}^{\mathrm{b}}$	$A_{\mathrm{FB}}^{\mathrm{c}}$	$\overline{\chi}$
$A_{\mathrm{FB}}^{\mathrm{b}}$	1.00	0.17	0.30
$A_{\mathrm{FB}}^{\mathrm{c}}$		1.00	0.01
$\overline{\chi}$			1.00

peak−2	$A_{\mathrm{FB}}^{\mathrm{b}}$	$A_{\mathrm{FB}}^{\mathrm{c}}$	$\overline{\chi}$
$A_{\mathrm{FB}}^{\mathrm{b}}$	1.00	0.18	0.03
$A_{\mathrm{FB}}^{\mathrm{c}}$		1.00	0.00
$\overline{\chi}$			1.00

peak+2	$A_{\mathrm{FB}}^{\mathrm{b}}$	$A_{\mathrm{FB}}^{\mathrm{c}}$	$\overline{\chi}$
$A_{\mathrm{FB}}^{\mathrm{b}}$	1.00	0.17	0.10
$A_{\mathrm{FB}}^{\mathrm{c}}$		1.00	0.00
$\overline{\chi}$			1.00

Table 5.9: Statistical correlation matrices at each centre-of-mass energy using the entire (1990–2000) data sample. The correlations with the fitted background fractions are negligibly small (< 0.01) and are not given here.

$A_{\mathrm{FB}}^{\mathrm{c}} = 6.3$ %) as predicted by ZFITTER [34]. The background is assumed to be symmetric. The values are in good agreement with the results from the full fit. It can be seen from the plots, that the sign of the observed forward-backward asymmetry is clearly different in the two regions.

5.8 QCD and Bias Correction

The expression for the differential cross-section (Eq. 2.23) used to derive the differential forward-backward asymmetry (Eq. 5.5-5.7), which is the basis for the likelihood function (Eq. 5.8, 5.9 and 5.17) used for this measurement, is only valid for the pure $\mathrm{e^+e^-} \rightarrow \mathrm{Z} \rightarrow \mathrm{q\overline{q}}$ process [96]. To account for the modification of the differential cross-section induced by gluon radiation in the final state, the expression for the differential cross-section (Eq. 5.5) can be rewritten as [96]:

$$\frac{\mathrm{d}\,\sigma_{\mathrm{q}}}{\mathrm{d}\,\cos\theta} \propto 1 + \cos^2\theta + \frac{6+2a}{3} A_{\mathrm{FB}}^{\mathrm{q}} \ \cos\theta \ . \tag{5.32}$$

This change implies a relation between the determination of the forward-backward asymmetry with ($A_{\mathrm{FB}}^{\mathrm{q,\ QCD}}$) and without ($A_{\mathrm{FB}}^{0,\mathrm{q}}$) considering gluon emission:

$$A_{\mathrm{FB}}^{\mathrm{q,\ QCD}} = (1 - C_{\mathrm{QCD}})\, A_{\mathrm{FB}}^{0,\mathrm{q}} \ . \tag{5.33}$$

Estimates of QCD corrections C_{QCD} to heavy quark forward-backward asymmetries have been computed in perturbative QCD at a fixed order in α_{s} by several authors [35,91–95]. In Reference [92] first order QCD corrections are given where the direction of the thrust is used, calculated using all final state partons. The translation from the parton level to the hadron level thrust axis (defined using all

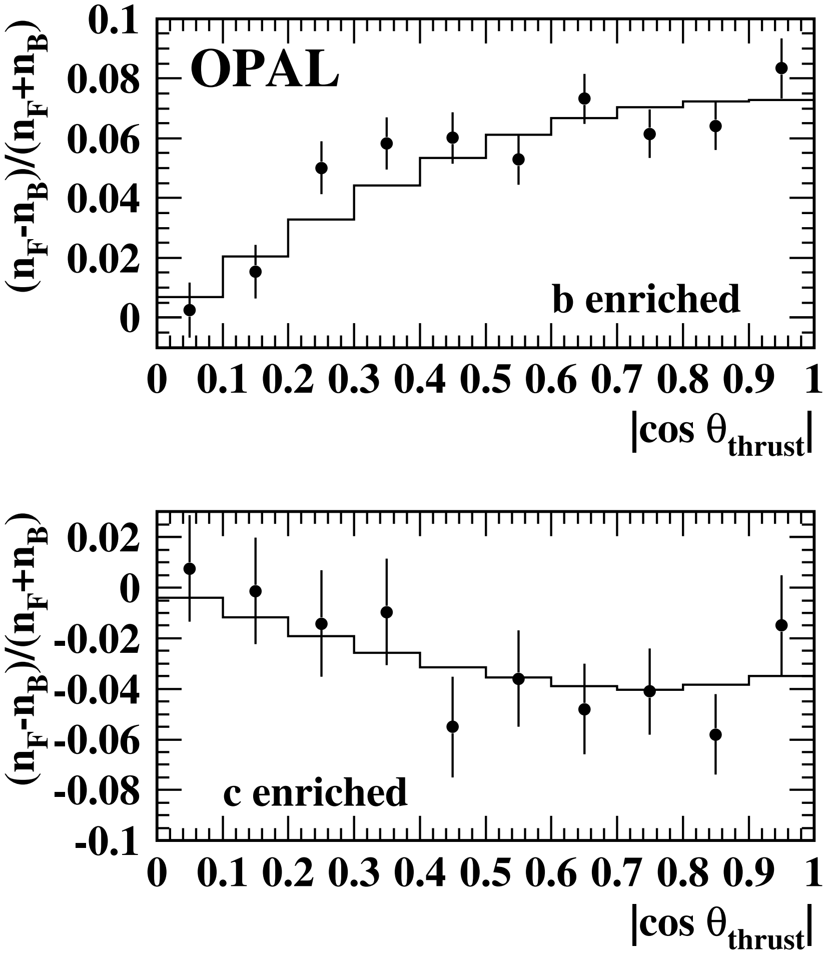

Figure 5.16: An illustration of the fit results for (a) a b enriched region and (b) a c enriched region of NETb $\times$ NETc space. The asymmetry observed in the data (dots) in each bin of $|y|$ is compared with the expectation calculated from the full fit (horizontal lines). The errors are purely statistical.

final state particles without detector effects) has been determined using Monte Carlo hadronisation models [96, 97].

A calculation at first order QCD of the shape coefficient a has been performed [132]. They show that a changes significantly, when going from the quark to the thrust direction (using partons only), while changes of the quark mass and/or flavour induce much smaller effects [96]. The impact of the shape coefficient a on the determination of the forward-backward asymmetries is closely related to the technique used to analyse the data. To scale the QCD corrections C_{QCD} with the experimental sensitivity to QCD effects of the various measurements, a bias factor, s_{q}, is introduced [96, 97]:

$$A_{\mathrm{FB}}^{\mathrm{q}} = (1 - s_{\mathrm{q}} \cdot C_{\mathrm{QCD}})\, A_{\mathrm{FB}}^{0,\,\mathrm{q}} = (1 - c_{\mathrm{q}})\, A_{\mathrm{FB}}^{0,\,\mathrm{q}} \tag{5.34}$$

Three main effects are known why s_{q} is different from one:

Analysis cuts: If a selection criterion is sensitive to the event topology, then a ranking of events by their strength of the gluon emission is done, modifying the size of the QCD correction. For example in events containing high momentum heavy hadrons there is a reduced phase space for gluon radiation compared to all events. In the analysis presented here, the lepton momentum is strongly correlated with the momentum of the heavy hadron where it came from. Increasing the cut on the lepton momentum will decrease the size of the QCD corrections significantly. The lepton identification uses a momentum cut of 2 GeV/c, rejecting a large fraction of events with hard gluon emission.

Fitting method: The forward-backward asymmetries are extracted via a fit to the event polar angle distribution (Eq. 5.5), with the shape parameter a set to one. This influences the measured values for the asymmetries. As a consequence the QCD corrections needed to come to the true quark level asymmetries are changed.

Event axis reconstruction: Due to particles like neutrinos, which cannot be detected as well as the limitations in acceptance and resolution of the detectors, the reconstructed thrust axis differs from the thrust axis determined with all final state particles.

The size of the QCD correction is evaluated individually for this analysis by comparing the asymmetries fitted on a large sample of Monte Carlo simulated events with the true quark level asymmetries of the Monte Carlo sample.

To determine the true quark level forward-backward asymmetries, the same JETSET 7.4 [37, 73] Monte Carlo generator program which is taken to generate the physics events for the full OPAL detector-level Monte Carlo is used to generate $7.5 \cdot 10^7$ events. The true b and c quark forward-backward asymmetries are calculated with these events with Eq. 2.28. After that the analysis is performed on a large sample of full detector-level Monte Carlo events. To increase the sensitivity of the test, the hadron level thrust axis QCD corrections in the Monte Carlo are scaled to their maximal theoretical values [52]. Since the statistical error of the forward-backward asymmetry measurement only weakly depends on the actual value of the asymmetry, this can be done by artificially increasing the values of the forward-backward asymmetries in the Monte Carlo. The asymmetries are multiplied by a factor of seven, bringing them close to their maximal value of $A_{\mathrm{FB}}^{\mathrm{max}} = 75\ \%$.

This method not only determines the shifts in the results due to QCD effects but also accounts for any kind of bias. This adds another term to the correction factor:

$$A_{\mathrm{FB}}^{\mathrm{q}} = (1 - c_{\mathrm{q}} - c_{\mathrm{bias}})\, A_{\mathrm{FB}}^{0,\mathrm{q}} \tag{5.35}$$

Combining all effects, the raw fitted asymmetries $A_{\mathrm{FB}}^{\mathrm{q}}$ are scaled by factors of

$$\frac{1}{1 - c_{\mathrm{q}} - c_{\mathrm{bias}}} = \begin{cases} 1.0050 \pm 0.0063 \pm 0.0050 & \text{for b-quarks} \\ 1.0117 \pm 0.0063 \pm 0.0062 & \text{for c-quarks} \end{cases} \tag{5.36}$$

to determine the quark level results $A_{\mathrm{FB}}^{0,\mathrm{q}}$, where the first errors result from theoretical uncertainties [52, 96] and the second from limited Monte Carlo statistics.

5.9 Evaluation of the Systematic Uncertainties

In this section, the evaluation of the systematic errors for the analyses of the forward-backward asymmetries and the B mixing parameter presented here are discussed. Uncertainties of any kind are studied by propagating variations of external input parameters or other assumptions through the whole analysis chain. The variations of the measured quantities are then taken as the estimates of the systematic uncertainties.

Systematic uncertainties result from a number of sources, including modelling of b and c hadron production and decay (Section 5.9.1), external branching ratio inputs (Section 5.9.2), background uncertainties (Section 5.9.3), and the performance of the OPAL detector (Section 5.9.4). Where errors are only assessed by a variation in one direction, for example to an alternative model or when slightly asymmetric errors are assessed, the larger deviation is taken as 1σ. The systematic errors are summarised in Tables 5.10 and 5.11 and discussed in more detail below. The signs of the errors indicate the direction of change in the result when the corresponding quantity is varied.

	$A^{\mathrm{b}}_{\mathrm{FB}}(\%)$	$A^{\mathrm{c}}_{\mathrm{FB}}(\%)$	$\overline{\chi}(\%)$
Fitted Value	9.716	5.683	13.121
Statistical error	±0.418	±0.542	±0.485
Systematic error	±0.150	±0.386	±0.421
Sources of systematic errors			
$\mathrm{b} \to \ell^-$ semileptonic decay model	±0.011	∓0.101	±0.175
$\mathrm{c} \to \ell^+$ semileptonic decay model	±0.064	∓0.036	∓0.286
$\langle x^{\mathrm{b}}_E \rangle$ ±0.008	∓0.012	∓0.008	∓0.074
$\langle x^{\mathrm{c}}_E \rangle$ ±0.008	±0.054	∓0.024	±0.010
Total models	0.085	0.110	0.344
$\mathrm{BR}(\mathrm{b} \to \ell^-)$ (10.65 ±0.23) %	∓0.020	±0.104	±0.120
$\mathrm{BR}(\mathrm{b} \to \mathrm{c} \to \ell^+)$ (8.08±0.18) %	∓0.006	∓0.050	∓0.105
$\mathrm{BR}(\mathrm{b} \to \overline{\mathrm{c}} \to \ell^-)$ (1.62±0.44) %	±0.011	±0.174	±0.014
$\mathrm{BR}(\mathrm{b} \to \tau^- \to \ell^-)$ (0.419±0.05) %	∓0.001	±0.028	±0.007
$\mathrm{BR}(\mathrm{c} \to \ell^+)$ (9.77±0.32) %	±0.028	∓0.151	±0.008
R_{b} (21.647±0.072) %	∓0.003	±0.009	0.000
R_{c} (16.83±0.47) %	±0.019	∓0.099	±0.002
Total branching ratios	0.041	0.277	0.161
e ID efficiency ± 4.1 %	∓0.005	∓0.007	±0.004
μ ID efficiency ± 3.0 %	∓0.002	∓0.021	±0.022
Conversions ±15 %	±0.001	±0.012	∓0.007
Muon background (K) ±30 %	±0.011	±0.023	∓0.034
Muon background (π) ±5 %	±0.004	±0.026	∓0.015
Muon background (other) ±100 %	±0.009	±0.017	∓0.058
Background asymmetry u,d,s events	±0.002	±0.102	±0.002
Background flavour separation	±0.020	±0.020	0.000
Total background effects	0.026	0.114	0.073
Correction of $\bar{\chi}$ for $\mathrm{b} \to \mathrm{c} \to \ell^+$	−0.008	−0.069	−0.068
$\cos\theta_{\mathrm{T}}$ dependence (fractions)	−0.018	+0.001	+0.000
Tracking resolution	−0.025	−0.046	−0.016
Flavour separation variables	±0.067	±0.163	±0.099
Time dependent mixing	+0.032	+0.098	−0.091
Monte Carlo statistics	±0.050	±0.041	±0.070
Charge reconstruction	±0.015	±0.004	0.000
LEP centre-of-mass energy	±0.010	±0.027	0.000
QCD correction	±0.061	±0.036	0.000
Total other systematics	0.114	0.216	0.167

Table 5.10: Results and breakdown of systematic uncertainties for the on-peak forward-backward asymmetries and the B mixing parameter $\overline{\chi}$. The total systematic uncertainty is the square root of the sum of the squared values from all different sources.

	Peak–2		**Peak+2**	
	$A^{\mathrm{b}}_{\mathrm{FB}}(\%)$	$A^{\mathrm{c}}_{\mathrm{FB}}(\%)$	$A^{\mathrm{b}}_{\mathrm{FB}}(\%)$	$A^{\mathrm{c}}_{\mathrm{FB}}(\%)$
Fitted Value	4.70	-6.83	10.31	14.59
Statistical error	±1.80	±2.52	±1.50	±2.04
Systematic error	±0.098	±0.928	±0.224	±0.837
Sources of systematic errors				
$\mathrm{b} \to \ell^-$ semileptonic decay model	±0.031	∓0.036	∓0.020	∓0.101
$\mathrm{c} \to \ell^+$ semileptonic decay model	∓0.019	±0.070	±0.106	∓0.108
$\langle x_E^{\mathrm{b}} \rangle$ ±0.008	∓0.008	∓0.037	∓0.019	∓0.034
$\langle x_E^{\mathrm{c}} \rangle$ ±0.008	∓0.013	±0.009	±0.090	∓0.051
Total models	0.039	0.088	0.142	0.160
BR($\mathrm{b} \to \ell^-$) (10.65 ±0.23) %	∓0.001	∓0.034	∓0.012	±0.198
BR($\mathrm{b} \to \mathrm{c} \to \ell^+$) (8.08±0.18) %	∓0.003	∓0.047	∓0.024	∓0.036
BR($\mathrm{b} \to \bar{\mathrm{c}} \to \ell^-$) (1.62±0.44) %	∓0.023	±0.024	±0.055	±0.250
BR($\mathrm{b} \to \tau^- \to \ell^-$) (0.419±0.05) %	∓0.003	∓0.002	∓0.002	±0.044
BR($\mathrm{c} \to \ell^+$) (9.77±0.32) %	±0.009	±0.161	±0.033	∓0.381
R_{b} (21.647±0.072) %	∓0.001	∓0.010	∓0.004	±0.023
R_{c} (16.83±0.47) %	±0.006	±0.106	±0.023	∓0.250
Total branching ratios	0.026	0.203	0.074	0.560
e ID efficiency ± 4.1 %	∓0.001	±0.005	∓0.007	∓0.019
μ ID efficiency ± 3.0 %	∓0.002	±0.030	∓0.002	∓0.049
Conversions ±15 %	±0.003	∓0.002	±0.003	±0.025
Muon background (K) ±30 %	±0.003	∓0.032	±0.010	±0.073
Muon background (π) ±5 %	±0.003	∓0.036	±0.005	±0.056
Muon background (other) ±100 %	±0.002	∓0.044	±0.009	±0.062
Background asymmetry u,d,s events	±0.018	±0.832	±0.006	±0.302
Background flavour separation	±0.020	±0.025	±0.010	±0.065
Total background effects	0.028	0.836	0.021	0.333
Correction of $\bar{\chi}$ for $\mathrm{b} \to \mathrm{c} \to \ell^+$	−0.000	−0.033	−0.027	−0.079
$\cos\theta_{\mathrm{T}}$ dependence (fractions)	+0.005	−0.024	−0.030	+0.001
Tracking resolution	−0.011	+0.261	−0.002	−0.215
Flavour separation variables	±0.029	±0.172	±0.097	±0.403
Time dependent mixing	−0.037	+ 0.036	+0.069	+0.112
Monte Carlo statistics	±0.058	±0.102	±0.064	±0.118
Charge reconstruction	±0.007	±0.005	±0.016	±0.010
LEP centre-of-mass energy	±0.007	±0.018	±0.003	±0.007
QCD correction	±0.030	±0.043	±0.062	±0.092
Total other systematics	0.082	0.337	0.155	0.500

Table 5.11: Results and breakdown of systematic uncertainties for the off-peak forward-backward asymmetries. The total systematic uncertainty is the square root of the sum of the squared values from all different sources.

Concerning the measurement and the systematic uncertainties quoted in the first two groups of the tables, the proposals of the LEP Heavy Flavour Electroweak Working Group are adopted [52] for the electroweak parameters (R_b, R_c, BR($\mathrm{b} \to \ell^-$), BR($\mathrm{c} \to \ell^+$), BR($\mathrm{b} \to \mathrm{c} \to \ell^+$), ..., $\langle x_E^\mathrm{b} \rangle$, and $\langle x_E^\mathrm{c} \rangle$) are used. These parameters enter in the NETb $\times$ NETc $\times$ $|y|$ reference distributions and in the fractions f_i and f_{ij} which are produced in order to perform the measurement. Variations of $\pm 1\sigma$ with respect to the LEP and SLD combined averages are included in the systematic error. The dependencies on the above parameters are not so much a systematic uncertainty, but provide valuable information for the LEP Electroweak Working Group when the combined fit is performed to the electroweak precision data in the heavy flavour sector [98] and correlations between the measured parameters have to be taken into account (see Section 6.1 and 6.3).

5.9.1 Modelling of b and c Production and Decay

Semileptonic Decay Models

A correct description of the lepton momentum spectra in the rest frame of decaying b and c hadrons is essential for the flavour separation. The semileptonic decays of heavy hadrons are described by the free-quark model of Altarelli *et al.* (ACCMM) [99]. The model has two free parameters:

- the Fermi momentum p_F and
- the mass of the quark produced in the decay of the heavy hadron (m_s or m_c).

These two free parameters are fixed to $p_\mathrm{F} = 298$ MeV/c and $m_\mathrm{c} = 1\,673$ MeV/c^2 for $\mathrm{b} \to \ell^-$ decays by a fit to CLEO data [100]. For $\mathrm{c} \to \ell^+$ decays $p_\mathrm{F} = 0.467$ GeV/c and $m_\mathrm{s} = 0.001$ GeV/c^2 are obtained from a combined measurements of DELCO [101] and MARK III [102].

For cascade decays $\mathrm{b} \to \mathrm{c} \to \ell^+$ and $\mathrm{b} \to \overline{\mathrm{c}} \to \ell^-$, the D momentum spectrum measured by CLEO [133] is combined with the $\mathrm{c} \to \ell^+$ model to generate the lepton momentum distribution. Uncertainties in this D momentum spectrum are negligible compared with the uncertainties in the $\mathrm{b} \to \ell^-$ and $\mathrm{c} \to \ell^+$ models.

Systematic uncertainties arising from the choice of the semileptonic decay model are treated differently for b and c hadron decays by varying either the model or its parameters:

- For $b \to \ell^-$ decays, the systematic uncertainties are assessed by reweighting the rest frame momentum spectrum according to the form-factor model of Isgur *et al.* [134], which has no free parameters (ISGW). This spectrum is harder than the central ACCMM model. As an alternative, the same model is used with the fraction of D^{**} mesons produced in b decays increased from 11 % to 32 % to give a better describtion of the CLEO data, denoted as ISGW**. This gives a softer spectrum than the default model.

  Although the weights to go from model to model are evaluated using only B^0 and B^+ meson decays, these weights are then applied to all b hadron decays.

- Variations in the $c \to \ell^+$ decay model are assessed by varying the free parameters of the ACCMM model to give harder or softer decay models, constrained by the DELCO and MARK III data. The results using the other models, denoted with ACCMM1 and ACCMM2, are compared to the results obtained with the ACCMM model using the central values:

$$\begin{array}{llll} \text{ACCMM:} & m_s = 0.001\ \text{GeV}/c^2 & \text{and} & p_F = 0.467\text{GeV}/c, \\ \text{ACCMM1:} & m_s = 0.001\ \text{GeV}/c^2 & \text{and} & p_F = 0.353\text{GeV}/c, \\ \text{ACCMM2:} & m_s = 0.153\ \text{GeV}/c^2 & \text{and} & p_F = 0.467\text{GeV}/c. \end{array}$$

For both $b \to \ell^-$ and $c \to \ell^+$ decays, the sign of the error assigned indicates the variation observed with the harder alternative spectrum.

Heavy Quark Fragmentation

The fragmentation of b and c quarks is described using phenomenological models tuned to experimental data. These models can be distinguished from each other by the shape of the predicted hadron energy distribution. The momentum spectra of leptons emitted in semileptonic decays in $b\bar{b}$ and $c\bar{c}$ events, depend on the energy distributions of the heavy hadrons. Hence, the modelling of the fragmentation process can influence the performance of the quark flavour separation resulting in a variation of the shape of the NETb $\times$ NETc distributions, leading to different values for the forward-backward asymmetries. The reference distributions and fractions used in the fit are produced with a Monte Carlo simulation using the fragmentation function of Peterson *et al.* [42]. The parameters controlling the shape of the fragmentation function are set to $\varepsilon_b = 38^{+48}_{-29} \cdot 10^{-4}$ and $\varepsilon_c = 31^{+38}_{-25} \cdot 10^{-3}$ corresponding to LEP averages of the mean scaled energy $\langle x_E \rangle = 0.702 \pm 0.008$ [52] for b hadrons and $\langle x_E \rangle = 0.484 \pm 0.008$ [52] for c hadrons. To calculate the size of the systematic errors the Monte Carlo events are reweighted so as to vary the average scaled energy $\langle x_E \rangle$ of the weakly decaying

Fragmentation function	ΔA_{FB}^{b}	ΔA_{FB}^{c}	$\Delta\overline{\chi}$
	b fragmentation		
Peterson	∓0.001	±0.001	∓0.042
Collins and Spiller	∓0.012	∓0.008	∓0.074
Kartvelishvili	∓0.005	∓0.005	∓0.028
Lund	∓0.010	∓0.008	∓0.062
	c fragmentation		
Peterson	±0.054	±0.024	±0.010
Collins and Spiller	±0.049	∓0.018	∓0.007
Kartvelishvili	±0.047	∓0.022	±0.008
Lund	±0.041	∓0.023	∓0.005

Table 5.12: Systematic errors due to the variation of the fragmentation parameters of the four different fragmentation functions (see text).

b and c hadrons in the given ranges by varying the parameters of the fragmentation function. The fragmentation functions of Peterson *et al.* [42], Collins and Spiller [43], Kartvelishvili *et al.* [48], and the Lund group [49] are each used as models to determine the event weights, and the largest observed variations are assigned as the systematic errors. The systematic uncertainties for all four fragmentation models are given in Table 5.12. For b fragmentation, the largest shifts of the results are observed with the function of Collins and Spiller and for c fragmentation with the function of Peterson *et al.*

5.9.2 Branching Ratios and Partial Widths

Semileptonic Branching Ratios

The rates for the major sources (direct b and c decays $\mathrm{BR}(\mathrm{b} \rightarrow \ell^-)$ and $\mathrm{BR}(\mathrm{c} \rightarrow \ell^+)$, cascade b decays $\mathrm{BR}(\mathrm{b} \rightarrow \mathrm{c} \rightarrow \ell^+)$) are measured at LEP. ALEPH [116], DELPHI [117], L3 [118], and OPAL [120] measure $\mathrm{BR}(\mathrm{b} \rightarrow \ell^-)$ as well as $\mathrm{BR}(\mathrm{b} \rightarrow \mathrm{c} \rightarrow \ell^+)$ from a sample of leptons opposite to a b tagged hemisphere and from a double lepton sample. DELPHI [121] and OPAL [122] measure $\mathrm{BR}(\mathrm{c} \rightarrow \ell^+)$ from a sample opposite to a high energy $\mathrm{D}^{*\pm}$. The rate for $\mathrm{b} \rightarrow \tau^- \rightarrow \ell^-$ decays is derived from existing measurements of $\mathrm{BR}(\mathrm{b} \rightarrow \tau^-)$ [135–138] combined with the τ leptonic branching fraction [26]. The values and uncertainties used for the branching ratios of semileptonic b and c hadron decays are listed in Tables 5.10 and 5.11 [52].

Partial Widths of the Z

For the measurement the average values for the fractions of hadronic Z decays to $\mathrm{b\overline{b}}$ and $\mathrm{c\overline{c}}$, R_b and R_c, are used [26] (2003 results from online version). These averages are calculated using LEP (R_b [86, 119, 139, 140], R_c [121, 141–145]) and SLC (R_b [146, 147], R_c [147, 148]) results. The fractions are varied according to their uncertainties: $R_\mathrm{b} = 0.21647 \pm 0.00072$ and $R_\mathrm{c} = 0.1683 \pm 0.0047$. In each case, the fraction of Z hadronic decays to light quarks is adjusted to compensate the variation.

5.9.3 Background Uncertainties

Lepton Identification

The analysis is only weakly sensitive to the lepton identification efficiency, since this mainly affects the ratio of prompt to background leptons [82, 83], which is effectively determined from the data via the fit of the background level (Eq. 5.9). However, a small component of the background is composed of genuine leptons (Section 5.4.1), so the lepton identification efficiencies are varied by $\pm 4.1\,\%$ for electrons and $\pm 3.0\,\%$ for muons [86].

Background Composition

The overall background fraction is a fitted parameter (Eq. 5.9). However, the background shape as a function of NETb, NETc, and $|y|$ may be different for different contributions to the background. The rate of untagged photon conversions is varied by $\pm 15\,\%$ [86, 109]. In addition, the $|y|$ distribution of conversions is varied according to the difference in the rate of identified conversions observed between data and Monte Carlo simulation. The contributions to the muon background from π, K, and other sources are varied in turn by $5\,\%$, $30\,\%$, and $100\,\%$. These uncertainties are evaluated using control samples of $\mathrm{K^0_s} \to \pi^+\pi^-$, three-prong tau decays, and tracks with an enhanced kaon fraction selected using $\mathrm{d}E/\mathrm{d}x$ cuts [110, 112, 113]. The variation of the source fractions, including backgrounds, as a function of $\cos\theta_\mathrm{T}$ is discussed in Section 5.9.4 below.

Background Asymmetries

The uncertainties in the forward-backward asymmetry of the background is evaluated by varying the light primary quark (u,d,s) forward-backward asymmetries by the uncertainties listed in Table 5.6 [127, 128]. Note that the up and down

	$A_{\mathrm{FB}}^{\mathrm{Background}}$ (%)			
	electrons		muons	
	NETb < 0.3	NETb > 0.3	NETb < 0.3	NETb > 0.3
NETc < 0.3	0.031	0.360	0.430	0.716
NETc > 0.3	0.063	0.239	0.277	0.636
total	0.093		0.410	

Table 5.13: The background asymmetry for four different NETb $-$ NETc bins. The uncertainties for the different bins are suppressed in the table. The total asymmetries are known to a precision of 0.1 % for muons and 0.2 % for electrons. The precision of the different bins is better than 0.3 % for muons and 0.4 % for electrons.

asymmetries measured by OPAL are +91 % correlated [128]. They are therefore varied at the same time, and the resulting uncertainty combined in quadrature with the uncertainty in the strange asymmetry. The b and c forward-backward asymmetries are treated self-consistently in the fit (see Section 5.5.1), and the uncertainty in these quantities is therefore automatically reflected in a very small contribution to the statistical uncertainty.

Background Flavour Separation

In the fit a constant value for the background asymmetry $A_{\mathrm{FB}}^{\mathrm{Background}}$ with respect to NETb and NETc is assumed (see Eq. 5.14). Due to the inhomogeneity of the background fraction one would expect a dependence of $A_{\mathrm{FB}}^{\mathrm{Background}}$ at least on the longitudinal momentum p and the transverse momentum p_{t} of the background lepton candidates. Since the separation variables NETb and NETc depend on both variables the various contributions to the background fraction is accumulated in different regions of the NETb $\times$ NETc plane. Electrons from photon conversions (symmetric) are predominant at low p, p_{t} while candidates with high values of p and/or p_{t} are more likely to come from leading particles in jets, and thus contribute more to a asymmetric background. This gives raise to an investigation of the background asymmetry as a function of the separation variables. The prediction of the Monte Carlo simulation is used to derive the background forward-backward asymmetry as a function of NETb and NETc. Due to limited Monte Carlo statistics the background asymmetry is determined only for 2×2 bins of the NETb $\times$ NETc plane with the bin edges at 0.3 to get reasonable background statistics in all bins. Background lepton candidates produced from each of the five quark flavours are used. The results are summarised in Table 5.13.

To quantify the effect of a non constant background asymmetry on the measurement, the fit is performed twice on the entire full detector Monte Carlo with different modelling of the background asymmetry:

1. with a constant background asymmetry and
2. with four different values for the background asymmetry as shown in Table 5.13.

To increase the statistical precision of the test the forward-backward asymmetries of the Monte Carlo sample used are scaled up by a factor of seven. The $A_{\mathrm{FB}}^{\mathrm{b}}$ and $A_{\mathrm{FB}}^{\mathrm{c}}$ results from both fits differ by 0.04 (if the asymmetries are given in per cent). If the Monte Carlo models the data well, this shift is effectively absorbed into the QCD correction (see Section 5.8). The shift is actually around the same size as the statistical uncertainty on the QCD correction, therefore it is difficult to test this directly. As a cross check the fit to real data is performed with both assumptions as above, even leading to slightly smaller shifts. Since the statistical error of the QCD correction also accounts for this uncertainty, half of the shift is assigned as a systematic error.

5.9.4 Other Uncertainties

Correction Factor for B Mixing in Cascade Decays

The value for the correction factor $\overline{\eta} = 1.083$ is estimated using a large number of $\mathrm{b\overline{b}}$ Monte Carlo events. The uncertainty of this estimate for the correction factor is of the order of 0.04. A theoretical calculation using the appropriate branching fractions and their errors [26] leads to a similar result and an uncertainty of the order of 0.06. Therefore the difference between using the standard value of $\overline{\eta} = 1.083$ and setting it equal to 1.000 is assigned as a conservative estimate of the uncertainty.

Dependence of Source Fractions on $\cos\boldsymbol{\theta}_{\mathbf{T}}$

The performances of the electron and muon identification is not constant over the polar angle θ (see Figure 5.9 and 5.11). For example the contribution of hadronic background to the electron sample is larger in the region $0.7 < |\cos\theta| < 0.8$, where the barrel and endcap parts of the detector overlap [60]. The number of conversions also increases with $|\cos\theta|$ due to the increasing amount of material in the detector [109]. This dependences on $\cos\theta$ induce a slight variation of the composition of the lepton candidates with y. For that reason the composition of each NETb × NETc × $|y|$ bin is calculated using the prediction of the simulation. To check how well this dependence is reproduced by the Monte Carlo, the description of the source fractions as a function of $\cos\theta_T$ is checked by selecting $b \to \ell^-$, $c \to \ell^+$ and background enriched regions of the NETb × NETc plane for each $|y|$ bin, and comparing the $\cos\theta_T$ distributions of data and Monte Carlo simulation. No systematic trend is seen for the $c \to \ell^+$ enriched sample. The ratio for background varied by up to 10 % in the endcap region, with smaller deviations for the $b \to \ell^-$ enriched sample. A systematic uncertainty is therefore assessed by reweighting the Monte Carlo background according to the data/Monte Carlo ratio observed for the background enriched sample and repeating the fit. The change in the background sample is compensated by an increase in the prompt leptons, so this procedure also accounted for any possible discrepancy in the $b \to \ell^-$ sample.

Tracking Resolution

The resolution of the tracking system is known to be too optimistic in the standard OPAL Monte Carlo simulation used for this measurement. To quantify the magnitude of this effect a global 10 % degradation in the tracking resolution is applied to the Monte Carlo sample, separately in the r-ϕ and r-z planes. This is done by applying a single multiplicative scale factor to the difference between the reconstructed and true track parameters, affecting especially the decay length, momentum and impact parameter distributions. The fit is repeated with each of these modified samples, and the sum in quadrature of the two shifts in the results is taken as a systematic uncertainty.

Flavour Separation Variables

The shapes of the flavour separation variables NETb and NETc and with them the shape of the normalised NETb × NETc distributions depend on the shapes of the input quantities to the neural networks. Due to mismodelling of the Monte Carlo simulation the NETb and NETc distributions shown in Figure 5.8 as well as the input quantities to the neural networks displayed in Figures 5.1-5.4 show slight different distributions for data and Monte Carlo events. These discrepancies can lead to shifts of the measured asymmetries by applying a slightly different flavour separation performance to Monte Carlo as to the data.

Possible uncertainties due to mismodelling of the neural network input variables are taken into account by reweighting the Monte Carlo events by the ratio between the data and Monte Carlo distributions of each variable in turn, and repeating the fit. The sum in quadrature of the shifts in the results is assigned as a systematic

Input	$\Delta A_{\mathrm{FB}}^{\mathrm{b}}$	$\Delta A_{\mathrm{FB}}^{\mathrm{c}}$	$\Delta\overline{\chi}$
momentum p	0.016	0.038	0.039
transverse momentum p_{t}	0.057	0.128	0.018
sub-jet energy $E_{\mathrm{sub-jet}}$	0.001	0.003	0.016
jet energy $E_{\mathrm{jet}}^{\mathrm{vis}}$	0.002	0.018	0.023
$(\sum p_{\mathrm{t}})_{\mathrm{jet}}$	0.004	0.012	0.001
$(L/\sigma_L)_1$ of lepton jet	0.000	0.068	0.018
$(L/\sigma_L)_2$ of other jet	0.027	0.058	0.013
output of NETel	0.010	0.019	0.018
output of NETcv	0.005	0.010	0.001
impact parameter sig. d/σ_d	0.004	0.006	0.079

Table 5.14: Breakdown of the systematic uncertainty due to the discrepancies concerning data/Monte Carlo agreement. The errors estimated by reweighting the distributions of each input quantities to the neural networks for quark flavour separation as to agree with the data appropriate distribution is given for the on-peak asymmetry measurement and the B mixing parameter. The relative contributions of the different input quantities to the total is similar for the off-peak measurements.

uncertainty, dominated by the result of reweighting the lepton p and p_t distributions for the forward-backward asymmetries and the input parameter significance for $\overline{\chi}$. An overview over the uncertainties caused by the different input quantities for the on-peak forward-backward asymmetries and the B mixing parameter is given in Table 5.14.

The neural network output distributions are also reweighted to account for the discrepancies between data and Monte Carlo visible in Figure 5.8, but the resulting changes in the results are much smaller than those seen when reweighting the inputs. This is because the discrepancies of some variables are compensated partially by each other. Since both methods described account for the same kind of uncertainties, no additional systematic error is assigned.

Time Dependent Mixing

The B mixing parameter $\overline{\chi}$ reflects the fraction of mixed events in an unbiased sample of all b hadrons. However, the time dependent oscillations for B^0 mesons are sufficiently slow that the lifetime variables $(L/\sigma_L)_{1,2}$, d/σ_d (decay length and impact parameter significance) used in NETc might change the effective value of $\overline{\chi}$ as a function of NETc(Figure 5.7). To evaluate the impact of such an effect,

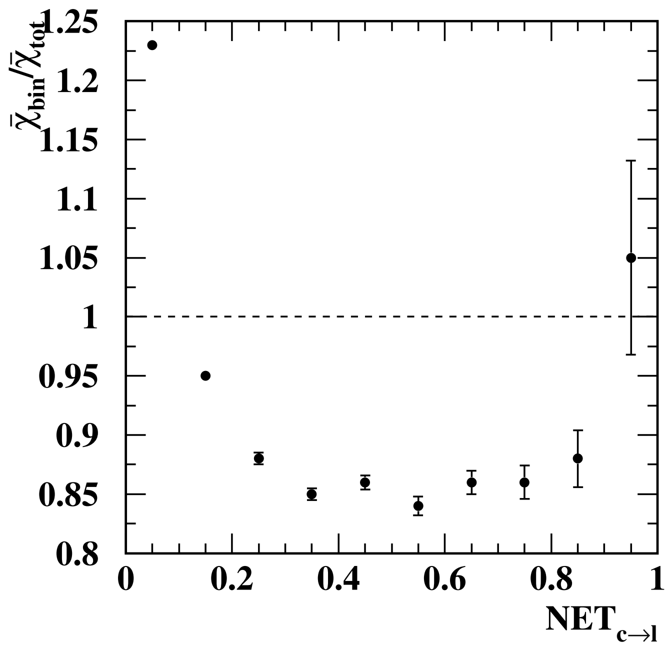

Figure 5.17: The diagram shows the behaviour of the B mixing parameter $\overline{\chi}$ as a function of NETc by plotting the fraction $\overline{\chi}_{\text{bin}}/\overline{\chi}_{\text{tot}}$. Here $\overline{\chi}_{\text{bin}}$ is the B mixing parameter for a specific NETc bin (see also Figure 5.7).

the value of $\overline{\chi}$ is evaluated for all $b\overline{b}$ Monte Carlo events with a lepton candidate. Besides the mixing parameter for the entire Monte Carlo sample $\overline{\chi}_{\text{tot}}$, the mixing parameters $\overline{\chi}_{\text{bin}}$ for ten bins in NETc are obtained. Correction factors $\overline{\chi}_{\text{tot}}/\overline{\chi}_{\text{bin}}$ are implemented in the likelihood function to correct the different contributions to $\overline{\chi}$ as a function of NETc. The behaviour of the mixing parameter as a function of NETc is shown in Figure 5.17. The mixing parameter $\overline{\chi}$ is much larger than usual for the first bin. For the last nine bins it is below average. The shift in the fit results caused by the correction is taken as a systematic uncertainty.

Monte Carlo Statistics

The limited Monte Carlo statistics available introduces a statistical uncertainty in the NETb $\times$ NETc reference distributions and in the values for the fractions f_i and f_{ij}, which introduces a fluctuation of the measured quantities. A modified version of the toy Monte Carlo generator is used to generate a total of 1 000 sets of reference distributions and fractions f_i and f_{ij}, being randomly varied according to the statistical uncertainty in each bin of NETb, NETc, and $|y|$. The fit to the data is then repeated 1 000 times, with these sets of reference distributions and

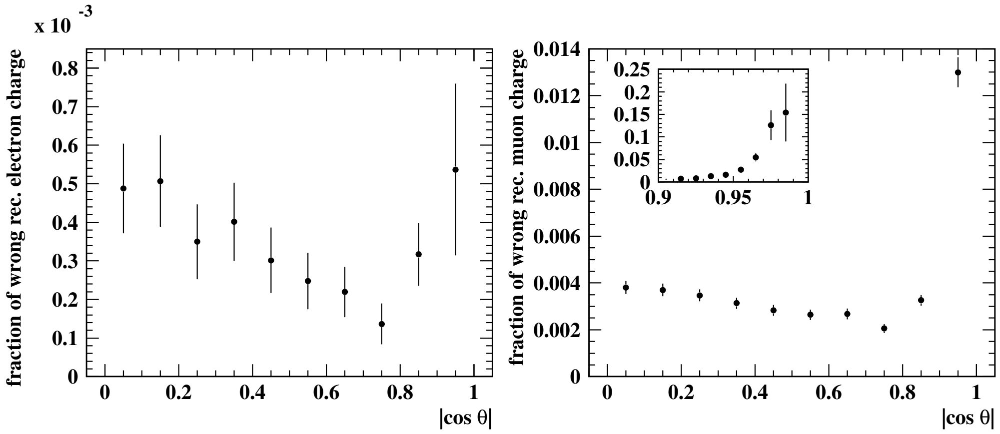

Figure 5.18: The plots show the fraction of wrong identified lepton charge for electrons (left) and muons (right) as a function of $|\cos\theta|$. The inset in the right plot shows the charge reconstruction quality for the last bin. The number of excluded tracks is rather small when a cut of $|\cos\theta| < 0.96$ is used for the angle of the lepton tracks in the analysis as can be seen from the error bars.

fractions. The RMS variation in the results is added in quadrature with the Monte Carlo statistical uncertainty on the bias corrections discussed in Section 5.8 to give the total uncertainty due to limited Monte Carlo statistics.

Lepton Charge Asymmetry

A difference of the reconstruction efficiency for positive and negative charged leptons has no effect on the asymmetry measurement, provided everything is symmetric in $\cos\theta$. Studies in [149] show a possible difference of around $8 \cdot 10^{-4}$ between the lepton identification efficiencies for positive and negative charged particles. However, the offset of the beamspot in z direction results in (1.7 ± 0.3) % more leptons in the backward hemisphere which, when combined with the charge asymmetry above, would introduce an artificial forward-backward asymmetry of the order $8 \cdot 10^{-4} \cdot 1.7\ \% = 1.4 \cdot 10^{-5}$. This is completely negligible on the scale of the errors in this analysis.

Year	**Data contribution (%)**			**Beam energy error [MeV]**		
	peak–2	**peak**	**peak+2**	**peak–2**	**peak**	**peak+2**
1990	6.04	2.42	5.65	20	18	20
1991	12.70	5.52	11.03	5	18	5
1992	—	18.04	—	—	18	—
1993	44.89	11.97	43.41	3.4	6.7	2.9
1994	—	41.00	—	—	3.6	—
1995	36.37	11.26	39.90	1.8	5.4	1.7
LEP2	—	9.79	—	—	12	—

Table 5.15: The precision of the LEP beam energy measurement for the different data taking periods is summarised on the left side [150]. The relative composition of the on- and off-peak data samples used for the forward-backward asymmetry measurement is shown on the right.

Lepton Charge Reconstruction

The discrimination between quarks and antiquarks using the charge correlation between the primary quark and the final state lepton is crucial for the asymmetry measurement. This implies that a proper reconstruction of the lepton charge is possible. The Monte Carlo simulation is used to check this. Figure 5.18 shows the fraction of leptons with a wrong reconstructed charge sign as a function of $|\cos\theta|$ for electrons and muons. There are much more muons with wrong identified charge than electrons due to harder track quality cuts for electron candidates which are necessary in order to use the $\mathrm{d}E/\mathrm{d}x$ information (see Section 5.4.1). If the muon candidates in the far forward region ($|\cos\theta| > 0.96$) are dropped, about 0.03 % of electrons and 0.3 % of muons are reconstructed in the tracking chamber with the wrong charge. To account for this effect, two different fits on Monte Carlo data are made: the first fit is done as the fit on data. Concerning the second fit, the charge is taken from the Monte Carlo truth and not from the reconstruction. The full difference from these two fits is taken as the systematic error.

LEP Centre-of-Mass Energy

The LEP centre-of-mass energy is known to a precision varying between 3.5 MeV and 20 MeV depending on the energy point and year [150]. The precision of the beam energy measurement for the different data taking periods is summarised in Table 5.15, together with the relative contribution of the data used for this analyses in the corresponding time. The derivative $\mathrm{d}\,A_{\mathrm{FB}}(\sqrt{s})/\mathrm{d}\sqrt{s}$ of the forward-

$\langle\sqrt{s}\rangle$	$\mathrm{d}\,A_{\mathrm{FB}}/\mathrm{d}\,\sqrt{s}$	
	$A_{\mathrm{FB}}^{\mathrm{b}}$	$A_{\mathrm{FB}}^{\mathrm{c}}$
peak−2	0.024	0.060
peak	0.018	0.048
peak+2	0.010	0.027

Table 5.16: For each of the three energy points and the two forward-backward asymmetries the slope $\mathrm{d}\,A_{\mathrm{FB}}/\mathrm{d}\,\sqrt{s}$ is calculated using ZFITTER [34].

backward asymmetry (see Table 5.16) is used to approximate the variations of the asymmetries. The slopes are calculated with ZFITTER [34] assuming the Standard Model dependencies of the asymmetries on $\sqrt{s}$ separately for each energy point. The validity of a linear approximation can be seen from Figure 2.5. Taking year-to-year correlations into account, this leads to the uncertainties given in Tables 5.10 and 5.11 on the asymmetries at the quoted values of $\sqrt{s}$.

QCD and Bias Correction

The corrections applied to the raw fitted asymmetries are known to precisions of 0.80 % for b quarks and 0.89 % for c quarks, as discussed in Section 5.8. The theoretical part of this uncertainty is assigned as the error on the QCD correction [52,96], whilst the Monte Carlo statistical uncertainty is accounted for separately as discussed in Section 5.9.4.

5.10 Consistency Checks

The analysis is performed separately for data from 1990 and 1991, for each year separately from 1992 to 1995, and for data from 1996 to 2000. The values for $A_{\mathrm{FB}}^{\mathrm{b}}$, $A_{\mathrm{FB}}^{\mathrm{c}}$ and $\overline{\chi}$, obtained from these fits are shown together with their statistical uncertainties in Figure 5.19. The results are consistent among themselves and with the standard result from fitting all data simultaneously. Taking into account statistical errors only, the χ^2/dof value for the six $A_{\mathrm{FB}}^{\mathrm{b}}$ measurements to be consistent with the same value is 5.9/5. The equivalent χ^2/dof value for $A_{\mathrm{FB}}^{\mathrm{c}}$ and $\overline{\chi}$ are 2.4/5 and 5.3/5.

Separate fits for events with only electron or muon candidates are made to measure $A_{\mathrm{FB}}^{\mathrm{b}}$ and $A_{\mathrm{FB}}^{\mathrm{c}}$ (see Table 5.17). Those values for the asymmetries are in excellent agreement amongst themselves and with the results from the full fit. In

A_{FB}^{b} (%)	A_{FB}^{c} (%)	$\langle\sqrt{s}\rangle$ [GeV]
electrons only		
3.0 ± 2.5	-8.9 ± 3.5	89.51
9.68 ± 0.57	5.16 ± 0.75	91.25
8.0 ± 2.2	13.4 ± 2.9	92.95
muons only		
5.3 ± 2.3	-4.9 ± 3.4	89.51
9.79 ± 0.51	6.08 ± 0.74	91.25
13.4 ± 1.9	15.7 ± 2.8	92.95

B mixing parameter (%)		
ee	$\mu\mu$	eμ
12.88 ± 1.10	13.04 ± 0.86	13.27 ± 0.69

Table 5.17: Results for the b and c quark forward-backward asymmetries and the B mixing parameter for electrons and muons.

addition the B mixing parameter $\overline{\chi}$ is determined using only two lepton events with

- two electron candidates,
- two muon candidates,
- one electron and one muon candidate.

The fitted values from this test are in good agreement with each other and with the total value. The results are also summarised in Table 5.17.

It is tested that the fit is independent of the binning in NETb, NETc and $|y|$. For this the binning is varied between 5 and 15 (in the analysis $10 \times 10 \times 10$ bins are used) separately for NETb, NETc, and $|y|$.

Finally it is checked that the analysis is independent of the cuts chosen to select the lepton candidates. The most important point is the cut on NETb in order to select the candidates included in the two lepton sample, which is used to determine the B mixing parameter $\overline{\chi}$. It can be seen from Figure 5.20 that the fitted values for $\overline{\chi}$ do not depend on the cut chosen (see also Figure 5.7). This is very important, since a bias at this point would also influence the result on A_{FB}^{b} and this bias would not be compensated by the bias correction applied (see Section 5.8).

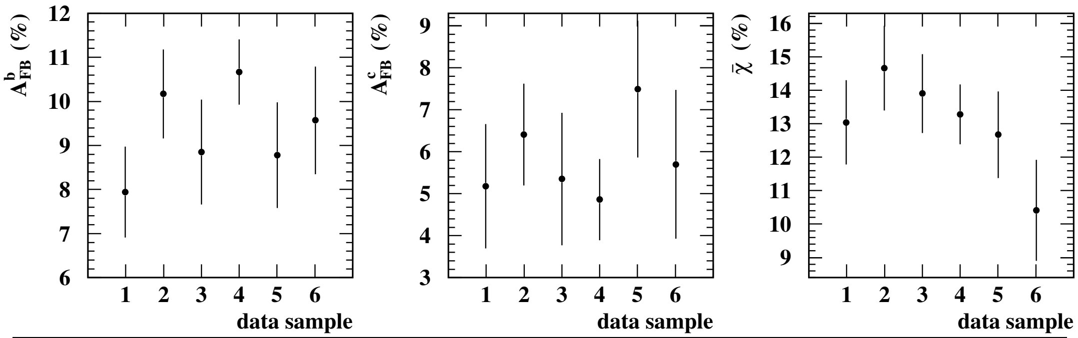

1: 1990-1991 *(no silicon detector)*	**2:** 1991-1992 *(with 2d silicon detector)*
3: 1993 *(with 3d silicon detector)*	**4:** 1994
5: 1995	**6:** 1996-2000 *(LEP2 calibration data)*

Figure 5.19: Fit results for the b and c quark forward-backward asymmetries $A_{\mathrm{FB}}^{\mathrm{b}}$ and $A_{\mathrm{FB}}^{\mathrm{c}}$ as well as for the averages B mixing parameter $\overline{\chi}$ for the six different data samples. The samples 1 and 2 include data from two different years, because they correspond to the same detector configuration. Separating those samples as well as the calibration data into pieces containing only data for one year reduces the statistics such that a full fit does not return meaningful results. The errors in the plots are just the statistical uncertainties estimated by the fit.

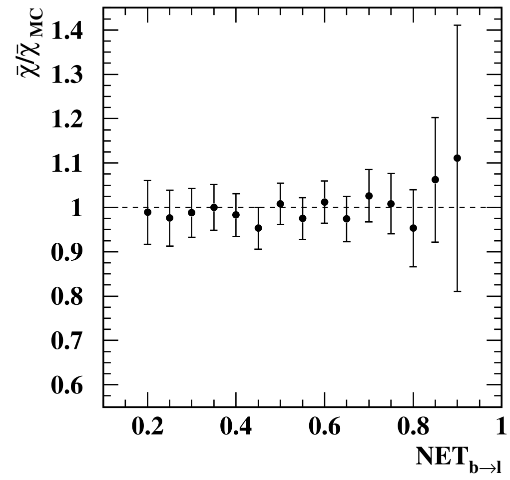

Figure 5.20: Fit result for the B mixing parameter $\overline{\chi}$ as a function of the cut on NETb. After the cut the sample contains only two lepton events with NETb $\geq$ NETb(cut). The fit results are normalised to $\overline{\chi}_{\mathrm{MC}}$, which is the value implemented in the Monte Carlo. For the final results the cut point is set to NETb(cut) $= 0.6$. The error bars quote statistical uncertainties only.

Chapter 6

Combination of Results and Discussion

The weak neutral current comprises the interaction between the Z boson and the initial and final state fermions f using the vector and axial-vector coupling constants v_{f} and a_{f}. In the framework of the Standard Model these coupling constants appear in the particle widths Γ_{f} and in the asymmetry parameters $\mathcal{A}_{\mathrm{f}}$. To investigate the coupling constants in the heavy flavour sector, three quantities are measured in multihadronic Z decays: The ratios of the b and c quark partial widths of the Z to its total hadronic partial width $R_{\mathrm{b,c}} = \Gamma_{\mathrm{b\bar{b},c\bar{c}}}/\Gamma_{\mathrm{hadron}}$, the heavy flavour forward-backward asymmetries $A_{\mathrm{FB}}^{0,\,\mathrm{b,c}} = (4/3)\mathcal{A}_{\mathrm{e}}\mathcal{A}_{\mathrm{b,c}}$, and the asymmetry parameters $\mathcal{A}_{\mathrm{b,c}}$, extracted from the measurement of the left-right asymmetry $A_{\mathrm{LR}}^{0} = \mathcal{A}_{\mathrm{e}}$, and the left-right forward-backward asymmetry $A_{\mathrm{LRFB}}^{0,\,\mathrm{b,c}} = (3/4)\mathcal{A}_{\mathrm{b,c}}$ using polarised initial states at SLC. Since the heavy flavour forward-backward asymmetries $A_{\mathrm{FB}}^{0,\mathrm{q}}$ only measure the product of the asymmetry parameters $\mathcal{A}_{\mathrm{q}}\mathcal{A}_{\mathrm{e}}$, in addition a precise determination of $\mathcal{A}_{\mathrm{e}}$ is necessary to extract $\mathcal{A}_{\mathrm{q}}$. Besides the determination of $\mathcal{A}_{\mathrm{e}}$ from the A_{LR}^{0} measurement at SLD also the leptonic forward-backward asymmetries $A_{\mathrm{FB}}^{0,\,\ell} = (3/4)\mathcal{A}_{\mathrm{e}}\mathcal{A}_{\ell}$ can be used if lepton universality ($\mathcal{A}_{\mathrm{e}} = \mathcal{A}_{\mu} = \mathcal{A}_{\tau}$) is assumed. In addition, $\mathcal{A}_{\tau}$ and $\mathcal{A}_{\mathrm{e}}$ can both be extracted using polarised τ leptons.

All experimental results on electroweak Z pole observables are used to derive values for the effective couplings of the neutral weak current at the Z pole:

- the asymmetry parameters $\mathcal{A}_{\mathrm{f}}$,
- the effective vector and axial-vector coupling constants v_{f}, and a_{f},
- the effective electroweak mixing angles $\sin^2\theta_{\mathrm{eff}}^{\mathrm{f}}$ and
- the leptonic effective electroweak mixing angle $\sin^2\theta_{\mathrm{eff}}^{\ell}$.

The results of these largely model independent parameters from different analyses are compared to the expectations within the framework of the Standard Model, thereby testing its validity[1]. Many different measurements are used for these calculations:

- Z lineshape and leptonic forward-backward asymmetries from LEP,
- polarised leptonic asymmetries from SLD,
- τ polarisation from LEP,
- heavy quark flavour results from SLD and LEP, and
- inclusive hadronic charge asymmetry from LEP.

The newly derived couplings are determined in fits to these input results. Within the OPAL experiment, there are different methods employed to measure the b and c quark forward-backward asymmetries $A_{\mathrm{FB}}^{\mathrm{b}}$ and $A_{\mathrm{FB}}^{\mathrm{c}}$ which have been introduced in Chapter 4. Equivalent methods are used also by the other LEP collaborations, so that a large number of asymmetry measurements is available [13, 76, 77, 151–158]. Besides the comparison of the new OPAL results from this work with the other OPAL and LEP results, the combination of the measurements is important in order to obtain OPAL and LEP average values for $A_{\mathrm{FB}}^{\mathrm{b}}$ and $A_{\mathrm{FB}}^{\mathrm{c}}$ with high precision. The same arguments are also valid for the $R_{\mathrm{b,c}}$ and $\mathcal{A}_{\mathrm{b,c}}$ measurements. There are several sources of systematic uncertainties which are common to more than one of the measurements. Some systematic uncertainties of single measurements are not real uncertainties but dependencies on other measurements. For example, the $A_{\mathrm{FB}}^{\mathrm{b}}$ and $A_{\mathrm{FB}}^{\mathrm{c}}$ measurements depend on values of R_{b}, however, measurements of $A_{\mathrm{FB}}^{\mathrm{b}}$, which are not simultaneous measurements of $A_{\mathrm{FB}}^{\mathrm{b}}$ and $A_{\mathrm{FB}}^{\mathrm{c}}$, depend also on $A_{\mathrm{FB}}^{\mathrm{c}}$. Considering these arguments, the only possibility to combine the heavy flavour observables from LEP and SLD is to make a fit to the observables desired, accounting for dependencies and correlations. Already in 1994 a procedure has been proposed to solve this problem [159], which has been improved since then. The method currently used [98] is briefly described in Section 6.1.

After combining the observables, the extraction of the asymmetry parameters is the first thing to do. For electrons, $\mathcal{A}_{\mathrm{e}}$ can be extracted from the left-right asymmetry $A_{\mathrm{LR}}^{0} = \mathcal{A}_{\mathrm{e}}$ at SLD. The other leptonic asymmetry parameters are obtained by the leptonic forward-backward asymmetries or the τ polarisation. The different $\mathcal{A}_{\ell}$ measurements are combined assuming lepton universality.

[1] At this point it is left to the philosophical background of the reader whether the validity of a model can be tested or just ruled out.

The asymmetry parameters $\mathcal{A}_\mathrm{f}$ only depend on the ratio $v_\mathrm{f}/a_\mathrm{f}$ of the effective vector and axial-vector coupling constants (Eq. 2.31):

$$\mathcal{A}_\mathrm{f} = \frac{2\, v_\mathrm{f}/a_\mathrm{f}}{1 + (v_\mathrm{f}/a_\mathrm{f})^2} = \frac{2\, v_\mathrm{f}\, a_\mathrm{f}}{v_\mathrm{f}^2 + a_\mathrm{f}^2} \ . \tag{6.1}$$

In contrast, the partial decay widths of the Z boson determine the sum of the squares of these two coupling constants (Eq. 2.26):

$$\Gamma_\mathrm{f} \propto a_\mathrm{f}^2 + v_\mathrm{f}^2 \ . \tag{6.2}$$

The expressions for both observables are invariant under the exchange $v_\mathrm{f} \leftrightarrow a_\mathrm{f}$, and only the relative sign between v_f and a_f is determined by $\mathcal{A}_\mathrm{f}$. The energy dependence of the forward-backward asymmetries measured at LEP resolves the $v_\mathrm{f} \leftrightarrow a_\mathrm{f}$ ambiguity, and the absolute sign of all couplings is established by the convention $a_\mathrm{e} < 0$. It is thus possible to disentangle the effective coupling constants v_f and a_f by analysing both the asymmetry measurements as well as the partial Z decay widths.

The effective vector and axial-vector coupling constants obey simple relations with the effective electroweak mixing angle (Eq.2.9). Because of the structure of the couplings in terms of the electric charge Q_f and of the third component of the weak isospin T_3^f in the Standard Model, the hadronic asymmetry parameters $\mathcal{A}_\mathrm{q}$ are very much less sensitive to $\sin^2\theta_\mathrm{eff}^\mathrm{f}$ (see Figure 2.6) than $\mathcal{A}_\ell$. As a consequence, the sensitivity to Standard Model parameters, such as m_t, m_H, and $\alpha(m_\mathrm{Z}^2)$, which are accessible via radiative corrections, is very weak. The larger experimental uncertainties of the hadronic measurements amplifies this effect. This independence of $\mathcal{A}_\mathrm{q}$ on Standard Model parameters allows to test the Standard Model at a fundamental structural level, and in a manner which is insensitive to electroweak radiative corrections or the knowledge of other Standard Model parameters.

Since the various asymmetry parameters only depend on the fraction (Eq. 2.9)

$$\frac{v_\mathrm{f}}{a_\mathrm{f}} = \left(1 - 4|Q_\mathrm{f}|\sin^2\theta_\mathrm{eff}^\mathrm{f}\right) \ , \tag{6.3}$$

they can be used to extract $\sin^2\theta_\mathrm{eff}^\mathrm{f}$. Using Standard Model expectations for $\mathcal{A}_\mathrm{b,c}$, the heavy quark forward-backward asymmetries $A_\mathrm{FB}^{0,\,\mathrm{b,c}}$ can be converted into $\sin^2\theta_\mathrm{eff}^\ell$. On the other hand, $A_\mathrm{FB}^{0,\,\mathrm{b,c}}$ can be used to extract $\sin^2\theta_\mathrm{eff}^\mathrm{b}$ or $\sin^2\theta_\mathrm{eff}^\mathrm{c}$ by using a measurement of $\sin^2\theta_\mathrm{eff}^\ell$ to constrain $\mathcal{A}_\mathrm{e}$ in the product.

6.1 Combination Procedure for Heavy Flavour Observables

This section describes the fit procedure used to combine the different measurements from the electroweak precision data collected at LEP and SLD. Special emphasis has been given to the aspects of the heavy flavour forward-backward asymmetries. A full description of the averaging procedure is published in [98]. The fit is used in the following sections in a slightly modified way to get final averages for $A_{\mathrm{FB}}^{\mathrm{b}}$ and $A_{\mathrm{FB}}^{\mathrm{c}}$ for OPAL, combined values for $A_{\mathrm{FB}}^{\mathrm{b}}$ and $A_{\mathrm{FB}}^{\mathrm{c}}$ using all asymmetry measurements made at LEP, and for a determination of combined values for all electroweak observables in the heavy flavour sector from LEP and SLD.

The relevant quantities in the heavy quark sector at LEP/SLC which are currently considered by the combination procedure performed by the LEP and SLD electroweak working group are:

- the ratios of the b and c quark partial widths of the Z to its total hadronic partial width:

$$R_{\mathrm{b}}^0 \equiv \Gamma_{\mathrm{b\overline{b}}}/\Gamma_{\mathrm{hadron}}, \tag{6.4}$$
$$R_{\mathrm{c}}^0 \equiv \Gamma_{\mathrm{c\overline{c}}}/\Gamma_{\mathrm{hadron}} \tag{6.5}$$
$$\tag{6.6}$$

  [86, 119, 121, 139–141, 141, 141–143, 143–148] (The symbols R_{b}, R_{c} are used to denote the experimentally measured ratios of event rates or cross-sections.),

- the forward-backward asymmetries $A_{\mathrm{FB}}^{\mathrm{b}}$ and $A_{\mathrm{FB}}^{\mathrm{c}}$ [13, 76, 77, 151–158],

- the final state coupling parameters $\mathcal{A}_{\mathrm{b}}$ and $\mathcal{A}_{\mathrm{c}}$ obtained from the left-right forward-backward asymmetry at SLD [160–165],

- the semileptonic branching ratios $\mathrm{b} \to \ell^-$, $\mathrm{b} \to \mathrm{c} \to \ell^+$ and $\mathrm{c} \to \ell^+$ and the average time-integrated B mixing parameter $\overline{\chi}$ (including them in the combination greatly reduces the errors) [116–122], and

- the probability that a c quark produces a D^+, $\mathrm{D}_{\mathrm{s}}^+$ or D^{*+} meson or a charmed baryon (the results are published together with R_{c} measurements). The probability that a c quark fragments into a D^0 is calculated from the constraint that the probabilities for the weakly decaying charmed hadrons add up to one (see Section 2.8).

Several of the analyses measure more than one parameter simultaneously (for example the forward-backward asymmetry measurements using semileptonic b and c decays or D mesons measure $A_{\mathrm{FB}}^{\mathrm{b}}$, $A_{\mathrm{FB}}^{\mathrm{c}}$ and $\overline{\chi}$).

The combination procedure is based on the method of Best Linear Unbiased Estimates (BLUE) [166]. The best estimates to be determined are denoted x^{μ}, where the index μ corresponds to the parameters (R_{b}, R_{c}, $A_{\mathrm{FB}}^{\mathrm{b}}$, ...). The individual measurements used as inputs to the fit are denoted r_i^{μ}, where i runs over the measurements of the quantities. The index μ is a convention to group the different measurements of the same quantity. The χ^2 to be minimised with respect to the parameters x^{μ} is given by [98]:

$$\chi^2 = \sum_{ij} (r_i^{\mu} - x^{\mu})\, \mathcal{C}_{ij}^{-1} (r_j^{\nu} - x^{\nu}) \ . \tag{6.7}$$

The full statistical and systematic covariance matrix $\mathcal{C}$ for all measurements has to be calculated. This matrix takes all correlations between different measurements of one experiment and between different experiments into account. The covariance matrix can be written as:

$$\mathcal{C} = \mathcal{C}^{\mathrm{stat.}} + \mathcal{C}^{\mathrm{syst.}} \ . \tag{6.8}$$

Because there are no common events used by measurements made by different experiments, there is also no statistical correlation between these results. This assumption does not hold for different measurements of the same quantity with different methods within the same experiment. In these cases the different types of measurement might use a certain number of common events. This leads to a statistical correlation of those measurements. The magnitude of this correlation is determined by the collaborations and included in the averaging procedure. The determination of the statistical correlation of the OPAL measurements is explained in the next section.

The sources for systematic uncertainties of a single measurement can be categorised into three different groups:

1. uncertainties originating from sources which are unique for this type of measurement and experiment,
2. errors which arise from sources which are common for at least two included measurements, and
3. dependencies of the measured quantity on other results included in the fit.

While the explicit dependence of each measurement on the other parameters are fully taken into account by the fit the true systematic uncertainties have to be included in the uncertainty of the final result. It is assumed that the systematic uncertainties are symmetric and of Gaussian shape.

Common sources of systematic uncertainties usually arise from physics quantities. Concerning the heavy quark forward-backward asymmetry measurements the QCD correction, the heavy quark fragmentation parameters or the LEP beam energy are examples for sources of common systematic errors. In addition to this, common tagging and analysis techniques used by different experiments lead to further common sources of systematic uncertainties.

The diagonal element $\mathcal{C}_{ii}^{\text{syst.}}$ is the square of the total systematic error for measurement i. If the signed systematic error on result r_i^μ due to a source of systematic uncertainty p is written as $s_i^\mu(p)$, then an off-diagonal element is given by:

$$\mathcal{C}_{ij}^{\text{syst.}} = \sum_p s_i^\mu(p) s_j^\mu(p), \tag{6.9}$$

where the sum is over all sources of uncertainty p, which are correlated between results i and j. The starting point for the combination is to ensure that all the analyses use a common set of assumptions for input parameters which give rise to systematic uncertainties.

The tables prepared by the experiments include a detailed breakdown of the systematic error of each measurement and its dependence on other electroweak parameters. The measurements are summarised in [167]. Concerning the heavy flavour forward-backward asymmetry measurements at LEP, the results are given in Table 6.4 and 6.5 (corrections are applied in case they are necessary) [13,76,77, 151–158], to give an impression of the magnitude of correlation of the systematic uncertainties.

Some of the measurements of electroweak parameters depend explicitly on the values of other parameters (for example A_{FB}^{b} and A_{FB}^{c} depend on R_{b} and R_{c}, and the semileptonic analyses of A_{FB}^{b} and A_{FB}^{c} in addition depend on $\text{BR}(\text{b} \to \ell^-)$, $\text{BR}(\text{b} \to \text{c} \to \ell^+)$, $\text{BR}(\text{c} \to \ell^+)$ and $\overline{\chi}$). If some quantities are measured in the same analysis, this is reflected in the correlation matrix for the results. This can be seen for example in the correlation of the results for A_{FB}^{b} and A_{FB}^{c} or A_{FB}^{b} and $\overline{\chi}$ (see Table 5.9) presented in the previous chapter. However the analyses do not determine R_{b} and/or R_{c} simultaneously with A_{FB}^{b} and A_{FB}^{c}. Instead A_{FB}^{b} and A_{FB}^{c} are measured for assumed values of R_{b} and R_{c}. In this case the dependence is parameterised as:

$$A_{\text{FB}} = A_{\text{FB}}^{\text{meas}} + a(R_{\text{b}}) \frac{R_{\text{b}} - R_{\text{b}}^{\text{used}}}{R_{\text{b}}} \; . \tag{6.10}$$

In this expression, $A_{\text{FB}}^{\text{meas}}$ is the result of the analysis assuming a value of $R_{\text{b}} = R_{\text{b}}^{\text{used}}$. The dependence of all other measurements on other electroweak

Source	$\delta A_{\mathrm{FB}}^{\mathrm{b}}$	$\delta A_{\mathrm{FB}}^{\mathrm{c}}$
$\sqrt{s} = m_{\mathrm{Z}}$	-0.0013	-0.0034
QED corrections	$+0.0041$	$+0.0104$
γ exchange, γ/Z interference, m_{b}	-0.0003	-0.0008
Total	$+0.0025$	$+0.0062$

Table 6.1: Corrections to be applied to the quark asymmetries as $A_{\mathrm{FB}}^{0,\mathrm{q}} = A_{\mathrm{FB}}^{\mathrm{meas}} + \delta A_{\mathrm{FB}}$.

parameters is treated in the same way, with coefficients $a(x)$ describing the dependence on parameter x.

All b and c asymmetries included in the fit correspond to full polar angle acceptance.

The QCD corrections to the forward-backward asymmetries depend strongly on the experimental analyses. For this reason the numbers given by the collaborations are also corrected for QCD effects. A detailed description of the procedure can be found in [96, 97] with updates reported in [52].

Before the combination, the heavy flavour forward-backward asymmetries are corrected to common off- and on-peak energies. In a first fit, combined values separately for on- and off-peak asymmetries are calculated. A second fit is made to determine the pole asymmetries (see Eq. 2.31). In order to do that, the on- and off-peak forward-backward asymmetries are corrected to $\sqrt{s} = 91.26$ GeV (the mean energy of all recorded Z events at LEP) using the predicted energy dependence from ZFITTER [34]. The slope of the asymmetries around m_{Z} depends almost only on the axial coupling and the charge of the initial and final state fermions and is thus largely independent of the value of the asymmetry itself (see Figure 2.5).

After calculating the overall averages, the quark pole asymmetries $A_{\mathrm{FB}}^{0,\mathrm{q}}$ are derived from the measured asymmetries by applying corrections as listed in Table 6.1 [167]. These corrections are due to the energy shift from 91.26 GeV to m_{Z}, initial state radiation, γ exchange, and γ/Z interference. A very small correction due to the non-zero value of the b quark mass is included in the last correction. All corrections are calculated using ZFITTER [34]. These values for the corrections are proposed by the LEP and SLD electroweak working group [167].

6.2 Combination of the OPAL Forward-Backward Asymmetry Measurements

The results of the forward-backward asymmetry measurement of $e^+e^- \rightarrow b\overline{b}$ and $e^+e^- \rightarrow c\overline{c}$ events using electrons and muons produced in semileptonic decays of bottom and charm hadrons presented in Chapter 5 are combined with the inclusive measurement of A_{FB}^{b} [76] (see Section 4.1) and the exclusive measurement of A_{FB}^{b} and A_{FB}^{c} using D mesons [77] (see Section 4.2). The averaging procedure is similar to that used by the LEP electroweak working group [98] (see Section 6.1). For the OPAL combination the fit is done with six free parameters: A_{FB}^{b} and A_{FB}^{c}, each at three centre-of-mass energies. In addition, the B mixing parameter $\overline{\chi}$, the semileptonic branching fractions $BR(b \rightarrow \ell^-)$, $BR(b \rightarrow c \rightarrow \ell^+)$ and $BR(c \rightarrow \ell^+)$, and the particle widths R_b and R_c together with their uncertainties measured at LEP are given as constraints to the fit. In order to use common values for the nominal centre-of-mass energies, very small corrections are applied to the inclusive and charm meson forward-backward asymmetries to account for their energy dependence. The common energy values are listed below together with the combined OPAL results.

Statistical as well as systematical correlations are fully taken into account. Whilst the statistical correlation between the asymmetries measured in Chapter 5 and those from reconstructed charm hadrons is negligible, the inclusive and the lepton measurement could be correlated because the jet charges of some of the events involving $b \rightarrow \ell^-$ decays are also used to measure A_{FB}^{b} in the inclusive analysis [76]. Therefore the correlation between the inclusive analysis and the measurement using semileptonic decays is determined using a large Monte Carlo sample of about 14 million $e^+e^- \rightarrow q\overline{q}$ events of all five quark flavours. The sample is divided into subsamples of 200 000 to 300 000 events. Each sample is then analysed with both methods. This results in a statistical correlation of 0.11 ± 0.12. The results used to calculate the correlation are plotted in Figure 6.1 in the A_{FB}^{b}-lepton $\times$ A_{FB}^{b}-inclusive plane.

The systematic covariance matrix $\mathcal{C}^{\mathrm{syst.}}$ can be calculated from the detailed breakdown of systematic uncertainties given in Table 5.10 and 5.11 concerning this analysis and in [76, 77] for the other two measurements. The dominant sources of common systematic uncertainties for the combined OPAL measurements are summarised in Table 6.2. The values given are for on-peak measurements only. Because this is just a combination of measurements using different methods, the common uncertainties arising from equivalent methods do not appear here.

The final OPAL results for the b and c quark asymmetries around the Z resonance are:

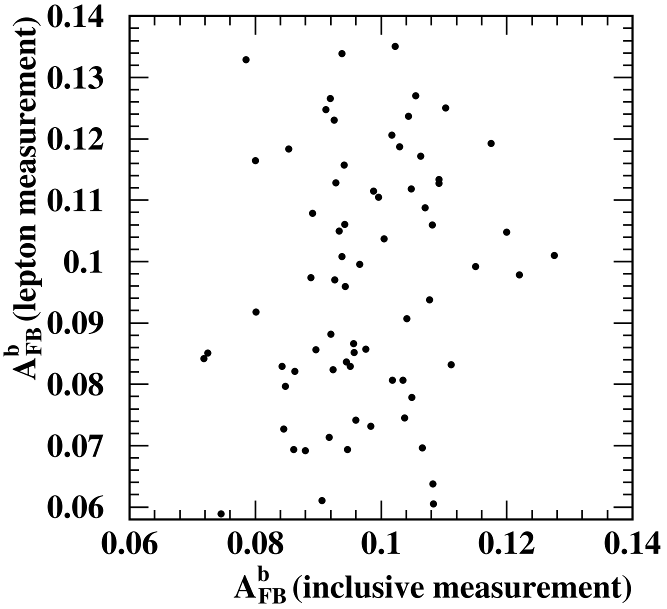

Figure 6.1: Correlation of the two measurements for the b quark forward-backward asymmetry. Each dot represents the results from both measurements in the $A^{\mathrm{b}}_{\mathrm{FB}}$-lepton $\times$ $A^{\mathrm{b}}_{\mathrm{FB}}$-inclusive plane for a Monte Carlo sample. For further explanation see text. No correlation $((11 \pm 12)\%)$ is visible.

$$A^{\mathrm{b}}_{\mathrm{FB}} = (\ 5.3\ \pm 1.2\ \pm 0.1\ )\%,\quad A^{\mathrm{c}}_{\mathrm{FB}} = (-4.8\ \pm 2.2\ \pm 0.7\ )\%\ \text{ at } \langle\sqrt{s}\rangle = 89.51\ \text{GeV},$$
$$A^{\mathrm{b}}_{\mathrm{FB}} = (\ 9.69 \pm 0.29 \pm 0.13)\%,\quad A^{\mathrm{c}}_{\mathrm{FB}} = (\ 5.83 \pm 0.49 \pm 0.32)\%\ \text{ at } \langle\sqrt{s}\rangle = 91.25\ \text{GeV},$$
$$A^{\mathrm{b}}_{\mathrm{FB}} = (11.4\ \pm 1.0\ \pm 0.2\ )\%,\quad A^{\mathrm{c}}_{\mathrm{FB}} = (\ 14.7\ \pm 1.8\ \pm 0.7\ )\%\ \text{ at } \langle\sqrt{s}\rangle = 92.95\ \text{GeV}.$$

The statistical correlations amongst these results and with the average B mixing parameter $\overline{\chi}$ are shown in Table 6.3.

The values for the OPAL on- and off-peak forward-backward asymmetry measurements together with the OPAL averages are shown in Figure 6.2. The gray band gives the Standard Model expectation for the asymmetries in the interesting energy range for different Higgs masses. It can be seen that the OPAL measurements are in good agreement with each other and with the Standard Model. The dependence of the forward-backward asymmetries on the centre-of-mass energy is well modelled by the Standard Model. In addition, it can be seen from the figure that this result favours large values of the Higgs boson mass m_{H}, in agreement with other measurements of heavy flavour forward-backward asymmetries at LEP.

The on- and off-peak forward-backward asymmetries are corrected to $\sqrt{s}$ = 91.26 GeV. After the combination the quark pole asymmetries $A^{0,\mathrm{b,c}}_{\mathrm{FB}}$ (see

Source of uncertainty	**Jet** $A_{FB}^{0,b}$ $(\cdot 10^{-3})$	**Lepton** $A_{FB}^{0,b}$ $(\cdot 10^{-3})$	$A_{FB}^{0,c}$ $(\cdot 10^{-3})$	**D meson** $A_{FB}^{0,b}$ $(\cdot 10^{-3})$	$A_{FB}^{0,c}$ $(\cdot 10^{-3})$
b fragmentation	0.3	0.1	0.1	—	—
c fragmentation	0.2	0.5	0.2	0.5	0.3
B decay multiplicity	0.0	0.1	1.0	1.7	1.6
D decay multiplicity	0.1	0.6	0.4	1.2	1.1
QCD correction	0.6	0.6	0.4	0.2	0.0
track resolution	0.9	0.3	0.5	—	—
LEP beam energy	0.1	0.1	0.3	—	—

Table 6.2: The dominant sources of common systematic uncertainties of the b and c quark forward-backward asymmetry measurements at OPAL. The errors on the B and D decay multiplicities concerning the measurement using semileptonic b and c decays also include the uncertainties arising from the $b \to \ell^-$, $b \to c \to \ell^+$ and $c \to \ell^+$ semileptonic decay models.

		pm A_{FB}^{b}	A_{FB}^{c}	**pk** A_{FB}^{b}	A_{FB}^{c}	**pp** A_{FB}^{b}	A_{FB}^{c}	**all** $\overline{\chi}$
pm	A_{FB}^{b}	1.00	0.15	0.03	0.00	0.01	0.00	0.03
	A_{FB}^{c}		1.00	0.03	0.01	0.01	0.00	0.00
pk	A_{FB}^{b}			1.00	0.15	0.08	0.01	0.11
	A_{FB}^{c}				1.00	0.02	0.16	0.04
pp	A_{FB}^{b}					1.00	0.15	0.03
	A_{FB}^{c}						1.00	0.04
all	$\overline{\chi}$							1.00

Table 6.3: Statistical correlation matrix for the OPAL forward-backward asymmetry measurements separately for on- and off-peak data. Both methods which measure A_{FB}^{b} and A_{FB}^{c} simultaneously contribute to the correlation between A_{FB}^{b} and A_{FB}^{c}. The correlation between A_{FB}^{b} and $\overline{\chi}$ is mainly caused by the measurements using semileptonic b and c decays.

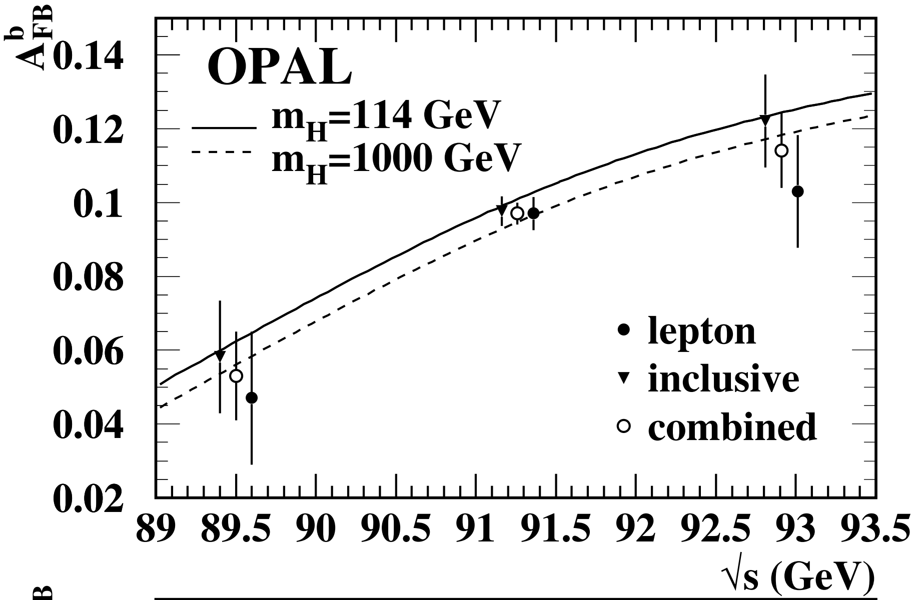

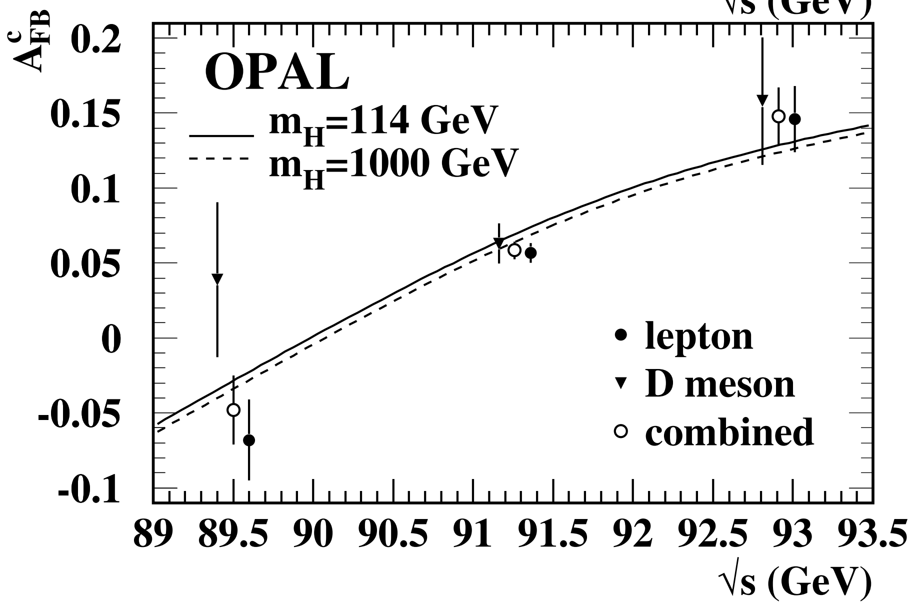

Figure 6.2: The measured b and c quark asymmetries as a function of centre-of-mass energy for the lepton, inclusive (b only) [76] and D meson (c only) [77] analyses. The measurement of the b quark asymmetry from D mesons is of low precision and is not shown. The measurements from different analyses are slightly displaced on the horizontal axis for clarity. The combination of the lepton analysis and the other analyses is also shown, together with the Standard Model expectation for Higgs masses between 114 GeV and 1 000 GeV calculated using ZFITTER [34].

Eq. 2.31) are derived from the measured asymmetries by applying corrections (see Table 6.1 [167]). The OPAL pole asymmetries are:

$$\begin{aligned} A_{\mathrm{FB}}^{0,\,\mathrm{b}} &= (9.89 \pm 0.27 \pm 0.13)\,\%, \\ A_{\mathrm{FB}}^{0,\,\mathrm{c}} &= (6.57 \pm 0.47 \pm 0.32)\,\%. \end{aligned}$$

In all cases, the first error is statistical and the second systematic. The χ^2/dof of the fit to all OPAL asymmetry measurements to give the two pole asymmetries is 11.2/13. (There are six asymmetry measurements from the lepton tag analysis, three from the inclusive analysis and six from the charm meson analysis, which consists of a simultaneous fit to the b and c quark asymmetries.) Taking statistical and systematic uncertainties into account, these average pole asymmetries have a +15 % correlation.

6.3 LEP and World Averages of Electroweak Heavy Flavour Parameters

This section describes the fit to the electroweak precision data from the LEP experiments and SLD. Special emphasis has been given to the aspects of the heavy flavour forward-backward asymmetry measurements. The latest results are summarised in [167]. The relevant quantities in the heavy quark sector which are considered by the fit are summarised in Section 6.1.

The measurements of the heavy quark forward-backward asymmetries used in the averaging procedure are:

- Measurements of $A_{\mathrm{FB}}^{\mathrm{b}}$ and $A_{\mathrm{FB}}^{\mathrm{c}}$ using semileptonic b and c decays from ALEPH [151], DELPHI [152], L3 [153], and OPAL [13]. In the case of OPAL the lepton information is combined with hadronic variables in a neural net. DELPHI uses in addition lifetime information and jet charge in the hemisphere opposite to the lepton to separate the different lepton sources. Some asymmetry analyses also measure $\overline{\chi}$ within the same analysis.

- Measurements of $A_{\mathrm{FB}}^{\mathrm{b}}$ based on lifetime tagged events with a hemisphere charge measurement from ALEPH [154], DELPHI [155], L3 [156], and OPAL [76]. These measurements dominate the combined result.

- Analyses with D mesons to measure $A_{\mathrm{FB}}^{\mathrm{c}}$ from ALEPH [157] or $A_{\mathrm{FB}}^{\mathrm{c}}$ and $A_{\mathrm{FB}}^{\mathrm{b}}$ from DELPHI [158] and OPAL [77].

- Measurements of $\mathcal{A}_{\mathrm{b}}$ and $\mathcal{A}_{\mathrm{c}}$ from SLD. These results include measurements using lepton [160], D meson [161], and vertex mass plus hemisphere charge tags [162], which have similar sources of systematic errors as the LEP asymmetry measurements. SLD also uses vertex mass for bottom or charm tagging in conjunction with a kaon tag or a vertex charge tag for both $\mathcal{A}_\mathrm{b}$ and $\mathcal{A}_\mathrm{c}$ measurements [163–165].

Results from these measurements, together with their statistical and systematical uncertainties are summarised in Table 6.4 and 6.5. The asymmetries are shifted so that they correspond to common values for the three centre-of-mass energy points. In addition, corrections are applied by the collaborations to account for final state QCD effects [52, 96]. The statistical correlations concerning the different measurements of the same quantity with the same event sample used by a specific experiment are evaluated by the collaboration. The correlations between the b asymmetry measurements with jet charge and with leptons for example range from 6% to 30%.

The individual results for the b and c pole asymmetries obtained from the lepton, D meson, and inclusive analyses from each of the four LEP experiments are shown in Figure 6.3 and 6.4. The measurements labelled "OPAL leptons" are the results from this thesis. The results represent the status of winter 2004 and are very consistent with each other [167].

In a first fit, the asymmetry measurements on-peak, above-peak, and below-peak are combined at each centre-of-mass energy point [167]. The dependence of the average asymmetries on the centre-of-mass energy agrees with the prediction of the Standard Model, as shown in Figure 6.5. A second fit is made to derive the pole asymmetries $A_\mathrm{FB}^{0,\mathrm{q}}$ from the measured quark asymmetries, in which all the off-peak asymmetry measurements are corrected to the peak (91.26 GeV) energy before the combination [98]. This fit determines a total of 14 parameters:

- two partial widths R_b and R_c,
- two LEP forward-backward asymmetries A_FB^b and A_FB^c,
- two SLD coupling parameters $\mathcal{A}_\mathrm{b}$ and $\mathcal{A}_\mathrm{c}$,
- three semileptonic branching ratios $\mathrm{BR}(\mathrm{b} \to \ell^-)$, $\mathrm{BR}(\mathrm{b} \to \mathrm{c} \to \ell^+)$ and $\mathrm{BR}(\mathrm{c} \to \ell^+)$,
- the average mixing parameter $\overline{\chi}$, and
- the probabilities for a c quark to fragment into a D^+, $\mathrm{D_s}$, D^{*+} meson or a charmed baryon.

If the SLD measurements of R_b, R_c, $\mathcal{A}_\mathrm{b}$ and $\mathcal{A}_\mathrm{c}$ are excluded from the fit to get LEP averages only, 12 parameters are left to be determined. Results for

	ALEPH				DELPHI			L3		OPAL		
		lepton 91-95		jet 91-95	lepton 91-95	D meson 92-95	multi 92-00	jet 91-95	lepton 90-95	jet 91-00	lepton 90-00	D meson 90-95
$\langle\sqrt{s}\rangle$ GeV	88.38	89.38	90.21	89.47	89.43	89.43	89.45	—	89.50	89.50	89.51	89.49
Published $A_{\mathrm{FB}}^{\mathrm{b}}$	-13.10	5.47	-0.42	4.36	6.6	5.67	6.37	—	6.11	5.82	4.70	-8.6
Used $A_{\mathrm{FB}}^{\mathrm{b}}$		5.21		4.59	6.4	4.81	6.64	—	6.29	5.99	5.24	-4.8
Statistical		1.78		1.19	2.2	7.31	1.43	—	2.93	1.53	1.77	10.4
Internal Systematic		0.08		0.04	0.2	0.68	0.21	—	0.31	0.09	0.11	2.0
Common Systematic		0.10		0.01	0.1	0.21	0.02	—	0.17	0.04	0.05	1.1
Other Param. Sys.		0.15		0.14	0.2	0.75	0.02	—	0.07	0.09	0.16	0.8
Total Systematic		0.19		0.15	0.3	1.04	0.21	—	0.36	0.14	0.20	2.4
Total Error		1.79		1.20	2.2	7.39	1.45	—	2.95	1.54	1.78	10.7
$\langle\sqrt{s}\rangle$ GeV		91.21		91.23	91.26	91.235	91.231	91.24	91.26	91.26	91.25	91.24
Published $A_{\mathrm{FB}}^{\mathrm{b}}$		9.52		10.00	10.04	7.62	9.58	9.31	9.80	9.77	9.71 6	9.4
Used $A_{\mathrm{FB}}^{\mathrm{b}}$		9.98		10.03	10.15	7.86	9.67	9.27	9.65	9.71	9.767	9.7
Statistical		0.40		0.27	0.55	1.90	0.32	1.01	0.65	0.36	0.398	2.6
Internal Systematic		0.07		0.10	0.17	0.53	0.15	0.51	0.27	0.15	0.073	2.1
Common Systematic		0.10		0.02	0.16	0.57	0.04	0.21	0.16	0.08	0.133	0.3
Other Param. Sys.		0.12		0.05	0.10	0.18	0.03	0.07	0.12	0.05	0.098	0.2
Total Systematic		0.17		0.12	0.25	0.80	0.15	0.56	0.33	0.18	0.180	2.1
Total Error		0.44		0.29	0.60	2.06	0.35	1.15	0.73	0.40	0.437	3.4
$\langle\sqrt{s}\rangle$ GeV	92.05	92.94	93.90	92.95	92.99	92.99	92.99	—	93.10	92.91	92.95	92.95
Published $A_{\mathrm{FB}}^{\mathrm{b}}$	11.10	10.43	13.77	11.72	10.9	8.82	10.41	—	13.71	12.21	10.31	-2.1
Used $A_{\mathrm{FB}}^{\mathrm{b}}$		11.11		11.69	11.4	8.59	10.40	—	13.70	12.24	10.06	-0.2
Statistical		1.43		0.98	1.8	6.16	1.16	—	2.39	1.23	1.47	8.7
Internal Systematic		0.19		0.11	0.1	0.88	0.27	—	0.30	0.16	0.09	2.0
Common Systematic		0.16		0.02	0.1	0.48	0.03	—	0.19	0.12	0.17	1.2
Other Param. Sys.		0.19		0.12	0.2	0.54	0.04	—	0.14	0.10	0.17	0.7
Total Systematic		0.31		0.16	0.3	1.14	0.28	—	0.38	0.23	0.26	2.4
Total Error		1.46		0.99	1.8	6.27	1.19	—	2.42	1.25	1.50	9.0

Table 6.4: Results from the different b asymmetry measurements from the LEP experiments. The energies quoted are taken from the publications. The asymmetry values used are corrected to common energy points.

	ALEPH				**DELPHI**		**L3**	**OPAL**	
		lepton 91-95		D meson 91-95	lepton 91-95	D meson 92-95	lepton 90-95	lepton 90-00	D meson 90-95
$\langle\sqrt{s}\rangle$ GeV	88.38	89.38	90.21	89.37	89.43	89.43	—	89.51	89.49
Published $A_{\mathrm{FB}}^{\mathrm{c}}$	-12.4	-2.28	-0.34	-1.0	3.0	-4.96	—	-6.83	3.9
Used $A_{\mathrm{FB}}^{\mathrm{c}}$		-1.50		0.2	3.4	-4.35	—	-6.23	2.5
Statistical		2.44		4.3	3.4	3.55	—	2.48	4.9
Internal Systematic		0.17		0.9	0.3	0.34	—	0.89	0.8
Common Systematic		0.07		0.1	0.1	0.11	—	0.09	0.3
Other Param. Sys.		0.14		0.2	0.2	0.10	—	0.25	0.1
Total Systematic		0.23		0.9	0.4	0.37	—	0.93	0.8
Total Error		2.45		4.4	3.5	3.57	—	2.65	5.0
$\langle\sqrt{s}\rangle$ GeV		91.21		91.22	91.26	91.24	91.24	91.25	91.24
Published $A_{\mathrm{FB}}^{\mathrm{c}}$		6.45		6.3	6.31	6.59	7.84	5.683	6.3
Used $A_{\mathrm{FB}}^{\mathrm{c}}$		6.63		6.3	6.25	6.49	8.18	5.701	6.5
Statistical		0.56		0.9	0.92	0.93	3.03	0.539	1.2
Internal Systematic		0.24		0.2	0.52	0.26	1.71	0.192	0.5
Common Systematic		0.22		0.2	0.26	0.07	0.58	0.221	0.3
Other Param. Sys.		0.20		0.0	0.21	0.03	0.73	0.202	0.0
Total Systematic		0.38		0.3	0.61	0.27	1.95	0.356	0.6
Total Error		0.68		0.9	1.10	0.97	3.60	0.645	1.3
$\langle\sqrt{s}\rangle$ GeV	92.05	92.94	93.90	92.96	92.99	92.99	—	92.95	92.95
Published $A_{\mathrm{FB}}^{\mathrm{c}}$	10.58	11.93	12.09	11.0	10.8	11.80	—	14.59	15.8
Used $A_{\mathrm{FB}}^{\mathrm{c}}$		11.94		10.9	10.8	11.42	—	14.89	14.6
Statistical		1.98		3.3	2.8	3.09	—	2.02	4.0
Internal Systematic		0.35		0.7	0.4	0.55	—	0.50	0.7
Common Systematic		0.29		0.1	0.2	0.09	—	0.24	0.5
Other Param. Sys.		0.34		0.2	0.3	0.09	—	0.43	0.1
Total Systematic		0.57		0.7	0.5	0.56	—	0.70	0.9
Total Error		2.06		3.4	2.8	3.15	—	2.14	4.1

Table 6.5: Results from the different c asymmetry measurements from the LEP experiments. The energies quoted are taken from the publications. The asymmetry values used are corrected to common energy points.

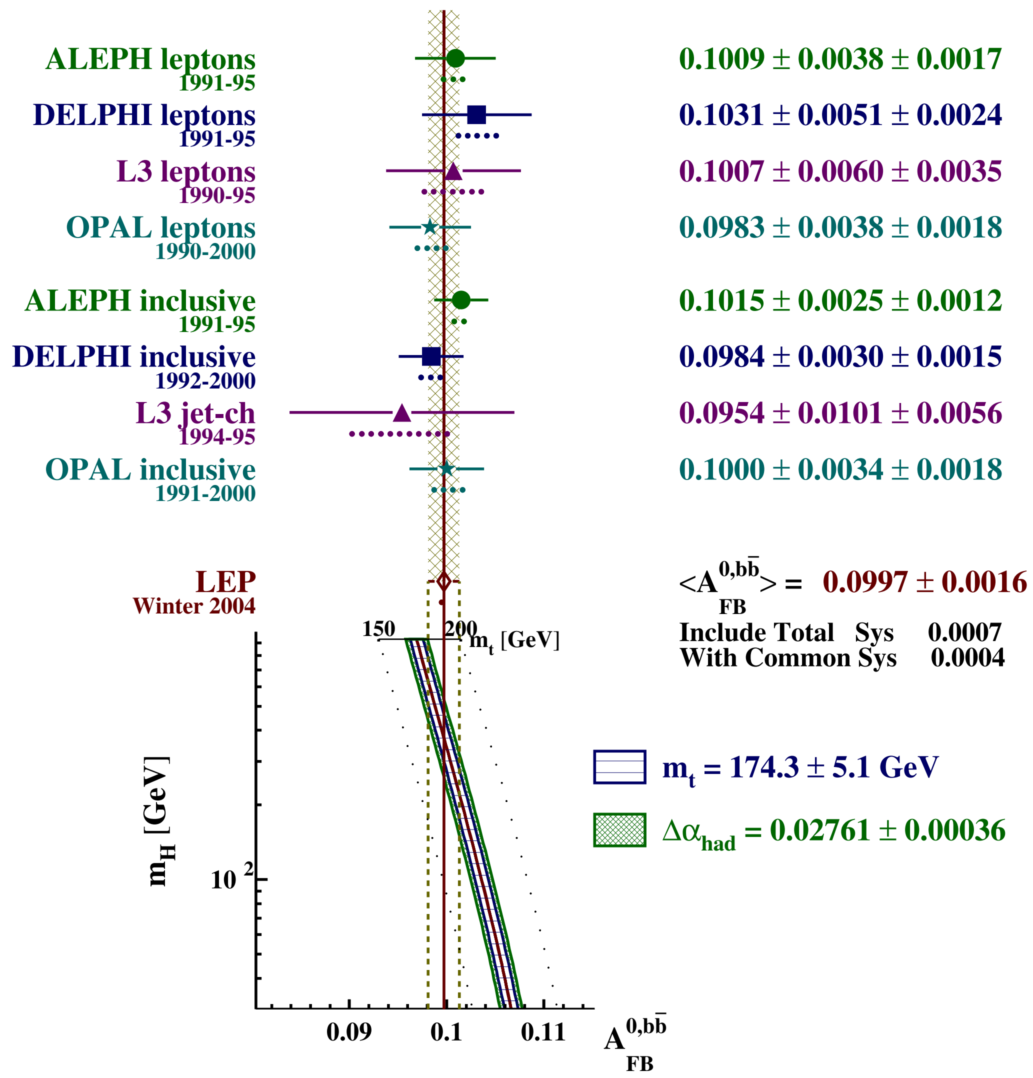

Figure 6.3: The b asymmetry measurements from the four LEP experiments. The contribution called "OPAL leptons" is the result from this thesis. The combined result represents the status of winter 2004. It is taken from the fit to all electroweak data obtained from heavy quark measurements [167].

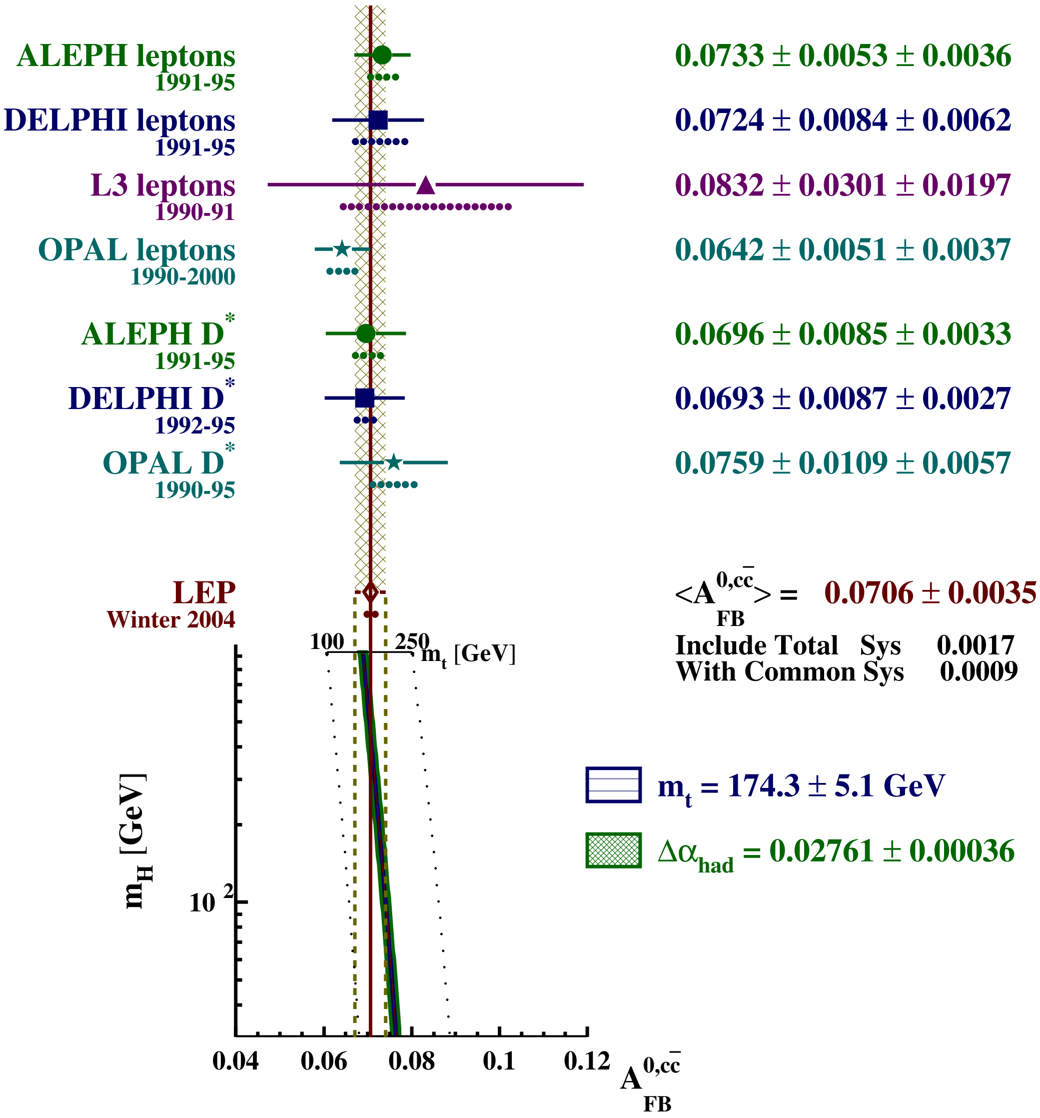

Figure 6.4: The c asymmetry measurements from the four LEP experiments. The contribution called "OPAL leptons" is the result from this thesis. The combined result represents the status of winter 2004. It is taken from the fit to all electroweak data obtained from heavy quark measurements [167].

Parameter	**LEP only**	**LEP + SLD**
R_{b}^0	0.21643±0.00073	0.21638±0.00065
R_{c}^0	0.1690 ± 0.0047	0.1720 ± 0.0030
$A_{\mathrm{FB}}^{0,\,\mathrm{b}}$ (%)	9.98 ± 0.16	9.97 ± 0.16
$A_{\mathrm{FB}}^{0,\,\mathrm{c}}$ (%)	7.02 ± 0.36	7.06 ± 0.35
$\mathcal{A}_{\mathrm{b}}$	—	0.925 ± 0.020
$\mathcal{A}_{\mathrm{c}}$	—	0.670 ± 0.026
χ^2/dof	49/(96 − 12)	53/(105 − 14)
Using only statistical uncertainties		
R_{b}^0	0.21616±0.00045	0.21618±0.00040
R_{c}^0	0.1689 ± 0.0023	0.1706 ± 0.0019
$A_{\mathrm{FB}}^{0,\,\mathrm{b}}$ (%)	9.96 ± 0.15	9.95 ± 0.15
$A_{\mathrm{FB}}^{0,\,\mathrm{c}}$ (%)	6.90 ± 0.29	6.91 ± 0.29
$\mathcal{A}_{\mathrm{b}}$	—	0.917 ± 0.015
$\mathcal{A}_{\mathrm{c}}$	—	0.666 ± 0.021
χ^2/dof	85/(96 − 12)	91/(105 − 14)

Table 6.6: Results from the fit to the LEP and SLD precision measurements in the heavy flavour sector. In the upper part of the table the results of the full fit are shown. The numbers on the left side only use inputs from LEP, those on the right side from LEP and SLD. The numbers listed in the lower part of the table are from fits which only use the statistical uncertainties of the inputs.

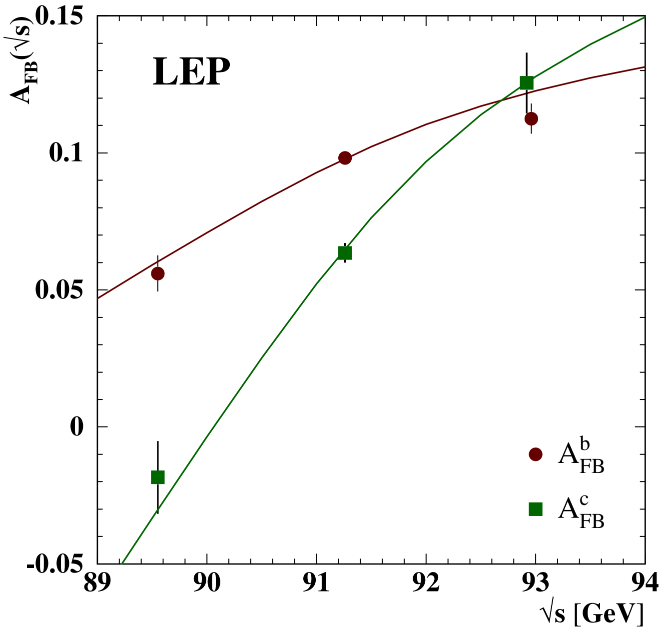

Figure 6.5: The LEP combined b and c quark forward-backward asymmetries as a function of the centre-of-mass energy $\sqrt{s}$.

	R_b^0	R_c^0	$A_{FB}^{0,b}$	$A_{FB}^{0,c}$	$\mathcal{A}_b$	$\mathcal{A}_c$
R_b^0	1.00	−0.14	−0.10	0.07	−0.07	0.05
	(1.00)	(−0.17)	(−0.08)	(0.07)		
R_c^0		1.00	0.03	−0.06	0.03	−0.05
		(1.00)	(0.08)	(−0.06)		
$A_{FB}^{0,b}$			1.00	0.15	0.03	−0.01
			(1.00)	(0.14)		
$A_{FB}^{0,c}$				1.00	−0.02	0.04
				(1.00)		
$\mathcal{A}_b$					1.00	0.13
$\mathcal{A}_c$						1.00

Table 6.7: The correlation matrix for the six electroweak parameters from the 14 parameter fit. In addition, the values of the correlation matrix of the four parameters of the 12 parameter fit are given in brackets.

	R_{b}^{0} $(\cdot 10^{-3})$	R_{c}^{0} $(\cdot 10^{-3})$	$A_{\mathrm{FB}}^{0,\mathrm{b}}$ $(\cdot 10^{-3})$	$A_{\mathrm{FB}}^{0,\mathrm{c}}$ $(\cdot 10^{-3})$	$\mathcal{A}_{\mathrm{b}}$ $(\cdot 10^{-2})$	$\mathcal{A}_{\mathrm{c}}$ $(\cdot 10^{-2})$
statistics	0.43	2.3	1.5	3.0	1.5	2.1
internal systematics	0.28	1.4	0.6	1.4	1.4	1.6
QCD effects	0.18	0.1	0.4	0.1	0.3	0.2
semil. B,D decay model	0.01	0.1	0.1	0.5	0.1	0.1
BR(D $\rightarrow$ neutral)	0.14	0.3	0	0	0	0
D decay multiplicity	0.13	0.3	0	0.2	0	0
BR($\mathrm{D}^{+} \rightarrow \mathrm{K}^{-}\pi^{+}\pi^{+}$)	0.08	0.2	0	0.1	0	0
BR($\mathrm{D}_{\mathrm{s}}^{+} \rightarrow \phi\pi^{+}$)	0.02	0.5	0	0.1	0	0
BR($\Lambda_{\mathrm{c}} \rightarrow \mathrm{p}\ \mathrm{K}^{-}\pi^{+}$)	0.06	0.5	0	0.1	0	0
D lifetimes	0.06	0.1	0	0.2	0	0
gluon splitting	0.22	0.1	0.1	0.2	0.1	0.1
c fragmentation	0.10	0.2	0.1	0.1	0.1	0.1
light quarks	0.07	0.2	0	0	0	0
beam polarisation	0	0	0	0	0.5	0.4
total	0.65	3.1	1.6	3.5	2.0	2.6

Table 6.8: The dominant error sources for the electroweak parameters from the 14 parameter fit.

the non-electroweak parameters are independent of the treatment of the off-peak asymmetries and the SLD data.

The combined results for the electroweak parameters obtained form the 12 and 14 parameter fit are quoted in Table 6.6 [167]. The corresponding statistical correlation matrices are given in Table 6.7 [167]. The correlated systematic errors for the fit parameters arise from mainly physics motivated sources like the QCD correction and quark fragmentation. A list of the dominant sources of common systematic uncertainties together with their contribution to the total errors on the six heavy flavour fit parameters R_{b}^{0}, R_{c}^{0}, $A_{\mathrm{FB}}^{0,\mathrm{b}}$, $A_{\mathrm{FB}}^{0,\mathrm{c}}$, $\mathcal{A}_{\mathrm{b}}$, and $\mathcal{A}_{\mathrm{c}}$ are given in Table 6.8. All common systematic errors add up to a total of 0.04 for the b asymmetry and 0.09 for the c asymmetry (Figure 6.3 and 6.4) [167]. Compared to the total uncertainties of $A_{\mathrm{FB}}^{0,\mathrm{b}}$ and $A_{\mathrm{FB}}^{0,\mathrm{c}}$ these values are very small.

For comparison the fits are performed using only statistical uncertainties (lower part of Table 6.6). The small shifts of the values are due to the different ratio of statistical and systematical uncertainties within the different analyses. The large difference in the χ^2 value indicates that the systematical uncertainties are estimated in a conservative way.

Results from additional tests are summarised in Table 6.9. To show the impact of the off-peak data on the pole asymmetries and their uncertainties, the com-

	$A_{\mathrm{FB}}^{0,\,\mathrm{b}}$ (%)	$A_{\mathrm{FB}}^{0,\,\mathrm{c}}$ (%)
Full 14 parameter fit	9.97 ±0.16	7.06±0.35
Peak asymmetries only	10.05±0.17	6.93±0.36
no OPAL leptons	10.00±0.17	7.29±0.39
inclusive	10.05±0.19	—
lepton	10.01±0.25	7.04±0.44
D meson	7.63 ±1.67	7.42±0.61

Table 6.9: The upper part of the table shows the impact of the off-peak measurements and the OPAL measurement using semileptonic b and c decays on the combined asymmetries. In the lower part the combined values of different types of measurement are given.

bination is made using only on-peak asymmetry measurements. The errors are just affected very little, but the b asymmetry increases by half a standard deviation while the c asymmetry decreases by 1/3 of its uncertainty. To illustrate the influence of the OPAL measurement of $A_{\mathrm{FB}}^{\mathrm{b}}$ and $A_{\mathrm{FB}}^{\mathrm{c}}$ using the semileptonic decays (Chapter 5) on the combined LEP results, the fit is repeated excluding these measurements. This leaves the b asymmetry almost unchanged. The c asymmetry increases by 2/3 of its standard deviation. Table 6.9 also lists LEP averages for $A_{\mathrm{FB}}^{0,\,\mathrm{b}}$ and $A_{\mathrm{FB}}^{0,\,\mathrm{c}}$ using only a particular type of measurement. These combined values are in very good agreement among each other.

6.4 Effective Couplings of the Neutral Weak Current

The experimental results on electroweak observables are used to derive values for the effective couplings of the neutral weak current at the Z pole: the asymmetry parameters $\mathcal{A}_{\mathrm{f}}$, the effective vector and axial-vector coupling constants v_{f} and a_{f}, the effective electroweak mixing angles for b and c quarks $\sin^2\theta_{\mathrm{eff}}^{\mathrm{b}}$ and $\sin^2\theta_{\mathrm{eff}}^{\mathrm{c}}$, and the leptonic effective electroweak mixing angle $\sin^2\theta_{\mathrm{eff}}^{\ell}$.

6.4.1 The Asymmetry Parameters $\mathcal{A}_{\mathrm{f}}$

Due to polarised electron beams at SLC a direct determination of the asymmetry parameters $\mathcal{A}_{\mathrm{f}}$ is possible by analysing the left-right and left-right forward-backward asymmetry $A_{\mathrm{LR}}^{0} = \mathcal{A}_{\mathrm{e}}$ and $A_{\mathrm{LRFB}}^{\mathrm{f}} = (3/4)\mathcal{A}_{\mathrm{f}}$. The analyses of the τ polarisation and its forward-backward asymmetry at LEP determine $\mathcal{A}_{\tau}$ and $\mathcal{A}_{\mathrm{e}}$

Parameter	**Average**	**Correlations**		
		$\mathcal{A}_e$	$\mathcal{A}_\mu$	$\mathcal{A}_\tau$
$\mathcal{A}_e$	0.1514±0.0019	1.00		
$\mathcal{A}_\mu$	0.1456±0.0091	−0.10	1.00	
$\mathcal{A}_\tau$	0.1449±0.0040	−0.02	0.01	1.00
$\mathcal{A}_\ell$	0.1501±0.0016			

Table 6.10: Results on the leptonic asymmetry parameters $\mathcal{A}_\ell$ not assuming neutral-current lepton universality using the 14 electroweak measurements from [167]. The combination has a χ^2/dof of 3.6/5, corresponding to a probability of 61%.

parameter	$\mathcal{A}_q = \frac{4}{3}\frac{A_{FB}^{0,q}}{\mathcal{A}_\ell}$	**Direct** $\mathcal{A}_q$	**Standard Model**
$\mathcal{A}_b$	0.886±0.017	0.925±0.020	0.935±0.001
$\mathcal{A}_c$	0.627±0.032	0.670±0.026	0.668±0.002

Table 6.11: Determination of the quark asymmetry parameters $\mathcal{A}_q$, based on the ratio $A_{FB}^{0,q}/\mathcal{A}_\ell$ and the direct measurement A_{LRFB}^{q}. Lepton universality for $\mathcal{A}_\ell$ is assumed. The expectation of $\mathcal{A}_q$ in the Standard Model is listed in the last column [167].

separately. The forward-backward pole asymmetries $A_{FB}^{0,f} = (3/4)\mathcal{A}_e\mathcal{A}_f$ constrain the product of two asymmetry parameters. The measurements are performed separately for all three charged lepton species as well as the heavy quark flavours b and c.

The combined results on the leptonic asymmetry parameters $\mathcal{A}_e$, $\mathcal{A}_\mu$, and $\mathcal{A}_\tau$, derived from measurements independent of quark asymmetry parameters, are listed in Table 6.10 together with the combined result for $\mathcal{A}_\ell$, assuming neutral-current lepton universality [167].

In Table 6.11 the measured quark asymmetry parameters $\mathcal{A}_q$ are shown. The ratio of the forward-backward pole asymmetries $A_{FB}^{0,b}/A_{FB}^{0,c} = \mathcal{A}_b/\mathcal{A}_c$ agree well with the ratio of the asymmetry parameters $\mathcal{A}_b$ and $\mathcal{A}_c$ from direct measurements.

Each ratio $(4/3)A_{FB}^{0,q}/\mathcal{A}_\ell$ also determines $\mathcal{A}_q$ indirectly using LEP data, with a precision comparable to that of the direct measurements at SLD. Good agreement between the direct and indirect results for c quarks is observed. In the case of b quarks, the ratio $(4/3)A_{FB}^{0,q}/\mathcal{A}_\ell$ is lower than the direct measurement of $\mathcal{A}_b$ by 1.4 standard deviations, and lower than the Standard Model expectation by 2.8 standard deviations.

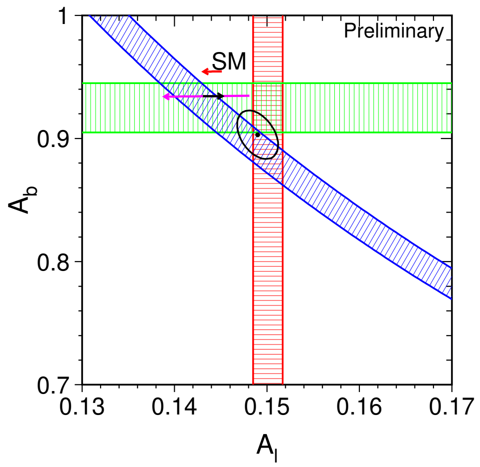

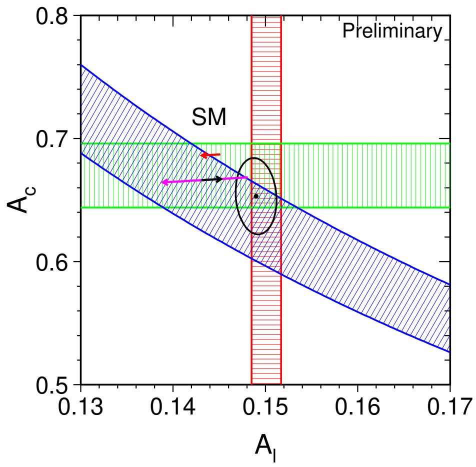

Figure 6.6: Comparison of the measurements of $\mathcal{A}_\ell$, $\mathcal{A}_\mathrm{q}$ and $A_\mathrm{FB}^{0,\mathrm{q}}$ for b quarks (left), and c quarks (right) assuming lepton universality [167]. Bands of ± 1 standard deviation width in the $(\mathcal{A}_\ell, \mathcal{A}_\mathrm{q})$ plane are shown for the measurements of $\mathcal{A}_\ell$ (vertical band), $\mathcal{A}_\mathrm{q}$ (horizontal band), and $A_\mathrm{FB}^{0,\mathrm{q}} = (3/4)\mathcal{A}_\mathrm{e}\mathcal{A}_\mathrm{q}$ (diagonal band). Also shown is the 68% confidence level contour for the two asymmetry parameters resulting from the joint analysis (Table 6.12). The arrows pointing to the right and to the left show the variation in the Standard Model prediction for varying m_t in the range 174.3 ± 5.1 GeV$/c^2$ and m_H in the range of 300^{+700}_{-186} GeV$/c^2$ respectively. The arrow showing the small dependence on the hadronic vacuum polarisation $\Delta\alpha^{(5)}_\mathrm{had}(m_\mathrm{Z}^2) = 0.02761 \pm 0.00036$ is displaced for clarity. The arrows point in the direction of increasing values of these parameters.

Parameter	**Average**	**Correlations**		
		$\mathcal{A}_\ell$	$\mathcal{A}_\mathrm{b}$	$\mathcal{A}_\mathrm{c}$
$\mathcal{A}_\ell$	0.1490±0.0015	1.00		
$\mathcal{A}_\mathrm{b}$	0.903±0.013	−0.42	1.00	
$\mathcal{A}_\mathrm{c}$	0.653±0.020	−0.11	0.15	1.00

Table 6.12: Results on the quark asymmetry parameters $\mathcal{A}_\mathrm{q}$ and the leptonic asymmetry parameter $\mathcal{A}_\ell$ assuming neutral-current lepton universality using all measurements from LEP and SLD [167]. The combination has a χ^2/dof of 8.9/9, corresponding to a probability of 44%.

The results of the joint analysis of the leptonic and heavy flavour measurements in terms of the asymmetry parameters $\mathcal{A}_\mathrm{f}$ are shown as the error ellipses in Figure 6.6 and listed in Table 6.12, where the constraint of lepton universality is also imposed. Since $\mathcal{A}_\ell$ and $A_\mathrm{FB}^{0,\,\mathrm{b}}$ are already determined with relatively small errors, the joint analysis primarily improves the determination of the b quark asymmetry parameter $\mathcal{A}_\mathrm{b}$. The results have a region of common overlap with the combined $A_\mathrm{FB}^{0,\,\mathrm{b,c}}$ from LEP if both $\mathcal{A}_\mathrm{b,c}$ and $\mathcal{A}_\ell$ are free parameters. Although the overlap region agrees poorly with the Standard Model expectation for b quarks, the single results and especially $A_\mathrm{FB}^{0,\,\mathrm{c}}$ from LEP are well compatible with the expectation.

6.4.2 The Effective Vector and Axial-Vector Coupling Constants

For charged leptons and neutrinos the results on v_f and a_f are listed in Table 6.13 [167]. By attributing the entire invisible decay width of the Z to the production of neutrino pairs, the magnitude of the effective coupling of the Z boson to neutrinos can be determined. Three light neutrino families with equal effective coupling constants and $v_\nu \equiv a_\nu$ are assumed. The combined results under the assumption of neutral-current lepton universality are also shown in Table 6.13. The value of a_ℓ is different from the corresponding Born-level value of $T_3^\ell = -1/2$ by 4.7 standard deviations, indicating the presence of non-QED electroweak radiative corrections.

Including the heavy quark measurements and assuming lepton universality, the couplings of quarks and charged leptons are shown in Table 6.14 [167]. The vector coupling constant for charged leptons is decreased in magnitude compared to its Standard Model expectation, as already observed for the asymmetry parameter $\mathcal{A}_\ell$ in the previous section. For the quark flavours b and c, the results are also shown in Figure 6.7. The apparent deviation of the measured b quark coupling constants from the Standard Model expectation is a direct consequence of the combined result on $\mathcal{A}_\mathrm{b}$ being lower than the Standard Model expectation, as discussed in the previous section.

6.4.3 The Effective Electroweak Mixing Angles

For the following analyses, the electric charge Q_f and the third component of the weak isospin T_3^f are assumed to be given by the Standard Model assignments as listed in Table 2.1. Tests of fermion universality, i.e. a comparison between leptons and quarks in terms of ρ_f and $\sin^2\theta_\mathrm{eff}^\mathrm{f}$, now become possible.

Parameter	**Average**	**Correlations**						
		a_ν	a_e	a_μ	a_τ	v_e	v_μ	v_τ
$a_\nu \equiv v_\nu$	$+0.50076\pm0.00076$	1.00						
a_e	-0.50111 ± 0.00035	-0.74	1.00					
a_μ	-0.50120 ± 0.00054	0.39	-0.13	1.00				
a_τ	-0.50204 ± 0.00064	0.37	-0.12	0.35	1.00			
v_e	-0.03816 ± 0.00047	-0.10	0.01	-0.01	-0.03	1.00		
v_μ	-0.0367 ± 0.0023	0.02	0.00	-0.30	0.01	-0.10	1.00	
v_τ	-0.0366 ± 0.0010	0.02	-0.01	0.01	-0.07	-0.02	0.01	1.00
a_ℓ	-0.50123 ± 0.00026							
v_ℓ	-0.03783 ± 0.00041							

Table 6.13: Results on the effective vector and axial-vector coupling constants for leptons not assuming neutral-current lepton universality [167]. The combination has a χ^2/dof of 3.6/5, corresponding to a probability of 61 %. The combination to the effective leptonic vector and axial-vector coupling constants has a χ^2/dof of 7.8/9, corresponding to a probability of 56 % with correlations of -0.48, -0.03 and -0.06 between (a_ν, a_ℓ), (a_ν, v_ℓ) and (a_ℓ, v_ℓ) respectively.

Parameter	**Average**	**Correlations**						
		a_ν	a_ℓ	a_b	a_c	v_ℓ	v_b	v_c
$a_\nu \equiv v_\nu$	$+0.50075\pm0.00077$	1.00						
a_ℓ	-0.50125 ± 0.00026	-0.49	1.00					
a_b	-0.5140 ± 0.0051	0.01	-0.01	1.00				
a_c	$+0.5027\pm0.0054$	-0.02	-0.02	0.00	1.00			
v_ℓ	-0.03758 ± 0.00037	-0.04	-0.04	0.38	-0.05	1.00		
v_b	-0.3231 ± 0.0078	0.01	0.05	-0.97	0.03	-0.39	1.00	
v_c	$+0.1880\pm0.0070$	-0.01	-0.02	0.15	-0.32	0.10	-0.17	1.00

Table 6.14: Results on the effective coupling constants for leptons and quarks assuming neutral-current lepton universality [167]. The combination has a χ^2/dof of 8.9/9, corresponding to a probability of 43 %.

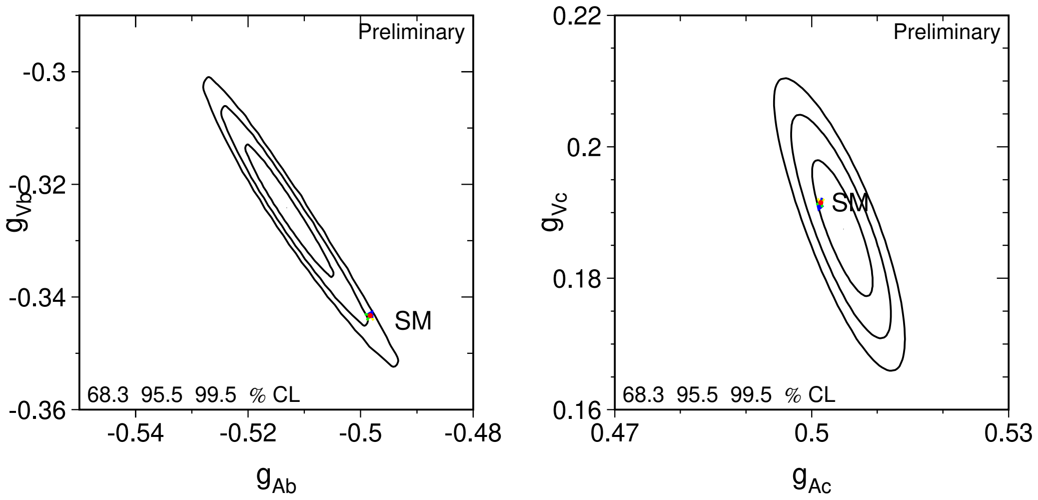

Figure 6.7: Comparison of the effective vector and axial-vector coupling constants for heavy quarks, using results on leptons and assuming lepton universality (see Table 6.14) [167]. Varying the hadronic vacuum polarisation by $\Delta\alpha^{(5)}_{\mathrm{had}}(m^2_{\mathrm{Z}}) = 0.02761 \pm 0.00036$ yields an additional uncertainty on the Standard Model prediction. Compared to the experimental uncertainties, the Standard Model predictions for the heavy quarks b and c are nearly constant for the quark coupling constants.

The results on ρ_{f} and the effective electroweak mixing angle for leptons and quarks are listed in Table 6.15. As before, neutral-current lepton universality is assumed. The value of ρ_ℓ is different from the corresponding Born-level value of unity by 5.0 standard deviations, indicating the presence of non-QED electroweak radiative corrections. The strong correlation between ρ_{b} and $\sin^2\theta^{\mathrm{b}}_{\mathrm{eff}}$ arises as the anti-correlation between v_{b} and a_{b} (see Table 6.14) from the tight constraint given by the measurement of $R^0_{\mathrm{b}} \propto v^2_{\mathrm{b}} + a^2_{\mathrm{b}}$.

Within the Standard Model, slightly different values for $\sin^2\theta^{\mathrm{f}}_{\mathrm{eff}}$ are expected for different fermions due to non-universal flavour-specific electroweak radiative corrections. These specific corrections are largest for b quarks and more than a factor of five smaller for the other quark flavours. Except for b quarks, the non-universal flavour-specific corrections expected in the Standard Model are small compared to the experimental errors.

6.4.4 The Leptonic Effective Electroweak Mixing Angle

The measurements of the various asymmetries determine the effective electroweak mixing angle $\sin^2\theta^{\mathrm{f}}_{\mathrm{eff}}$ independently of ρ_{f}, because they depend only on $v_{\mathrm{f}}/a_{\mathrm{f}}$. As

Parameter	Average	Correlations						
		ρ_ν	ρ_ℓ	ρ_b	ρ_c	$\sin^2\theta^\ell_\mathrm{eff}$	$\sin^2\theta^\mathrm{b}_\mathrm{eff}$	$\sin^2\theta^\mathrm{c}_\mathrm{eff}$
ρ_ν	1.0030±0.0031	1.00						
ρ_ℓ	1.0050±0.0010	0.49	1.00					
ρ_b	1.055±0.021	−0.01	−0.01	1.00				
ρ_c	1.011±0.022	−0.02	0.02	0.00	1.00			
$\sin^2\theta^\ell_\mathrm{eff}$	0.23129±0.00018	−0.01	0.09	−0.38	−0.04	1.00		
$\sin^2\theta^\mathrm{b}_\mathrm{eff}$	0.278±0.016	0.00	−0.04	0.99	0.02	−0.39	1.00	
$\sin^2\theta^\mathrm{c}_\mathrm{eff}$	0.2347±0.0059	0.00	−0.01	0.13	0.54	−0.10	0.15	1.00
ρ_ν	1.0030±0.0031	1.00						
ρ_ℓ	1.0049±0.0010	+0.48	1.00					
$\sin^2\theta^\ell_\mathrm{eff}$	0.23113±0.00021	−0.01	0.11			1.00		

Table 6.15: Results on the ρ parameter and the effective electroweak mixing angle $\sin^2\theta^\mathrm{f}_\mathrm{eff}$ assuming neutral-current lepton universality, using the 14 electroweak measurements [167]. The combination has a χ^2/dof of 4.3/4, corresponding to a probability of 40%. The lower part of the table gives values for ρ and $\sin^2\theta^\ell_\mathrm{eff}$ considering the leptonic measurements only. This average has a χ^2/dof of 7.8/9, corresponding to a probability of 56%.

illustrated in Figure 2.6 the relative sensitivity of $\mathcal{A}_\mathrm{q}$ to $\sin^2\theta^\mathrm{q}_\mathrm{eff}$ is much smaller than is the case for leptons. In particular for b quarks this sensitivity is almost a factor 100 less than it is for leptons. Therefore, the heavy quark forward-backward asymmetries $A^{0,\mathrm{q}}_\mathrm{FB} = (3/4)\mathcal{A}_\mathrm{e}\mathcal{A}_\mathrm{q}$ as well as the hadronic charge asymmetry $Q^\mathrm{had}_\mathrm{FB}$ are sensitive to $\sin^2\theta^\ell_\mathrm{eff}$ through the factor $\mathcal{A}_\mathrm{e}$ and rather insensitive to $\sin^2\theta^\mathrm{q}_\mathrm{eff}$.

There are six asymmetry measurements sensitive to $\sin^2\theta^\ell_\mathrm{eff}$. The resulting $\sin^2\theta^\ell_\mathrm{eff}$ values are compared in Figure 6.8. The measurements fall into two sets of three results each:

- measurements depending on leptonic couplings only ($A^{0,\ell}_\mathrm{FB}$, $\mathcal{A}_\ell$(SLD) and $\mathcal{A}_\ell(P_\tau)$) or
- measurements depending on both, leptonic and quark couplings ($A^{0,\mathrm{b}}_\mathrm{FB}$, $A^{0,\mathrm{c}}_\mathrm{FB}$ and $Q^\mathrm{had}_\mathrm{FB}$).

In the first case only lepton universality is assumed. No further corrections are necessary to interpret the results in terms of $\sin^2\theta^\ell_\mathrm{eff}$. In the second case small flavour-specific electroweak corrections, making $\sin^2\theta^\ell_\mathrm{eff}$ different from $\sin^2\theta^\mathrm{q}_\mathrm{eff}$, are taken from Standard Model predictions. The effect of these corrections and their uncertainties on the extracted value of $\sin^2\theta^\ell_\mathrm{eff}$ is negligible.

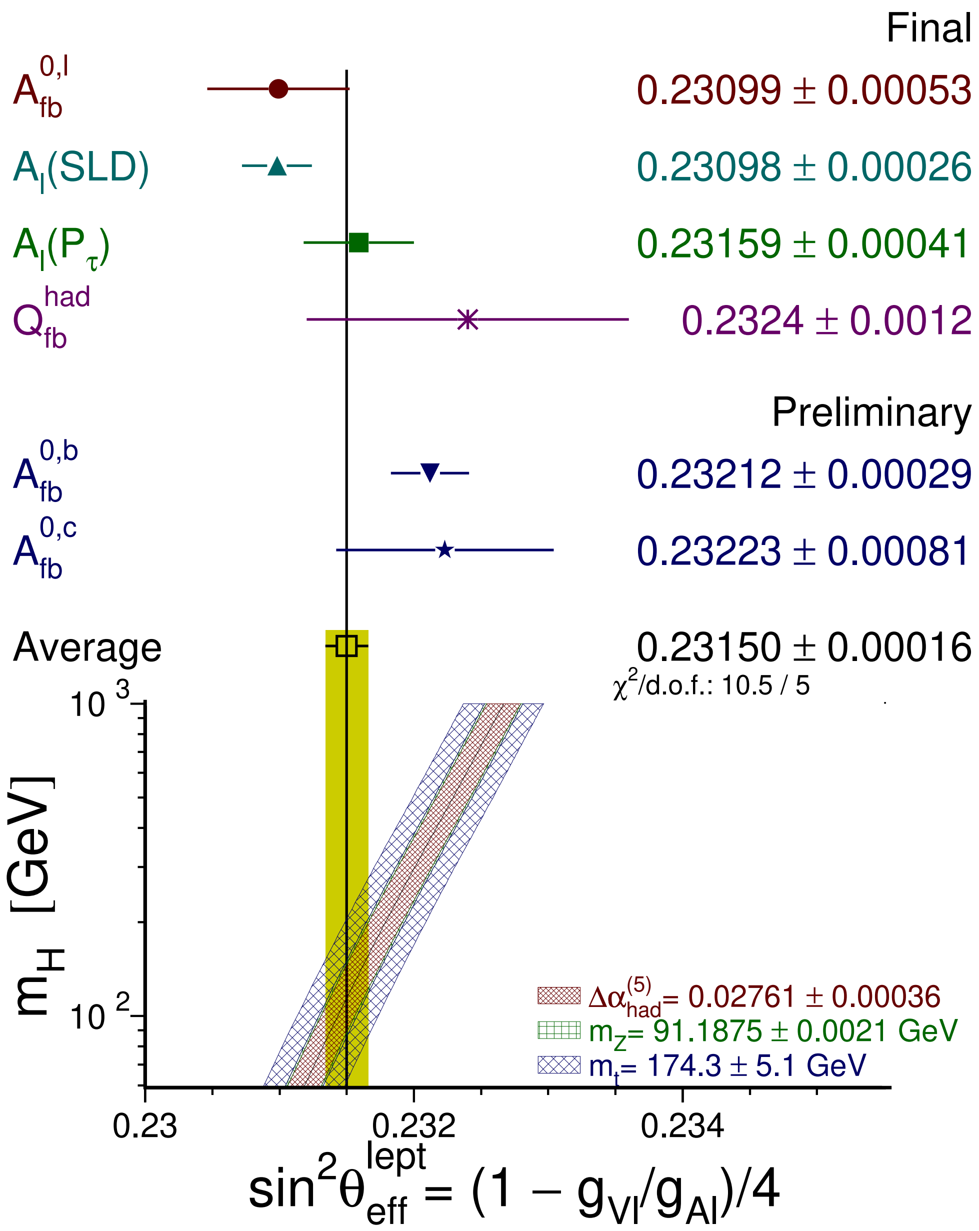

Figure 6.8: Comparison of the effective electroweak mixing angle $\sin^2\theta^\ell_{\mathrm{eff}}$ derived from measurement results depending on lepton couplings only (top) and also quark couplings (bottom) [167]. Also shown is the prediction of $\sin^2\theta^\ell_{\mathrm{eff}}$ in the Standard Model as a function of m_{H}.

The average of all six $\sin^2\theta^{\ell}_{\mathrm{eff}}$ determinations is quoted to be [167]:

$$\sin^2\theta^{\ell}_{\mathrm{eff}} \;=\; 0.23150 \pm 0.00016\,, \tag{6.11}$$

with a χ^2/dof of 10.5/5, corresponding to a probability of 6.2%. The enlarged χ^2/dof is solely driven by the two most precise measurements used for the determinations of $\sin^2\theta^{\ell}_{\mathrm{eff}}$:

- the SLD measurement of $\mathcal{A}_{\ell}$, dominated by the A^{0}_{LR} result, and
- the LEP value of $A^{0,\,\mathrm{b}}_{\mathrm{FB}}$.

Those yield the largest pulls[2] and fall on opposite sides of the $\sin^2\theta^{\ell}_{\mathrm{eff}}$ average. These two measurements differ by 2.9 standard deviations. Thus, the two sets of measurements, yielding average values for $\sin^2\theta^{\ell}_{\mathrm{eff}}$ of 0.23113 ± 0.00021 (χ^2/dof = 1.64/2, probability 44 %) and 0.23214 ± 0.00027 (χ^2/dof = 0.06/2, probability 97 %) [167] respectively, also differ by about 2.9 standard deviations. This is a consequence of the same effect: the deviation of $\mathcal{A}_{\mathrm{b}}$ as extracted from $A^{0,\,\mathrm{b}}_{\mathrm{FB}}$ compared to its Standard Model value is reflected in the value of $\sin^2\theta^{\ell}_{\mathrm{eff}}$ extracted from $A^{0,\,\mathrm{b}}_{\mathrm{FB}}$.

The difference in $\sin^2\theta^{\ell}_{\mathrm{eff}}$ from the $A^{0,\,\mathrm{b}}_{\mathrm{FB}}$ measurement at LEP and the A^{0}_{LR} measurement at SLD is observed since the beginning of asymmetry measurements at LEP and SLD with almost constant level of significance. The history of the contributions to $\sin^2\theta^{\ell}_{\mathrm{eff}}$ from $A^{0,\,\mathrm{b}}_{\mathrm{FB}}$ and A^{0}_{LR} is illustrated in Figure 6.9.

Especially the $A^{0,\,\mathrm{b}}_{\mathrm{FB}}$ average has been stable over the time, while the precision has been continuously improved due to updated measurements using latest data reprocessing and new analysis techniques. While the precision was improved, the central values of the two contributions to $\sin^2\theta^{\ell}_{\mathrm{eff}}$ came closer so that the significance of their difference did not change much. In this way the effect is neither confirmed nor ruled out, and a statistical fluctuation as the cause cannot be excluded.

6.5 Interpretation

6.5.1 Effective Couplings

The results of the analyses for asymmetry parameters, effective coupling constants, ρ_{f} and $\sin^2\theta^{\ell}_{\mathrm{eff}}$ presented in the previous section show shifts and differences

[2] Here, the pull is defined as the difference between measured value and predicted value in units of the measurement uncertainty.

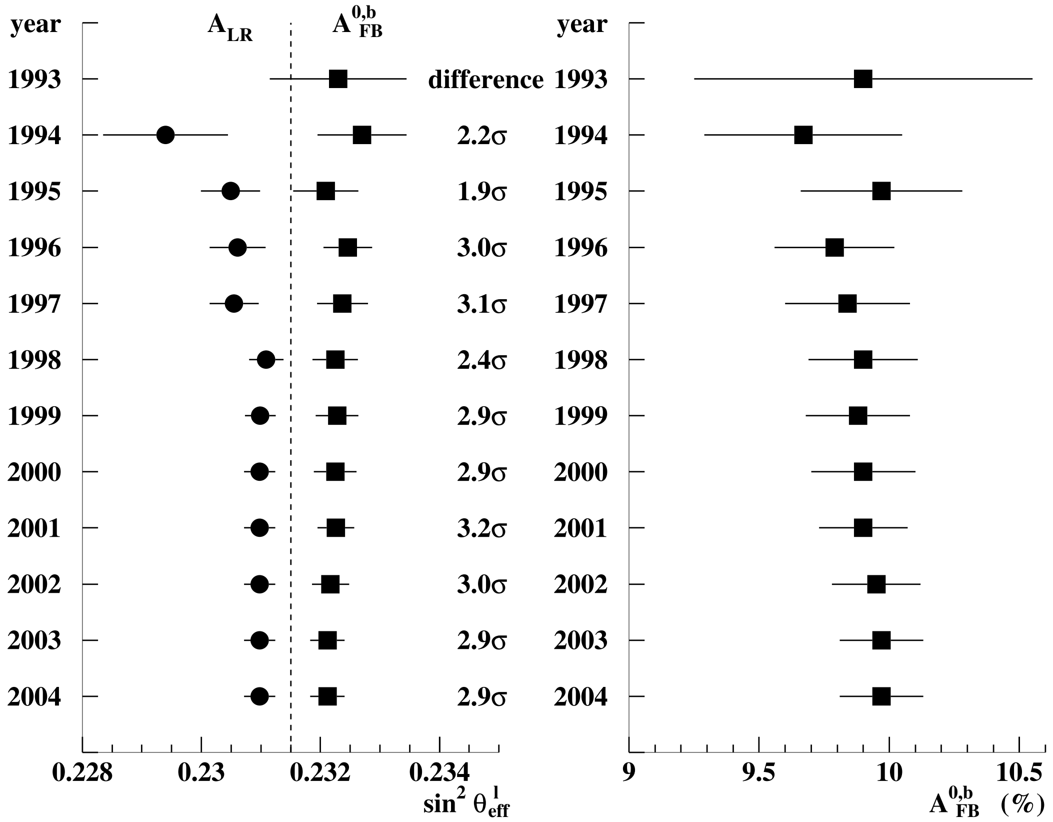

Figure 6.9: Time development of $\sin^2\theta^{\ell}_{\mathrm{eff}}$ and $A^{0,\mathrm{b}}_{\mathrm{FB}}$ results [51, 159, 167–174].

which are most clearly visible in the averages of effective couplings (Figure 6.7) and $\sin^2\theta^{\ell}_{\mathrm{eff}}$ (Figure 6.8). These discrepancies are dominated by the measurements of A^0_{LR} (SLD) and $A^{0,\mathrm{b}}_{\mathrm{FB}}$ (LEP). Concerning $\sin^2\theta^{\ell}_{\mathrm{eff}}$, the leptonic forward-backward asymmetry $A^{0,\ell}_{\mathrm{FB}}$ and the τ polarisation measurement confirm the A^0_{LR} result, while $A^{0,\mathrm{c}}_{\mathrm{FB}}$ delivers a value for $\sin^2\theta^{\ell}_{\mathrm{eff}}$ very close to that of $A^{0,\mathrm{b}}_{\mathrm{FB}}$. The main effect responsible for these differences is caused by the effective couplings for b quarks (Figure 6.7). The vector and axial-vector couplings for b quarks v_{b} and a_{b} deviate from the Standard Model expectation at the level of two standard deviations.

Using the left- and right-handed couplings $c^{\mathrm{b}}_{\mathrm{L}}$ and $c^{\mathrm{b}}_{\mathrm{R}}$ introduced in Eq. 2.10 (they are much better aligned with the axes of the error ellipse), only $c^{\mathrm{b}}_{\mathrm{R}}$ shows a noticeable deviation from the expectation. Due to $c^{\mathrm{b}}_{\mathrm{R}} \ll c^{\mathrm{b}}_{\mathrm{L}}$ (Eq. 2.10 together with measured values of a_{f} and v_{f} from Table 6.14) the value of $R^0_{\mathrm{b}} \propto (c^{\mathrm{b}}_{\mathrm{R}})^2 + (c^{\mathrm{b}}_{\mathrm{L}})^2$ shows no discrepancy from the expectation.

The results summarised in Section 6.4 therefore suggest an explanation in terms of a possible shift in the Standard Model prediction of the right-handed b quark coupling alone, even at Born-level. This affects $\mathcal{A}_{\mathrm{b}}$ and $A_{\mathrm{FB}}^{0,\mathrm{b}}$, which both depend only on the ratio $c_{\mathrm{R}}^{\mathrm{b}}/c_{\mathrm{L}}^{\mathrm{b}}$, more strongly than R_{b}^{0}.

From the experimental point of view, no systematic effect has been identified, which explains such shifts in the $A_{\mathrm{FB}}^{0,\mathrm{b}}$ measurement [13, 76, 77, 151–158]. While the QCD corrections are significant, their uncertainties are small compared to the total errors and are taken into account. Within the Standard Model, flavour specific electroweak radiative corrections [175] are much too small to explain the difference in the extracted $\sin^2\theta_{\mathrm{eff}}^{\ell}$ values. The same holds for the A_{LR}^{0} measurement. Here the most important source of systematic uncertainty is the determination of the beam polarisation. This uncertainty is believed to be small and well controlled.

Thus the shift is either a sign for new physics, invalidating the simple relations to convert between the effective parameters used, or a fluctuation in one or more of the input measurements.

6.5.2 Prediction of the Higgs Boson Mass

Due to higher order electroweak radiative corrections many electroweak precision observables can be used to probe the Higgs sector of the Standard Model. The sensitivity of the forward-backward asymmetries to the Higgs boson mass m_{H} has been discussed in Section 2.4. It provides an indirect way of gaining information on m_{H}, assuming that the Standard Model provides an adequate description of nature. The resulting constraints can be compared to the mass values which have been excluded by the direct search for the Higgs boson. The constraints on the Higgs boson mass from the measurements of the different electroweak observables are shown in Figure 6.10. It can be seen that $A_{\mathrm{FB}}^{0,\mathrm{b}}$ and A_{LR}^{0} are the two quantities that yield the highest sensitivity to m_{H}, followed by the W boson mass.

The current combined prediction for m_{H} is quoted to be $m_{\mathrm{H}} = 113^{+62}_{-42}\mathrm{GeV}/c^2$ (68 % C.L.) [15]. This value is extracted from a 5 parameter (m_{Z}, Γ_{Z}, α_{s}, $\Delta\alpha_{\mathrm{had}}^{(5)}(m_{\mathrm{Z}}^2)$ and m_{H}) Standard Model fit to all high Q^2 precision measurements[3] available from LEP and SLD. The global χ^2/dof of the Standard Model fit is 16.3/13, corresponding to a probability of 23 %. The largest contribution to the overall χ^2 originates from the pull of 2.4 standard deviations of the measurement of $A_{\mathrm{FB}}^{0,\mathrm{b}}$ at LEP. Two other measurements, the left-right asymmetry measured at SLD and the W boson mass, also have a large pull of 1.7 and 1.2 standard deviations, respectively.

Only $A_{\mathrm{FB}}^{0,\mathrm{b}}$ clearly favours a large value for m_{H}. It is interesting that also $A_{\mathrm{FB}}^{0,\mathrm{c}}$ indicates a Higgs mass which is very close to the average. The direct relation

[3] m_{Z}, Γ_{Z}, σ_{h}^{0}, R_{ℓ}, $A_{\mathrm{FB}}^{0,\ell}$, R_{b}, R_{c}, $A_{\mathrm{FB}}^{0,\mathrm{b}}$, $A_{\mathrm{FB}}^{0,\mathrm{c}}$, $\mathcal{A}_{\ell}$, $\mathcal{A}_{\mathrm{b}}$, $\mathcal{A}_{\mathrm{c}}$, $\Delta\alpha_{\mathrm{had}}^{(5)}(m_{\mathrm{Z}}^2)$, m_{W}, Γ_{w}, m_{t}

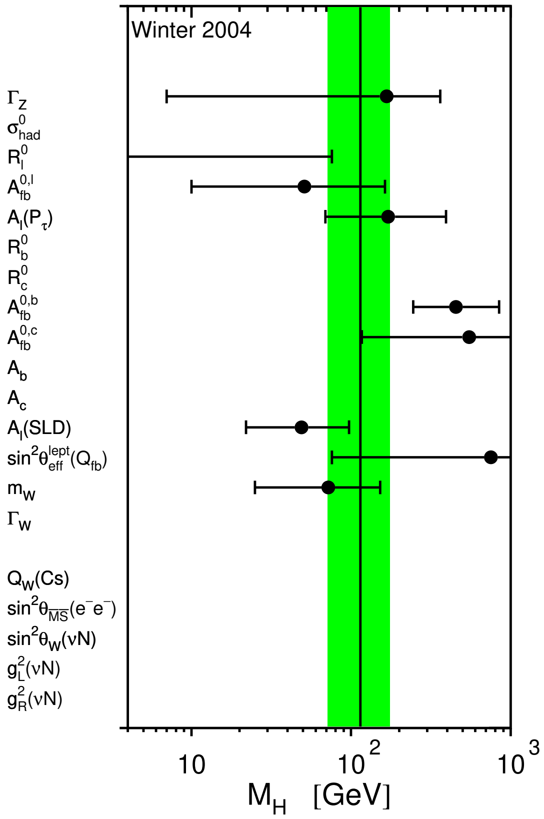

Figure 6.10: Constraints on the mass of the Higgs boson from the most sensitive electroweak observables. The constraints are determined by setting the other free parameters in the electroweak fit to the values which are obtained in the combined fit to all data. This combined fit also yields the shaded band.

between the $A_{\mathrm{FB}}^{0,\,\mathrm{b}}$ and $A_{\mathrm{FB}}^{0,\,\mathrm{c}}$ results and m_{H} has already been displayed in the lower part of the Figures 6.3 and 6.4. As a matter of fact, the $A_{\mathrm{FB}}^{0,\,\mathrm{b}}$ and $A_{\mathrm{FB}}^{0,\,\mathrm{c}}$ results make the electroweak fit more compatible with the exclusion limit on m_{H} from the direct search, where $m_{\mathrm{H}} < 114.4$ GeV$/c^2$ (95 % CL) [15] is found.

As far as m_{H} is concerned, $A_{\mathrm{FB}}^{0,\,\mathrm{b}}$ and A_{LR}^{0}, both exhibit a high sensitivity, but prefer a high and a low value, respectively. Within the Standard Model analysis, other observables also prefer low values for m_{H}, such as the other leptonic forward-backward asymmetry measurements and in particular the combined measurement of the mass of the W boson. This is the reason why the pull of the $A_{\mathrm{FB}}^{0,\,\mathrm{b}}$ measurement is enlarged compared to the $\sin^2\theta_{\mathrm{eff}}^{\ell}$ combination discussed in Section 6.4, while the pull of A_{LR}^{0} is reduced.

As already mentioned also the determination of m_{W} contributes to the prediction of m_H. In the previous years [51, 159, 168–174] this contribution has shown, very similar to A^0_LR, a discrepancy to the one from $A^{0,\mathrm{b}}_\mathrm{FB}$, seemingly confirming the A^0_LR result. This discrepancy is now smaller with the updated result for m_W from summer 2003, which moved towards higher values for m_H [167].

Chapter 7

Summary and Outlook

This thesis presents the final OPAL measurement of the b and c quark forward-backward asymmetries and the B mixing parameter using semileptonic decays of bottom and charm hadrons. For the first time the analysis considers the entire OPAL dataset recorded between 1990 and 2000 at energies close to the Z resonance. After correcting for all biases, the results are:

$$\begin{aligned}
A_{\mathrm{FB}}^{\mathrm{b}} &= (\;4.7 \pm 1.8 \pm 0.1\;)\,\%, & A_{\mathrm{FB}}^{\mathrm{c}} &= (-6.8 \pm 2.5 \pm 0.9\;)\,\% & \text{at } \langle\sqrt{s}\rangle &= 89.51 \text{ GeV},\\
A_{\mathrm{FB}}^{\mathrm{b}} &= (\;9.72 \pm 0.42 \pm 0.15)\,\%, & A_{\mathrm{FB}}^{\mathrm{c}} &= (\;5.68 \pm 0.54 \pm 0.39)\,\% & \text{at } \langle\sqrt{s}\rangle &= 91.25 \text{ GeV},\\
A_{\mathrm{FB}}^{\mathrm{b}} &= (10.3 \pm 1.5 \pm 0.2\;)\,\%, & A_{\mathrm{FB}}^{\mathrm{c}} &= (\;14.6 \pm 2.0 \pm 0.8\;)\,\% & \text{at } \langle\sqrt{s}\rangle &= 92.95 \text{ GeV}.
\end{aligned}$$

For the average B mixing parameter, a value of:

$$\overline{\chi} = (13.12 \pm 0.49 \pm 0.42)\,\%$$

is obtained. The first error is always the statistical and the second the systematic uncertainty. Compared to the previous measurement with semileptonic decays using data from 1990 to 1995 [82] the precision of the OPAL values entering the LEP averages are improved by 8 % for $A_{\mathrm{FB}}^{\mathrm{b}}$ and 15 % for $A_{\mathrm{FB}}^{\mathrm{c}}$. Furthermore, also the total uncertainty of the B mixing parameter is reduced by 11 %. The decrease of the statistical component of the error is reached by utilising the most modern analysis techniques to increase both, the efficiency and the purity of the semileptonic b and c decays and the higher number of available hadronic Z decays. Several factors are found to reduce the magnitude of the systematic uncertainty by 20 % for $A_{\mathrm{FB}}^{\mathrm{b}}$, 23 % for $A_{\mathrm{FB}}^{\mathrm{c}}$ and 13 % for $\overline{\chi}$:

- new neural network for electron identification,
- improved quark flavour separation,

- smaller uncertainties of external measurements entering the analysis (particle decay widths, semileptonic branching ratios, etc.),
- better understanding of the production and decay of heavy quarks, and
- new calibration of the OPAL dataset.

The largest contributions to the systematic error of $A_{\mathrm{FB}}^{\mathrm{b}}$ arise from the disagreement of the variables used for quark flavour separation between data and Monte Carlo (0.07), the modelling of $\mathrm{c} \to \ell^+$ decays (0.06), and the QCD correction (0.06). For $A_{\mathrm{FB}}^{\mathrm{c}}$ the dominant sources are the branching ratio $\mathrm{BR}(\mathrm{b} \to \overline{\mathrm{c}} \to \ell^-)$ (0.17), the agreement between data and Monte Carlo with respect to the flavour separation variables (0.16), and the branching ratio $\mathrm{BR}(\mathrm{c} \to \ell^+)$ (0.15).

The results from this thesis confirm the preliminary OPAL results [82] from 1995 with improved accuracy. Now all OPAL b and c quark forward-backward asymmetry measurements are in very good agreement with each other and with the Standard Model.

Together with the corresponding ALEPH measurement [151], the results above represent the most precise exclusive determination of $A_{\mathrm{FB}}^{\mathrm{b}}$. Only the inclusive analyses from ALEPH, DELPHI, and OPAL [76, 154, 155] provide values with smaller uncertainties. The results given for $A_{\mathrm{FB}}^{\mathrm{c}}$ and $\overline{\chi}$ currently are the most precise numbers available.

Since all LEP collaborations have by now published final b and c quark forward-backward asymmetry measurements, the results are combined to the LEP pole asymmetries $A_{\mathrm{FB}}^{0,\mathrm{b}} = (9.98 \pm 0.16)\%$ and $A_{\mathrm{FB}}^{0,\mathrm{c}} = (7.02 \pm 0.36)\%$. Statistical as well as systematic correlations are taken fully into account by the averaging procedure. All $A_{\mathrm{FB}}^{0,\mathrm{b}}$ and $A_{\mathrm{FB}}^{0,\mathrm{c}}$ results from the LEP collaborations are in good agreement with each other. They also agree well with the predictions of the Standard Model. The value of the electroweak mixing angle $\sin^2\theta_{\mathrm{eff}}^{\ell}$ derived from only the heavy flavour asymmetry measurements agrees with the one determined from the overall fit to all electroweak data taken by LEP. A small discrepancy still remains between the value of $\sin^2\theta_{\mathrm{eff}}^{\ell}$, determined from the LEP heavy flavour forward-backward asymmetries alone, and the same quantity derived from the left-right asymmetry measured at SLD, at the level of 2.9 standard deviations.

The measurements of the heavy flavour forward-backward asymmetries can be interpreted under the assumption that a Higgs boson exists in the Standard Model. The $A_{\mathrm{FB}}^{0,\mathrm{b}}$ and $A_{\mathrm{FB}}^{0,\mathrm{c}}$ measurements alone favour a light Higgs boson, in agreement with the results from a global electroweak fit.

The precision of the LEP $A_{\mathrm{FB}}^{\mathrm{b}}$ and $A_{\mathrm{FB}}^{\mathrm{c}}$ values is clearly limited by their statistical uncertainties. A further reduction of the errors is therefore only possible with a new generation of $\mathrm{e}^+\mathrm{e}^-$ accelerators with very high luminosity. Currently there are three proposals for a linear e^+e^- collider: The GLC (Global Linear Collider), which originally is known as the JLC (Japanese Linear Collider) [176], the NLC (Next Linear Collider) [177], and the TESLA (TeV Energy Superconducting Linear Accelerator) [178] project. The TESLA Technical Design Report contains studies concerning a dedicated Z production period (GigaZ), offering the possibility to make precision measurements of electroweak observables using 10^9 Z decays. In addition, the TESLA detector is expected to reconstruct b and c hadrons with improved efficiency and purity compared to any detector operated at LEP or SLC. Therefore, GigaZ would complement discoveries made at higher energies with tests of the theoretical models with a precision never reached before.

Altogether, the measurements, the one presented in this thesis and the multitude of other measurements performed at LEP, paint an amazingly consistent picture of nature as described by the Standard Model. So far, no discrepancy between experiment and theory is found in a large number of measurements. The precision of the comparison between data and theory reached a level well below 1 %, and thus has become sensitive to effects from physics not in the scope of the Standard Model. Up to now, no evidence for any physics beyond the Standard Model is found at mass scales accessible at LEP, SLC or TEVATRON. However, the data very strongly suggest that the next big discoveries – at least the Higgs boson, or maybe even more exotic phenomena – are just around the corner. There is strong, though only indirect evidence for a light Higgs boson with a mass below 200 GeV. It is believed that totally new classes of particles, e.g. supersymmetric particles, will be discovered at masses just slightly above the currently accessible mass region.

In the next decade the Large Hadron Collider LHC [179] at CERN, a proton proton machine with a beam energy of 7 TeV, will collect a huge amount of data, pushing the energy frontier by one order of magnitude. In case the Higgs boson exists, it will be discovered at the LHC. If new phenomena are to be found in the energy regime covered by the LHC, this collider should find traces of these. It is hoped that at least one of the currently planned linear colliders delivers data not too far behind the LHC. Results from a linear collider will be necessary for an accurate theoretical formulation of the mechanism of electroweak symmetry breaking and thus help to assemble one of the great puzzles of modern particle physics. Together, both types of accelerators would carry on the great collaboration between lepton and hadron machines, which we have experienced in the last 20 years with LEP, SLC, and the TEVATRON, advancing our knowledge about the most fundamental properties of nature.

Appendix A

Introduction to Artificial Neural Networks

A measurement of a physical quantity in general is based on a particular class of events, called signal. The other events are called background. To separate this two classes of events, an appropriate algorithm is needed. Usually the properties of the signal and the background classes can be described by a set of variables $x_1, x_2 \ldots x_{n_{\text{in}}} \in \mathbb{R}$, spanning a n_{in} dimensional real vector space $\mathbb{R}^{n_{\text{in}}}$ with elements $\vec{x}$. Together with the information to which class a specific event belongs, $\vec{x}$ is called a "pattern". Ideally the $\vec{x}$ for signal and background populate distinct regions in the sample space $\mathbb{R}^{n_{\text{in}}}$. Finding the decision boundary constructed of a set of intersecting hyperplanes, which divide the sample space in a signal and a background region, solves the event classification problem. In high-energy physics, the classification to be performed is mostly a not-total-separable problem, meaning that there is no set of intersecting hyperplanes in the sample space which can separate the two classes completely. The best decision boundary is then the set of hyperplanes which have the smallest classification error for a particular sample of events.

Cutting on the variables x_i individually results in a cuboid-shaped decision boundary, neglecting a more complicated form of the volume of the signal region. Multivariate methods, which allow the construction of more complicated decision boundaries, are best suitable for solving the classification problem. These statistical techniques look at the pattern of relationships between several variables simultaneously. Particularly interesting are "machine learning" methods. These are algorithms which are able to improve their performance based on the evaluation of past performance. A very prominent representative of this group is the artificial neural network. This mathematical concept had been inspired by the neurophysiological study of the human brain, consisting of a huge number of interconnected specialised cells (neurons), communicating across synapses

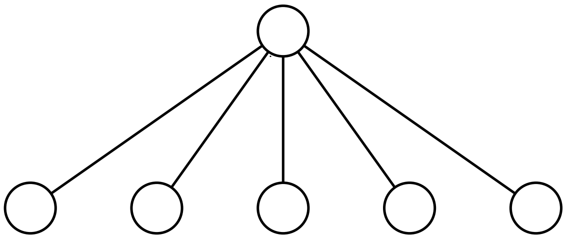

Figure A.1: Schematic diagram of a perceptron. The output o is a linear combination of the inputs x_i, where the weights ω_i serve as coefficients. The threshold θ is not shown.

by exchanging neurotransmitting chemicals. Neurons take input through their dendrites and process an output, being a non-linear function of the input stimuli. Output is only produced if there are enough inputs of a certain strength to overcome a certain threshold value. A processor, consisting of multiple nodes, each producing an output value from a weighted combination of several input values is constructed. In high-energy physics analyses, the feed-forward multilayer perceptron is the most used network type. It is briefly described here. More information can be found in the literature, see e.g. [125].

Six different neural networks are contributing at several points in a beneficial way to the results presented in this text. They were used for the electron identification [109], the rejection of electrons coming from the reaction $\gamma \to \mathrm{e}^+\mathrm{e}^-$ (see Section 5.4.1) [109] and for the separation of $\mathrm{b} \to \ell^-$ and $\mathrm{c} \to \ell^+$ decays from each other and from background for electrons and muons separately (see Section 5.4.2).

A.1 Architecture of a Neural Network

A.1.1 The Perceptron

A neuron is a binary switch with individual threshold $\theta \in \mathbb{R}$, driven by n_{in} external inputs $x_i \in \mathbb{R}$, which are given weights $\omega_i \in \mathbb{R}$ according to their significance. Threshold and weights have to be adjusted (“learning process”). This definition has been formulated first by W. Pitts and W. S. McCulloch [180]. The elementary form of a neural network is the perceptron (Figure A.1) which is the mathematical implementation [181] of a single McCulloch-Pitts-neuron. The Heaviside step function

$$g(z) = \begin{cases} 1 & \text{for} \quad z \geq 0 \\ 0 & \text{for} \quad z < 0 \end{cases} \tag{A.1}$$

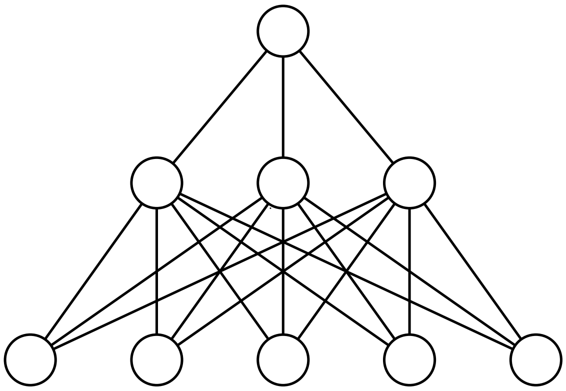

Figure A.2: Schematic diagram of a multi-layer perceptron. The output o is a linear combination of the outputs h_i of the nodes of the hidden layer. The h_i themselves are linear combinations of the inputs x_i. In both cases the weights ω serve as coefficients. The thresholds θ are not shown.

can be used to express the binary character of a neuron. Usually $g(z)$ is called activation or transfer function. Ccomparing the weighted sum of the inputs x_i with the threshold θ gives the output value $o \in \{0, 1\}$ of the perceptron:

$$o := g(z) = g\left(\sum_{i=1}^{n_{\text{in}}} \omega_i \, x_i - \theta\right) \; . \tag{A.2}$$

o classifies the input patterns into two classes, "0" and "1" by the hyperplane $\sum_i \omega_i x_i - \theta = 0$, dividing the input space $\mathbb{R}^{n_{\text{in}}}$ into two subspaces. Here the weights ω_i specify the direction of a vector normal to the hyperplane, while the threshold θ is proportional to the distance of the plane to the origin of the coordinate system.

A.1.2 The Multi-Layer Perceptron

If the input patterns of the two classes populate different regions of the $\mathbb{R}^{n_{\text{in}}}$, which are separated by more complex boundaries, a multi-layer perceptron as shown in Figure A.2 is necessary to categorise the patterns. Its components – the nodes – are organised in layers. The first layer contains all input nodes x_i, the last one the n_{out} outputs o_i. More than one output node is needed if more than two classes have to be separated. In the following, structures with only one output node are described. In-between the input layer and the output layer there is one hidden layer with n_{hid} hidden nodes h_i. In the following the inputs are considered as nodes too. Deviant from the hidden and output nodes, the transfer function of the input nodes is $\tilde{g}(x) = x_i$. There is no threshold ($\theta_{\text{input}} = 0$) for the input nodes. More than one hidden layer is needed if one of the two classes populates two or more disconnected regions in the input space. This case is not needed for the analysis presented in this text and therefore not described in more detail. Weights (labelled w_{ik} and w_i) connect each node of a layer with all nodes of the preceding layer. The output value o of a multi-layer perceptron with one hidden layer is calculated to be

$$o = g\left(\overbrace{\sum_{i=1}^{n_{\mathrm{hid}}} \omega_i \cdot g\left(\underbrace{\sum_{k=1}^{n_{\mathrm{in}}} \omega_{ik} x_k - \theta_i}_{h_i}\right) - \theta}^{a}\right) \quad . \tag{A.3}$$

This formula can be interpreted geometrically. Each hidden node h_i divides the input patterns into two classes on either side of a hyperplane $\sum_k \omega_k x_k - \theta_i = 0$, depending whether h_i is "0" or "1". The linear combination a of the values of the hidden nodes can be interpreted as a combination of the half-spaces defined by the hyperplanes. Up to this point a multi-layer perceptron is nothing more than a more sophisticated cut based method. In case of a not-total-separable problem, there can be the situation that $n_{\mathrm{in}} - 1$ input variables of a signal pattern give strong evidence that this pattern belongs to the signal class, but one input is slightly displaced onto the "wrong" side of one of the hyperplanes. In this case the event would be classified as background even though it is very likely to be a signal event. This problem can be solved by replacing the Heaviside step function with a continuously differentiable, non-linear transfer function

$$g(z) = \frac{1}{1 + \exp\left(-\frac{2z}{T}\right)} \ , \tag{A.4}$$

with "temperature" T. The form of the transfer function is shown in Figure A.3 for different temperatures. At very low temperatures, $g(z)$ becomes a step function. This changes the behaviour of the output of a multi-layer perceptron to be continuous with $o \in [0, 1] \in \mathbb{R}$. Using the definition from Eq. A.4 for $g(z)$ in Eq. A.3 the multi-layer perceptron behaves like a neural network. The response of these algorithms is more than just a yes/no answer. The input patterns are ranked by assigning a value between 0 and 1 to each pattern, which indicates, how well this pattern can be classified as signal or background.

To illustrate the impact of the temperature on the behaviour of a multi-layer perceptron, the output distributions of two multi-layer perceptrons with different temperature T are shown in Figure A.4. In the two three dimensional plots the output is plotted over the two dimensional input space. The hyperplanes, which are defined by the weights and thresholds of the eight hidden nodes are

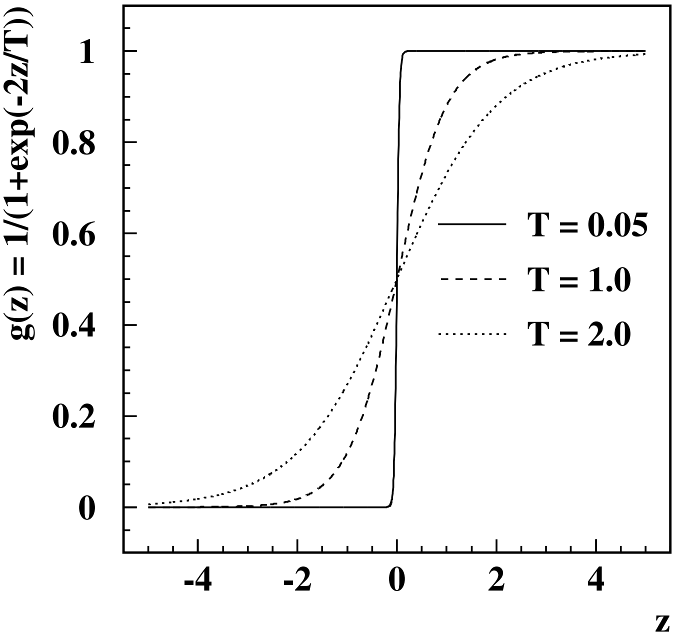

Figure A.3: Transfer function $g(z)$ for three different temperatures. As the temperature T decreases the transfer function approaches a step function with a 0 to 1 transition for $z = 0$.

just straight lines in the input plane. In both cases the signal populates exactly the same region. Plot (a) shows the behaviour of the multi-layer perceptron at a temperature $T = 0$, while plot (b) and (d) that at some higher temperature. The multi-layer perceptron in (a) performs linear cuts defined by the internal weights. At higher temperature (b) the output becomes continuous. The cuts are not anymore linear. This is an important advantage of a neural network compared to a method which only use linear cuts. A neural network in principle can cut any arbitrary region out of the space spanned by the input variables, whereas conventional methods usually cut regions which are defined by a set of intersecting planes perpendicular to the axes. This results in a better performance of neural networks compared to conventional methods if applied to the same problem.

A.2 Training and Testing of a Neural Network

To obtain a neural network, suitable for a specific application, two tasks have to be performed:

1. A layout for the network (number of layers, number of input, hidden, and output nodes) has to be chosen. The optimal architecture can be found

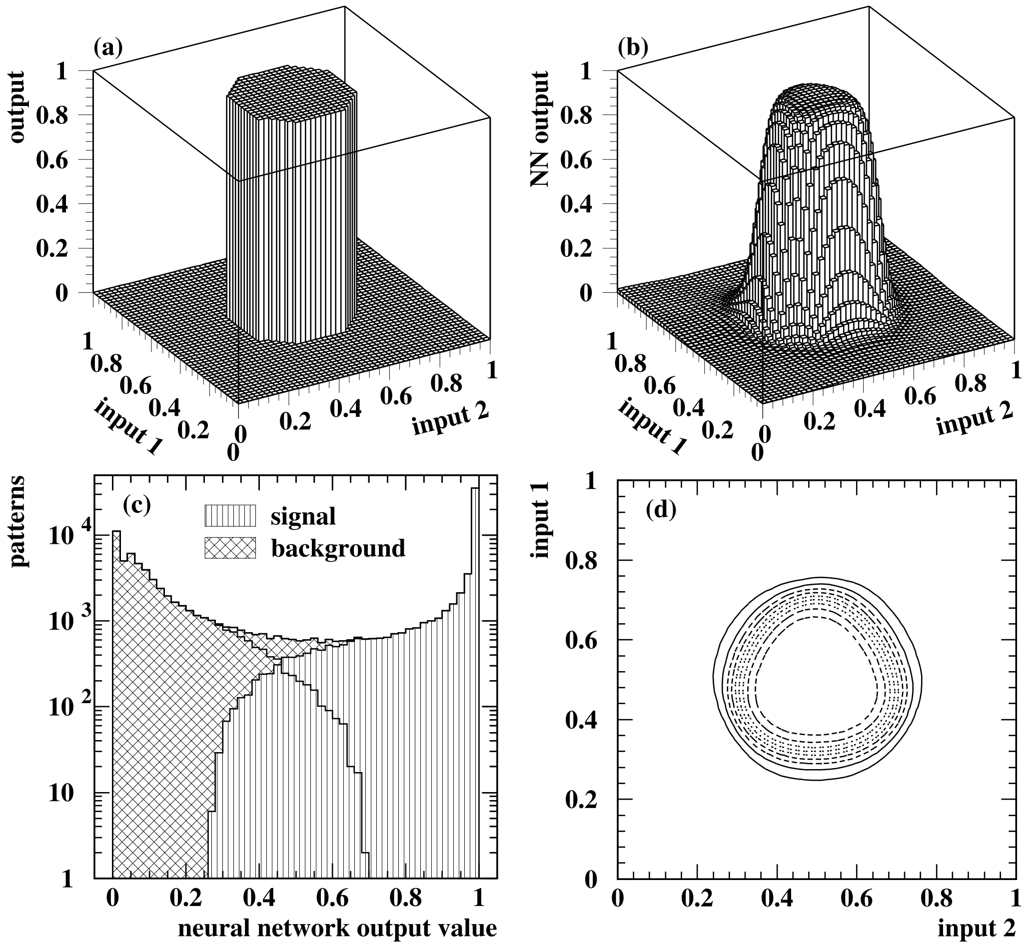

Figure A.4: Figures (a) and (b) show the output of two artificial neural networks with different temperatures as a function of the two input variables. Both networks have eight hidden nodes and were trained with the same set of events. The network shown in (a) has a temperature of $T = 0$. A sharp region of the input space with the shape of an octagon is cut out. The network shown in figure (b) has a higher temperature ($T = 2$). Now the lines of constant network output (d) do not anymore follow the straight lines but are non-linear as explained in the text. Figure (c) shows the output distribution of the network with $T = 2$. The separation between signal and background is very good.

only by a series of different trials.

2. Values for weights and thresholds need to be determined, because they are not defined a priori by the initialisation process of a neural network.

The values for the weights[1], which are set to random values after the initialisation process, have to be determined in a procedure called "training". For the training events with known classification (patterns) p are needed. In the training procedure the correlation between the calculated network output o_p and the known classification (desired network output) $\tilde{o}_p$ of a given pattern p is maximised. This is accomplished by minimising the "error function"

$$E = \frac{1}{2\, n_{\mathrm{pat}}} \sum_{p=1}^{n_{\mathrm{pat}}} (o_p - \tilde{o}_p)^2 \ . \tag{A.5}$$

Here the sum runs over a group of training patterns for which the error is calculated. No exact rule exists to find the minimum of the error function E. One method is the gradient descent method, which serves well in case a large training sample is available and computing time is not a critical factor.

After the determination of the error E of a group of n_{pat} training patterns, this method iteratively updates the weights ω from step t to step $t+1$ by calculating corrections $\Delta\omega$:

$$\omega_i^{t+1} = \omega_i^t + \Delta\omega_i^t \quad \text{and} \tag{A.6}$$

$$\omega_{ik}^{t+1} = \omega_{ik}^t + \Delta\omega_{ik}^t \ . \tag{A.7}$$

To simplify the notation in the following, it is assumed that the updating is done after each training event. So the sum over p can be dropped. The adjustments $\Delta\omega_i$ and $\Delta\omega_{ik}$ to the weights are derived using the gradient of the error function in the space of the weights. The corrections to the weights:

$$\begin{aligned} \Delta\omega_i^t &= -\eta\, \frac{\partial E^t}{\partial \omega_i^t} = -\eta\, \frac{\partial E^t}{\partial o^t} \cdot \frac{\partial o^t}{\partial \omega_i^t} && \text{(A.8)} \\ &= -\eta\, (o^t - \tilde{o})\, g'(a^t)\, g(b_i^t) \quad \text{and} \\ \Delta\omega_{ik}^t &= -\eta\, \frac{\partial E^t}{\partial \omega_{ik}^t} = -\eta\, \frac{\partial E^t}{\partial o^t} \cdot \frac{\partial o^t}{\partial h_i^t} \cdot \frac{\partial h_i^t}{\partial \omega_{ik}^t} && \text{(A.9)} \\ &= -\eta\, (o^t - \tilde{o})\, g'(a^t)\, g'(b_i^t) \end{aligned}$$

are a step in the direction opposite to the gradient, where the "learning parameter" $0 < \eta < 1 \in \mathbb{R}$ parameterises the step size, which is proportional to the gradient of E. The $\Delta\omega$ just have non zero values if the derivatives $\mathrm{d}E/\mathrm{d}\omega_i$ and $\mathrm{d}E/\mathrm{d}\omega_{ik}$ do not vanish. This is only the case for $T > 0$ in the activation function.

[1] Here and in the following, the weights include also the threshold terms.

The goal of the training is to find the global minimum of the error function E in the space of the weights. This is done by examining E in the surrounding of ω_i and ω_{ik}. To ensure that the training algorithm is able to come across plateaus in E, that it can leave local minima and that the weights ω_i and ω_{ik} do not oscillate around a minimum of the error function, a "momentum" term α is introduced in the updating equations for the $\Delta\omega$:

$$\Delta\omega_i^t = -\eta \frac{\partial E}{\partial \omega_i} + \alpha \, \Delta\omega_i^{t-1} \tag{A.10}$$

$$\Delta\omega_{ik}^t = -\eta \frac{\partial E}{\partial \omega_{ik}} + \alpha \, \Delta\omega_{ik}^{t-1} \, , \tag{A.11}$$

with $0 < \alpha < 1 \in \mathbb{R}$.

During the training all training events are usually presented to the network many times and in randomised order. All training events should be presented to the network the same number of times. The number of training events in the different event classes should be of the same magnitude and the events should be presented to the network alternately.

The training is organised in cycles and epochs. During a cycle all events of the training sample are presented to the net once. Usually the training lasts for several cycles. An epoch is a more or less arbitrary number of events of the order of 100-5000, depending on the classification problem. Some parameters like momentum parameter α, temperature T, and learning parameter η are adjusted (usually reduced) after each training epoch.

The input variables should be scaled to values of the order of one. If the order of magnitude of the input values varies a lot, then the network will take a long time to scale the corresponding weights sufficiently so that the information of all inputs are exploited equally. The training will be very slow and inefficient. The learning parameter η, the momentum parameter α, and the network temperature T have to be optimised by a trial and error method.

The training is finished as soon as the weights do not change any more and the value of the error function stays constant. Then a minimum for the function E is found.

To evaluate the performance quality of the neural network during and after the training period, a second – statistically independent – sample of events with known classification – the test sample – is needed. The performance can be determined by using the figure of merit (FOM). The figure of merit F measures the separation achieved in the neural network output distribution between the signal and background distributions. Values close to zero indicate no separation, whilst one indicates complete separation. The figure of merit is defined by the "inverse correlation integral":

$$F = \alpha(1-\alpha)\int \frac{(f_1(x) - f_2(x))^2}{\alpha f_1(x) + (1-\alpha) f_2(x)} \mathrm{d}x \ , \tag{A.12}$$

where class 1 contributes a fraction α of the sample with normalised distribution $f_1(x)$ and class 2 contributes $1-\alpha$ with normalised distribution $f_2(x)$ [124].

Another important phenomenon is "overtraining". Given a fixed number of training events one could construct a neural network sufficiently complex to classify all presented training events correct. Such a network will not perform very well on a statistically independent sample, because, given the complexity of the network, the number of free parameters allowed the network to "learn" the specific features of the training sample. These features are specific to the training sample and are not necessarily properties of the event classes. The performance of an overtrained neural network on an independent test sample as a function of the training epoch reaches a maximum and then decreases as soon as the network starts to "learn" the features specific to the training sample. The final performance of such a network on the training sample will be better than that on the test sample. Overtraining indicates that the number of free parameters to be adjusted during the training is too large for the available training events. A solution is to either increase the number of training events or simplify the architecture of the network. Neural networks with two hidden layers are much more likely to become overtrained than those with just one hidden layer.

In general the number of training events needed not only depends on the complexity of the network but also on the degree to which the input variable distributions of the different event classes overlap. In case of small differences between the distributions statistical fluctuations can obscure the different properties of the event classes. In these cases the number of training events has to be large enough so that the statistical error on the input variable distribution becomes small compared to the differences of the distributions between the event classes.

For example the networks to identify $\mathrm{b} \to \mathrm{e}^-$ or $\mathrm{c} \to \mathrm{e}^+$ events, used in the measurement presented in Chapter5, have 136 (120 weights and 16 thresholds) and 181 (165 weights and 16 thresholds) parameters, respectively. It has been found that at least 3000 training events are necessary to train the network without overtraining. Figure A.5 shows the figure of merit calculated using the test sample as a function of the number of used training events per weight for the $\mathrm{b} \to \mathrm{e}^-$ and the $\mathrm{c} \to \mathrm{e}^+$ neural network. Both networks need about the same number of training events per weight to reach a sufficient performance. Due to the larger number of inputs to the $\mathrm{c} \to \mathrm{e}^+$ network (10) compared to the $\mathrm{b} \to \mathrm{e}^-$ network (7) and the more difficult problem of separating $\mathrm{c} \to \mathrm{e}^+$ events from the backgrounds than to identify $\mathrm{b} \to \mathrm{e}^-$ events, the $\mathrm{c} \to \mathrm{e}^+$ network needs more training events in total than the $\mathrm{b} \to \mathrm{e}^-$ network.

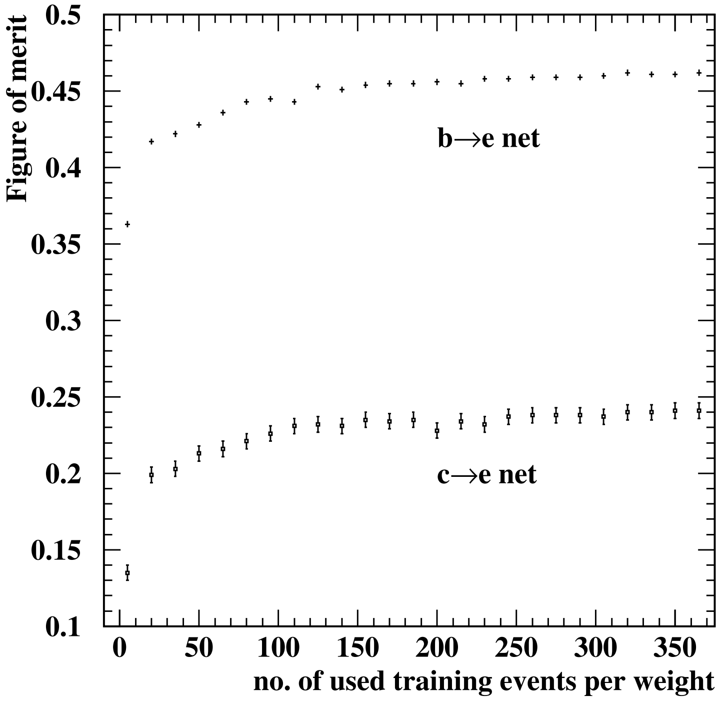

Figure A.5: Figure of merit of the $b \rightarrow e^-$ and $c \rightarrow e^+$ neural networks calculated using a statistically independent test sample as a function of the used number of training events per weight. 365 training events per weight correspond to 49 640 and 66 065 events for the $b \rightarrow e^-$ and the $c \rightarrow e^+$ networks respectively. In both cases the test sample consists of a total of 100000 signal and background events.

A.3 Application of a Neural Network to Data

After the training procedure the meaning of the network output has to be found. The interpretation of the network output as the probability that the corresponding event belongs to the signal fraction is only possible, if the signal to background ratio of the training sample is the same than that of the data to which the network should be applied. For various reasons this is a rather rare case. The network output can still be used to determine this probability in case the over all signal to background ratio realized in the data is known. Fortunately this is the case for all data used for the asymmetry measurement presented in this text. This allows to determine the shape of the network output distribution expected from data by calculating the superposition of the shapes of the signal and background distributions, computed using a set of simulated events. As an example, Figure A.4 (c) shows the output distribution of the simple neural network introduced in the previous section. With the help of such a distribution the efficiency and the purity for each output bin can be calculated. Now a meaningful interpretation of the network output produced with real data is possible.

Neural networks are used in three different ways in the asymmetry analysis:

1. To support a yes/no decision: to identify electrons coming from direct quark decays, cuts are placed on the outputs of two different neural networks. The first network is trained to decide whether the found particle is an electron or not. The second network rejects electrons, originating from photon conversions. An electron is considered to be identified in case it fulfils both cuts.

2. To deliver more information to another neural network: to improve the quality of the quark flavour separation the outputs of the neural networks used for the electron identification are fed as an input into the two neural networks, trained to identify $b \to e^-$ and $c \to e^+$ decays.

3. To separate multiple event classes and produce event weights: in order to use the whole sample of lepton candidates, two types of neural networks are trained: the first is trained to separate $b \to \ell^-$ decays from all others, the second to separate $c \to \ell^+$ decays from all other decays. The outputs of both networks are used to produce a two dimensional distribution (10×10 bins) of the lepton candidates. Over all, there are four different classes of lepton candidates ($b \to \ell^-$, $b \to c \to \ell^+$, $c \to \ell^+$ and background). In different regions of the plane the contribution of the different channels vary. Since the ratio between the four event classes is known, the same neural networks can be used to produce weights representing probabilities for the different event classes for each of the bins separately. These weights are used in the maximum likelihood fit to calculate the appropriate asymmetry of each bin.

Bibliography

[1] Gargamelle Neutrino Collaboration, F. J. Hasert *et al.*, *Observation of neutrino-like interactions without muon or electron in the Gargamelle neutrino experiment*, Phys. Lett. **B46**(1973) 138.

[2] UA1 Collaboration, G. Arnison *et al.*, *Experimental observation of isolated large transverse energy electrons with associated missing energy at* $\sqrt{s} = 540\ GeV$, Phys. Lett. **B122**(1983) 103.

UA2 Collaboration, M. Banner *et al.*, *Observation of single isolated electrons of high transverse momentum in events with missing transverse energy at the CERN* $p\bar{p}$ *collider*, Phys. Lett. **B122**(1983) 476.

[3] UA1 Collaboration, G. Arnison *et al.*, *Experimental observation of lepton pairs of invariant mass around* $95 GeV/c^2$ *at the CERN SPS collider*, Phys. Lett. **B126**(1983) 398.

UA2 Collaboration, P. Bagnaia *et al.*, *Evidence for* $Z \to \mathrm{e}^+\mathrm{e}^-$ *at the CERN* $p\bar{p}$ *collider*, Phys. Lett. **B129**(1983) 130.

[4] C. Y. Prescott *et al.*, *Parity non-conservation in inelastic electron scattering*, Phys. Lett. **B77**(1978) 347.

C. Y. Prescott *et al.*, *Further measurements of parity nonconservation in inelastic electron scattering*, Phys. Lett. **B84**(1979) 524.

[5] MAC Collaboration, W. Ash *et al.*, *Observation of charge asymmetry in hadron jets from e+ e- annihilation at* $\sqrt{s} = 29\mathrm{GeV}$, Phys. Rev. Lett. **58**(1987) 1080.

JADE Collaboration, T. Greenshaw *et al.*, *A measurement of the charge asymmetry of hadronic events in electron positron annihilation*, Z. Phys. **C42**(1989) 1.

TASSO Collaboration, W. Braunschweig *et al.*, *Evidence for direct photons from quarks in electron - positron annihilation*, Z. Phys. **C41**(1988) 385.

AMY Collaboration, D. Stuart *et al.*, *Forward - backward charge asymmetry in e+ e-* $\to$ *hadron jets*, Phys. Rev. Lett. **64**(1990) 983.

TOPAZ Collaboration, I. Adachi *et al.*, *Charge asymmetry of hadronic events in e+ e- annihilation at* $\sqrt{s} = 57.9$GeV, Phys. Lett. **B255**(1991) 613.

[6] L. Camilleri *et al.*, *Physics with very high energy* e^+e^- *colliding beams* (1976), CERN/76-18, CERN 1980.

LEP design report: vol. 2. The LEP main ring, Technical report, CERN (1984), *LEP Design Report*, CERN-LEP/84-01, June 1984.

S. Myers and E. Picasso, *The design, construction and commissioning of the CERN Large Electron Positron collider*, Contemp. Phys. **31**(1990) 387.

D. Brandt, H. Burkhardt, M. Lamont, S. Myers, and J. Wenninger, *Accelerator physics at LEP*, Rept. Prog. Phys. **63**(2000) 939.

R. Assmann, M. Lamont, and S. Myers, *A brief history of the LEP collider*, Nucl. Phys. Proc. Suppl. **109B**(2002) 17.

[7] *SLAC linear collider conceptual design report*, Technical report, SLAC (1980), SLAC-R-229 , June 1980.

[8] P. W. Higgs, *Broken symmetries, massless particles and gauge fields*, Phys. Lett. **12**(1964) 132.

P. W. Higgs, *Broken symmetries and the masses of gauge bosons*, Phys. Rev. Lett. **13**(1964) 508.

P. W. Higgs, *Spontaneous symmetry breakdown without massless bosons*, Phys. Rev. **145**(1966) 1156.

F. Englert and R. Brout, *Broken symmetry and the mass of gauge vector mesons*, Phys. Rev. Lett. **13**(1964) 321.

[9] CDF Collaboration, F. Abe *et al.*, *Evidence for top quark production in anti-p p collisions at* $\sqrt{s} = 1.8$ *TeV*, Phys. Rev. Lett. **73**(1994) 225, `arXiv:hep-ex/9405005`.

[10] CDF Collaboration, F. Abe *et al.*, *Evidence for top quark production in anti-p p collisions at* $\sqrt{s} = 1.8$ *TeV*, Phys. Rev. **D50**(1994) 2966.

[11] CDF Collaboration, F. Abe *et al.*, *Observation of top quark production in anti-p p collisions*, Phys. Rev. Lett. **74**(1995) 2626, `arXiv:hep-ex/9503002`.

[12] D0 Collaboration, S. Abachi *et al.*, *Observation of the top quark*, Phys. Rev. Lett. **74**(1995) 2632, `arXiv:hep-ex/9503003`.

[13] OPAL Collaboration, G. Abbiendi *et al.*, *Measurement of heavy quark forward-backward asymmetries and average B mixing using leptons in hadronic Z decays*, Phys. Lett. **B577**(2003) 18, `arXiv:hep-ex/0308051`.

[14] T. Krämer, *Measurement of heavy quark forward-backward asymmetries using a lepton tag in hadronic Z decays*, Eur. Phys. J. **C33, s01**(2004) 717.

[15] ALEPH, DELPHI, L3, and OPAL Collaboration, R. Barate *et al.*, *Search for the Standard Model Higgs boson at LEP*, Phys. Lett. **B565**(2003) 61, `arXiv:hep-ex/0306033`.

[16] S. L. Glashow, *Partial symmetries of weak interactions*, Nucl. Phys. **22**(1961) 579.

[17] S. Weinberg, *A model of leptons*, Phys. Rev. Lett. **19**(1967) 1264.

[18] A. Salam and J. C. Ward, *Electromagnetic and weak interactions*, Phys. Lett. **13**(1964) 168.

[19] S. L. Glashow, J. Iliopoulos, and L. Maiani, *Weak interactions with lepton - hadron symmetry*, Phys. Rev. **D2**(1970) 1285.

[20] N. Cabibbo, *Unitary symmetry and leptonic decays*, Phys. Rev. Lett. **10**(1963) 531.

[21] M. Kobayashi and T. Maskawa, *CP violation in the renormalizable theory of weak interaction*, Prog. Theor. Phys. **49**(1973) 652.

[22] C. S. Wu, E. Ambler, R. W. Hayward, D. D. Hoppes, and R. P. Hudson, *Experimental test of parity conservation in beta decay*, Phys. Rev. **105**(1957) 1413.

[23] M. Gell-Mann, *Quarks*, Acta Physica Austriaca, Suppl. **IX**(1972) 733.

[24] H. Fritzsch, M. Gell-Mann, and H. Leutwyler, *Advantages of the color octet gluon picture*, Phys. Lett. **B47**(1973) 365.

[25] G. Zweig, *Quark catalysis of exothermal nuclear reactions*, Science **201**(1978) 973.

[26] K. Hagiwara *et al.*, The Particle Data Group, *Review of particle physics*, Phys. Rev. **D66**(2002) 010001, the update using published results for the 2003 online release (`http://pdg.lbl.gov/2003/contents_listings.html`) was used here for the LEP average values of R_{b} and R_{c}.

[27] D. A. Ross and J. C. Taylor, *Renormalization of a unified theory of weak and electromagnetic interactions*, Nucl. Phys. **B51**(1973) 125.

[28] C. Giunti, *Status of neutrino fits* (2003), `hep-ph/0305139`.

[29] R. E. Behrends, R. J. Finkelstein, and A. Sirlin, *Radiative corrections to decay processes*, Phys. Rev. **101**(1956) 866.

[30] M. Consoli and W. Hollik, *Electroweak radiative corrections for Z physics*, in *Z physics at Lep1.* Proceedings, Workshop, Geneva, Switzerland, September 4 - 5, 1989. Vol. 1: *Standard Physics,* CERN 89-08, edited by G. Altarelli, R. Kleiss, and C. Verzegnassi, CERN, Geneva, Switzerland (1989) 5–88, Yellow Report CERN 89-08.

[31] M. J. G. Veltman, *Limit on mass differences in the Weinberg model*, Nucl. Phys. **B123**(1977) 89.

[32] M. Consoli, S. Lo Presti, and L. Maiani, *Higher order effects and the vector boson physical parameters*, Nucl. Phys. **B223**(1983) 474.

[33] J. Fleischer and F. Jegerlehner, *Testing heavy fermions in Higgs production by* $\mathrm{e^+e^-} \to \mathrm{Z}H$, Nucl. Phys. **B228**(1983) 1.

[34] D. Y. Bardin, M. S. Bilenkii, G. Mitselmakher, T. Riemann, and M. Sachwitz, *A realistic approach to the standard Z peak*, Z. Phys. **C44**(1989) 493.

D. Y. Bardin, M. S. Bilenkii, T. Riemann, M. Sachwitz, and H. Vogt, *DIZET: A program package for the calculation of electroweak one loop corrections for the process* $\mathrm{e^+e^-} \to \mathrm{f\bar{f}}$ *around the Z peak*, Comput. Phys. Commun. **59**(1990) 303.

D. Y. Bardin *et al.*, *Analytic approach to the complete set of QED corrections to fermion pair production in* $\mathrm{e^+e^-}$ *annihilation*, Nucl. Phys. **B351**(1991) 1, `arXiv:hep-ph/9801208`.

D. Y. Bardin *et al.*, *QED corrections with partial angular integration to fermion pair production in* $\mathrm{e^+e^-}$ *annihilation*, Phys. Lett. **B255**(1991) 290, `arXiv:hep-ph/9801209`.

D. Y. Bardin *et al.*, *ZFITTER: An analytical program for fermion pair production in* $\mathrm{e^+e^-}$ *annihilation* (1992)(hep-ph/9412201), `hep-ph/9412201`.

D. Y. Bardin *et al.*, *ZFITTER v.6.21: A semi-analytical program for fermion pair production in* $\mathrm{e^+e^-}$ *annihilation*, Comput. Phys. Commun. **133**(2001) 229, recently updated with results from [182], `hep-ph/9908433`.

[35] A. Djouadi, J. H. Kuhn, and P. M. Zerwas, *b jet asymmetries in Z decays*, Z. Phys. **C46**(1990) 411.

[36] R. Barbieri and L. Maiani, *Renormalization of the electroweak* ρ *parameter from supersymmetric particles*, Nucl. Phys. **B224**(1983) 32.

[37] T. Sjostrand, *High-energy physics event generation with PYTHIA 5.7 and JETSET 7.4*, Comput. Phys. Commun. **82**(1994) 74.

[38] A. Krzywicki and B. Petersson, *Breakdown of hadronic scaling or evidence for clustering?*, Phys. Rev. **D6**(1973) 924.

[39] R. D. Field and R. P. Feynman, *A parametrization of the properties of quark jets*, Nucl. Phys. **B136**(1978) 1.

[40] A. Casher, H. Neuberger, and S. Nussinov, *Chromoelectric flux tube model of particle production*, Phys. Rev. **D20**(1979) 179.

[41] M. Holder *et al.*, *Opposite sign dimuon events produced in narrow band neutrino and anti-neutrino beams*, Phys. Lett. **B69**(1977) 377.

[42] C. Peterson, D. Schlatter, I. Schmitt, and P. M. Zerwas, *Scaling violations in inclusive* $\mathrm{e}^+\mathrm{e}^-$ *annihilation spectra*, Phys. Rev. **D27**(1983) 105.

[43] P. D. B. Collins and T. P. Spiller, *The fragmentation of heavy quarks*, J. Phys. **G11**(1985) 1289.

[44] S. J. Brodsky and G. R. Farrar, *Scaling laws at large transverse momentum*, Phys. Rev. Lett. **31**(1973) 1153.

[45] S. D. Drell, D. J. Levy, and T.-M. Yan, *A theory of deep inelastic lepton - nucleon scattering and lepton pair annihilation processes. 3. deep inelastic electron - positron annihilation*, Phys. Rev. **D1**(1970) 1617.

[46] V. N. Gribov and L. N. Lipatov, $\mathrm{e}^+\mathrm{e}^-$ *pair annihilation and deep inelastic e p scattering in perturbation theory*, Yad. Fiz. **15**(1972) 1218.

[47] R. Gatto, P. Menotti, and I. Vendramin, *Threshold relation between deep-inelastic electron scattering and electron-positron annihilation*, Phys. Rev. **D7**(1973) 2524.

[48] V. G. Kartvelishvili, A. K. Likhoded, and V. A. Petrov, *On the fragmentation functions of heavy quarks into hadrons*, Phys. Lett. **B78**(1978) 615.

[49] B. Andersson, G. Gustafson, and B. Soderberg, *A general model for jet fragmentation*, Z. Phys. **C20**(1983) 317.

[50] D. E. Groom *et al.*, The Particle Data Group, *Review of particle physics*, Eur. Phys. J. **C15**(2000) 1.

[51] The LEP Electroweak Working Group and the SLD Heavy Flavor Group, *A combination of preliminary electroweak measurements and constraints on the Standard Model.* (2002), `hep-ex/0212036`.

[52] The LEP Electroweak Working Group, the SLD Electroweak Working Group and the SLD Heavy Flavour Group, *Final input parameters for the LEP/SLD heavy flavour analyses* (2001)(LEPHF/2001-01), see also `http://www.cern.ch/LEPEWWG/heavy/` .

[53] ALEPH Collaboration, D. Decamp *et al.*, *ALEPH: A detector for electron - positron annihilations at LEP*, Nucl. Instrum. Meth. **A294**(1990) 121.

[54] ALEPH Collaboration, D. Buskulic *et al.*, *Performance of the ALEPH detector at LEP*, Nucl. Instrum. Meth. **A360**(1995) 481.

[55] DELPHI Collaboration, P. Aarnio *et al.*, *The DELPHI detector at LEP*, Nucl. Instrum. Meth. **A303**(1991) 233.

[56] DELPHI Collaboration, P. Abreu *et al.*, *Performance of the DELPHI detector*, Nucl. Instrum. Meth. **A378**(1996) 57.

[57] L3 Collaboration, B. Adeva *et al.*, *The construction of the L3 experiment*, Nucl. Instrum. Meth. **A289**(1990) 35.

[58] M. Acciarri *et al.*, *The L3 silicon microvertex detector*, Nucl. Instrum. Meth. **A351**(1994) 300.

[59] A. Adam *et al.*, *The forward muon detector of L3*, Nucl. Instrum. Meth. **A383**(1996) 342.

[60] OPAL Collaboration, K. Ahmet *et al.*, *The OPAL detector at LEP*, Nucl. Instrum. Meth. **A305**(1991) 275, references to the different sub-detector systems are given in this paper. Only publications with later date are mentioned.

[61] OPAL Collaboration, P. P. Allport *et al.*, *The OPAL silicon microvertex detector*, Nucl. Instrum. Meth. **A324**(1993) 34.

[62] OPAL Collaboration, P. P. Allport *et al.*, *The OPAL silicon strip microvertex detector with two coordinate readout*, Nucl. Instrum. Meth. **A346**(1994) 476.

[63] OPAL Collaboration, S. Anderson *et al.*, *The extended OPAL silicon strip microvertex detector*, Nucl. Instrum. Meth. **A403**(1998) 326.

[64] OPAL Collaboration, B. E. Anderson *et al.*, *The OPAL silicon - tungsten calorimeter front end electronics*, IEEE Trans. Nucl. Sci. **41**(1994) 845.

[65] LEP Polarization Collaboration, L. Arnaudon *et al.*, *Measurement of LEP beam energy by resonant spin depolarization*, Phys. Lett. **B284**(1992) 431.

[66] L. Arnaudon *et al.*, *Accurate determination of the LEP beam energy by resonant depolarization*, Z. Phys. **C66**(1995) 45.

[67] M. Hauschild *et al.*, *Particle identification with the OPAL jet chamber*, Nucl. Instrum. Meth. **A314**(1992) 74.

[68] O. Biebel *et al.*, *Performance of the OPAL jet chamber*, Nucl. Instrum. Meth. **A323**(1992) 169.

[69] OPAL Collaboration, P. Mättig, *Photon energy resolution in the leadglass calorimeters,* OPAL Technical Note TN-324 (1995).

[70] OPAL Collaboration, G. Alexander *et al.*, *Measurement of the Z line shape parameters and the electroweak couplings of charged leptons*, Z. Phys. **C52**(1991) 175.

[71] R. Brun, F. Bruyant, M. Maire, A. C. McPherson, and P. Zanarini, *GEANT3* (1987), CERN-DD/EE/84-1.

[72] OPAL Collaboration, J. Allison *et al.*, *The detector simulation program for the OPAL experiment at LEP*, Nucl. Instrum. Meth. **A317**(1992) 47.

[73] T. Sjostrand, *PYTHIA 5.7 and JETSET 7.4: Physics and manual* (1995), `hep-ph/9508391`.

[74] OPAL Collaboration, G. Alexander *et al.*, *A comparison of b and (u d s) quark jets to gluon jets*, Z. Phys. **C69**(1996) 543.

[75] OPAL Collaboration, G. Abbiendi *et al.*, *Inclusive analysis of the b quark fragmentation function in Z decays at LEP* (2002), `arXiv:hep-ex/0210031`.

[76] OPAL Collaboration, G. Abbiendi *et al.*, *Measurement of the b quark forward-backward asymmetry around the Z peak using an inclusive tag*, Phys. Lett. **B546**(2002) 29, `arXiv:hep-ex/0209076`.

[77] OPAL Collaboration, G. Alexander *et al.*, *A measurement of the charm and bottom forward-backward asymmetries using D mesons at LEP*, Z. Phys. **C73**(1997) 379.

[78] S. Brandt, C. Peyrou, R. Sosnowski, and A. Wroblewski, *The principal axis of jets. An attempt to analyze high-energy collisions as two-body processes*, Phys. Lett. **12**(1964) 57.

E. Farhi, *A QCD test for jets*, Phys. Rev. Lett. **39**(1977) 1587.

[79] OPAL Collaboration, R. Akers *et al.*, *A measurement of charged particle multiplicity in* $\mathrm{Z} \rightarrow \mathrm{c\overline{c}}$ $\mathrm{Z} \rightarrow \mathrm{b\overline{b}}$ *events*, Phys. Lett. **B352**(1995) 176.

[80] OPAL Collaboration, K. Ackerstaff *et al.*, *Measurements of the b quark forward-backward asymmetry around the Z peak using jet charge and vertex charge*, Z. Phys. **C75**(1997) 385.

[81] OPAL Collaboration, R. Akers *et al.*, *A measurement of the forward-backward asymmetry of* $\mathrm{e^+e^-} \rightarrow \mathrm{b\overline{b}}$ *by applying a jet charge algorithm to lifetime tagged events*, Z. Phys. **C67**(1995) 365.

[82] OPAL Collaboration, G. Alexander *et al.*, *Measurement of the heavy quark forward-backward asymmetries and average B mixing using leptons in multihadronic events*, Z. Phys. **C70**(1996) 357.

[83] OPAL Collaboration, G. Alexander *et al.*, *Measurement of the heavy quark forward-backward asymmetries and average B mixing using leptons in multihadronic events*, Z. Phys. **C70**(1996) 357.

[84] OPAL Collaboration, R. Akers *et al.*, *A measurement of the forward-backward asymmetry of* $\mathrm{e^+e^-} \rightarrow \mathrm{c\overline{c}}$ *and* $\mathrm{e^+e^-} \rightarrow \mathrm{b\overline{b}}$ *at center-of-mass energies on and near the Z peak using D mesons*, Z. Phys. **C60**(1993) 601.

[85] OPAL Collaboration, R. Akers *et al.*, *QCD studies using a cone based jet finding algorithm for* $\mathrm{e^+e^-}$ *collisions at LEP*, Z. Phys. **C63**(1994) 197.

[86] OPAL Collaboration, G. Abbiendi *et al.*, *A measurement of* R_b *using a double tagging method*, Eur. Phys. J. **C8**(1999) 217, `arXiv:hep-ex/9810002`.

[87] OPAL Collaboration, R. Akers *et al.*, *A study of B meson oscillations using dilepton events*, Z. Phys. **C66**(1995) 555.

[88] OPAL Collaboration, K. Ackerstaff *et al.*, *Investigation of CP violation in B0* $\rightarrow$ *J/psi K0(s) decays at LEP*, Eur. Phys. J. **C5**(1998) 379, `arXiv:hep-ex/9801022`.

[89] OPAL Collaboration, R. Akers *et al.*, *Observations of* π*-B charge-flavor correlations and resonant* $B\,\pi$ *and* $B\,K$ *production*, Z. Phys. **C66**(1995) 19.

[90] OPAL Collaboration, P. D. Acton *et al.*, *The forward-backward asymmetry of* $\mathrm{e^+e^-} \rightarrow \mathrm{b\overline{b}}$ *and* $\mathrm{e^+e^-} \rightarrow \mathrm{c\overline{c}}$ *using leptons in hadronic Z decays*, Z. Phys. **C60**(1993) 19.

[91] A. B. Arbuzov, D. Y. Bardin, and A. Leike, *Analytic final state corrections with cut for* $\mathrm{e^+e^-} \rightarrow$ *massive fermions*, Mod. Phys. Lett. **A7**(1992) 2029.

[92] A. Djouadi, B. Lampe, and P. M. Zerwas, *A note on the QCD corrections to forward-backward asymmetries of heavy quark jets in Z decays*, Z. Phys. **C67**(1995) 123, `hep-ph/9411386`.

[93] G. Altarelli and B. Lampe, *Second order QCD corrections to heavy quark forward-backward asymmetries*, Nucl. Phys. **B391**(1993) 3.

[94] V. Ravindran and W. L. van Neerven, *Heavy flavour mass corrections to the longitudinal and transverse cross sections in* e^+e^- *collisions*, Phys. Lett. **B445**(1998) 206, hep-ph/9810258.

[95] S. Catani and M. H. Seymour, *Corrections of* $\mathcal{O}(\alpha_s^2)$ *to the forward-backward asymmetry*, JHEP **07**(1999) 023, hep-ph/9905424.

[96] D. Abbaneo *et al.*, The LEP Heavy Flavor Working Group, *QCD corrections to the forward-backward asymmetries of c and b quarks at the Z pole*, Eur. Phys. J. **C4**(1998) 185.

[97] OPAL Collaboration, *QCD corrections to the bottom and charm forward-backward asymmetries* (1997), OPAL-PN-284.

[98] *Combining heavy flavour electroweak measurements at LEP*, Nucl. Instrum. Meth. **A378**(1996) 101.

[99] G. Altarelli, N. Cabibbo, G. Corbo, L. Maiani, and G. Martinelli, *leptonic decay of heavy flavors: A theoretical update*, Nucl. Phys. **B208**(1982) 365.

[100] CLEO Collaboration, S. Henderson *et al.*, *Measurements of semileptonic branching fractions of B mesons at the upsilon (4s) resonance*, Phys. Rev. **D45**(1992) 2212.

[101] DELCO Collaboration, W. Bacino *et al.*, *The semileptonic decays of the D meson*, Phys. Rev. Lett. **43**(1979) 1073.

[102] MARK-III Collaboration, R. M. Baltrusaitis *et al.*, *A direct measurement of charmed* D^+ *and* D^0 *semileptonic branching ratios*, Phys. Rev. Lett. **54**(1985) 1976.

[103] OPAL Collaboration, K. Ackerstaff *et al.*, *An improved measurement of* R_b *using a double tagging method*, Z. Phys. **C74**(1997) 1.

[104] OPAL Collaboration, R. Akers *et al.*, *Updated measurement of the tau lifetime*, Phys. Lett. **B338**(1994) 497.

[105] OPAL Collaboration, P. D. Acton *et al.*, *Measurement of the tau lifetime*, Z. Phys. **C59**(1993) 183.

[106] JADE Collaboration, W. Bartel *et al.*, *Experimental studies on multi-jet production in* e^+e^- *annihilation at PETRA energies*, Z. Phys. **C33**(1986) 23.

[107] JADE Collaboration, S. Bethke *et al.*, *Experimental investigation of the energy dependence of the strong coupling strength*, Phys. Lett. **B213**(1988) 235.

[108] C. Peterson, T. Rognvaldsson, and L. Lonnblad, *JETNET 3.0: A versatile artificial neural network package*, Comput. Phys. Commun. **81**(1994) 185.

[109] OPAL Collaboration, O. Cooke and C. Jones, *Neural network electron and photon conversion identification,* OPAL Technical Note TN-556, (1998).

[110] OPAL Collaboration, P. D. Acton *et al.*, *Measurement of* $\gamma(\mathrm{Z} \to \mathrm{b\overline{b}})/\gamma(\mathrm{Z} \to \mathrm{hadrons})$ *using leptons*, Z. Phys. **C58**(1993) 523.

[111] OPAL Collaboration, The Muon Identification Working Group*, Identification of muons in hadronic* Z *decays,* OPAL Technical Note TN-107, (1992).

[112] OPAL Collaboration, D. Charlton, *Muon identification efficiency and background for Pass5 data,* OPAL Technical Note TN-211, (1994).

[113] OPAL Collaboration, D. Charlton and P. Gagnon, *Muon identification efficiency and background for PASS7 LEP1 data,* OPAL Technical Note TN-572, (1998).

[114] OPAL Collaboration, F. Fiedler, *A neural net for muon identification,* OPAL Technical Note TN-591, (1999).

[115] OPAL Collaboration, P. D. Acton *et al.*, *A measurement of the forward-backward charge asymmetry in hadronic decays of the Z*, Phys. Lett. **B294**(1992) 436.

[116] ALEPH Collaboration, A. Heister *et al.*, *Inclusive semileptonic branching ratios of b hadrons produced in Z decays*, Eur. Phys. J. **C22**(2002) 613, `hep-ex/0108007`.

[117] DELPHI Collaboration, P. Abreu *et al.*, *Measurement of the semileptonic b branching fractions and average B mixing parameter in Z decays*, Eur. Phys. J. **C20**(2001) 455, `hep-ex/0105080`.

[118] L3 Collaboration, M. Acciarri *et al.*, *Measurement of the branching ratios* $p_{\mathrm{B}} \to \mathrm{e}\nu X, \mu\nu X, \tau\nu X$ *and* νX, Z. Phys. **C71**(1996) 379.

[119] L3 Collaboration, M. Acciarri *et al.*, *Measurement of* R_{b} *and* $Br(b \to \ell\nu X)$ *at LEP using double-tag methods*, Eur. Phys. J. **C13**(2000) 47, `hep-ex/9909045`.

[120] OPAL Collaboration, G. Abbiendi *et al.*, *Measurements of inclusive semileptonic branching fractions of b hadrons in Z decays*, Eur. Phys. J. **C13**(2000) 225, `hep-ex/9906041`.

[121] DELPHI Collaboration, P. Abreu *et al.*, *Determination of $P(c \to D^{*+})$ and $BR(c \to \ell^+)$ at LEP1*, Eur. Phys. J. **C12**(2000) 209.

[122] OPAL Collaboration, G. Abbiendi *et al.*, *Measurement of the semileptonic branching ratio of charm hadrons produced in* $Z \to c\bar{c}$ *decays*, Eur. Phys. J. **C8**(1999) 573, `hep-ex/9810016`.

[123] OPAL Collaboration, H. Lafoux, *Measurement of heavy quark forward-backward asymmetries and average B mixing using leptons in multihadronic events,* OPAL Technical Note TN-326, (1995).

[124] G. Bahan and R. J. Barlow, *Identification of b jets using neural networks*, Comput. Phys. Commun. **74**(1993) 199.

[125] J. Hertz, A. Krogh, and R. Palmer, *Introduction to theory of neural computation*, Addison-Wesley, Wokingham, UK (1991).

[126] F. James and M. Roos, *'MINUIT' a system for function minimization and analysis of the parameter errors and correlations*, Comput. Phys. Commun. **10**(1975) 343.

[127] DELPHI Collaboration, P. Abreu *et al.*, *Measurement of the strange quark forward-backward asymmetry around the Z peak*, Eur. Phys. J. **C14**(2000) 613.

[128] OPAL Collaboration, K. Ackerstaff *et al.*, *Measurement of the branching fractions and forward-backward asymmetries of the Z into light quarks*, Z. Phys. **C76**(1997) 387, `arXiv:hep-ex/9707019`.

[129] M. Luscher, *A portable high quality random number generator for lattice field theory simulations*, Comput. Phys. Commun. **79**(1994) 100, `hep-lat/9309020`.

[130] F. James, *RANLUX: A FORTRAN implementation of the high quality pseudorandom number generator of Luscher*, Comp. Phys. Commun. **79**(1994) 111.

[131] L. N. Shchur and P. Butera, *The RANLUX generator: Resonances in a random walk test*, Int. J. Mod. Phys. **C9**(1998) 607, `hep-lat/9805017`.

[132] A. Djouadi and P. Zerwas, *Memorandum: QCD corrections to* $A_{\rm FB}^{\rm b}$, DESY-Report T-97-04 (Int. Report).

[133] CLEO Collaboration, D. Bortoletto *et al.*, *Inclusive and exclusive decays of B mesons to final states including charm and charmonium mesons*, Phys. Rev. **D45**(1992) 21.

[134] N. Isgur, D. Scora, B. Grinstein, and M. B. Wise, *Semileptonic B and D decays in the quark model*, Phys. Rev. **D39**(1989) 799.

[135] ALEPH Collaboration, R. Barate *et al.*, *Measurements of* $BR(b \to \tau^- \bar{\nu}_\tau X)$ *and* $BR(b \to \tau^- \bar{\nu}_\tau \mathrm{D}^{*+} X)$ *and upper limits on* $BR(B^- \to \tau^- \bar{\nu}_\tau)$ *and* $BR(b \to s\nu\bar{\nu})$, Eur. Phys. J. **C19**(2001) 213, `hep-ex/0010022`.

[136] DELPHI Collaboration, P. Abreu *et al.*, *Upper limit for the decay* $B^- \to \tau^- \bar{\nu}_\tau$ *and measurement of the* $b \to \tau\bar{\nu}_\tau X$ *branching ratio*, Phys. Lett. **B496**(2000) 43.

[137] L3 Collaboration, M. Acciarri *et al.*, *Measurement of the inclusive* $B \to \nu_\tau X$ *branching ratio*, Phys. Lett. **B332**(1994) 201.

[138] L3 Collaboration, M. Acciarri *et al.*, *Measurement of the branching ratios* $b \to e\nu X, \mu\nu X, \tau\nu X$ *and* νX, Z. Phys. **C71**(1996) 379.

[139] ALEPH Collaboration, R. Barate *et al.*, *A measurement of* R_b *using mutually exclusive tags*, Phys. Lett. **B401**(1997) 163.

[140] DELPHI Collaboration, P. Abreu *et al.*, *A precise measurement of the partial decay width ratio* $R_\mathrm{b}^0 = \gamma_{\mathrm{b}\overline{\mathrm{b}}}/\gamma_{had}$, Eur. Phys. J. **C10**(1999) 415.

[141] ALEPH Collaboration, R. Barate *et al.*, *Measurement of the fraction of hadronic Z decays into charm quark pairs*, Eur. Phys. J. **C4**(1998) 557.

[142] ALEPH Collaboration, R. Barate *et al.*, *Study of charm production in Z decays*, Eur. Phys. J. **C16**(2000) 597, `hep-ex/9909032`.

[143] DELPHI Collaboration, P. Abreu *et al.*, *Measurements of the Z partial decay width into* $\mathrm{c\overline{c}}$ *and multiplicity of charm quarks per b decay*, Eur. Phys. J. **C12**(2000) 225.

[144] OPAL Collaboration, K. Ackerstaff *et al.*, *Measurement of* $f(c \to \mathrm{D}^{*+} X)$, $f(b \to \mathrm{D}^{*+} X)$ *and* $\gamma_{\mathrm{c\overline{c}}}/\gamma_{had}$ *using* D^{*+} *mesons*, Eur. Phys. J. **C1**(1998) 439, `hep-ex/9708021`.

[145] OPAL Collaboration, G. Alexander *et al.*, *A study of charm hadron production in* $Z \to \mathrm{c\overline{c}}$ *and* $Z \to \mathrm{b\overline{b}}$ *decays at LEP*, Z. Phys. **C72**(1996) 1.

[146] SLD Collaboration, K. Abe *et al.*, *Measurement of* R_b *using a vertex mass tag*, Phys. Rev. Lett. **80**(1998) 660, `hep-ex/9708015`.

[147] N. de Groot, *The couplings of heavy quarks to the Z boson*, Nucl. Phys. Proc. Suppl. **115**(2003) 267.

[148] SLD Collaboration, K. Abe *et al.*, *A measurement of* R_{c} *using the SLD detector,* talk given at 29th International Conference on High-Energy Physics (ICHEP 98), Vancouver, Canada, Jul 23 - 29 1998.

[149] OPAL Collaboration, K. Ackerstaff *et al.*, *A study of B meson oscillations using hadronic Z decays containing leptons*, Z. Phys. **C76**(1997) 401, hep-ex/9707009.

[150] Working Group on LEP Energy Collaboration, L. Arnaudon *et al.*, *Measurement of the mass of the Z boson and the energy calibration of LEP*, Phys. Lett. **B307**(1993) 187.

R. Assmann *et al.*, *Calibration of centre-of-mass energies at LEP1 for precise measurements of Z properties*, Eur. Phys. J. **C6**(1999) 187.

R. Assmann *et al.*, LEP Energy Working Group, *Evaluation of the LEP centre-of-mass energy for data taken in 2000,* LEPEWG 01/01, http://lepecal.web.cern.ch/LEPECAL/.

[151] ALEPH Collaboration, A. Heister *et al.*, *Measurement of the forward-backward asymmetry in* $\mathrm{Z} \to \mathrm{b\overline{b}}$ *and* $\mathrm{Z} \to \mathrm{c\overline{c}}$ *decays with leptons*, Eur. Phys. J. **C24**(2002) 177.

[152] DELPHI Collaboration, J. Abdallah *et al.*, *Measurement of the forward-backward asymmetries of* $\mathrm{e^+e^-} \to \mathrm{Z} \to \mathrm{b\overline{b}}$ *and* $\mathrm{e^+e^-} \to \mathrm{Z} \to \mathrm{c\overline{c}}$ *using prompt leptons*, Eur. Phys. J. **C34**(2004) 109, arXiv:hep-ex/0403041.

[153] L3 Collaboration, M. Acciarri *et al.*, *Measurement of the* $\mathrm{e^+e^-} \to \mathrm{Z} \to \mathrm{b\overline{b}}$ *forward-backward asymmetry and the B mixing parameter using prompt leptons*, Phys. Lett. **B448**(1999) 152.

[154] ALEPH Collaboration, A. Heister *et al.*, *Measurement of* $A_{\mathrm{FB}}^{\mathrm{b}}$ *using inclusive b-hadron decays*, Eur. Phys. J. **C22**(2001) 201, arXiv:hep-ex/0107033.

[155] DELPHI Collaboration, W. Liebig, *Precision measurements of the b forward-backward asymmetry at the Z pole from LEP*, Nucl. Phys. Proc. Suppl. **115**(2003) 208, see also *Determination of* A_{FB}^{b} *using inclusive charge reconstruction and lifetime tagging at the Z pole*, DELPHI 2003-056-CONF-676.

[156] L3 Collaboration, M. Acciarri *et al.*, *Measurement of the effective weak mixing angle by jet-charge asymmetry in hadronic decays of the Z boson*, Phys. Lett. **B439**(1998) 225.

[157] ALEPH Collaboration, R. Barate *et al.*, *The forward-backward asymmetry for charm quarks at the Z*, Phys. Lett. **B434**(1998) 415, arXiv:hep-ex/9811015.

[158] DELPHI Collaboration, P. Abreu *et al.*, *Measurement of the forward-backward asymmetry of c and b quarks at the Z pole using reconstructed D mesons*, Eur. Phys. J. **C10**(1999) 219, `arXiv:hep-ex/9903074`.

[159] The LEP Electroweak Working Group*, Combined preliminary data on Z parameters from the LEP experiments and constraints on the Standard Model,* CERN-PPE/94-187. Contributed to the 27th International Conference on High-Energy Physics - ICHEP 94, Glasgow, Scotland, UK, Jul 20 - 27 1994.

[160] SLD Collaboration, K. Abe *et al.*, *Improved direct measurement of* $\mathcal{A}_\mathrm{b}$ *and* $\mathcal{A}_\mathrm{c}$ *at the Z pole using a lepton tag*, Phys. Rev. Lett. **88**(2002) 151801, `hep-ex/0111035`.

[161] SLD Collaboration, K. Abe *et al.*, *Measurement of* $\mathcal{A}_\mathrm{c}$ *with charmed mesons at SLD*, Phys. Rev. **D63**(2001) 032005, `hep-ex/0009035`.

[162] SLD Collaboration, K. Abe *et al.*, *Improved direct measurement of the parity-violation parameter* $\mathcal{A}_\mathrm{b}$ *using a mass tag and momentum-weighted track charge.*, Phys. Rev. Lett. **90**(2003) 141804, `hep-ex/0208044`.

[163] SLD Collaboration, K. Abe *et al.*, *Direct measurement of* $\mathcal{A}_\mathrm{b}$ *in Z decays using charged kaon tagging*, Phys. Rev. Lett. **83**(1999) 1902.

[164] SLD Collaboration, K. Abe *et al.*, *Direct measurement of* $\mathcal{A}_\mathrm{b}$ *using charged kaons at the SLD detector* (1999), contributed paper to EPS 99, Tampere, Finland, HEP 99 #6473 , `hep-ex/9907066`.

SLD Collaboration, K. Abe *et al.*, *Direct measurement of* $\mathcal{A}_\mathrm{b}$ *using charged vertices,* talk given at the 30th International Conference on High- Energy Physics (ICHEP 2000), Osaka, Japan, 27 Jul - 2 Aug 2000.

[165] SLD Collaboration, K. Abe *et al.*, *Direct measurement of* $\mathcal{A}_\mathrm{c}$ *using inclusive charm tagging at the SLD detector* (1999), `hep-ex/9907065`.

[166] L. Lyons, D. Gibaut, and P. Clifford, *How to combine correlated estimates of a single physical quantity*, Nucl. Instrum. Meth. **A270**(1988) 110.

[167] The LEP Electroweak Working Group, the SLD Heavy Flavor Group and the SLD Electroweak Working Group*, A combination of preliminary electroweak measurements and constraints on the Standard Model* (2003), the most recent combinations are published at `http://lepewwg.web.cern.ch/LEPEWWG.`, `hep-ex/0312023`.

[168] D. Abbaneo *et al.*, The LEP Electroweak Working Group, the SLD Heavy Flavor Group and the SLD Electroweak Working Group*, A combination of preliminary electroweak measurements and constraints on the Standard Model* (2001), `hep-ex/0112021`.

[169] The LEP Electroweak Working Group and the SLD Heavy Flavor Group the SLD Electroweak Working Group, *A combination of preliminary electroweak measurements and constraints on the Standard Model* (2001), `hep-ex/0103048`.

[170] D. Abbaneo *et al.*, The LEP Electroweak Working Group, the SLD Heavy Flavor Group and the SLD Electroweak Working Group, *A combination of preliminary electroweak measurements and constraints on the Standard Model,* CERN-EP-2000-016. Contribution to the 1999 summer conferences.

[171] D. Abbaneo *et al.*, The LEP Electroweak Working Group and the SLD Heavy Flavor Group, *A combination of preliminary electroweak measurements and constraints on the Standard Model,* CERN-PPE/97-154. Contribution to the Europhysics Conference on High-Energy Physics - EPS-HEP 1997 in Jerusalem and Lepton-Photon 1997 in Hamburg.

[172] D. Abbaneo *et al.*, The LEP Electroweak Working Group and the SLD Heavy Flavor Group, *A combination of preliminary electroweak measurements and constraints on the Standard Model,* CERN-PPE/96-183. Contribution to the International Conference on High-Energy Physics - ICHEP 96 in Warsaw, Poland.

[173] The LEP Electroweak Working Group, *A combination of preliminary lep electroweak measurements and constraints on the Standard Model,* CERN-PPE/95-172. Contributed to the 1995 Europhysics Conference on High-Energy Physics - EPS-HEP, Brussels, Belgium, 27 Jul - 2 Aug 1995 and to the 17th International Symposium on Lepton-Photon Interactions, Beijing, China, Aug 10 - 15 1995.

[174] The LEP Electroweak Working Group, *Updated parameters of the Z resonance from combined preliminary data of the LEP experiments,* CERN-PPE/93-157. Contributed to European Conf. on High-Energy Physics, Marseille, France, Jul 22 - 28 1993 and the Int. Symp. on Lepton Photon Interactions at High Energies, Ithaca, NY, Aug 10 - 15 1993.

[175] F. Jegerlehner, *Renormalizing the Standard Model*, in *Testing the Standard Model* - TASI-90, Proceedings: *Theoretical Advanced Study Institute in Elementary Particle Physics,* Boulder, Colorado, Jun 3 - 27 1990, edited by M. Cvetic and P. Langacker, World Scientific, Singapore (1991) 916, PSI-PR-91-08.

[176] ACFA Linear Collider Working Group Collaboration, K. Abe *et al.*, *Particle physics experiments at JLC* (2001), `hep-ph/0109166`.

[177] American Linear Collider Working Group Collaboration, T. Abe *et al.*, *Linear collider physics resource book for Snowmass 2001. 1: Introduction* (2001), hep-ex/0106055.

[178] R. Brinkmann *et al.*, *TESLA: The superconducting electron positron linear collider with an integrated X-ray laser laboratory. Technical Design Report. Pt. 2: The accelerator* (2001), DESY-01-011.

ECFA/DESY LC Physics Working Group Collaboration, J. A. Aguilar-Saavedra *et al.*, *TESLA Technical Design Report. Pt. 3: Physics at an e+e- Linear Collider* (2001), hep-ph/0106315.

T. Behnke, S. Bertolucci, R. D. Heuer, R. Settles, *et al.*, *TESLA: The superconducting electron positron linear collider with an integrated X-ray laser laboratory. Technical Design Report. Pt. 4: A detector for TESLA* (2001), DESY-01-011.

[179] ATLAS and CMS Collaboration, J. G. Branson *et al.*, *High transverse momentum physics at the Large Hadron Collider: The ATLAS and CMS Collaborations*, Eur. Phys. J. direct **C4**(2002) N1.

ATLAS detector and physics performance. Technical design report. Vol. 2, CERN-LHCC-99-15.

CMS, the Compact Muon Solenoid: Technical proposal, CERN-LHCC-94-38.

[180] W. S. McCulloch and W. Pitts, *A logical calculus of the ideas immanent in nervous activity*, Bull. Math. Biophysics **5**(1943) 115.

[181] F. Rosenblatt, *The perceptron: A probabilistic model for information storage and organisation in the brain*, Psychological Review **65**(1958) 386.

[182] A. B. Arbuzov, *Light pair corrections to electron positron annihilation at LEP/SLC* (1999), hep-ph/9907500.

Danksagung

Mein Dank gilt all den Menschen, die mir die Erfüllung meines Kindheits- und Jugendtraums ermöglichten, einige der Naturgesetze kennenzulernen, in deren universeller Anwendbarkeit und Einfachheit sich die ästhetische Schönheit und innere Einheit der Naturphänomene widerspiegelt. Während meiner Jugend hätte ich sicher nie geahnt, dass dieses Interesse meinen Lebensweg bis zur Erlangung des Doktorgrades bestimmen würde.

Ich danke meinem Doktorvater Herrn Prof. Dr. Rolf-Dieter Heuer, sowie Herrn Dr. Ties Behnke – wissenschaftlicher Leiter der Gruppe „Forschung mit Leptoncollidern“ (FLC) am „Deutschen Elektronensynchrotron“ (DESY), der ich zugeordnet war – dafür, dass sie mir die Möglichkeit zur Promotion im Bereich der physikalischen Grundlagenforschung eröffneten. Beide haben mich nicht nur bei der Suche nach einem geeigneten Thema unterstützt, sondern auch meine Arbeit stets mit großem Interesse verfolgt. Ihre wissenschaftliche Kompetenz und menschliche Integrität haben die vorliegende Arbeit in vielfältiger Weise beflügelt.

Das Forschungszentrum DESY hat mich nicht nur durch die Finanzierung meines Lebensunterhaltes, sondern auch maßgeblich durch die Schaffung einer ausgezeichneten Arbeitsumgebung unterstützt.

Am erfolgreichen Abschluss meiner Promotion waren weiterhin Herr Prof. Dr. Friedrich-Wilhelm Büßer, Frau Prof. Dr. Beate Naroska und Herr Dr. Hans Dirk Rüter beteiligt, denen ich für die Anfertigung der Gutachten beziehungsweise für die Leitung der Disputation danke.

Ohne Zweifel stellte der einjährige Forschungsaufenthalt am „European Organization for Nuclear Research“ (CERN) einen der Höhepunkte im Rahmen meiner Promotion dar. Während dieser Zeit habe ich eng mit Herrn Dr. Richard Hawkings und Frau Dr. Pippa Wells zusammengearbeitet und dadurch viel über die Physik schwerer Quarks, die elektroschwache Wechselwirkung, den OPAL-Detektor, Analysemethoden, neuronale Netze und vieles mehr gelernt. Besonderer Dank gebührt den Herrn Doctores Michael Hauschild, David Plane, Christoph Rembser und Matthias Schröder, die mir stets auch bei nichtwissenschaftlichen Problemen inner- und außerhalb des CERN mit Rat und Tat zur Seite standen. Bedanken möchte ich mich auch bei Mrs. Dawn Hudson, die mir immer eine wertvolle Hilfe im Umgang mit der CERN Bürokratie war.

Eine angenehme und freundschaftliche Atmosphäre herrscht in der DESY-Gruppe FLC, bei deren Mitgliedern ich mich dafür ebenfalls bedanken möchte. Besonders zu erwähnen sind hier zunächst meine ehemaligen Bürokollegen Herr Dr. Götz Gaycken, sowie die Herrn Dr. Peter Wienemann, Dr. Thorsten Kuhl und Hendrik Meyer, die durch viele interessante und vielseitige Diskussionen zu dieser

Arbeit beigetragen haben. Dem FLCschen Haus- und Hof-Fotografen, Herrn Andreas Imhof, und Frau Blanka Sobloher danke ich für die Hilfe beim Layout bzw. Ausmerzen zahlloser Tippfehler. Weiterhin danke ich den Herren Marius Groll, Niels Meyer, Dr. Roman Pöschl und (in Kürze Prof.) Dr. Klaus Desch, die mir gerade in der Endphase meiner Promotion in vielerlei Hinsicht geholfen haben. Natürlich gilt mein Dank auch unserer Gruppensekretärin Frau Ramona Matthes für die gute und freundschaftliche Zusammenarbeit – auch über weite Entfernungen hinweg – bei der Lösung so manchen Verwaltungsproblems. Besonders herzlich möchte ich mich bei Frau Sabine Platz für das Durchsehen meines Manuskriptes bedanken.

Ohne die Unterstützung meiner Eltern, meiner Großeltern und meiner Schwester, sowie die ausgleichende Wirkung meiner Freunde, vor allem Andreas Matusch, Claudia Hengstel und Michael Schmidt, wäre die Fertigstellung der Dissertation in der vorliegenden Form nicht möglich gewesen. Ihnen allen bin ich tief verbunden.

Mir bleibt die Hoffnung, dass ich im Gegensatz zu dem einen oder anderen früheren Fall nicht die wichtigsten Personen vergessen habe. Aus diesem Grund danke ich zum Schluß, aber deswegen nicht weniger herzlich, all den zahllosen Personen in- und außerhalb der Institute CERN und DESY, die mich unterstützt haben, ohne die ihnen eigentlich zustehende namentliche Erwähnung.